Search for Excited Leptons with pp Collisions at $\sqrt{s} = 13\,\text{TeV}$ with the CMS Experiment at the LHC

Von der Fakultät für Mathematik, Informatik und Naturwissenschaften der RWTH Aachen University zur Erlangung des akademischen Grades eines Doktors der Naturwissenschaften genehmigte Dissertation

vorgelegt von

Jonas Till Roemer, M. Sc. RWTH Aachen University

aus

Braunschweig

Berichter:
Univ.-Prof. Dr. rer. nat. Thomas Hebbeker
Apl.-Prof. Dr. rer. nat. Oliver Pooth

Tag der mündlichen Prüfung: 26.11.2020

Abstract

This thesis presents the search for excited electrons and muons in proton-proton collisions at the CMS detector at a center-of-mass energy of 13 TeV. It analyses the collisions delivered by the LHC in 2016 and 2017. Excited leptons are a direct consequence of compositeness in the fermion sector. They are produced by a contact interaction and can decay via the radiation of a photon, W or Z boson, or via a contact interaction. This thesis investigates the latter three decay channels. No significant excess over the Standard Model expectation is observed. The high-mass exclusion limit reaches 5.6 TeV which is the current world-leading limit for excited leptons. This thesis proceeds to compare the sensitivity of all decay channels extensively for a wide range of model parameters. It concludes with an outlook to the HL-LHC era, which can increase the mass limit by 25% and improve the low-mass sensitivity in terms of maximally excluded values of the substructure scale by up to 100%.

Zusammenfassung

In dieser Dissertation wird eine Suche nach angeregten Elektronen und Myonen präsentiert, welche eine direkte Konsequenz einer möglichen Substruktur von Fermionen sind. Das untersuchte Modell stellt eine Erweiterung des Standardmodells dar. Die vorgestellten Ergebnisse beruhen auf den vom CMS Detektor in den Jahren 2016 und 2017 aufgenommenen Daten von Proton-Proton-Kollisionen am LHC. Angeregte Leptonen werden über eine Kontaktwechselwirkung erzeugt und zerfallen entweder über die Abstrahlung eines Photons, eines W oder Z Bosons, oder einer weiteren Kontaktwechselwirkung. In dieser Arbeit werden die drei letztgenannten Zerfallskanäle untersucht. Die Analyse zeigt keine signifikante Abweichung von der Erwartung des Standardmodells. Es können angeregte Leptonen mit einer Masse von bis zu 5.6 TeV ausgeschlossen werden. Dies ist derzeit die weltweit beste Ausschlussgrenze. Des Weiteren wird die Sensitivität aller Zerfallskanäle für eine breite Palette von Modellparametern ausführlich verglichen. Abschließend wird der erwartete Zuwachs der Sensitivität für die HL-LHC-Ära untersucht: Die Ausschlussgrenze für schwere angeregte Leptonen wird sich um etwa 25% erhöhen. Der maximal ausgeschlossene Wert der Substrukturskala kann sich für leichte angeregte Leptonen sogar verdoppeln.

Contents

1 | Introduction

The quest of particle physicists is one which has been exciting humankind for ages: Understanding what our universe, our world, consists of and how it functions. Back, four hundred years before Christ, the ancient Greek philosophers Leucippus and his pupil Democritus described our universe as a composition of indivisible objects called atoms [1]. Though being motivated only philosophically, this concept is surprisingly similar to our modern understanding of particle physics. We describe our universe as a composition of fundamental building blocks that interact with each other in different ways. The Standard Model incorporates the knowledge gained during several decades of experiments and theoretical work and provides remarkable predictions for how our universe functions [2–4]. Yet, the road towards the Standard Model was bumpy at best. For a long time, humanity thought that atoms are the elemental building blocks before we found that they consist of much smaller sub-particles. We had to extend our theory and adapt it numerous times due to discoveries or predictions of new particles. Today, we ask ourselves: Is this it? Is this the theory that describes the universe? But we already know the answer: It is not. Despite its tremendously successful predictions, it fails to explain several phenomena like gravity or dark matter.

This thesis investigates a possible extension of the Standard Model which would continue the story outlined above: Maybe, the fundamental particles of the Standard Model are not fundamental – just like atoms that were once thought to be the building blocks of our universe. Perhaps, even smaller particles exist and constitute the matter of our world. Possibly, the quarks and leptons of our Standard Model are not elemental but composite structures. Such composite particles could be produced in excited states, just like atoms can be excited. The de-excitation would leave a signature in our modern particle detectors that we can observe and link back to the composite particle.

But how could we observe such decays? During the last decades, the field of high energy physics saw a rapid improvement of accelerator technology and scale of accelerators. The most modern accelerator, the *Large Hadron Collider*, has a circumference of 27 km and is the largest machine ever built by humankind. It accelerates protons up to currently 6.5 TeV per beam and collides them in four interaction points. The collision at these extremely high energies rips the protons apart and creates new particles in the process. The *Compact Muon Solenoid* is located in one of the interaction points. This particle detector can record and measure the debris of the collisions with unprecedented precision. Using those debris, we can reconstruct the initial interaction of the protons and look, among many other things, for possible signs of excited leptons.

This dissertation searches for excited electrons and muons. Excited leptons can decay in four distinct ways: Via radiation of a photon, a W boson, or a Z boson, or by a contact interaction leading to a final state with two leptons and two jets. This thesis focuses on the latter three decay channels. The first one has been analyzed recently by the CMS collaboration, and the results are publically available at Ref. [5].

The thesis commences with an overview of the Standard Model and the model of excited leptons (Chap. 2). It continues with a description of the Large Hadron Collider and the Compact Muon

Solenoid in chapter 3 before it outlines the reconstruction and identification algorithms to identify physical objects in the measured data of the detector (Chap. 4). Afterward, chapter 5 analyzes the signatures that an excited lepton decay would leave in the detector. Next, chapter 6 reports the related Standard Model processes and their description and concludes the introductory chapters. Chapter 7 explains the analysis strategy of all three decay channels. The next chapter (Chap. 8) compares the sensitivity of all four decay channels for a wide range of model parameters. This section follows a forecast of the sensitivity for the expected full dataset, which will be collected in the next fifteen years of operation in chapter 9 before chapter 10 concludes this thesis with a summary of the obtained results.

Parts of the presented results have been published by the CMS collaboration in Ref. [6].

2 Theoretical Foundation for Standard Model and Excited Leptons

This chapter introduces the theoretical foundation for this analysis. It focuses on the description of excited leptons – A beyond Standard Model (BSM) model in which leptons are not pointlike elemental particles but composite constructs.

The first part of this chapter (section 2.1) introduces some conventions used for the remainder of this thesis. Secondly, I will provide a very condensed summary of the SM (section 2.2). The final part (section 2.3) focuses entirely on the description of excited leptons.

2.1 Conventions

In contrast to the commonly used SI unit system, this thesis uses *natural units* for most parts. Natural units are better suited to express quantities at LHC's typical energy scale and use physical constants to express quantities like, for example, velocities as a fraction of the speed of light c and electrical charges as multiple of the elemental charge e. To achieve this goal, the natural unit scheme sets some natural constants like $\hbar$ and c to unity. These conditions define all other units. The base unit is GeV. One eV is the energy a particle with charge e acquires when it passes an accelerating field of 1 V. At the LHC, the typical energy scale is much larger than one eV, so we use the prefix 10^9 to avoid large powers of ten. In natural units masses, momentum and energy have the same unit because the speed of light is set to unity. Distances and time have the unit GeV^{-1}.

2.2 The Standard Model of Particle Physics

Before we can test new physics models we need to define the reference, the *known physics*. It is described by the Standard Model of particle physics (SM). The SM is a well tested and highly successful model [2–4] which describes all observed particles and the dynamics of their interactions. It allowed to predict several new particles, most recently the Higgs boson [8–13] which was discovered by the CMS and ATLAS collaboration in 2012 [14,15]. Due to its well-known properties, I do not describe the Standard Model here but refer to the literature (e.g. [4, 16, 17]) and only provide a brief overview of the particles and their interactions.

The SM is a quantum field theory which differentiates between particles with integer spin (*bosons*) and half-integer spin (*fermions*). Table 2.1 lists all known elemental fermions with their properties

[1] Neutrino masses are predicted by the SM to be zero. The observation of neutrino oscillations indicate, that they must not be massless [7].

Table 2.1: List of all fermions described in the Standard Model of particle physics. q_e, q_w and q_s are the electromagnetic, weak and strong charge respectively. Values are taken from Ref. [4].

	Generation	Particle	Mass / MeV	Spin	q_e	q_w	q_s
Leptons	1st	e	0.511	1/2	−1	1	0
		ν_e	$< 2\,\text{eV}$[1]	1/2	0	1	0
	2nd	μ	105.7	1/2	−1	1	0
		ν_μ	< 0.18[1]	1/2	0	1	0
	3rd	τ	1776.9	1/2	−1	1	0
		ν_τ	< 18.2[1]	1/2	0	1	0
Quarks	1st	u	2.2	1/2	2/3	1	1
		d	4.7	1/2	−1/3	1	1
	2nd	c	1027	1/2	2/3	1	1
		s	93	1/2	−1/3	1	1
	3rd	t	173 GeV	1/2	2/3	1	1
		b	4018	1/2	−1/3	1	1

Table 2.2: List of all bosons described in the Standard Model of particle physics. q_e, q_w and q_s are the electromagnetic, weak and strong charge respectively. Values are taken from Ref. [4].

Mediated Force	Particle	Mass / GeV	Spin	q_e	q_w	q_s
Electromagnetic	γ	0	1	0	0	0
Weak	$W^\pm$	80.4	1	±1	1	0
	Z	91.2	1	0	1	0
Strong	g	0	1	0	0	1
	H	125.1	0	0	1	0

like mass and charge. The leptons form left-handed isopsin doublets while the right-handed charged leptons form singlets. Neutrinos with right-handed chirality do not exist in the Standard Model and have not been observed yet. Table 2.2 displays the known bosons which act as mediators for the strong-, weak-, and electromagnetic force, as well as the Higgs boson. The particle has to carry the proper charge to participate in an interaction. For example only electrical charged particles and the photon can interact via the electromagnetic interaction and only particles carrying color charge can interact strongly. The SM describes all known interactions of particles besides gravity, which the description does not include.

2.3 Composite Leptons

Despite its powerful and successful predictions, the Standard Model of particle physics has several shortcomings. For example, it does not explain the three-family structure of quarks and leptons. Furthermore, it lacks an explanation for their hierarchically structured masses. A deeper – yet unresolved – substructure of quarks and leptons might resolve these puzzles of the Standard Model.

In such compositeness models, quarks and leptons are bound states of new, actual fundamental

particles - just like protons and neutrons consist of quarks. The new fundamental particles are often called *preons* [18]. We can only make assumptions about the dynamics of the preon interactions because of the lacking theoretical description. The preons are bound together by a new force which is not part of the Standard Model. This model assumes that quarks and leptons consist of similar preons.

Composite fermions could manifest themselves in excited states similar to the existence of excited meson or baryon states. Decays of such excited leptons would leave striking signatures in the detector.

In this section, I present the theory and its historical development (section 2.3.1), the production mechanism and cross section (section 2.3.2), decay modes (section 2.3.3) and an excursion to excited quarks (section 2.3.4). Ultimately, I review existing limits from previous experiments (section 2.3.5).

2.3.1 Introduction to Compositeness and Excited Fermions

The first theoretical models were presented in the middle of the sixties by F. E. Low [19], ten years before the discovery of the tau-lepton, during the postulation of the quark system. Afterward, several papers [18, 20–25, 25–27, 27–33] refined the theory and developed a deeper understanding of both the production of excited states and their decays. They discuss possibilities to observe excited leptons in different experiments and colliders, e.g., e^+e^- colliders [25–28], ep [26–28], or pp / $p\overline{p}$ colliders [18, 22–25, 29, 30]. Other papers interpret their results e.g. the excess observed by the UA1 [34] and UA2 [35] collaboration at the SPS collider in the $Z \to \ell\ell\gamma$ channel [31–33] in terms of excited lepton models.

The paper "Excited-quark and -lepton production at hadron colliders" from U. Baur, M. Spira, and P. M. Zerwas written in 1990 [18] provides the theoretical foundation for this thesis. I will follow the notation used in this paper and use it as the reference if not stated otherwise.

In general, the compositeness of leptons can change the magnetic moment a of the ground state. Such contributions would occur linearly in the mass ratio of the ground state (m_ℓ) and the excited lepton ($m^\star$) [21]:

$$\delta a \propto \frac{m_\ell}{m^\star}. \tag{2.1}$$

However, the magnetic moment of electrons and muons is measured incredibly precise by various experiments, e.g. the E821 experiment [36]. Therefore, the masses of excited leptons must be in the order of 100 TeV to conform with those measurements [21].

Yet, the linear term vanishes by introducing a chiral symmetry between left- and right-handed excited leptons and only quadratic terms $\delta a \propto \left(\frac{m_\ell}{m^\star}\right)^2$ (e.g. due to vacuum polarization) remain. Consequently, the indirect limits on the excited lepton masses are much less stringent and allow accelerators like the LHC to probe excited leptons with unprecedented sensitivity.

We assume that excited leptons have spin and weak isospin equal to $\frac{1}{2}$ and sort them into isospin-doublets for example for first-generation leptons:[2]

$$\begin{pmatrix} \nu_e \\ e \end{pmatrix}_L, \quad e_R^- \begin{pmatrix} \nu_e^\star \\ e^\star \end{pmatrix}_L, \quad \begin{pmatrix} \nu_e^\star \\ e^\star \end{pmatrix}_R \tag{2.2}$$

The gauge mediated transition from left-handed SM leptons f_L to right-handed excited leptons $\bar{f}_R^\star$ is described by the Lagrangian

$$\mathcal{L}_{\mathrm{GI}} = \frac{1}{2\Lambda} \bar{f}_R^\star \sigma^{\mu\nu} \left(g_s f_s \frac{\lambda^a}{2} G_{\mu\nu}^a + g f \frac{\boldsymbol{\tau}}{2} \cdot \boldsymbol{W}_{\mu\nu} + g' f' \frac{Y}{2} B_{\mu\nu} \right) f_L + \mathrm{h.c.}, \tag{2.3}$$

where $\sigma^{\mu\nu}$ are the Pauli matrices, Λ is the energy scale of the interaction, and g_s, $g = e \sin\theta_W$, $g' = e \cos\theta_W$ are the strong and electroweak couplings. $G_{\mu\nu}^a$, $\boldsymbol{W}_\mu$ and $B_{\mu\nu}$ denote the gluon, SU(2), and U(1) gauge fields with their generators λ^a, $\boldsymbol{\tau}$, and Y, respectively. The parameter Λ is common for all three interactions. However, according to Prof. Dr. D. Zeppenfeld the energy scales for the different interactions are independent from each other and the *couplings* f_s, f and f'[3] rescale the shared parameter Λ for the different interactions (private communication, 16. July 2019).

At hadron colliders, the production cross section can be strongly enlarged by including contact interactions (CI). The CI allows direct preon interactions. The corresponding Lagrangian has the form

$$\mathcal{L}_{\mathrm{CI}} = \frac{g_\star^2}{2\Lambda} \frac{1}{2} j^\mu j_\mu \tag{2.4}$$

with the fermion current

$$j_\mu = \eta_L \bar{f}_L \gamma_\mu f_L + \eta_L' \bar{f}_L^\star \gamma_\mu f_L^\star + \eta_L'' \bar{f}_L^\star \gamma_\mu f_L + \mathrm{h.c.} + (L \to R). \tag{2.5}$$

$g_\star^2$ is chosen to be equal to 4π, γ_μ are the Gamma matrices, and the left-handed η-factors η_L are set to unity while the right-handed factors η_R are set to zero for simplicity [18]. The underlying preon interaction is hidden behind the interaction scale Λ.[4] For center-of-mass energies approaching the characteristic scale Λ, this pointlike vertex needs to be resolved in order to avoid an unphysical rise of the cross section [18]. Such an interaction is only possible if quarks and leptons have common substituents.

The scales Λ in equation 2.3 and 2.4 are independent within the theory as they describe entirely different interactions (private communication with Prof. Dr. D. Zeppenfeld, 16. July 2019). However, the notation was chosen to have a common parameter. The couplings f_s, f, and f' may be used to scale the gauge interaction relative to the CI.

2.3.2 Production of Excited Leptons

The CI Lagrangian (equation 2.4) allows for two kinds of production processes: Associated production and pair production. In the associated production, a single excited lepton is produced together with a Standard Model lepton while pair production creates two excited leptons. The Feynman diagrams for both processes are shown in figure 2.1. The cross section is given by

$$\sigma(q\bar{q} \to \ell\bar{\ell}^\star, \ell^\star\bar{\ell}) = \frac{\pi}{6\hat{s}} \left(\frac{\hat{s}}{\Lambda^2}\right)^2 \left(1 + \frac{v}{3}\right) \left(1 - \frac{m^{\star 2}}{\hat{s}}\right)^2 \left(1 + \frac{m^{\star 2}}{\hat{s}}\right) \tag{2.6}$$

and

$$\sigma(q\bar{q} \to \ell^\star\bar{\ell}^\star) = \frac{\pi\tilde{v}}{12\hat{s}} \left(\frac{\hat{s}}{\Lambda^2}\right)^2 \left(1 + \frac{\tilde{v}}{3}\right) \tag{2.7}$$

for the single and double excited lepton production, respectively. $\hat{s} = x_1 x_2 s$ is the center-of-mass energy of the parton system with the two parton momentum fractions x_1 and x_2, v is short for $\frac{\hat{s}-m^{\star 2}}{\hat{s}+m^{\star 2}}$ and $\tilde{v} = \left(1 - 4\frac{m^{\star 2}}{\hat{s}}\right)^{1/2}$. x_1 and x_2 are determined by the parton density function (c.f. section 3.2). The functional behaviour of the cross section can be seen in figure 2.2. The cross section is calculated by Pythia 8 [37] for $\Lambda = m^\star$ in green and $\Lambda = 10\,\text{TeV}$ in blue.[5] Especially for high masses the cross section of the associated production is much larger compared to the pair production. Hence, the discovery potential is larger for associated production if the background can be suppressed.

At hadron colliders, the cross section is dominated by the CI process for couplings close to unity [18]. Hence, the gauge mediated production is neglected for this thesis. However, for lepton colliders the gauge mediated production channel is dominant as described in the next section.

Recently, theorists investigated the validity of the model for masses close to the compositeness scale Λ by examining partial wave unitarity [38]. As mentioned above, the CI Lagrangian is only valid for masses below the compositeness scale, but we did not implement a specific bound. Figure 2.3 shows the unitarity bound in the Λ-mass-plane. The grey dash-dotted line denotes the bound $\Lambda < m^\star$. The unitarity bound is calculated using Monte Carlo simulation. The three purple lines correspond in decreasing thickness to the unitarity bounds obtained when 100%, 95%, and 50% of the simulated events pass the implemented criterion. In the area below the purple lines, the unitarity condition is violated and the model not valid. The considerable distance between the different lines calls for further investigations, and the authors do not provide a recipe for how to apply the calculated bounds. Therefore, this thesis does not include these bounds in the discussion of the sensitivity since even the 95% criterion significantly differs from the 100% line, and both bounds are not considerably more stringent at high masses compared to the $\Lambda < m^\star$ bound.

[2] Excited neutrinos may be massive and can form right-handed states.

[3] f sometimes denotes the couplings and sometimes fermions. The meaning should be clear from the context.

[4] Λ has the same value as for the GI Lagrangian. Differences are expressed using the couplings as explained above.

[5] The production cross section is independent of the couplings f and f' since we only take the CI production into account.

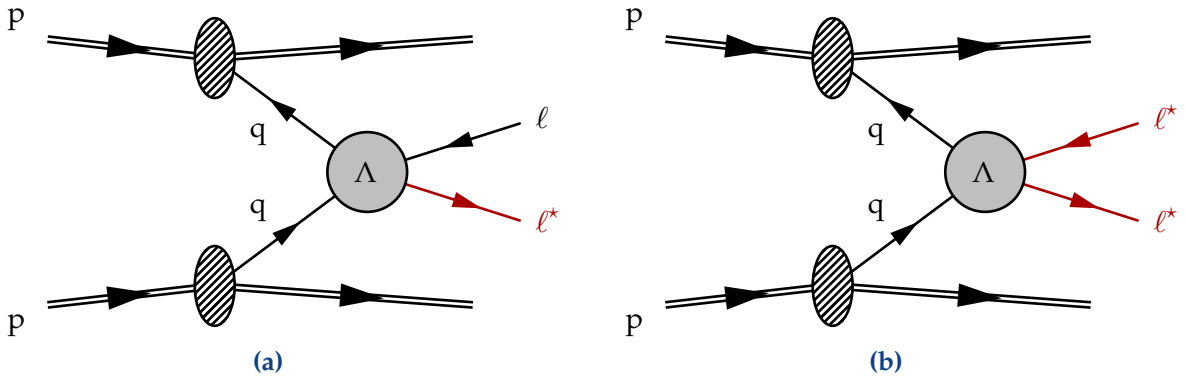

Figure 2.1: Feynman diagrams for (a) associated and (b) pair production of excited leptons at a hadron collider via a contact interaction. The unknown preon interaction is hidden behind a four-vertex at the scale Λ.

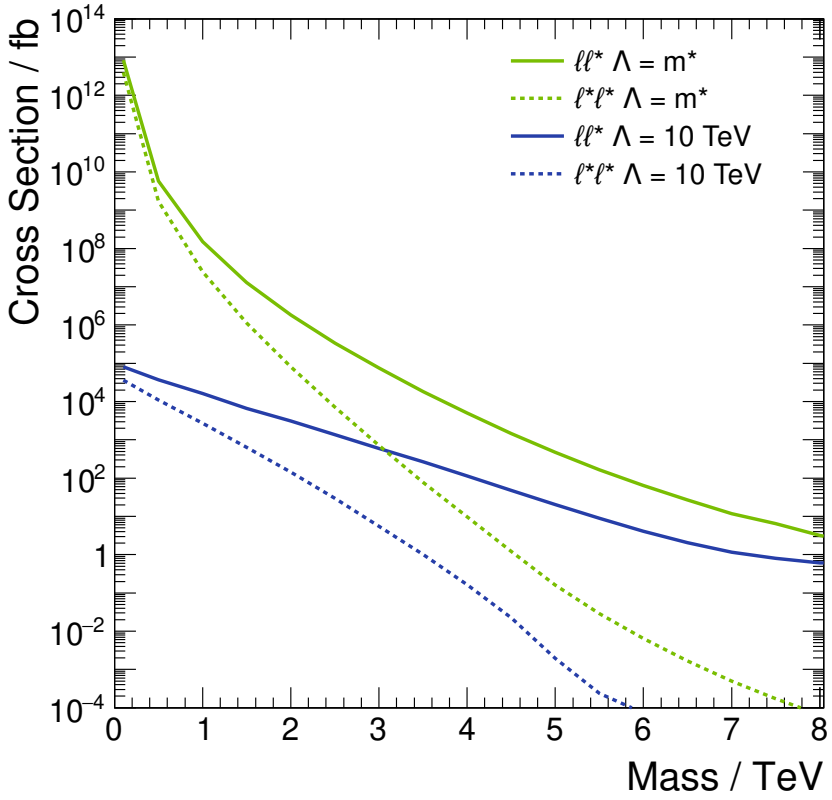

Figure 2.2: Contact interaction production cross sections for associated (solid) and pair (dashed) production of excited leptons at $\sqrt{s} = 13\,\text{TeV}$ for $\Lambda = 10\,\text{TeV}$ in green and $\Lambda = m^{\star}$ in blue. The cross section is calculated using Pythia 8 [37]. The cross section for associated production is much larger than for pair production.

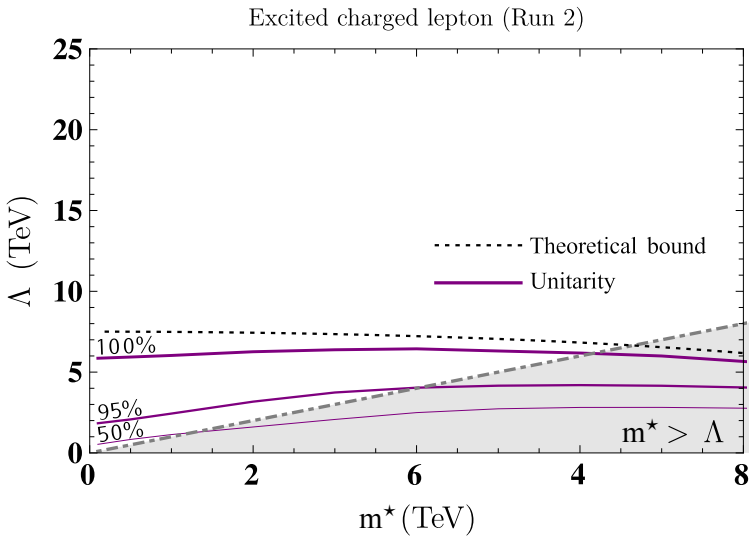

Figure 2.3: Unitarity bounds for the production of excited leptons at the LHC. The purple lines correspond to the bounds obtained when 100%, 95%, and 50% of the simulated events pass the implemented criterion. Everything below is excluded. The grey area indicates the area where $\Lambda < m^{\star}$. The black dashed line represents the theoretical unitarity bound for $\hat{s} = s$. Adapted from [38].

Production of Excited Leptons at Lepton Colliders

At e^+e^- and ep colliders excited leptons can be produced by exciting the electron with a Z/γ as can be seen in figure 2.4a. For an e^+e^- collider excited leptons can also produced in pairs by exciting both electrons. At ep colliders only one electron is available. For single production, the spectator particle is often emitted at small angles and escapes the detector acceptance leading to an $e\gamma$ final state [39].

It is not possible to produce excited muons with the t-channel diagram as lepton flavor must be conserved in this model. Excited muons can only be produced in the s-channel diagram shown in figure 2.4b. It can produce either electrons or muons or any other fermions. However, it is only possible for e^+e^- colliders but not for ep colliders. Hence, only excited electrons can be produced in ep colliders and not excited muons. The s-channel is also the dominant production mechanism for pair-produced excited leptons in e^+e^- colliders since the t-channel diagram involves two $\ell\ell^{\star}V$ couplings.

Pair production in the s-channel is of special interest because it can exclude excited leptons independent of Λ since no $\ell\ell^{\star}V$ vertices are present. The downside is the lower production limit of maximal $m^{\star} = \sqrt{s}/2$.

2.3.3 Decay Channels of Excited Leptons

Having reviewed the production mechanisms, I will now focus on the decay of excited leptons. As described at the beginning of section 2.3 the transition between an excited lepton and a Standard Model lepton can be mediated by gauge interactions (GI, see equation 2.3) or by contact interactions (CI, see equation 2.4). Three different decay channels exist for the GI decay: The

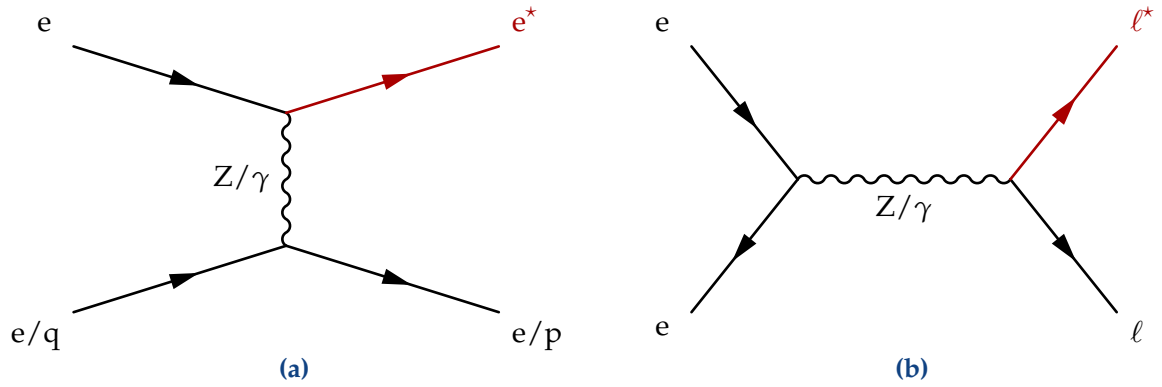

Figure 2.4: Production of excited leptons in ep and e^+e^- colliders. (a) shows the t-channel diagram with the excitation of one of the electrons. Pair production is also possible in case of an e^+e^- collider by exciting the second electron as well. For ep colliders only one electron is available. Only excited electrons can be produced by the t-channel diagram due to lepton flavor conservation. Production of excited muons is only possible via the s-channel diagram displayed in (b). Pair production is also possible.

gamma channel, the Z channel, and the W channel. The latter two channels are only allowed for excited leptons, which are heavier than the Z and W. The gamma and Z channel lead to two oppositely charged same-flavor leptons with a photon or a Z. The W channel lets the excited charged lepton decay into a neutrino and a W boson. The CI decay leads to final states with two same-flavor, opposite-charge leptons and a pair of similar fermions.

The partial decay widths for gauge mediated decays are [18]

$$\Gamma(f^\star \to f\gamma) = \frac{1}{4}\alpha f_\gamma^2 \frac{m^{\star 3}}{\Lambda} \tag{2.8}$$

and

$$\Gamma(f^\star \to fV) = \frac{1}{8}\frac{g_V^2}{4\pi} f_V^2 \frac{m^{\star 3}}{\Lambda}\left(1 - \frac{m_V^2}{m^{\star 2}}\right)\left(2 + \frac{m_V^2}{m^{\star 2}}\right), \tag{2.9}$$

with

$$f_\gamma = fT_3 + f'\frac{Y}{2}, \tag{2.10}$$

$$f_Z = fT_3\cos^2\theta_W - f'\frac{Y}{2}\sin^2\theta_W, \tag{2.11}$$

$$f_W = \frac{f}{\sqrt{2}}. \tag{2.12}$$

$T_3 = -\frac{1}{2}$ is the third component of the weak isospin of the excited lepton and $Y = -1$ the hypercharge of $f^\star$. $g_W = e/\sin\theta_W$ and $g_Z = g_W/\cos\theta_W$ are the Standard Model couplings of the W and Z boson. e is equal to $\sqrt{4\pi\alpha}$ with the finestructure constant α. The term $1 - \frac{m_V^2}{m^{\star 2}}$ in equation 2.9 dampens the partial decay width into W and Z bosons for light excited leptons close to the mass of the boson while the factor becomes constant for $m^\star \gg m_V$.

The partial decay width of the CI decay is given by

$$\Gamma(f^\star \to f + f'\bar{f}') = \frac{m^\star}{96\pi}\left(\frac{m^\star}{\Lambda}\right)^4 N_C' S' \tag{2.13}$$

with $N_C' = 3$ the number of quark colors and a combinatorial factor S' defined as[6]

$$S' = 1 \text{ for } f \neq f', \tag{2.14}$$

$$S' = \frac{4}{3} \text{ for } f = f' \text{ and quarks,} \tag{2.15}$$

$$S' = 2 \text{ for } f = f' \text{ and leptons.} \tag{2.16}$$

The Feynman diagrams for the four decays are shown in figure 2.5. The photon decay channel leads to an $\ell\ell\gamma$ as the photon is already stable. The Z can decay into hadrons, leptons, or neutrinos leading to either four lepton final states or two leptons with two neutrinos or two leptons and two jets. For a boosted topology with a transverse momentum of more than $p_T(Z) > 200\,\text{GeV}$, the two jets are close to each other and may only be resolved in a single wide-cone jet. Substructure algorithms can help to distinguish these jets originating from a Z decay from a simple QCD jet. Section 4.4 describes these algorithms. The W channel results in final states with one lepton, one neutrino, and either two jets or another lepton and neutrino from the W decay. If the W decays hadronically, both jets can merge in the same way as described for the Z decay. The last decay mode, the CI decay, produces final states either with four leptons, or two leptons and two neutrinos, or two leptons and two jets. For this decay channel, the jets will be resolved as there is no intermediate gauge boson in the decay chain. Section 5 describes the expected kinematic properties of the different decay channels in detail.

Branching Fractions

The partial decay widths can be used to study the branching fractions depending on the model parameters $m^\star$, Λ, f, and f'. The interesting mass range which can be probed by the LHC is in the order of a few TeV. Constraints on Λ were discussed in section 2.3.2. Λ has to be at least smaller than $m^\star$. f and f' should be in the order of one [18] but can also certainly be smaller than unity or even negative.[7]

Dependence on $m^\star/\Lambda$ Figure 2.6 shows the dependence of the branching fraction for the four different decay channels over the ratio of the mass of the excited lepton and Λ. Low masses and high values of Λ are on the left side while high masses close to Λ are on the right-hand side. The term suppressing the decay width for light excited leptons with masses close to the W and Z mass are ignored, i.e. excited leptons are assumed to be sufficiently heavy. f and f' are set to unity.

The CI decay channels dominate for high masses while the GI decays have higher branching fractions for low masses relative to Λ. The ratio of $m^\star/\Lambda$ does scale the total branching fraction

[6] f denotes here fermions and not the coupling.
[7] The partial decay width will always be positive as the couplings occur quadratically in equation 2.8 and eq. 2.9.

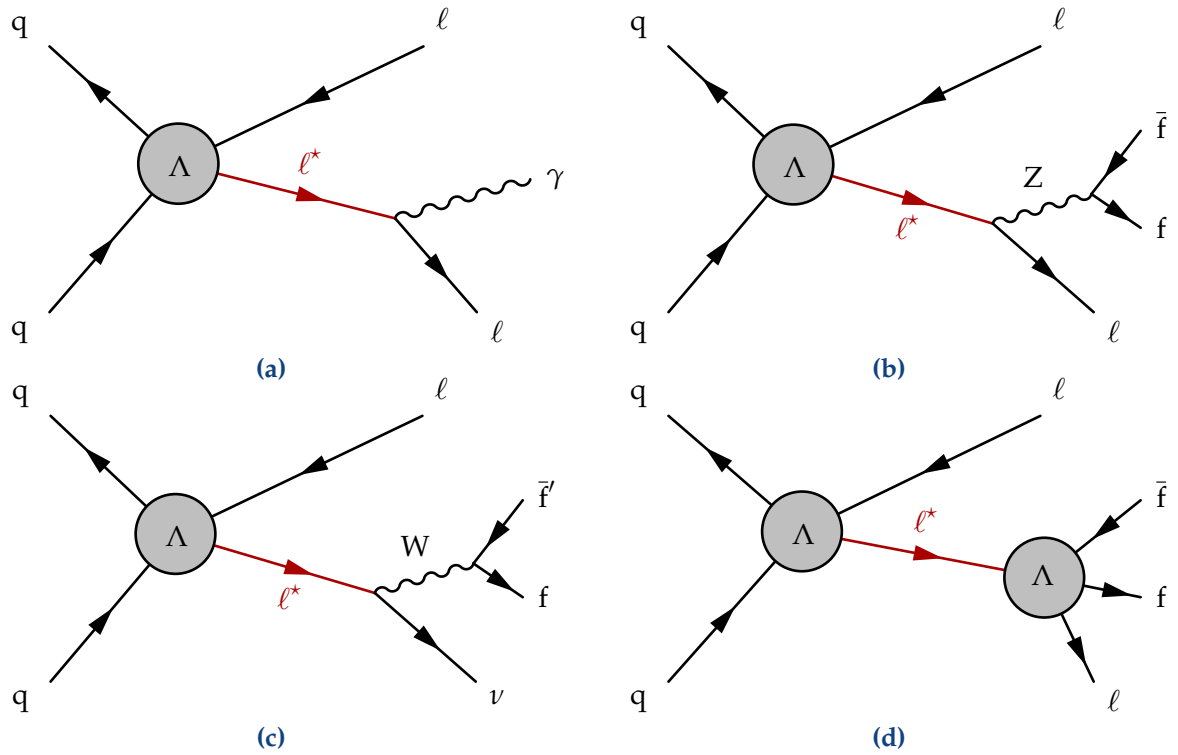

Figure 2.5: Feynman diagrams for the gauge mediated (a) photon, (b) the Z, (c) the W decay channel, and (d) the CI channel. In (b) and (d) f is either a quark, charged lepton or neutrino, while in (c) f and f' are either two different quarks or a charged lepton and its corresponding neutrino.

of GI decays but does not influence the relative strength of the GI channels with respect to each other. For this choice of f and f', the W channel is dominating, followed by the photon channel and the Z channel.

A more complete study involving the dependence of all model parameters is presented in chapter 8.1.

Hadronic and Leptonic Final States Figure 2.6 shows the inclusive branching fractions. Figure 2.7 compares the relative hadronic and leptonic branching fractions of the Z, W, and CI channel. The photon in the $\ell\ell\gamma$ channel is stable and does not decay. Due to the color factor the hadronic decays are dominant for all three decay channels. *Charged leptonic* decay means the decay into two charged leptons and *neutrinos* the decay into two neutrinos. For the W channel, the *leptonic* decay means the decay into a charged lepton and corresponding neutrino.

2.3.4 Excursion: Excited Quarks

The signal model provides a common framework for excited leptons and excited quarks. While not directly related to my work, I still want to devote one section to excited quarks for completeness.

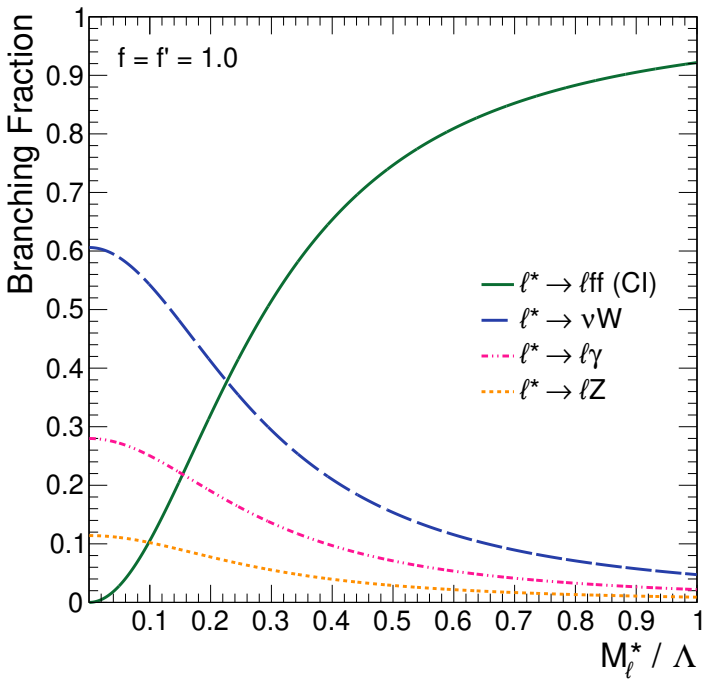

Figure 2.6: Branching fraction of GI decays (W- blue, γ- pink, Z- yellow) and CI decay (green) over m^*/Λ. The mass must be smaller than Λ constraining the ratio to be between zero and unity.

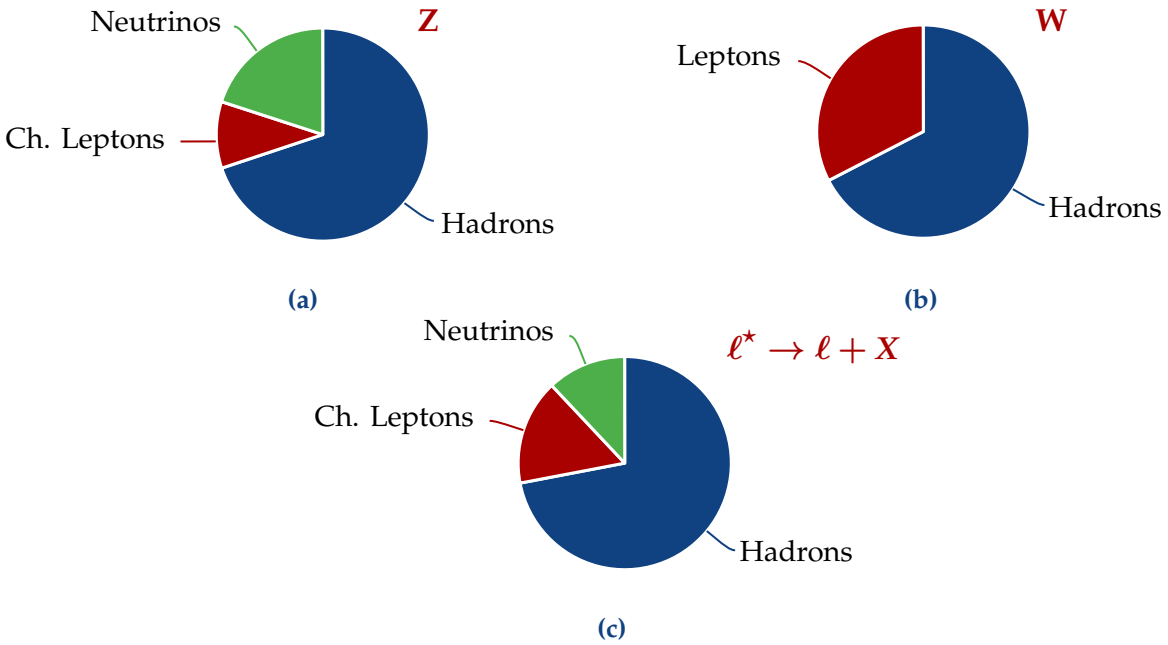

Figure 2.7: Fraction of hadronic decays, charged leptonic decays and decays into neutrinos of (a) the Z boson, (b) the W boson, and (c) the CI decay of an excited lepton.

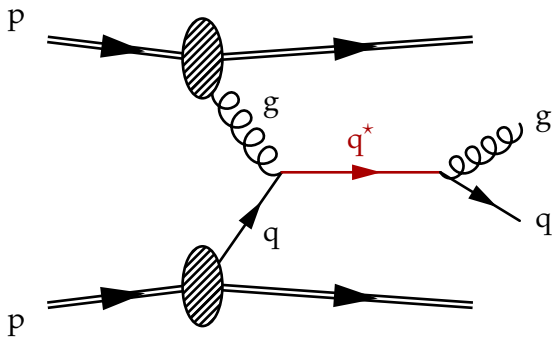

Figure 2.8: Feynman diagram showing the gauge mediated production of an excited quark using the quark-gluon fusion and its subsequent gauge mediated decay via the same interaction.

The gauge mediated interaction is already described in the Lagrangian in formula 2.3. The part relevant for excited quarks is especially the coupling to the gluon field $G^a_{\mu\nu}$. It also introduces the coupling f_s which is treated analogously to f and f'. The CI described by the Lagrangian in formula 2.4 functions in the same way as for excited leptons.

In addition to the vertices discussed for excited leptons, the $qgq^\star$ vertex is allowed for excited quarks due to the first term in the GI Lagrangian in equation 2.3. The new vertex allows an excited quark to decay into an SM quark and a gluon. The decay width is given by

$$\Gamma(q^\star \to qg) = \frac{1}{3}\alpha_s f_s^2 \frac{m^{\star 3}}{\Lambda} \tag{2.17}$$

with the coupling f_s and the strong coupling constant α_s.

It also adds another important production method in addition to the CI at hadron colliders: The excited lepton is produced by the gauge mediated excitation of an SM quark by a gluon. Figure 2.8 shows the Feynman diagram for the production of an excited lepton by quark-gluon fusion and its decay into a quark and a gluon.

2.3.5 Existing Limits

Many collaborations at various accelerators have searched for evidence of compositeness of fermions. This list does not aim for completeness as it would be beyond the scope of this thesis. I instead chose some results representing different accelerators and collaborations. First, I present results from electron-positron colliders. After that, I discuss findings from electron-proton colliders before finally moving over to hadron colliders. The last section is devoted to excited quarks.

Electron-Positron Colliders

In the past, multiple electron-positron colliders were constructed in different parts of the world. I will present results from collaborations located at the Positron-Electron Tandem Ring Accelerator

(PETRA) [40], the Positron-Electron Project (PEP) [41], the Transposable Ring Intersecting STorage Accelerator in Nippon (TRISTAN) [42], and the Large Electron-Positron Collider (LEP) [43,44].[8]

PETRA was located at DESY, Hamburg and started operation in 1979 delivering electron-positron collisions at a center-of-mass energy of 36.7 GeV and hosted several experiments:

- The Mark J published a search for excited electrons and muons in 1982 [45]. They looked for excited muons in the $\mu^+\mu^-\gamma\gamma$ and the $\mu^+\mu^-\gamma$ channel utilizing the photon decay channel for both associated and pair production. By relating the $e^+e^- \to \mu^\star\mu^\star \to \mu^+\mu^-\gamma\gamma$ and the $e^+e^- \to \mu^+\mu^-$ cross sections excited muons below 10 GeV were excluded. Using the associated production channel, they were able to exclude excited leptons below 30 GeV depending on the coupling to the electromagnetic field strength tensor.[9] Additionally, excited electrons would manifest themselves in a modulation of the $e^+e^- \to \gamma\gamma$ cross section by mixings of excited electron exchanges in the t-channel diagram. Looking at the differential cross section excited electrons with masses of up to 58 GeV were excluded depending on the coupling of excited electrons to the electromagnetic field strength tensor.
- The JADE collaboration performed a similar search for excited electrons yielding comparable results [46].
- The CELLO collaboration performed an additional search for excited taus, excluding them up to 22.7 GeV [47].

The DELCO experiment was located at the PEP (Positron-Electron Project) at Stanford, which delivered electron-positron collisions at a center-of-mass energy of 29 GeV. It went into operation in 1980. DELCO published a search for excited electrons in 1986 [48], excluding excited electrons depending on the coupling constant up to 27 GeV. They performed the search in the $e^-\gamma(e^-)$ final state, where one of the electrons escape the detector acceptance.

The predecessor of KEKB, TRISTAN, was able to deliver electron-positron collisions with a center-of-mass energy of 64 GeV starting from 1986. The AMY [49], TOPAZ [50], and VENUS [51] experiments searched for excited leptons in photon decay channels for single and pair production and the $e^+e^- \to \gamma\gamma$ channel. The limits of the different experiments coincide and exclude excited leptons below 30.2 GeV (29.9 GeV) for the electron (muon) channel and extend the exclusion range dependent on the coupling parameter[10] λ up to around 55 GeV for excited electrons and muons. The TOPAZ collaboration performed a search for excited taus in the $\tau\tau\gamma\gamma$ final state, excluding them for masses below 29 GeV [50]. Figure 2.9 presents the results compared to results obtained by the ALEPH and UA2 collaborations.[11]

The electron-positron collider reaching the highest energy center-of-mass energy to date was the Large Electron-Proton Collider (LEP) with 209 GeV. All four collaborations hosted by LEP published search results for excited leptons yielding similar exclusion limits:

[8] Production mechanisms for electron-proton accelerators are discussed in section 2.3.2.

[9] The Mark J collaboration – as many others in the early years of excited lepton searches – did not use the notation introduced in this thesis. As future experiments were able to provide much stronger limits on excited leptons, I will not go into detail of the coupling strengths used in this notation.

[10] As mentioned above, the notation changed over time. λ is defined as $m^\star f/\sqrt{2}\Lambda$.

[11] I summarize their results further down in this chapter.

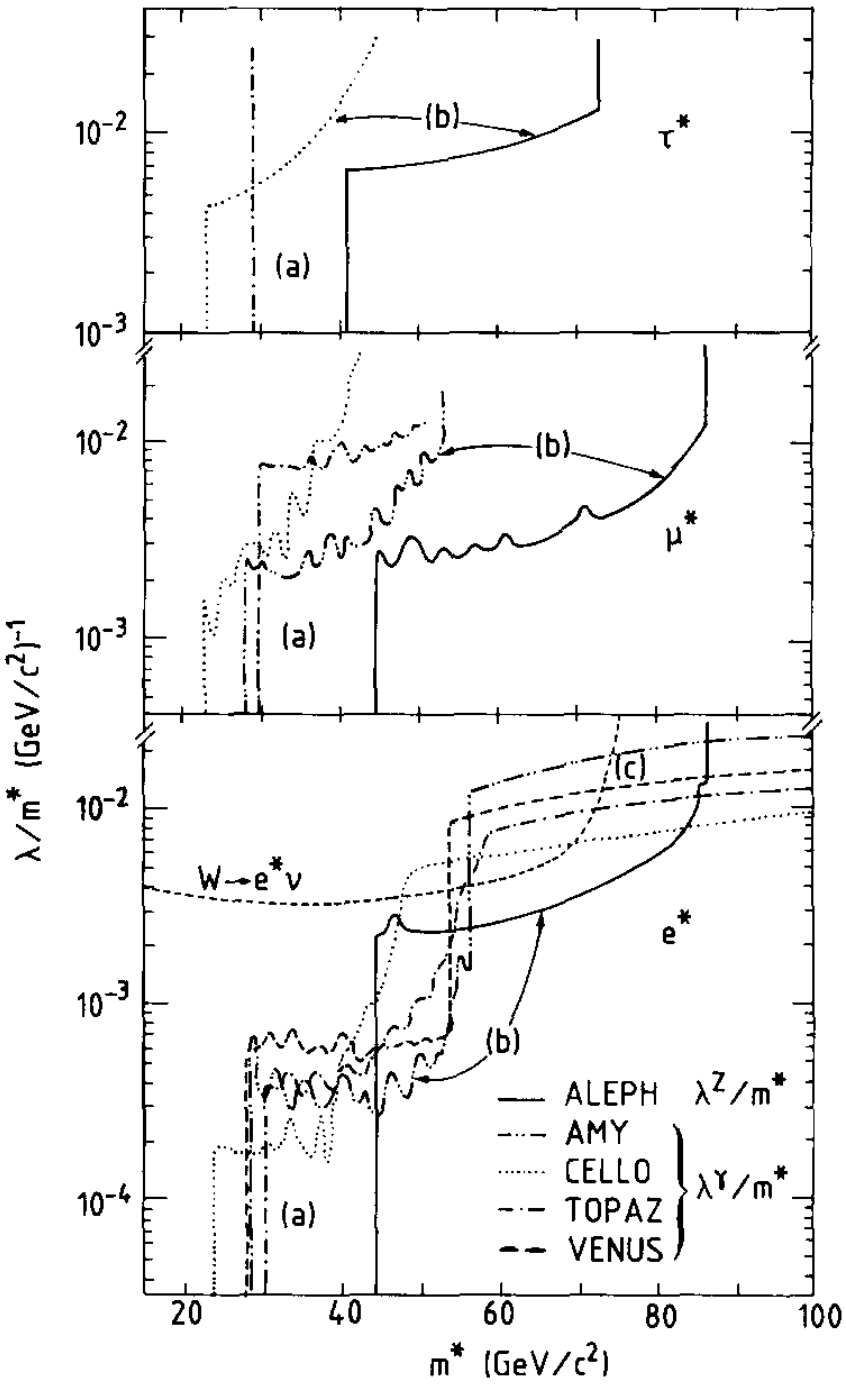

Figure 2.9: Limits obtained by the ALEPH collaboration in comparison with the results obtained by the AMY, CELLO, TOPAS, VENUS, and UA2 collaborations. The line of the W limit corresponds to the limit presented by the UA2 collaboration, the others are labeled in the legend. The top panel shows the limits for excited taus, the middle one for excited muons, and the bottom one for excited electrons which are all distinct particles. (a), (b), and (c) correspond to the $\ell\ell\gamma\gamma$, $\ell\ell\gamma$ and eγ, and $\gamma\gamma$ reactions, respectively. Everything on the upper-left side of the curves is excluded. λ is a parameter used in the old notation and is proportional to the inverse of Λ. Figure taken from Ref. [52].

- The ALEPH collaboration published a search for excited electrons, muons, and taus for single and pair production in the photon channels for collisions at center-of-mass energies of 130–140 GeV [53]. They excluded excited leptons below $m^\star = 44.6\,\text{GeV}$ (41.2 GeV for excited taus) and extended the exclusion mass range up to approximately 130 GeV depending on Λ.
- The DELPHI collaboration analyzed collision data at a center-of-mass energy of 183–209 GeV in the photon, W, and Z channel [39]. Using the pair production analysis, they excluded excited electrons, muons, and taus below masses of $94 - 103\,\text{GeV}$. They extended the exclusion range using the single production mechanism up to the center of mass energy, depending on Λ.
- Even before DELPHI, L3 published a very similar search with comparable results [54].
- The fourth experiment, OPAL, also searched for excited leptons in the photon, W, and Z channel in collision data recorded at $\sqrt{s} = 161 - 172\,\text{GeV}$ [55]. They later extended the search in the $\ell\ell\gamma\gamma$, $\ell\ell\gamma$ and $e\gamma$ channels using data recorded at $\sqrt{s} = 183 - 209\,\text{GeV}$ [56]. The results are similar to the ones reported by the other collaborations.

Electron-Proton Colliders

Despite recent discussions about electron-proton colliders (e.g., LHeC [57]), they are much more rare than electron-positron colliders. The only relevant accelerator for excited lepton searches was the Hadron-Elektron-RingAnlage (HERA) [58] at DESY, Hamburg. It delivered electron-proton and positron-proton collisions at a maximum center-of-mass energy 318 GeV by colliding a 27.5 GeV lepton beam with a nearly 1 TeV proton beam. It went into operation in 1992 and was shut down in 2007. Both multi-purpose experiments performed searches for excited leptons:

- H1 performed a search for excited electrons[12] in the photon, W, and Z channel [59]. They excluded excited electrons up to 272 GeV. The cross section limits are generally worse than the ones obtained by LEP but extend to higher masses due to the larger available energy in the collision. H1 also incorporated the CI production mechanism for the first time, although it turned out to be small compared to the GI production. They did not consider CI decays.
- The ZEUS collaboration also published a search for excited electrons, neutrinos, and quarks [60]. However, they used only one-tenth of the dataset H1 was using, which resulted in worse mass limits of 228 GeV for excited electrons.

Proton-(Anti)Proton Colliders

Proton-proton or proton-antiproton colliders can deliver collisions at much higher energies than accessible with electron-based colliders. Proton-antiproton colliders provide larger cross sections at low center-of-mass energies as the valence quarks have opposite charge. For large center-of-mass energies like LHC's [61], the difference is negligible [62] since sea quarks and gluons carry most of the energy.[13] Searches for excited leptons were performed at experiments

[12] See section 2.3.2 for an explanation why only excited electrons can be produced in ep colliders.
[13] See section 3.2.

located at the Super Proton-Antiproton Synchroton [63] at CERN, the Tevatron [64] at Fermilab, Illinois (USA) and most recently the LHC. The Super Proton-Antiproton Synchroton ($Sp\bar{p}S$) was a proton-antiproton collider reaching center-of-mass energies up to 630 GeV. The accelerator is still in use today – not as a collider but as a pre-accelerator for the LHC. It is now called Super Proton Synchroton (SPS). The Tevatron was a proton-antiproton collider, reaching higher center-of-mass energies of 1.96 TeV. It was shut down in 2011. The LHC is the newest high-energy particle accelerator to date, reaching a center-of-mass energy of 13 TeV by colliding two proton beams. Section 3.1 describes the LHC in detail. Besides the UA2 analysis, the relevant production mechanism is the contact interaction.

- The UA2 collaboration located at the $Sp\bar{p}S$ searched for excited electrons in W decays leading to $e\gamma\nu$ final states and excluded them up to 70 GeV [65].
- The CDF collaboration was one of the two collaborations looking for excited leptons at the Tevatron accelerator. They excluded excited electrons up to 879 GeV by analyzing the $ee\gamma$ channel [66].[14] CDF also performed a search for excited muons in the gauge mediated and contact interaction production mode and excluded them below 853 GeV [68]. The resulting limits are presented in figure 2.10. The figure shows also the results from the H1, ZEUS, and OPAL collaboration.
- The other experiment at Tevatron was D0. They excluded excited muons up to 618 GeV for $\Lambda = 1$ TeV [67].[15]
- The LHC delivered collisions at $\sqrt{s} = 7$, 8 and 13 TeV. The ATLAS collaboration excluded excited electrons and muons up to 2.2 TeV in the $\ell\ell\gamma$ channel [69] and excited muons up to 2.8 TeV in the CI decay channel using the 8 TeV data set [70]. Most recently, ATLAS published a search for excited electrons featuring the 13 TeV dataset taken in 2016 in the CI channel (eeqq) and the W decay channel ($e\nu W$), yielding upper limits of 4.8 TeV [71]. Figure 2.11a presents this most recent result.
- Using the 7 TeV dataset, the CMS collaboration excluded excited electrons and muons in the $\ell\ell\gamma$ channel up to 1.9 TeV [72]. Adding the 8 TeV data and a new analysis in the $\ell\ell$Z channel increased the sensitivity up to 2.5 and 2.3 TeV for $f = -f' = 1$ [73].[16] CMS published a 13 TeV search as well, utilizing the 2016 data set. They excluded excited electrons (muons) below 3.9 TeV (3.8 TeV) for $\Lambda = M$ by analyzing the $\ell\ell\gamma$ final state [5]. The result for the muon channel is shown in figure 2.11b.

In conclusion, the search for excited leptons has a nearly forty-year long history while the first theory papers date even 55 years back. New generations of particle accelerators provided us with phenomenal opportunities to perform beyond the Standard Model searches increasing the exclusion limit from a few GeV to several TeV.

The next section will describe our latest accelerator, the LHC, and the Compact Muon Solenoid experiment.

[14] The CDF collaboration assumed a production via CI but neglected any decays via contact interactions. They were also affected by a bug in the signal MC generator yielding too large cross-sections [67]. This let to too aggressive limits.

[15] The limits would have been competitive to the ones obtained by CDF if they had used the same cross sections and branching fractions as the CDF collaboration.

[16] See section 2.3.3 for more information about the couplings.

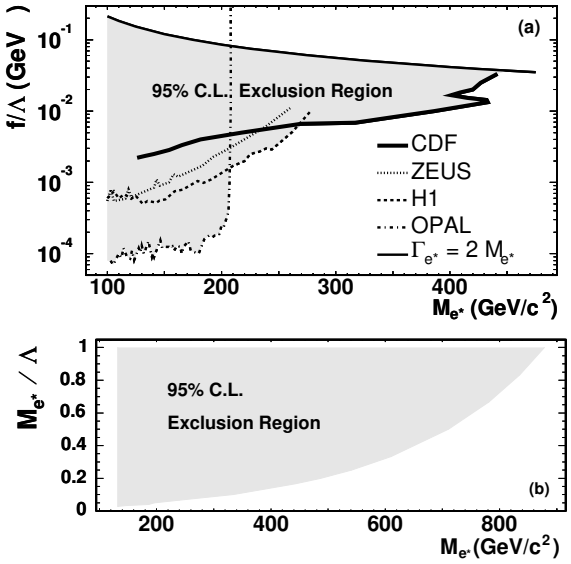

Figure 2.10: Limits (uncorrected) obtained by the CDF collaboration in the gauge mediated channel (upper plot) and the contact interaction channel (lower plot). The limits are compared to results from the ZEUS, H1, and OPAL collaboration. Figure taken from Ref. [66].

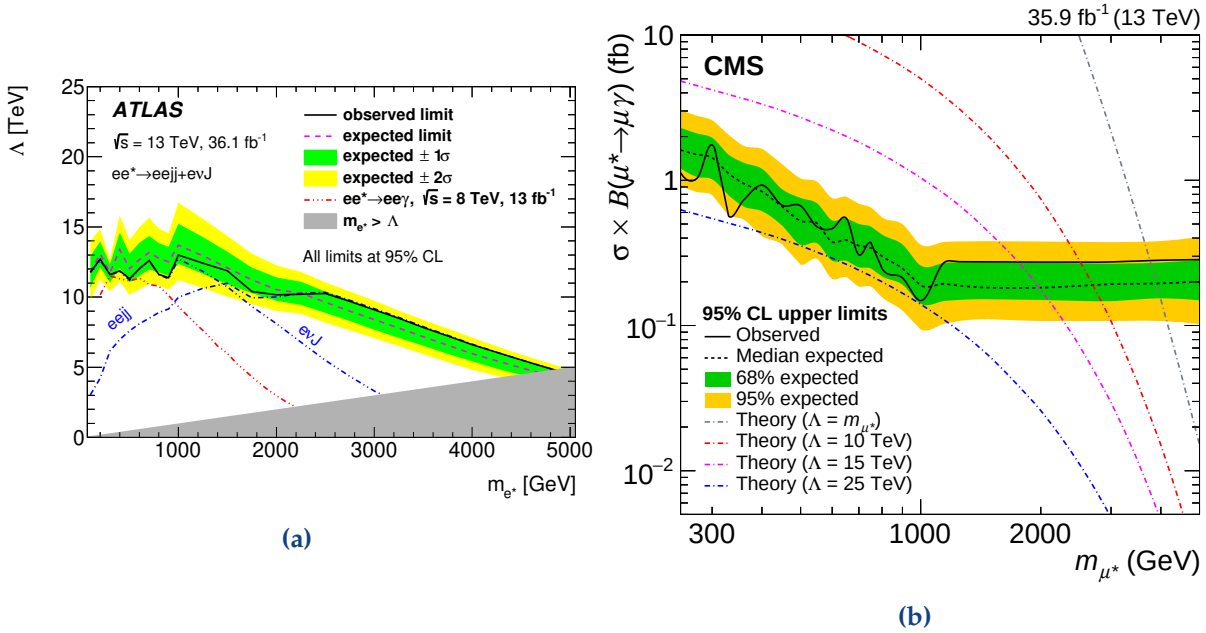

Figure 2.11: Results of the most recent publications of (a) the ATLAS and (b) the CMS collaboration regarding excited leptons. The CMS publication shows the analysis of the $\ell\ell\gamma$ channel while the ATLAS analysis presents the combined lower limit of the contact interaction and W channel. Both searches were carried out on the 2016 dataset of the LHC. Figures taken from Ref. [71] and [5].

3 | Experimental Setup

After having introduced the theoretical foundation for the search for excited leptons in the previous chapter, I will shift the focus to the experimental setup. First of all (section 3.1), I describe the accelerator complex at CERN, especially the Large Hadron Collider (LHC). Next (section 3.2), I provide a summary of some fundamentals of particle physics at hadron colliders. Finally (section 3.3), I will explain the layout of the CMS detector.

3.1 The Large Hadron Collider

The LHC [61] is a high-energy hadron collider located at CERN, Geneva. It provides proton-proton collisions for CMS [75] and consequently lays the foundation for every analysis done in CMS. However, it cannot accelerate protons from rest but is the final link in an entire accelerator chain. Figure 3.1 depicts the whole accelerator complex at CERN. The relevant pre-accelerators for the LHC are the Linac2, which accelerates protons up to 50 MeV, the Proton Synchroton Booster (PSB), boosting them up to 1.4 GeV in four superimposed rings and the Proton Synchroton (PS) [76] increasing the energy to 25 GeV. The PS is also responsible for creating the bunch structure used in the LHC.[1] Finally, the beam is injected into the Super Proton Synchroton [77], which accelerates the protons to 450 GeV- the injection energy of the LHC.

The LHC itself is located in a tunnel approximately 100 m below ground with a circumference of 27 km. It uses 1232 superconducting dipole magnets producing a magnetic field of up to 8 T to keep the particles on a nearly circular orbit. It accelerates not only protons but also ions like lead and xenon [78]. The LHC houses four large experiments: CMS [75] and ATLAS [79], the two multi-purpose experiments, ALICE [80] focusing on heavy-ion collisions, and LHCb [81] investigating b-physics in the forward region.

The design energy for proton beams is 7 TeV for both beams leading to a center-of-mass energy of 14 TeV in the experiments. However, this energy has not been reached yet and is only planned to be achieved in Run 3 starting in 2021.[2] In Run 2 (2015-2018), the energy per beam was limited to 6.5 TeV hence a center-of-mass energy of 13 TeV. This energy makes the LHC the most powerful proton-proton collider to date. Compared to the center-of-mass energy of 7 – 8 TeV in Run 1, this is a substantial upgrade increasing the sensitivity of nearly all searches for new physics. It also marks the last major increase of energy for the following decades in particle physics with new high-energy accelerators just at the horizon. Discussions about the next generation of particle accelerators are vivid. Most probably the next major accelerator will be an e^+e^- precision machine either as a linear accelerator (CLIC [82], ILC [83]) or circular collider (FCC-ee [84], CEPC [85]). Both the FCC and CEPC designs feature a 100 km long tunnel, which can later

[1] The LHC does not collide a continuous stream of protons but rather bunches of them. Two bunches have a separation of 25 ns and pack around 10^{11} protons each.

[2] The limiting factor of the LHC energy is the maximum current in the dipole magnets. They need more training to reach stable operation at the current needed for 7 TeV.

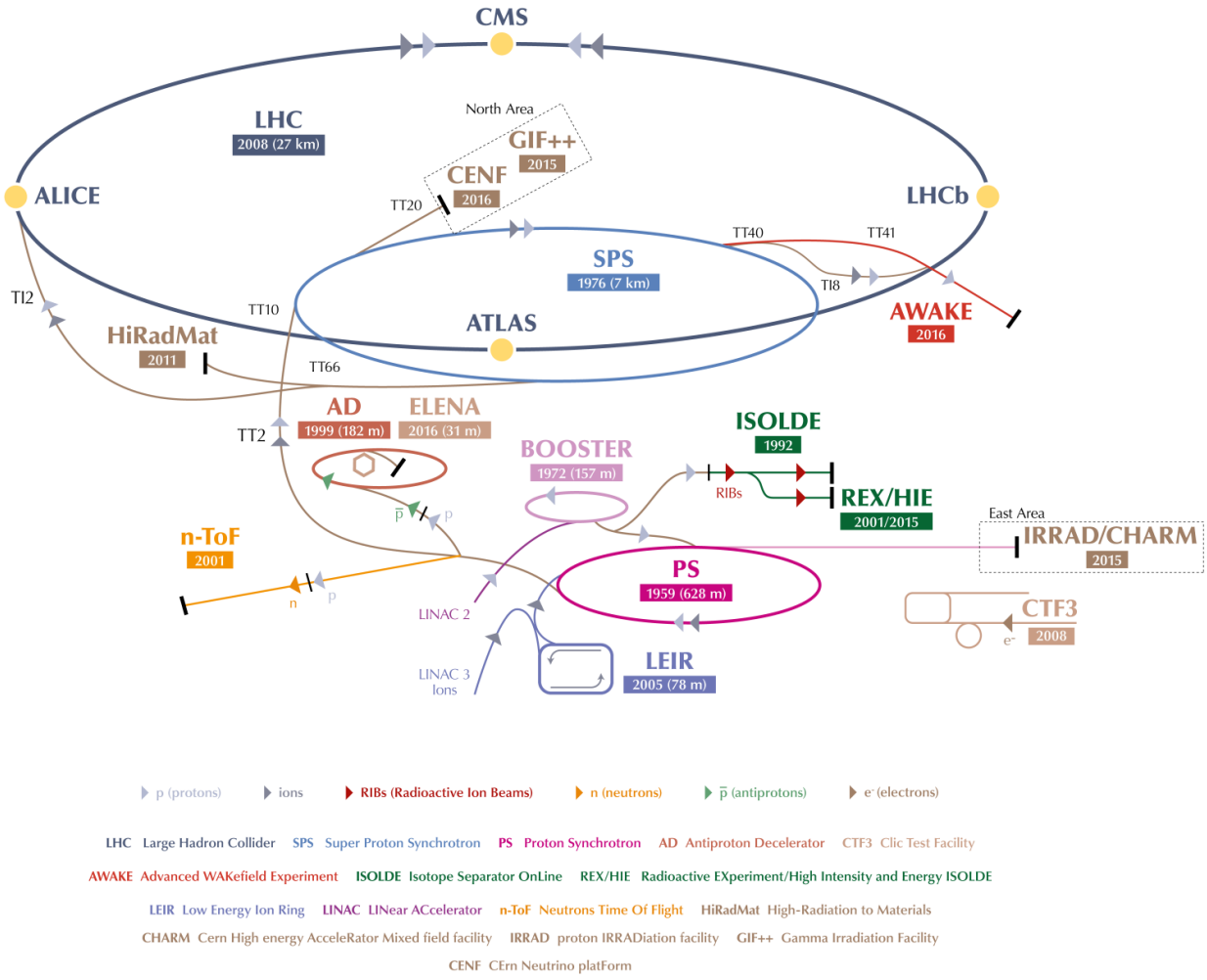

Figure 3.1: CERN accelerator complex. The relevant parts for LHC proton physics are the Linac2, PSB, PS, SPS and LHC. Figure taken from Ref. [74].

host a hadron machine as well [86], much like LHC uses the LEP tunnel. The High-Lumi LHC (HL-LHC) program [87] defines the immediate future of high energy physics. The target is to increase the amount of data by one order of magnitude compared to LHC. Another idea is to upgrade LHC with new magnets but keep the same tunnel. Such a design would reach a center-of-mass energy of 27 TeV [88].

For experimentalists, the other important quantity alongside the energy is the number of events of a process. It is determined by the product of two properties: The cross section σ and the integrated luminosity $\mathcal{L}_{\text{int}} = \int \mathcal{L}\,\mathrm{d}t$

$$N = \sigma \mathcal{L}_{\text{int}}. \tag{3.1}$$

The cross section is a physical constant for each process as explained in the previous chapter.

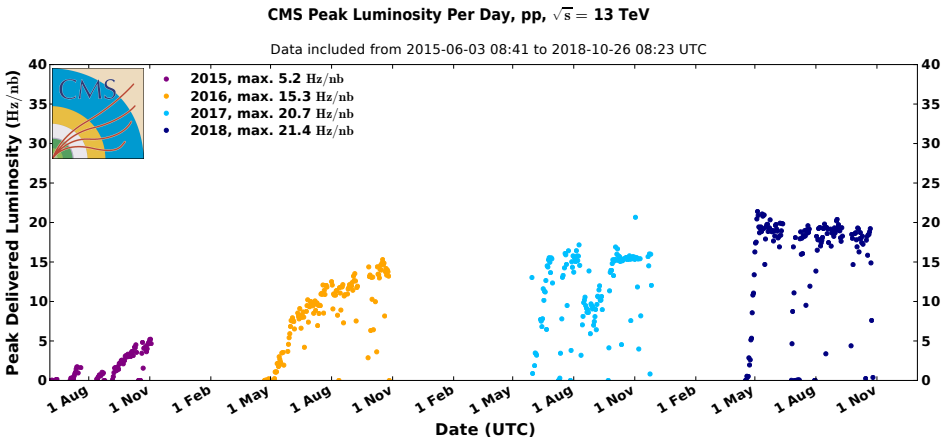

Figure 3.2: Peak luminosity over time in Run 2. The design luminosity of the LHC is $1.0 \cdot 10^{34}\,\mathrm{cm}^{-2}\,\mathrm{s}^{-1} = 10\,\mathrm{Hz\,nb}^{-1}$. Figure taken from Ref. [89].

The luminosity depends on the machine parameters:

$$\mathcal{L} = \frac{N_1 N_2 f N_b}{4\pi\sigma_x\sigma_y} \cdot W e^{\frac{B^2}{A}} S. \tag{3.2}$$

N_1 and N_2 are the numbers of particles per bunch, f is the revolution frequency, N_b denotes the number of particles per bunch, and σ_x and σ_y are the sizes of the beam in the direction perpendicular to the direction of flight. The factors W, $e^{\frac{B^2}{A}}$ and S are smaller than unity and take reductions caused by separation and the crossing angle at the interaction point into account.

Two parameters determine the beam size: The transverse emittance ε and the focusing strength of the optics $\beta^\star$. The transverse emittance is a measure for the beam quality and is mainly determined by the injector chain. A small emittance signifies that all particles have a vanishing transverse momenta and are close together. Greater transverse emittances imply larger spreads in transverse momentum or larger beam sizes. The LHC cannot improve the emittance of the beam; it can only grow. Thus one of the LHC's tasks is to preserve the emittance during acceleration as much as possible.

Nevertheless, the beam size can be reduced locally at the interaction points using quadrupole magnets at the cost of an increased variance of the transverse momentum. $\beta^\star$ provides a measure for how much the beam is squeezed at the interaction point. The smaller $\beta^\star$, the smaller the beam. The formula assumes a constant beam size for the whole crossing region, which is principally not correct but sufficient for the scope of this thesis.

The peak design luminosity[3] of the LHC is $1.0 \cdot 10^{34}\,\mathrm{cm}^{-2}\,\mathrm{s}^{-1} = 10\,\mathrm{Hz\,nb}^{-1}$ and was reached for the first time early in 2016 as can be seen in figure 3.2 which displays the instantaneous luminosity delivered to CMS by the LHC. It demonstrates the steady growth of the instantaneous luminosity over Run 2. This growth was made possible by a better understanding of the machine, which allowed us to push the limits and reach twice the design luminosity in 2018. This milestone

[3]The luminosity decreases over the run due to the burn-off of protons due to collisions, increasing emittance and other losses [90].

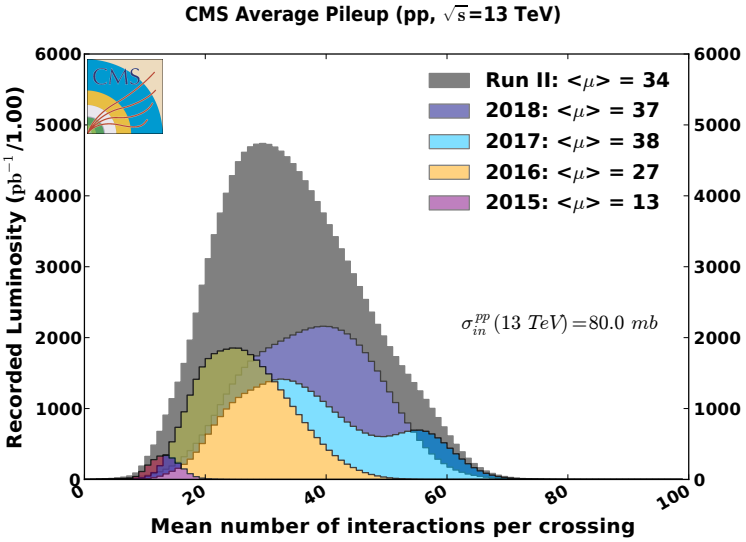

Figure 3.3: Mean number of interactions per bunch crossing in Run 2. The increasing instantaneous luminosity led to an increase in pileup over the years. Figure taken from Ref. [89].

was achieved by exploring novel beam modes in the injector chain, decreasing the emittance of the beams to around 2 µm and reducing the $\beta^\star$ far below its design value down to 25 cm at the end of a run [91].[4]

However, the increased luminosity came at a cost. Multiple interactions need to happen simultaneously during the same bunch crossing to reach such sizeable luminosities. They do not inherently impact the performance of the detector if it can cope with such conditions. Even so, it does put stress on the trigger and reconstruction algorithms because of the higher rate of particles. It is unlikely that two interesting hard-scattering events happen simultaneously during the same bunch crossing because most interactions happening during proton-proton collisions are soft scatterings of jets [92]. The cross sections of processes like Higgs production or new exotic processes like the one analyzed in this thesis are much smaller. It is, therefore, an advantageous trade-off to increase the number of interactions per bunch crossing to boost the rate of rare processes provided we can filter out the less interesting processes and not hamper the performance.

The number of simultaneous interactions is called *pileup*. Particles originating from these pileup interactions are called *pileup particles*. Figure 3.3 displays the distribution of pileup for Run 2 in CMS. It shows that the boost in luminosity over the years correlates to increasing pileup. Despite that, the largest peak pileup was reached in 2017 when the beam operation was switched from "standard" 25 ns-*trains* to the *8b4e*-scheme[5] for the second half of the year. The switch

[4] $\beta^\star$ was decreased in two steps from 30 cm to 25 cm in 2018 as the runs continued in order to gain luminosity. The limiting factor for $\beta^\star$ is the aperture of the instrumentation since a small $\beta^\star$ leads to larger amplitudes in the inner triplets [91].

[5] Typically bunches are separated by 25 ns. However, due to injection limitations, it is not possible to inject one continuous "train" of bunches spaced with 25 ns but only smaller trains with around 150 bunches. The 8b4e-scheme injects 8 bunches with a 25 ns spacing and leaves the next four *buckets* empty. This scheme helps to suppress electron cloud effects in the machine [93]. Electron clouds emerge when the beam releases electrons from residual gas atoms left in the beam pipe. They are accelerated and can release additional electrons. The following bunch then has to

was necessary due to issues in one of the dipole magnets.[6] The structure of the 8b4e-scheme allows fewer injected bunches into the LHC. Fewer bunches lead to lower luminosities. The LHC operators increased the number of protons per bunch to compensate for the loss of luminosity. A higher number of protons per bunch also leads to more pileup explaining the second bump in the 2017 spectrum.

3.2 Interlude - Fundamentals of Physics at Hadron Colliders

Before describing the CMS detector, I am going to introduce some fundamentals regarding the physics happening during proton-proton collisions.

In contrast to lepton colliders, we do not collide elemental particles[7] but composite ones. The *deep inelastic scattering* (DIS) happens between the constituents of the protons and not the proton itself. This has several consequences: First, the actual center-of-mass energy of a collision is not $\sqrt{s} = 2E_{\text{beam}}$ but

$$\sqrt{\hat{s}} = \sqrt{x_1 x_2 s}, \tag{3.3}$$

where x_1 and x_2 are the momentum fractions of the *partons* interaction with each other.

The second consequence is that the initial energy of the system in the longitudinal direction is unknown. This incapability becomes important for the detection of invisible particles, e.g., neutrinos that escape the detector unnoticed and can solely be measured by missing energy. We can only reconstruct the transverse component as the initial longitudinal energy is unknown.

In order to calculate cross sections we need to know the probability distribution to find a quark or gluon with a momentum fraction x at the energy scale Q^2. These functions are called *Parton Distribution Functions* (PDFs). The dependence on Q^2 can be calculated using the *DGLAP* equations [95–97] but the dependence of x needs to be extracted from data. The PDFs for protons for different values of Q^2 are presented in figure 3.4. The extrapolation in Q^2 can be done in various orders of the strong coupling constant $\alpha_s(Q^2)$. First order approximations are called *leading-order* (LO), followed by *next-to-leading-order* (NLO) and *next-to-next-to-leading-order* (NNLO).

There are several collaborations calculating PDFs. This thesis, in particular, uses the ones obtained by the NNPDF collaboration [94]. Every PDF comes with an assigned uncertainty. The primary sources of the PDF uncertainty are systematic uncertainties of the measurements going into

pass through a dense cloud of electrons. The 8b4e-scheme suppresses such electron clouds since they are typically short-lived and disappear during the *4e* section.

[6] One of the vacuum pumps left some air inside the dipole magnet in sector 16L2. After cool-down, the air froze. The beam can release parts of the ice the beam pipe. They fall through the beam pipe and interact with the beam in the process. Interactions with the beam can lead to sizable beam losses and instabilities. The beam is then dumped to protect the machine. The 8b4e scheme helped to suppress electron cloud effects, which led to a reduction of releases of the ice [93]. Amusingly, only the attempt to solve the issue by warming up the beam screen led to a state where normal operation became impossible. The difficulties are visible in the dip of the instantaneous luminosity at the end of the summer 2017 in figure 3.2.

[7] Although this thesis investigates if leptons are not elemental as well, we assume them to be elemental until proven otherwise, at least in this context.

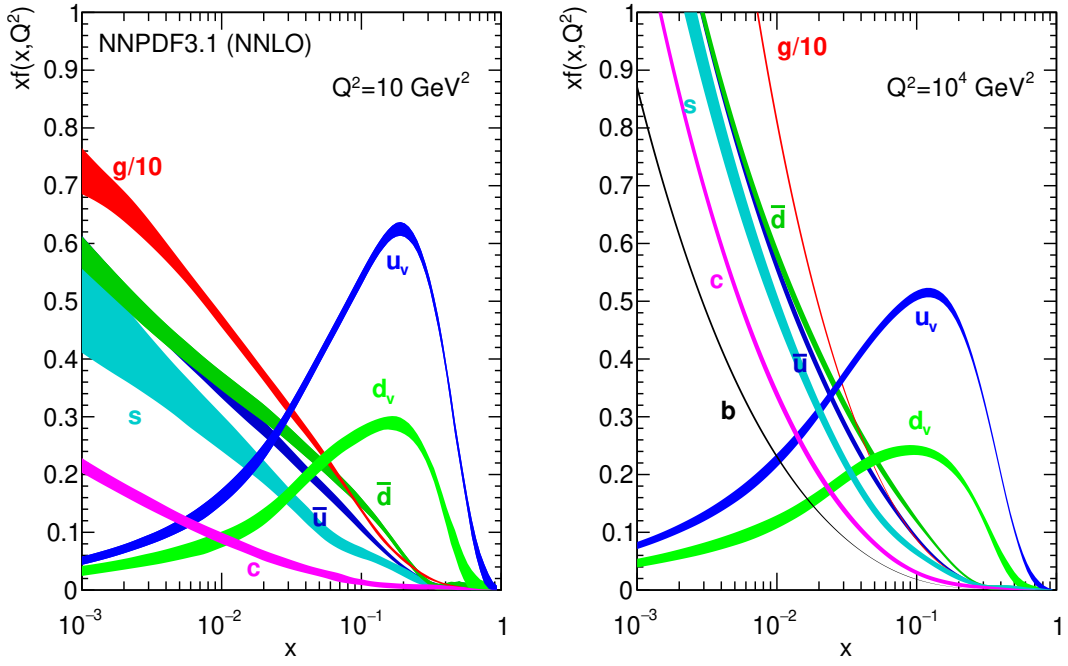

Figure 3.4: Parton distribution functions of NNPDF3.1 [94] for two different energy scales Q^2. Figures adopted from Ref. [94].

the fit. Two methods exist to propagate the uncertainties of the fitted data to the PDF: The Monte Carlo method and the Hessian method [98]. The first has the advantage that we need no assumptions on the error propagation through the covariance matrix. Instead, it uses discrete representations to describe the underlying probability density. It also enables the fit to use more complex parametrizations. The Hessian method uses a least-square fit and propagates the uncertainties linearly through the covariance matrix. The advantage is that the obtained uncertainties can be plugged in as nuisance parameters into the analysis.

We can then calculate the cross section of a process by evaluating the integral

$$\sigma(pp \to X) = \sum_{(i,j)} \int_0^1 \mathrm{d}x_1 \int_0^1 \mathrm{d}x_2 f_i(x_1, \mu_F^2) f_j(x_2, \mu_F^2) \hat{\sigma}(ij \to X; \sqrt{\hat{s}}, \mu_F^2, \mu_R^2). \tag{3.4}$$

It sums up all possible initial parton states (i, j) and integrates over the product of the PDFs for both partons with the parton-level cross section $\hat{\sigma}$. μ_F is the factorization scale that needs to be implemented to avoid infrared divergences in the amplitude calculation when a massless particle radiates another massless particle. Contrary, the renormalization scale μ_R governs ultraviolet divergences introduced by particle loops with infinite momentum by letting the coupling constant α_s depend on it. Both scales are implemented ad-hoc and the observable should not depend on it. However, as we can only calculate cross sections up to a certain order in the perturbation theory, the final cross section will still depend on both quantities up to a certain amount. The dependence becomes smaller with every order of the perturbation theory taken into account. An uncertainty needs to be applied to accommodate the dependence of the cross section from the

value of the energy scales.

3.3 The Compact Muon Solenoid

The Compact Muon Solenoid (CMS) is – together with ATLAS – one of the two multi-purpose detectors at the LHC. It is located in a cavern at the fifth interaction point of the LHC close to the French village Cessy, one hundred meters underground. CMS has a length of 21.6 m, a diameter of 14.6 m and weighs 12500 t – more than the Eiffel tower.[8] CMS is composed of several components with distinct purposes, which altogether allow reconstructing nearly the entire outcome of a collision of two particles. The paper [75] describes CMS in all details.

This section focuses on the description of the various subdetectors. I will describe the reconstruction algorithms which exploit the detector in the following chapter. During the Long Shutdown 1 and Run 2 several upgrades to the detector were made [99].[9] Relevant upgrades will be discussed below as well.

3.3.1 General Layout and Coordinate System

Before describing the components of the detector, I want to introduce some general design concepts and the coordinate system, which is referenced later by the subdetectors. Figure 3.5 shows a schematic view of the detector. CMS roughly consists of three parts: The barrel and two endcaps. The barrel is the central part of the detector, while the endcaps cover the *forward regions* in the direction of the beam pipe. The barrel itself consists of five freely movable wheels. The endcaps can be detached easily from the barrel part as well, which allows easy maintenance and testing as the subdetectors can be turned on even in a detached state.

To reconstruct the entire event, it is paramount to cover as much angular space as possible. The ideal coverage of the angular space would be 4π. Unfortunately, due to the beam pipe, parts in the very forward region cannot be covered. It is still critical to extend the coverage as much as conceivable to miss as few particles as possible. Another reason for a good coverage is the calculation of *missing transverse momentum* ($\boldsymbol{p}_T^{\text{miss}}$).[10] Missing transverse momentum is the negative value of the vectorial sum of the transverse fraction of momentum of all particles:

$$\boldsymbol{p}_T^{\text{miss}} = -\sum \boldsymbol{p}_T \tag{3.5}$$

This quantity is important to indirectly identify particles that escape detection, e.g., neutrinos or possibly dark matter. We analyze only the transverse component because the initial longitudinal momentum of the system is unknown as we collide composite and not elemental objects, as discussed in section 3.2.

[8] Despite being massive, this design is indeed rather compact as the name suggests when compared to its capabilities. The ATLAS detector is with a length of 46 m and a diameter of 25 m much larger.

[9] These upgrades are called *phase-1 upgrades*. Another set of upgrades (*phase-2 upgrades*) will be installed before the installation of the High-Lumi LHC.

[10] Actually, although the term "Missing Transverse Energy" is used most commonly, it is the sum of transverse momenta.

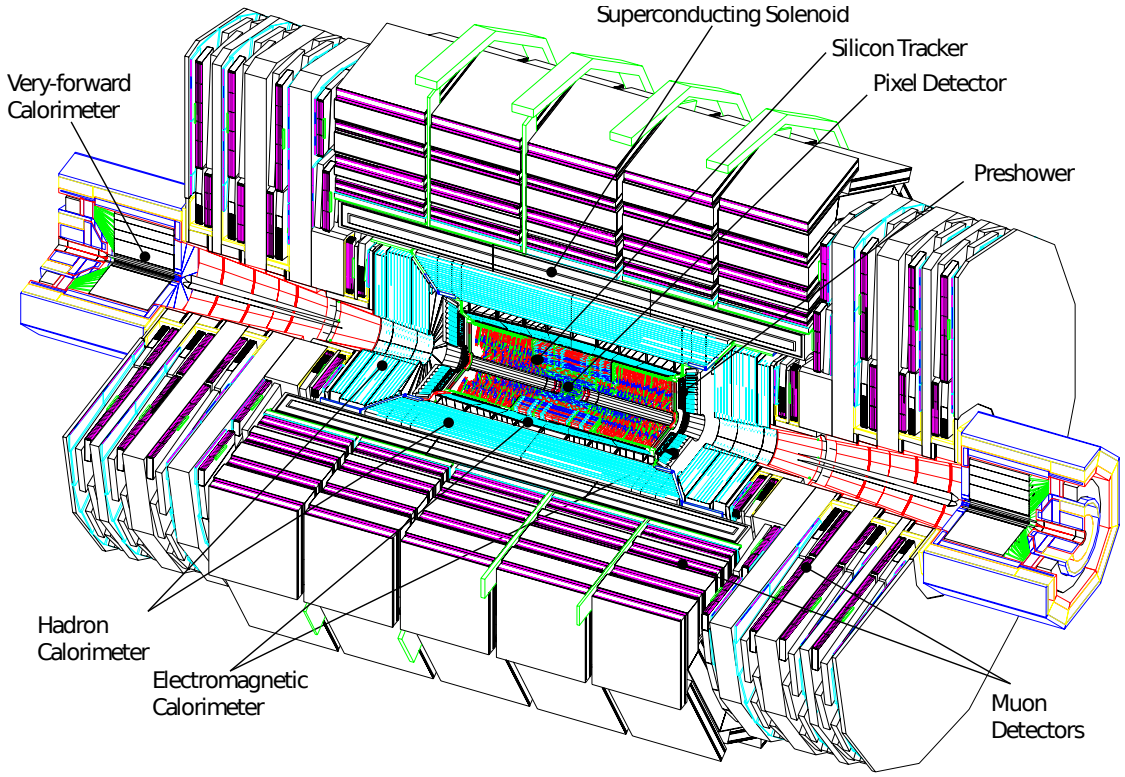

Figure 3.5: Schematic view of the CMS detector with all detector sub-systems. Figure taken from Ref. [75].

It is useful to define a universal coordinate system to introduce the subdetectors and describe collision events. Its origin is the interaction point. The x-axis points towards the center of the LHC ring, the y-axis vertically upwards, and the z-axis counterclockwise along the beam pipe.

It is often more useful to use spherical coordinates than Cartesian. r denotes the distance to the origin of the system, ϕ is the azimuthal angle in the x-y-plane measured from the x-axis, and θ the polar angle measured from the z-axis. Instead of θ we often use the pseudorapidity

$$\eta = -\log(\tan(\theta/2)). \tag{3.6}$$

It has the advantage that distances between particles measured by η are invariant under Lorentz transformations while differences in θ are not. We can measure distances between two particles in the ϕ-η space by

$$\Delta R = \sqrt{\Delta\phi^2 + \Delta\eta^2}. \tag{3.7}$$

This framework helps to understand the interplay of the different subdetectors described next. The detector is assembled out of multiple layers like an onion. I will describe the detector parts inside out, but start with the heart of the detector: Its magnet.

3.3.2 The Solenoid Magnet

The Solenoid magnet is the core of the detector.[11] It has a length of 12.5 m and a diameter of 6 m, making it the largest superconducting solenoid ever built [75]. Inside the magnetic coil, it creates a uniform 3.8 T magnetic field. The required current for this field strength is around 18000 A. Therefore the magnet needs to be superconducting and cooled down to 1.8 K.

Outside the magnet, the field is guided by the iron return yoke, which is made up out of steel and weighs more than 10000 t. It serves as a frame for the muon chambers too.

The magnet is essential to bend the tracks of charged particles. The curvature of the track provides a measure for the momentum of the particle.

3.3.3 The Tracker

The tracker is the innermost part of the CMS detector and consists of the pixel and the strip detector. It is entirely made out of silicon and is the largest silicon tracker ever built [75]. The tracker measures the position of particles traversing the detector. In conjunction with the magnetic field, it is possible to reconstruct individual particles and measure their momenta. The tracker needs to withstand the enormous radiation close to the interaction point and has ideally not much material to reduce multiple scatterings of particles. It needs tiny cell sizes in the center of the detector to achieve the required spatial resolution. The cell size in the outer regions of the tracker can be larger than at the interaction point since the particle density decreases with increasing radius.

The tracker covers the entire region below $|\eta| < 2.5$ which corresponds to about 98 % coverage. A schematic view of the legacy[12] tracker can be seen in figure 3.6.

Pixel Detector

The pixel detector is the innermost subdetector of CMS. The goal is to provide good tracking seeds and a good spatial resolution for primary and secondary vertices to, among others, suppress pileup and tag b-hadrons. It was exchanged during the extended year-end technical stop in the winter from 2016 to 2017 with a new, upgraded version. First, I will discuss the legacy pixel detector and then highlight the improvements in the new detector design.

The legacy pixel detector consisted of 66 million $100 \times 150\,\mu m^2$ large pixels arranged in three barrel layers at the radii of 4.4, 7.3, and 10.2 cm and two endcap disks on each side at ± 34.5 and ± 46.5 cm. It achieved a transverse impact parameter resolution of 10 µm and a longitudinal resolution of 30 µm [100].

With the luminosity increasing beyond its design value[13], a new pixel detector was needed to cope with the higher rates of particles and the more substantial pileup. The old pixel detector would have had massive inefficiencies due to limitations in the readout chip [101]. Its technical

[11] As can be easily recognized due to its appearance in the name of the detector.
[12] See next sub-section for a description of the legacy and upgraded design of the pixel detector.
[13] See above, section 3.1.

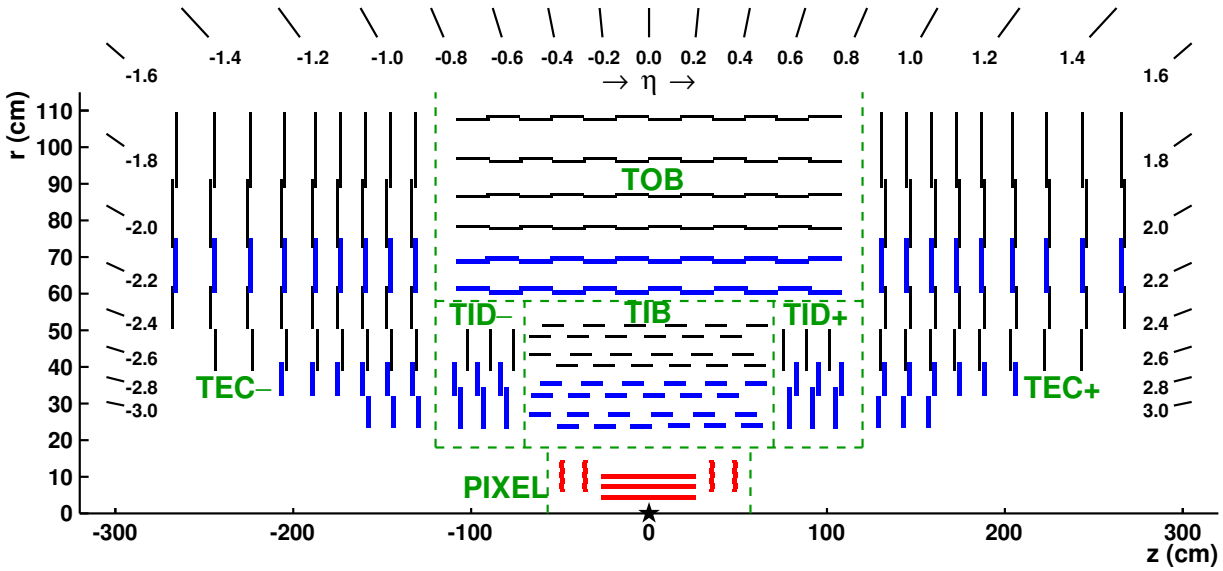

Figure 3.6: Schematic view of the upper half of the inner tracker in the CMS detector in the r-z view. The pixel detector in red corresponds to the legacy design. Figure taken from Ref. [100].

design report [101] provides a detailed description of the new pixel detector. It provides a superb performance under more challenging conditions. It also increases the number of layers in the barrel from three to four and pushes the first layer closer to the interaction point with a distance of only 3.0 cm.[14] Furthermore, the new detector adds a new disk in the endcap, increasing the total number to three. Figure 3.7 shows a comparison of the old and new designs. The total number of pixels increased to 122 million while the sensor size stayed the same.

During operation in 2017, several issues occurred[15] and impacted the performance negatively, especially in the later runs of the year, as the active number of channels decreased [102]. The performance of the new pixel detector was still superior to the old design.

Strip Detector

The silicon strip detector shown in figure 3.6is placed outside the pixel detector and uses larger sensors of 10 cm $\times$ 80 µm up to 25 cm $\times$ 180 µm. In total, it has ten barrel layers and twelve disks. As the strips have a significant length, they can only measure the position in r and ϕ but not in z. Therefore some layers are equipped with a second layer mounted back-to-back at an angle of 100 mrad to determine the z position of a track as well.

[14] This became only achievable with the exchange of the old beam pipe which was replaced by one with a smaller diameter.

[15] The Token Bit Manager got stuck by single event upsets and required a power cycle to get back to a working state. However, it turned out that the DCDC converters could not withstand the intense radiation and could break after being power cycled, leading to a permanent dysfunction of the DCDC converters affecting all connected pixel boards. For 2018 all DCDC converters were exchanged and a different procedure was applied to remedy the failures. The root cause will be fixed for Run 3 [102].

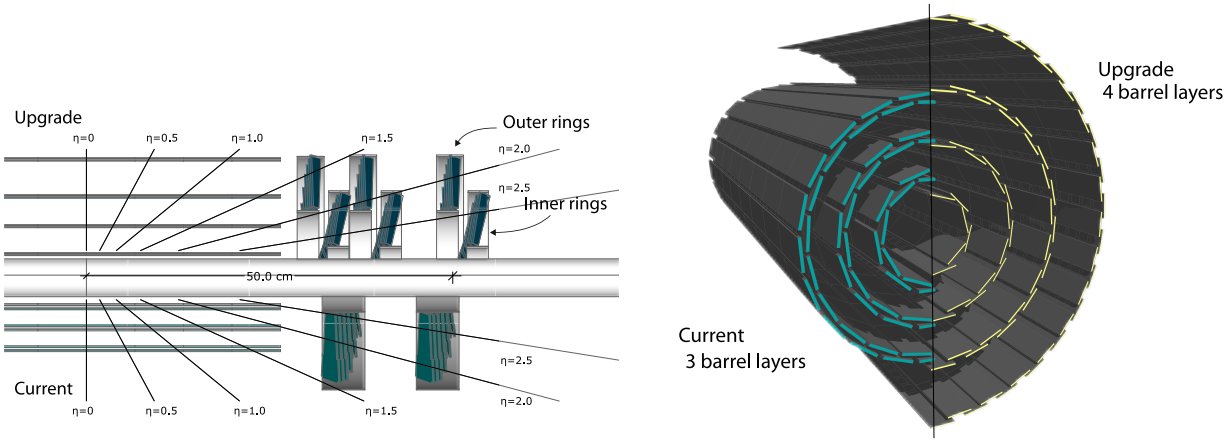

Figure 3.7: Comparison of the old and new pixel designs. The left-hand side shows the new design in the upper half and the old design in the lower half in the r-z view. The new design adds a new layer closer to the beam pipe and a new disk in the endcap. The right-hand side shows the r-ϕ view of the barrel. Figure taken from Ref. [101].

The relative p_T resolution of the reconstructed tracks is about 2-3% in the central region for $p_T = 100\,\text{GeV}$. The resolution decreases to higher transverse momenta and $|\eta|$ due to less-bent tracks and shorter lever arms [75].

In 2016 a dynamic inefficiency led to a deterioration of the hit efficiency and the tracking efficiency. Adapting the setting of the pre-amplifier of the read-out chip ultimately resolved this issue late in the data taking period. Effected data could not be recovered since the issue was part of the data taking chain and not the reconstruction. Instead, CMS deployed a set of mitigation algorithms to limit the effect on the physics performance of the affected data [103, 104].

3.3.4 The Calorimetry System

CMS possesses two calorimeters: The electromagnetic calorimeter (ECAL) and the hadronic calorimeter (HCAL). As their names suggest, the ECAL detects photons and electrons, while the HCAL detects hadrons. Since the hadronic interaction length is greater than the electromagnetic interaction length for suitable materials, the ECAL is inside the HCAL, right behind the tracker.

The Electromagnetic Calorimeter

The ECAL consists of 78000 scintillating $PbWO_4$ crystals. They have a size of $22 \times 22\,\text{mm}$ at the front end and $26 \times 26\,\text{mm}$ at the rear end, and a length of 230 mm corresponding to 25.8 radiation lengths. Because of that, the ECAL has a fine granularity in the η-ϕ plane but no segmentation in r. It covers the entire ϕ region up to $|\eta| < 3.0$.

The design of the ECAL played a vital role in the design of CMS because the $\gamma\gamma$ channel was one of the premiere channels to discover the Higgs boson [75].

The resolution can be parametrized by

$$\left(\frac{\sigma}{E}\right)^2 = \left(\frac{S}{\sqrt{E/\,\mathrm{GeV}}}\right)^2 + \left(\frac{N}{E/\,\mathrm{GeV}}\right)^2 + C^2. \tag{3.8}$$

S is the stochastic term representing event-to-event fluctuations in the shower, N a noise term incorporating electronic-, digitization- and pileup noise, and C a constant term inheriting intercalibration errors and shower leakage. S was measured to 2.8%, N to 12% and C to 0.3%. Contrary to the tracker, the energy resolution improves to high energies as the number of particles in the shower increases.

The radiation which the ECAL receives negatively impacts its transparency. Despite the constant monitoring of the transparency and the application of corrections, a timing shift of the Level-1 trigger primitives[16] was introduced by the transparency loss in 2016 and 2017 because the shape of the fitted signal pulse changed. Sometimes, this led to the assignment of the trigger primitive to the wrong bunch crossing. Consequently, the trigger received the event before the one that was supposed to be triggered. Since the previous event is most likely not interesting, it is then rejected by the HLT[17]. Also, after a successful Level-1 trigger, the trigger system is blind for the following events to throttle trigger rates; thus, the trigger discards the interesting event.

Since the cause of the issue is the transparency loss caused by radiation damage, the effect increased linearly over time and was particularly strong in the endcaps. In 2018 the issue was fixed [105].

The Hadronic Calorimeter

The HCAL is located in between the ECAL and the solenoid. It consists of four parts: The HB in the barrel ($|\eta| < 1.3$), the HE in the endcaps ($|\eta| < 3.0$), the HO outside the magnet[18], and the HF in the forward direction ($|\eta| < 5.2$). The HB and HE share a common design for most parts, while the HF features a completely different design due to the harsher conditions in the forward region.

The HE and HB are sampling calorimeters with brass[19] absorption layers interleaved with plastic scintillators. In total, both have sixteen scintillator layers. For $\eta = 0$, it has a depth of 5.4 hadronic interaction lengths increasing to around ten in the endcap. The ECAL adds another 1.1 hadronic interaction lengths.

Hybrid Photodiodes (HPDs) detect the scintillation light. The readout has different radial segmentations depending on η. In the barrel, all layers share a single readout while the ones in the endcap have up to three readouts.

[16] See section 3.3.6 for an explanation of the trigger system in CMS.

[17] Again, see section 3.3.6.

[18] The HO is a tail catcher in the central region as the traversed length of the HCAL is shortest there. Because of restrictions in space caused by the magnet, it had to be installed outside the magnet.

[19] High-quality brass is a costly material. To get enough brass for the CMS HCAL for a reasonable price an agreement with the Russian military was made to recycle old WW2 navy cartridges and put them into civil use.

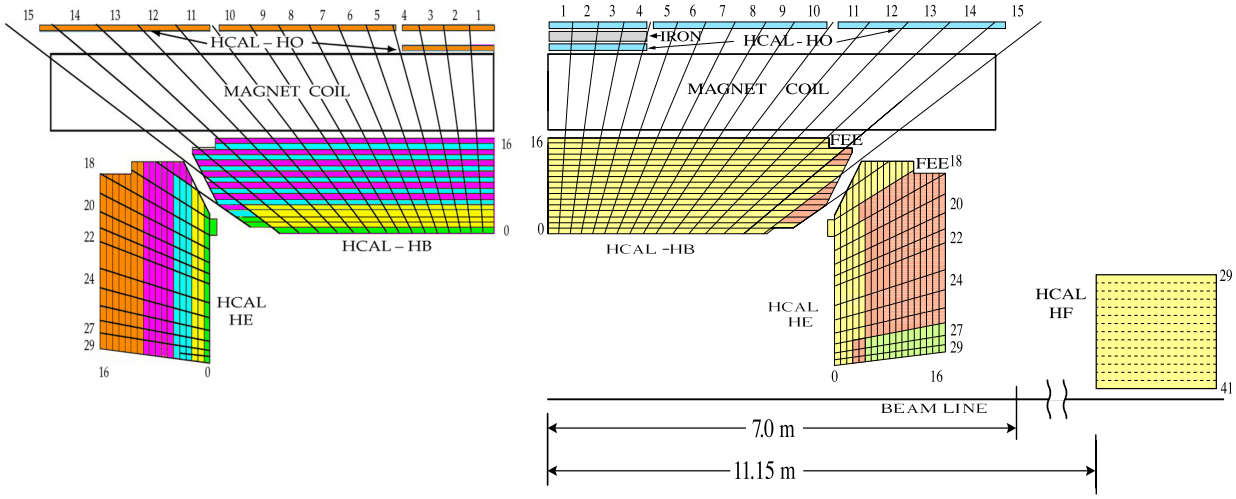

Figure 3.8: Schematic view of the hadronic calorimeter. It shows on the left-hand side the upgraded design and on the right-hand side the legacy design. The different colors illustrate the segmentations. Figure adopted from Ref. [75, 106].

CMS upgraded the HE between 2017 and 2018[20] and the HB during LS2 [108]. The upgrade replaced the HPDs with new Silicium Photomultipliers (SiPMs), which helps to decrease the noise level. It increased the longitudinal segmentation of the readout in barrel and endcap as well [106]. Figure 3.8 compares the old and the new design. The color of the calorimeter tiles indicates the segmentation. Among other things, the improved segmentation enhances the suppression of pileup.

The relative energy resolution was measured to

$$\left(\frac{\sigma}{E}\right)^2 = \left(\frac{100\%}{\sqrt{E/\,\mathrm{GeV}}}\right)^2 + (4.5\%)^2. \tag{3.9}$$

The Hadron Forward (HF) detector needs to survive in a much more hostile area close to the beam pipe with radiation doses of up to $1\,\mathrm{MGy\,yr^{-1}}$. It consists of a steel absorber with quartz fibers catching Cherenkov light. The light is collected by photo multipliers which are positioned behind additional shielding. The HF is mainly used for more precise $\boldsymbol{p}_T^{\mathrm{miss}}$ and luminosity measurements.

3.3.5 The Muon System

The detection of muons is of maximal importance for CMS, manifesting itself in the middle letter of its name. The $\mathrm{H} \to \mathrm{ZZ} \to 4\mu$ channel is one of the leading channels for the discovery of the Higgs boson [75].

CMS has three different muon detectors: The Drift Tube (DT) system, the Cathode Strip Chamber (CSC) system, and the Resistance Plate Chambers (RPCs). The barrel region uses DTs and the endcap region CSCs. Both utilize the RPCs. Starting from Run 3, CMS will also utilize GEM

[20] A single section was installed before 2017 to allow extensive testing during normal data taking [107].

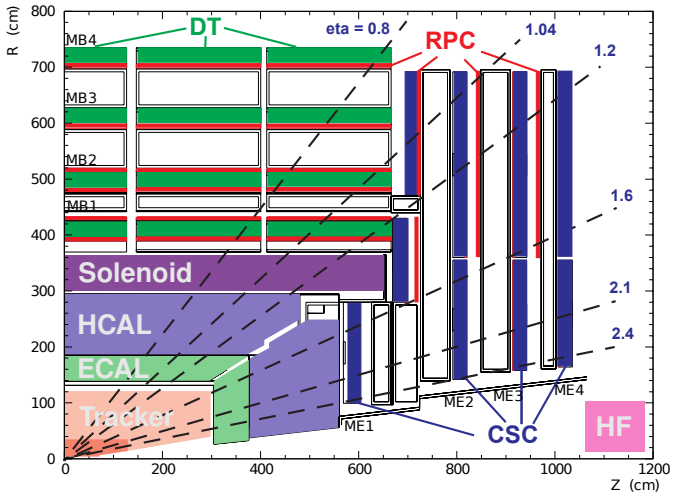

Figure 3.9: Schematic view of the muon system in CMS. The DT system is exclusively used in the barrel region, while the CSCs are only mounted in the endcap. Both regions have RPCs installed. The position of Tracker, ECAL, and HCAL is shown, too. Figure adopted from Ref. [110].

chambers in the endcap [109]. Figure 3.9 shows the three systems and their location in the detector. Muons can pass the calorimeter since they are much heavier than electrons and radiate less bremsstrahlung. Only at very high momentum, radiative losses become an issue.

Relative momentum resolutions of $1-3\%$ can be reached for muons at $p_T = 100\,\text{GeV}$ in the barrel and endcap by combining the information of the muon system and the tracker [111]. The resolution remains better than 7% for muons up to 1 TeV in the barrel. The standalone muon reconstruction efficiency is above 98% over the full p_T spectrum [111].[21]

Drift Tubes

The DT system consists of multiple cylindrical cells with a length of 2.4 m and a width and height of a few centimeters. Each cell is filled with an Argon-CO_2 mixture, has cathode strips on its wall and an anode wire in the middle of the gas volume. A muon passing through the chamber ionizes the gas. The electrons and ions move to the anode and cathode due to the applied high voltage and the signal can be read out.

Multiple cells are grouped into *layers*. Four layers form one *superlayer* and three superlayers form one DT chamber.[22] Two superlayers measure the ϕ component and one the θ component. In total, CMS has 250 DT chambers placed at four distinct radii around the interaction point.

Cathode Strip Chambers

Drift tubes are working well in the barrel region with low rates and an approximately homogeneous magnetic field. They are not suited for the endcap region where the rates are much

[21] See section 4.1.1 for more information about the muon reconstruction.
[22] The outmost chamber only has two superlayers.

higher and the magnetic field is non-uniform as they are installed outside the solenoid. The CSC chambers are well suited for this environment and are placed four layers perpendicular to the beam direction. CSCs are multiwire chambers and have cathode strips mounted to the plates of the chambers and anode wires crossing them perpendicular.[23] This detector layout enables simultaneous measurement of the η and ϕ coordinate.

Resistive Plate Chambers

A disadvantage of the DTs and CSCs is the relatively long drift times, which are longer than the time between two bunch crossings. The RPCs compensate for this by providing better timing information at the cost of spatial resolution. Both systems are, therefore, complementary to each other. One RPC chamber consists of two highly resistive plates with readout strips in between. They achieve their good timing resolution by running in the avalanche mode. The RPCs are only installed up to $|\eta| = 2.1$ so between $|\eta| = 2.1$ and 2.4 the CSCs are the sole muon system currently available.[24]

Calibration of the Drift Tube System

The drift tubes are calibrated in three steps. First, the inter-channel synchronization, second, the drift velocity calibration, and third, the time pedestal calibration. Reference [112] describes the methods in detail. The time measured by the Time to Digital Converter (TDC) t_{TDC} is given by

$$t_{\text{TDC}} = t_0 + t_{\text{drift}} + t_{\text{TOF}} + t_{\text{prop}} + t_{\text{L1}}, \tag{3.10}$$

with the inter-channel synchronization t_0, the drift time of the electrons t_{drift}, the time of flight of the muon t_{TOF}, the propagation time of the signal along the wire t_{prop}, and the Level-1 trigger[25] delay t_{L1}.

The first step equalizes time differences in the readout of individual wires. A test pulse is injected in the front-end board and the time until it arrives in the readout electronics is measured. This synchronization eliminates different arrival times of signals due to varying wire lengths and readout delays. It yields the value t_0 in equation 3.10.

The drift velocity calibration measures the effective drift time t_{drift} of the electrons inside the drift tube in all regions of the detector. The drift velocity is vital for the position measurement of the muon since the position is calculated by the product of the time delay between interaction and arrival of the electrons at the wire, and the drift velocity.

The time pedestal calibration measures the last three quantities of equation 3.10. They can be measured by analyzing the by t_0 corrected TDC time of the signal in cosmic muon events. A muon hitting the wire would leave the earliest possible signal and a muon hitting the drift tube on the far side of the wire the latest possible time. The rising edge of the box between those values provides an estimate for the sum of t_{TOF}, t_{prop}, and t_{L1}.

[23] The anode wires in the innermost chamber are tilted by an angle of 29° to compensate for the magnetic field.
[24] The redundancy will be restored in this area by the GEM project [109] which is currently under construction.
[25] c.f. section 3.3.6.

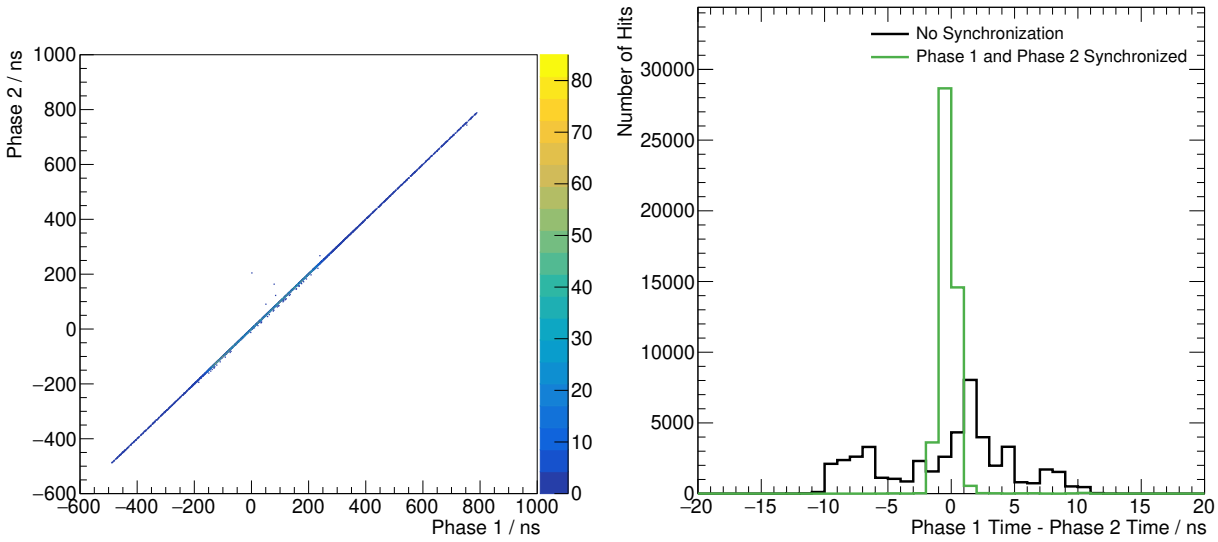

(a) (b)

Figure 3.10: Calibration of the phase-2 upgrade of the DT detector. (a) shows the two-dimensional representation of the phase-1 TDC time vs the phase-2 TDC time. (b) shows the width of the diagonal. Both values are perfectly correlated.

The readout system of the drift tube system will be upgraded for the HL-LHC [113]. In 2019, one slice of the drift tube system was equipped with the new electronics to test the new system. The signal is split to allow simultaneous readout with the legacy and upgraded readout. One of the first checks was to confirm that both readout systems measure the same events with similar arrival times. If the readout is working properly the TDC times should be perfectly correlated. Figure 3.10a shows the distribution of the legacy TDC time on the x-axis and the phase-2 TDC time on the y-axis. The values are shifted with respect to the mean of the chamber. The absolute value is not important because the readout delays and wire lengths are different. The values form a narrow diagonal.[26]

Figure 3.10b shows the width of the diagonal. The black curve corresponds to the unsynchronized TDC values, i.e., without the application of the inter-channel synchronization. The green curve displays the width after the synchronization. The green curve is much more narrow and shows the outstanding agreement between old and new readout as well as the importance of the synchronization.

3.3.6 The Trigger and Data Acquisition System System

The time between two collisions is 25 ns, which corresponds to an event rate of 40 MHz. With pileup interactions[27] the size of a proton-proton event is around 1 MB. This would correspond to

[26] Only wires with single hits per event are included in this figure because there is no a-priori matching between multiple hits per wire per event. If all combinations are taken into account, hits will appear off the diagonal but would not signal a malfunctioning readout. Therefore, these events are vetoed.

[27] See section 3.1 for more information.

a data rate of $40\,\mathrm{TB\,s^{-1}}$. No current computing system could provide such a gigantic bandwidth or even attempt to save such enormous amounts of data. We cannot easily reduce the event size without discarding potential critical information. However, most proton-proton events happening in CMS are soft QCD events, which do not have significant physics potential, are frequent, and, thus, can be scaled down. So, decreasing the event rate can bring the rate of data into acceptable regions without compromising the physics potential of CMS. The trigger system is precisely designed for this purpose.

CMS has a two-stage approach: First, the *Level-1* trigger reduces the event rate to around 100 kHz. It needs to be very fast to handle the high rates. For that reason, it is implemented at hardware level on the detector electronics. A hardware trigger is fast but comes at the cost of not having access to the complete event information. The Level-1 trigger was upgraded for Run 2 to handle the increased instantaneous luminosity and pileup [114]. According to the Level-1 trigger rate, the Data Acquisition System (DAQ) has to support a data link of around $100\,\mathrm{GB\,s^{-1}}$

The second stage is the *High-Level Trigger* (HLT). As the Level-1 trigger already decreases the rate, it does not have to be as fast as the Level-1 trigger and can be implemented on software level. It runs on a computing farm of commercial processing units. The HLT has access to the full event content. Thus, it can calculate high-level variables. It reduces the rate by another two orders of magnitude, leading to a final rate of 1 kHz [115].

3.3.7 Software and Computing

The analysis is performed in three steps:

1. *Skimming* from the *MiniAOD* format to the *pxlio* format. MiniAOD [116] is a data format developed by CMS. It contains less data than the AOD (Analysis Object Data) format and became the standard format for most analyses in Run 2. It stores the information in a *ROOT* file based, on the ROOT framework for data analysis [117, 118]. The skimming step discards all data which are not needed for this analysis and writes the output into a pxlio file. The Physics eXtension Library (PXL) [119, 120] simplifies many operations and provides an easy-to-use I/O library.
2. Analyzing the data and writing the results. The analyzer is written within the *Three A Physics Analysis* (TAPAS) framework [121]. It takes the pxlio files as input and produces again a ROOT file containing the aggregated results as histograms.
3. Postprocessing and statistical analysis. We obtain the final result by analyzing these ROOT files. The statistical interpretation is performed by the *combine* tool [122] developed by the CMS collaboration.

The first step runs on the *Worldwire LHC Computing Grid* (WLCG) [123], while the second step runs on the local RWTH Tier 2/Tier 3 cluster.[28] The third step runs on a local PC or the computing cluster of the physics department.

[28] The Grid is organized in various tiers. The Tier 0 mainly takes care of the reconstruction of data, while the Tier 1 data centers provide capacities for simulation. Tier 2 and Tier 3 data centers are utilized for simulation too but also for user analysis.

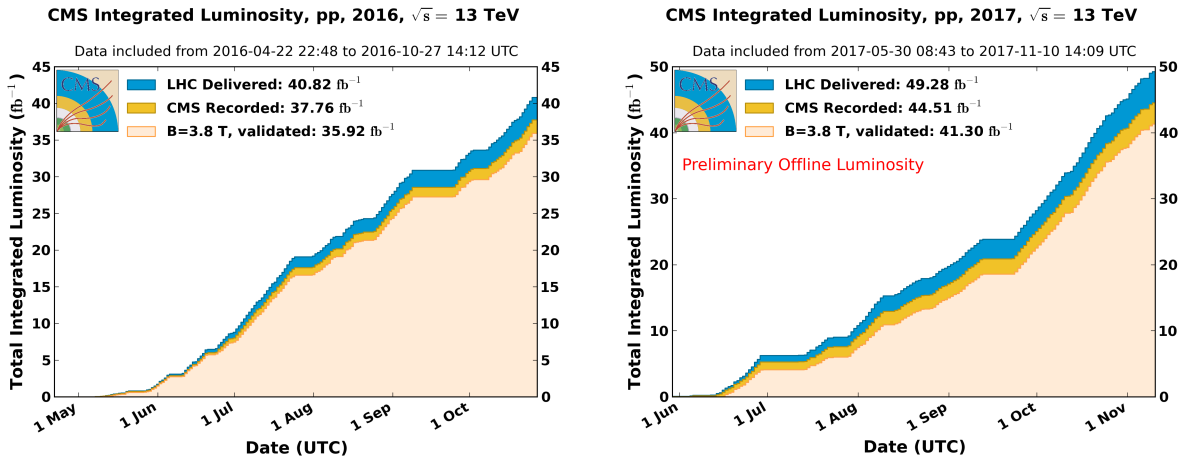

(a) (b)

Figure 3.11: Delivered, recorded and certified luminosity for (a) 2016 and (b) 2017. Figures taken from ref. [124].

3.3.8 Analyzed CMS Data

This thesis uses the proton-proton data taken in 2016 and 2017. They were recorded at a center-of-mass energy of $\sqrt{s} = 13\,\text{TeV}$. The integrated luminosities are $35.9\,\text{fb}^{-1}$ and $41.5\,\text{fb}^{-1}$ for 2016 and 2017 respectively, adding up to a total of $77.4\,\text{fb}^{-1}$.

The CMS dataset is split into several *trigger streams* where each of those contains events triggered by a set of related triggers. This thesis uses the *SingleMuon*, *SinglePhoton*, *SingleElectron* and the *DoubleEG* streams for the different analyses.

Every recorded event must have an unambiguous identifier. CMS uses three *event coordinates* to identify events: The number of the *run*, the *luminosity section (LS)* and the *event number*. A period of continuous data taking defines a run. If an issue arises during operation and a part of the detector has to be restarted, the operators stop the run and start a new one after resolving the issue. Ideally, we have a single run per fill. A luminosity section is a part of a run in which the luminosity is approximately constant. Finally, the event number is a continuous counter.

Every LS needs to be validated and certified for analysis. The certification ensures that detector issues do not compromise the data.

Figure 3.11 shows the integrated luminosity of 2016 and 2017. It includes the delivered, recorded, and certified luminosity. The recorded luminosity is smaller due to the dead time of the detector and pauses between runs caused by detector issues.

After this chapter has explained the detector itself, the next chapter will describe the reconstruction techniques to translate the raw detector output into physical objects.

4 Particle Reconstruction and Identification

The last chapter discussed the design of the CMS detector which is composed of multiple separate sub-detectors with different purposes. The tracker and muon system measure the trajectory of charged particles whose tracks are bent by the magnetic field of the solenoid. The ECAL measures the energy of photons and electrons and the HCAL the energy of neutral and charged hadrons. Muons are the only particles besides neutrinos which pass through the magnet. The muon system is designated to measure their properties. However, the detector provides only information about the direction of particles and their energies. It is up to advanced software algorithms to identify the nature of the particles themselves.

The most straightforward approach uses each sub-system standalone: The muon system reconstructs muons, the HCAL reconstructs jets, etc. However, the fine spatial granularity of the detector allows to reconstruct the entire event as a whole. This algorithm is called *Particle Flow* (PF) algorithm.

This chapter starts with a description of the PF algorithm in section 4.1 before it goes over into a detailed description of the reconstruction of electrons (section 4.3), muons (section 4.2) and jets (section 4.4). It follows a set of criteria to further enhance the quality of the reconstructed objects (section 4.5).

4.1 The Particle Flow Algorithm

The particle flow algorithm was first used by the ALEPH collaboration at LEP [125]. CMS adopted it, being the only experiment at a hadron collider to use it. It provides the core event reconstruction of CMS. One of the advantages is the superior resolution of $\boldsymbol{p}_T^{\text{miss}}$ compared to other algorithms [126]. The crucial pre-requisite is a detector with fine granularity, so different objects are not merging into a single large one. The algorithm is documented in all its details in Ref. [126].

This section goes through the different steps of the PF algorithm starting with tracking (section 4.1.1), clustering (section 4.1.2), and finally the linking (section 4.1.3).

4.1.1 Tracking

Iterative Tracking

A high tracking efficiency with a low misreconstruction rate is paramount for the PF algorithm. Both properties can be measured directly in simulation. The fraction of reconstructed tracks over all simulated tracks defines the efficiency and the fraction of reconstructed tracks that have no matched generated track gives the misreconstruction rate.

Tracking is difficult for multiple reasons. The main one is the substantial density of tracks at high pileup resulting in a vast number of possible combinations of hits. Also, particles can undergo interactions with the beampipe or the pixel and tracker layers, loose momentum and abruptly change their trajectory. To mitigate these issues, tracking is performed in multiple steps with different quality criteria like the number of associated hits, the track seeds, or the p_T and χ^2 of the fit. After each iteration, the algorithm removes the reconstructed tracks from the collection to limit the number of combinations. A combinatorial track finder does the track reconstruction based on Kalman filtering [127].

The first three iterations use the highest quality seeds from the pixel detector, but with loose requirements on displacement from the beam axis and low p_T requirement down to 200 MeV.[1] The looser requirement on the displacement allows a better reconstruction of particles originating from b-hadron decays as they have slightly displaced vertex due to the lifetime of the hadrons.

Later stages aim to reconstruct very displaced tracks by seeding the track in the strip and not the pixel detector. This alternative seeding recovers particles with very high p_T whose tracks might be merged into a single track in the pixel detector. They merge into a single track because the objects are more tightly confined due to the significant boost of the initial particle created at the hard interaction.

The final efficiency of the algorithm is above 90% at a misreconstruction rate below 3% for charged hadrons between 1 and 10 GeV. The efficiency decreases to 70% for particles with $p_T = 100$ GeV, but the excellent energy resolution of the calorimeters at these energies can compensate for this inefficiency.

Electron Track Finding

The track reconstruction of electrons has an additional obstacle. Ideally, energy clusters in the ECAL seed electrons. However, the tracker has a significant material budget of up to two radiation lengths [100]. Consequently, electrons likely radiate bremsstrahlung photons during the propagation through the tracker. This radiation results in a spread of the energy cluster in the ECAL along ϕ. For isolated electrons, these clusters still provide a proper measurement by taking the energy of the entire *supercluster* into account. Contrarily, the ECAL seeded approach might not work for electrons within jets because the energy density in the calorimeter is much larger, and for low p_T electrons where the spread along ϕ gets too large. In this case, electrons have to be seeded by the tracker.

The iterative tracking handles electron tracks already well. It reconstructs electrons without any radiation as described in the last section. Electron tracks with soft photon radiations are still entirely reconstructed, but have a larger χ^2. If the electron radiates hard photons, the reconstructed track will have less associated hits because the track will feature a significant kink.

[1] Actually, due to the magnetic field of the solenoid, tracks with a p_T below 700 MeV can never reach the barrel calorimeters and instead follow a spiral track towards the endcap calorimeters making it impossible to correctly reconstruct these particles without tracking.

As the probability of hadrons to undergo interactions in the tracker is smaller than for electrons[2], the χ^2 and number of hits can be used to differentiate between charged hadrons and electrons even on tracking level. After a pre-selection using these variables, the tracks of electron candidates are fit again using a Gaussian Sum Filter (GSF) [128], which handles sudden energy losses caused by radiation better.

This procedure improves the reconstruction efficiency of electrons contained in jets by a factor of two and reaches 40-85% depending on the transverse momentum. The misreconstruction rate also increases but can be mitigated by using the information of the calorimeters later. The reconstruction efficiency of isolated low-p_T electrons also improves by 5% and extends the reconstruction range for electrons down to 2 GeV.

Muon Track Finding

The muon reconstruction can be guided or at least supported by the dedicated muon system. The calorimeters stop all other particles (besides neutrinos), so only muons remain.[3] CMS supports three kinds of muon reconstruction:

Standalone Muons are reconstructed utilizing only the muon system using reconstructed segments of the muon chambers as seeds.

Tracker Muons are reconstructed using the inner tracker of CMS and matching at least one reconstructed segment in the muon system.

Global Muons match standalone-muon tracks to an *inner track* and re-fit the combined *global-muon* track.

The momentum resolution of the inner tracker is better for low-p_T muons. Muons with a p_T larger than 200 GeV profit from the global-muon fit. Muons with momenta below 10 GeV often undergo multiple scattering processes in the iron return yoke and are more efficiently reconstructed as tracker muons.

4.1.2 Energy Clusters in the Calorimeters

The calorimeters are the only detector system that can detect electrically neutral particles, i.e., photons and neutral hadrons. Therefore, their main goal is to measure the energy and direction of those particles. To do so, they need to differentiate between clusters formed by neutral and charged particles. They also assist in the electron reconstruction forming superclusters containing the electron and all radiated photons and the reconstruction of high-momentum charged hadrons for which the tracking efficiency and resolution are poor.

[2] The tracker material only adds up to a maximum of 0.6 hadronic interaction lengths [100].

[3] High-energetic hadrons can produce shower remnants, which extend through the calorimeter and magnet into the muon system. This behavior is called punch-through. Identification criteria can suppress these particles later. See section 4.5.1 for more information.

Clusters are seeded by taking the cell with the highest deposited energy and expanding it to neighboring cells up to a threshold corresponding to twice the noise level. An expectation-maximization algorithm calculates the energy and position of the measured particle in an iterative process. The algorithm is explained in detail in Ref. [126].

4.1.3 Linking

After all the steps described above, each detector system provides its own candidates. The PF algorithm establishes links between the candidates to obtain a global event view.

It links tracks to calorimeter clusters by extrapolating each track to the position of the cluster in the calorimeter. Then, it matches the track to the cluster closest to the extrapolated position. For electrons, the algorithm links possible clusters arising from bremsstrahlung photons to the electron by extrapolating tangents from the GSF track from each tracker layer. Matched clusters are then also linked to the electron. A dedicated method is applied to match bremsstrahlung photons which converted into an electron-positron pair [129] and links them to the electron as well. Clusters in ECAL and HCAL are linked when the cluster in the ECAL is in the envelope of the HCAL cluster since the ECAL has the finer granularity.

The PF algorithm also established links between different tracks sharing a common secondary vertex. The secondary vertex itself is saved if only one track connects it to the primary vertex and the invariant mass calculated from the outgoing tracks is above 0.2 GeV. Such topologies can hint to decays of b-hadrons.

The links between tracker and muon system were already explained in section 4.1.1.

4.2 Muon Reconstruction

After the description of the PF algorithm itself, I will now transition to the reconstruction methods of all particles relevant to this thesis.

Although the PF algorithm already provides well-reconstructed muons, it is possible to improve the momentum resolution even further for very-high momentum muons ($p_T > 200\,\text{GeV}$). The difficulty of reconstructing high-p_T muons is two-fold: First, the curvature of the track becomes very small, and the reconstruction relies on the usage of the muon system, but alignment uncertainties can have a significant impact on the momentum measurement. Second, for $p > 300\,\text{GeV}$[4] radiative losses become more important than ionization losses [111]. Such radiative losses can lead to electromagnetic showers in the muon system, which impacts this reconstruction efficiency and p_T resolution negatively.

To improve the reconstruction, three methods are explored in addition to the global muon fit: The *Tracker-Plus-First-Muon-Station* (TPFMS) fit, the *Dynamic Truncation* (DYT) fit, and the *Picky* fit. Ref. [111] describes them in detail.

[4]Note, this is not p_T but rather the total momentum which can be above 300 GeV even for muons with $p_T = 200\,\text{GeV}$ depending on η.

TPFMS makes use of the increased lever arm compared to the tracker-only fit, taking only the first muon station into account but limits the effect of electromagnetic showers discarding all other stations.

On the other hand, DYT tries to mitigate potential catastrophic energy losses, which cause a kink in the track leading to an inconsistent track fit for all hits after the catastrophic loss. DYT identifies such losses and does not take any following hits in the muon station into account.

The Picky algorithm aims to improve on the idea of TPFMS by explicitly identifying chambers with electromagnetic showers and vetoing those chambers for the fit. Due to the iron return yoke between two chambers, electromagnetic showers most likely do not extend into the next chamber but are contained in a single muon station.

The *TuneP* algorithm [111] decides on a track-by-track basis which of the six algorithms performs best. It uses both the χ^2/ndof and the relative p_T uncertainty as defined by the Kalman Filter [127]. First, it compares the relative p_T uncertainty of the Picky fit with the one of the DYT fit and keeps the better one. Then, it compares the χ^2/ndof of the kept fit from the previous stage with the tracker-only fit and, again, keeps the one with the smaller value. Finally, it compares the χ^2/ndof to the TPFMS fit and assigns the momentum of the better fit to the muon. If the alternative fitting algorithms fail, it uses the global-muon fit. If the p_T is smaller than 200 GeV, it uses the tracker-only momentum measurement. The TuneP algorithm selects in most cases either the Picky or DYT fit and only in a few percents of tracks one of the other algorithms.

The relative p_T resolution of TuneP muons is measured in cosmic events to be between 1 and 5% for muons between 50 GeV and 1 TeV in the barrel and 2 and 4% between 50 and 400 GeV in the endcap [111].

4.2.1 Measurement of the Muon Momentum Scale

Detector misalignment is the main reason for a mismeasured momentum scale. For high-p_T muons, a misaligned detector can lead to rather significant shifts of the momentum. A dedicated measurement using the generalized endpoint method [130] is performed to identify potential mismeasurements. It is important to remember that the momentum is measured by the curvature of the muon $\kappa \propto q/p$ with the charge q. A misalignment effect would be linear in κ and not in p_T, so we use κ for this study. We can detect potential misalignments by comparing the curvature in data and simulation. An additive bias κ_b is introduced by shifting $\kappa \to \kappa + \kappa_b$ and the value for κ_b is determined by minimizing the χ^2 in the comparison between data and simulation. The measurement is performed as a function of η and ϕ. It shows the largest misalignment in the endcaps of the detector with a bias of 0.15 / TeV in 2016 and 0.5 / TeV in 2017 [111].

4.3 Electron Reconstruction

Electrons reconstructed by the PF algorithm already have well-reconstructed energies. For high-energetic electrons, an additional correction is applied by only relying on the energy measurement of the calorimeter, which has a much better energy resolution than the tracker at

high energies [131]. The energy scale accuracy is measured in $Z \rightarrow ee$ events to 0.2 and 0.3% in the barrel and endcap, respectively and the energy resolution to 1.2 and 2.4%.

4.4 Jet Reconstruction

The PF algorithm provides a list of reconstructed particles and their momenta. Nevertheless, we have to apply a clustering algorithm to measure the momentum of the initial particle forming the jet. At first, this section summarizes shortly what jets are and why we have them in the detector (section 4.4.1). After that, I describe the jet clustering algorithms and the default algorithm used by CMS (section 4.4.2), and the handling of pileup (section 4.4.3). Finally, I introduce some algorithms which can identify jets originating from massive boson decays (section 4.4.4 and 4.4.5) and discuss applied corrections to the energy of jets (section 4.4.6).

4.4.1 Basics

The hard scattering process generates quarks and gluons, which cause the development of jets. Due to confinement, quarks and gluons cannot propagate freely through the detector but create a cascade of hadrons – the *parton shower*. The evolution of the shower is described by the splitting functions [95–97]. When the energy scale reaches the *hadronization scale*, the partons form hadrons, which can then traverse the detector as they have a net color charge of zero. Hadrons can also decay during their flight and, for example, create muons or photons which are also part of the jet.

Due to the initial momentum of the parton created at the interaction, all hadrons are boosted in the direction of the initial parton and are contained in a cone insight the detector.

4.4.2 Jet Clustering

The idea of a jet clustering algorithm is to reconstruct the energy and direction of the initial parton. It must aggregate all of the hadrons belonging to the jet and, at the same time, be able to separate between different jets caused by different partons.

It is also paramount that the algorithm provides infrared and collinear safety. The Feynman diagrams for the splitting of partons have two divergences: Soft gluon radiation where the energy of the gluon is close to zero and collinear splitting of a parton into two partons. The jet clustering algorithm must produce the same jet if a parton is replaced with a set of collinear partons or when soft gluons are added to the event [132].

We can divide jet clustering algorithms into two classes: *Recombination algorithms* and *cone algorithms*. Recombination algorithms combine particles (called *protojets*) pairwise and attempt to undo the steps of the parton shower. The *Cambridge/Aachen* [133, 134] algorithm or the kt algorithm [135] are prominent recombination algorithms. Cone algorithms, on the other side, use a fixed geometric shape and find stable configurations of jets for the entire event [136]. A well-known cone algorithm is *SISCone* [132].

CMS uses a recombination algorithm called *anti-kt* algorithm [136]. For the most parts, it is surprisingly similar to the Cambridge/Aachen and kt algorithms; therefore it, can be discussed together with them.

All three algorithms define two distances: ρ_{ij} is the distance between two protojets and ρ_i the beam distance. The exact definition of these distances distinguishes the algorithms and is discussed below. Besides that, they follow the same steps:

1. They form a list L of all protojets[5] and calculate the distances ρ_{ij} and ρ_i for all particles.

2. They look for the smallest distance in the set of all $\rho_{ij}, \rho i$ values:

   - If the smallest distance is ρ_{ij}: Merge i and j into a new protojet, calculate the new direction of the protojet, and replace i and j with it in L .

   - If the smallest distance is ρ_i: Promote i to a final jet and remove it from L.

3. Iterate until the list is empty.

The distances are defined as

$$\rho_{ij} \equiv \min(p_{Ti}^{2p}, p_{Tj}^{2p}) \cdot \Delta R_{ij}^2 / D^2 \text{ and} \tag{4.1}$$

$$\rho_i \equiv p_{Ti}^{2p}, \tag{4.2}$$

with the distance parameter D. The kt algorithm uses $p = 1$, the Cambridge/Aachen algorithm $p = 0$ and the anti-kt algorithm $p = -1$.[6] These definitions lead to vastly different behaviors:

Cambridge/Aachen has a pure angular ordering. This means it clusters collinear splittings first, and the last recombinations have wide angles. This method creates jets with a very diffuse border. The kt algorithm is ordered in p_T and angle and combines hard particles in the latest stage. Finally, the anti-kt algorithm uses an order inverse to the p_T of the particles. Therefore, the anti-kt algorithm tends to cluster all soft radiation to the hardest particle in the jet and never combines two soft particles. This behavior makes it very resilient against soft radiation.

Figure 4.1 compares the results of the different algorithms. One can see that – while being a recombination algorithm – anti-kt produces very cone-like jets centered around the hardest particle in the jet. Also, as can be seen in the upper region between the pink and green jet, it nicely allocates the energy in the overlap region between two jets to the harder one, unlike other algorithms as the kt algorithm.

In conclusion, the anti-kt algorithm yields the best results using an inverse ordering, and CMS chose it as the standard algorithm to cluster jets. It is implemented in the FastJet framework [137].

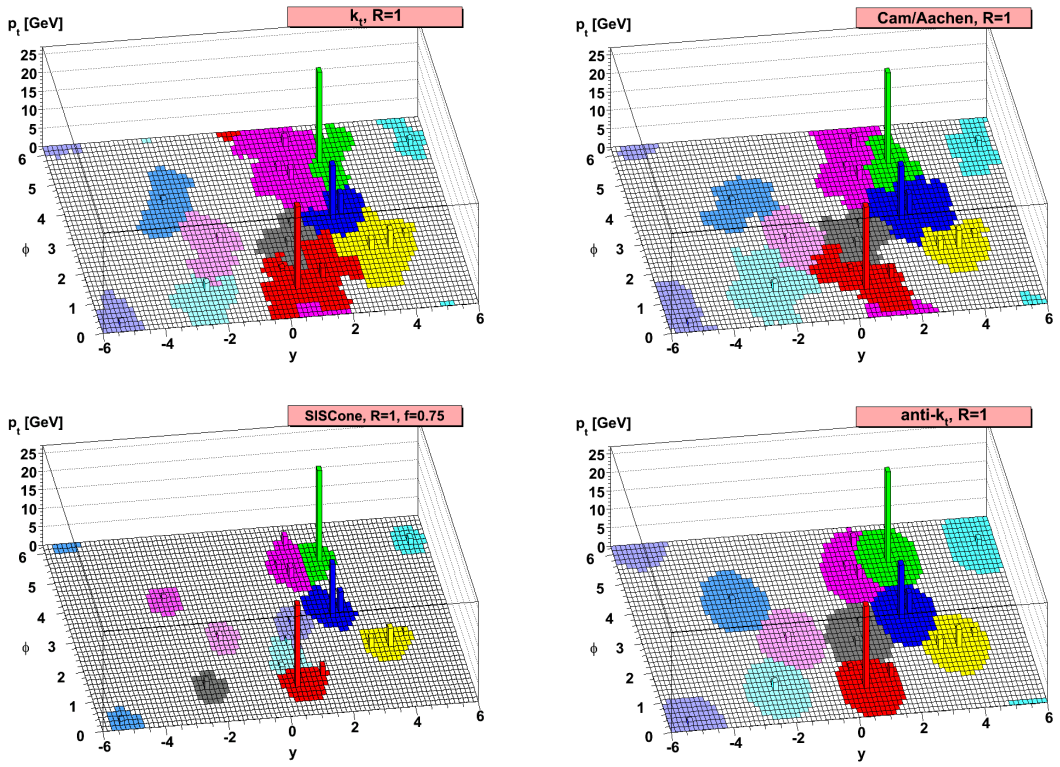

Figure 4.1: Comparison of different jet clustering algorithms. The plot shows the p_T on parton level in the η-ϕ plane. Figure taken from Ref. [136].

4.4.3 Pileup Rejection

If we only apply the jet clustering algorithm on a typical CMS event, we would overestimate the energy of the jets. The reason is the contamination through pileup.[7] Soft particles from other simultaneously occurring interactions might be superimposed with the jets from the hard scattering process of interest and we need to find a way to suppress their contributions. CMS commonly uses two different algorithms: *Charged Hadron Subtraction* (CHS) [126] and *PileUp Per Particle Identification* (PUPPI) [138]. There are many more algorithms available, but I will concentrate on these two algorithms applied by CMS and also used in this thesis.

Charged Hadron Subtraction is a pretty simple, yet effective, algorithm. It uses tracking information to identify tracks originating from charged pileup and removes them[8] from the collection before jet clustering. Only particles coming from the leading vertex are used to cluster the jet. It identifies the leading vertex as the one with the highest sum of transverse energy. The apparent disadvantage is that it cannot reject neutral pileup particles. For sufficiently low pileup, CHS still performs well as charged pileup accounts for about two-thirds of the entire pileup [126].

[5] At the beginning, a protojet corresponds to a particle (including electrons and muons) identified by the PF algorithm (see section 4.1). In later stages, it corresponds to an already combined particle.

[6] Hence the name of the algorithm.

[7] Pileup is described in detail in section 3.1.

[8] And the associated calorimeter clusters which were linked by the PF algorithm (cf. section 4.1).

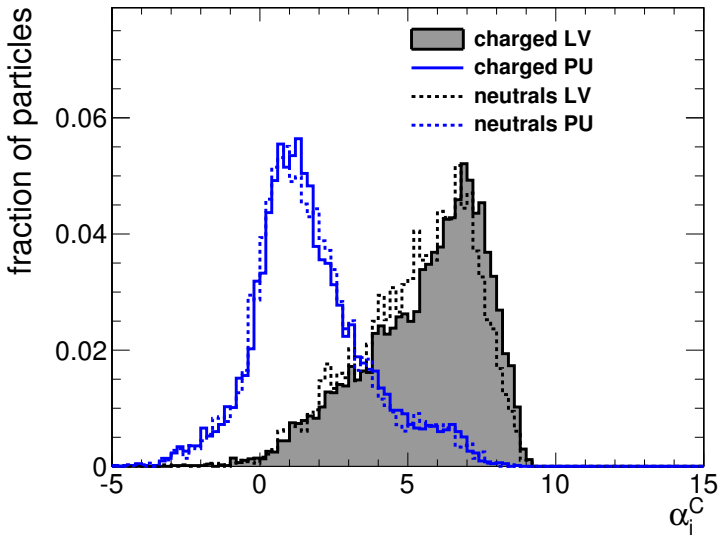

Figure 4.2: Distribution of the local shape α in the central part of the detector for charged and neutral hadrons as measured in simulation. LV denotes leading vertex and PU pileup. Figure taken from Ref. [138].

The contribution of neutral pileup particles is mitigated by applying an event-by-event jet-area based correction. However, this jet-area based corrections. One of the major shortcomings is the inability to tag individual neutral particles in the jet as pileup particles and remove them. This negatively impacts substructure algorithms.

PUPPI attempts to fix this disadvantage by identifying all pileup particles – charged as well as neutral. The algorithm defines a local shape α to differentiate between pileup particles and particles from the hard interaction. It is defined as

$$\alpha_i = \log \sum_{j \in event} \xi_{ij} \times \Theta(\Delta R_{ij} < D) \tag{4.3}$$

with the distance parameter of the jet clustering algorithm D and the metric

$$\xi_{ij} = \left(\frac{p_{Tj}}{\Delta R_{ij}} \right)^2 \tag{4.4}$$

which exploits the softer and more wide-spread spectrum of pileup particles in comparison to the harder, collinear jets.

In the central region where tracking is available, the detector can identify pileup particles as in the CHS algorithm described above. PUPPI makes use of the feature that the distribution of α is similar between charged pileup and neutral pileup. Therefore, it can use charged pileup as a proxy to create a template for neutral pileup. Figure 4.2 displays the distribution of α as measured in simulation. Finally, PUPPI applies a weight to each neutral particle according to the likelihood that it originates from a pileup vertex or a leading vertex based on the template created using charged hadrons. A weight of zero indicates a pileup particle, and a weight of

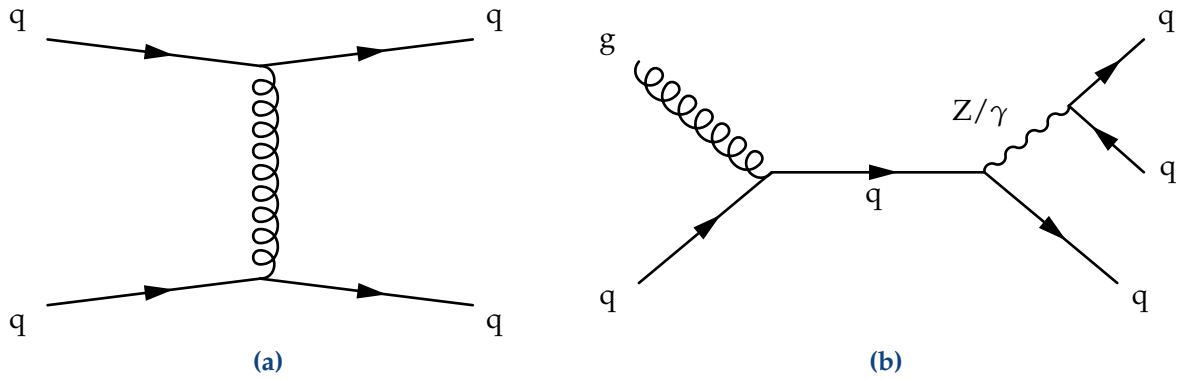

Figure 4.3: Feynman diagrams for (a) a pure QCD process and (b) a process including a hadronically decaying heavy boson. The outgoing quark in the right hand figure is important to provide an object against which the Z/γ can recoil to get a sufficient boost.

unity flags a particle stemming from the hard interaction. If the weight is between zero and unity, the p_T is re-scaled by the weight $p_T \to w p_T$. Particles with too small weight or re-scaled p_T are also discarded.

In the forward region where no tracking is available, i.e. $|\eta| > 2.5$, the templates from the central detector can still be used by applying a correction factor, which is measured in simulation.

The PUPPI algorithm is very flexible and allows experiments to tune its parameters to their own needs. Ref. [139] describes the adopted recipe by CMS. It also contains performance measurements underlying the strength of PUPPI, especially at high pileup multiplicities. Not only the jet resolution profits but also the $\boldsymbol{p}_T^{\text{miss}}$ resolution and muon isolation. The $\boldsymbol{p}_T^{\text{miss}}$ resolution using the PUPPI algorithm is nearly constant over the full range of primary vertices[9] and performs nearly twice as well at very high pileup values of more than 50 compared to the $\boldsymbol{p}_T^{\text{miss}}$ calculation using the CHS algorithm.

4.4.4 Substructure Algorithms: Soft Drop

Most of the jets in the CMS detector are QCD jets originating from a quark or gluon. The Feynman diagram in figure 4.3a illustrates such a QCD event. However, also processes involving heavy bosons like the W, Z, or H can create jets, as displayed in the Feynman graph 4.3b. The bosons predominantly decay hadronically into two quarks. This section introduces the *Soft Drop* algorithm [140]. It is designed to differentiate between QCD jets and jets originating from heavy boson decays.

The underlying idea is to reconstruct the decay products of the boson not in separate jets but as a single jet with a larger cone, often called *fat jet*. This is possible for bosons with $p_T > 200\,\text{GeV}$ using a jet clustering algorithm with a cone size of 0.8 (c.f. section 4.4.2). Both quarks are then sufficiently boosted by the initial momentum of the boson.

[9] Primary vertices are created by the interaction of two protons. Secondary vertices are formed by, e.g., b-meson decays and are displaced from the corresponding primary vertex. The vertex associated to the interaction of interest, i.e., the one with the largest sum of momenta is called leading vertex and all other ones pileup vertices.

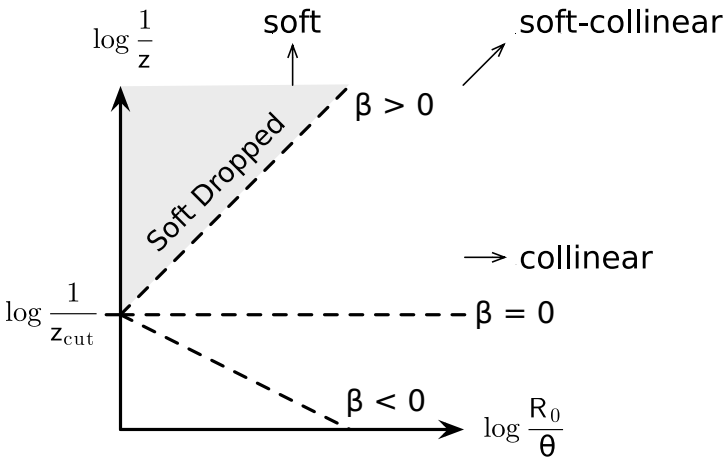

Figure 4.4: Sketch illustrating which particles are dropped by the Soft Drop algorithm for different values of β in the $\log 1/z - \log R_0/\Theta$ phase space. Everything above the dashed line is dropped. Figure taken from Ref. [140].

The Soft Drop algorithm makes use of the jet clustering algorithms described in section 4.4.2. The algorithm starts to de-cluster the jet undoing the last step of the clustering algorithm. Then, it applies the soft drop criteria

$$\frac{\min(p_{T_1}, p_{T_2})}{p_{T_1} + p_{T_2}} > z_{\text{cut}} \left(\frac{\Delta R_{12}}{R_0} \right)^{\beta}, \tag{4.5}$$

with the p_T of both protojets, the distance ΔR_{12} to each other, the distance parameter of the jet clustering algorithm R_0, and the two parameters z_{cut} and β.

If the criterion is fulfilled, the jet is the final soft drop jet; otherwise, the algorithm discards the jet with the smaller p_T and repeats the procedure. If the entire jet is de-clustered, it is removed from consideration.

Going back to the jet clustering algorithms we remember, that the anti-kt algorithm clusters all soft partons to the hardest parton. It does not provide insight into a potential substructure of the jet. Therefore, the Cambridge/Aachen algorithm is used, which combines protojet purely on an angular basis. The Soft Drop algorithm still works with jets clustered by any algorithm by reclustering the jet component with the Cambridge/Aachen algorithm, even if the anti-kt algorithm clustered the jet initially.

The parameter β governs the behavior of the algorithm. For $\beta > 0$ only soft radiation is dropped. If β is below zero, it also drops collinear radiation. The value chosen by CMS is $\beta = 0$ and is in the transition region between both modes. It removes soft and soft-collinear contributions. z_{cut} is set to 0.1. Figure 4.4 illustrates which particles are dropped by the algorithm for different values of β.

A disadvantage of the soft drop algorithm is its sensitivity to pileup. This deficiency is mitigated by using PUPPI instead of CHS (cf. section 4.4.3).

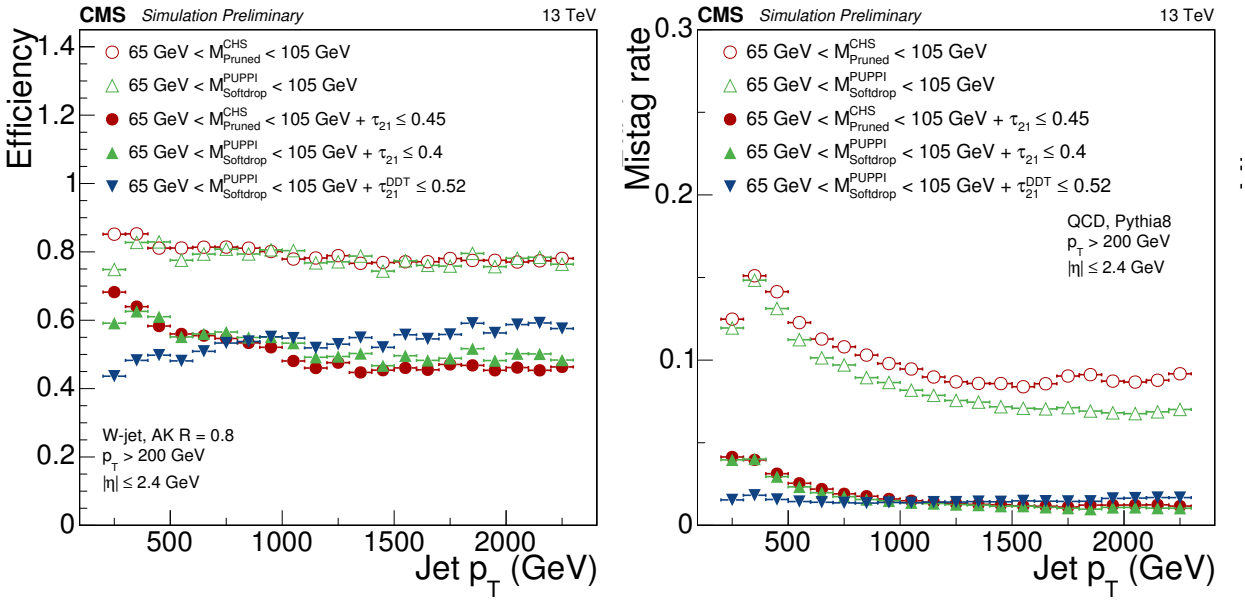

(a) (b)

Figure 4.5: (a) Efficiency and (b) mistag-rate of different substructure algorithms in CMS over the p_T of the wide-cone jet. The pure soft drop selection is shown in the hollow green triangles. It outperforms the previously used pruning algorithm. The solid points show additional selections exploiting the *N-Subjettiness* variable. Figure taken from Ref. [145].

Figure 4.5 illustrates the performance of the Soft Drop algorithm compared to the previously used *pruning* algorithm [141]. The Soft Drop algorithm achieves an efficiency of 80% at a mistag rate of 10%. The criterion to identify heavy boson jets is a mass window of 65 to 105 GeV on the soft drop mass. The solid markers represent the combination of the soft drop algorithm with the *N-Subjettiness* algorithm [142, 143] which further decreases the mistag rate at the cost of efficiency. It is described in the following section.

Another drawback of the soft drop algorithm is an introduced p_T dependence on the jet mass [144]. The source was identified to be the applied jet energy corrections.[10] A correction is applied to stabilize the mass and shift it to the correct value in a two-step process: First, we apply a p_T dependent correction of the generated mass to the nominal mass by fitting the ratio of both masses. Second, the reconstructed mass is shifted to the generated mass by fitting $(M_{\text{reco}} - M_{\text{gen}})/M_{\text{reco}}$. The result is a stable peak at the corresponding mass of the boson (cf. figure 4.6).

4.4.5 Substructure Algorithms: N-Subjettiness

In short, the N-Subjettiness algorithm tests the hypotheses that the jet has only a single initial particle, two particles, or three particles by dividing the jet into multiple sub-jets. It tests how well they align with the given number of axes [142, 143]. If two initial quarks form a jet, it should be aligned along two axes and not along a single one like a QCD jet. A boosted top-quark induced wide-cone jet should be aligned along three axes. Figure 4.7 shows event displays for a QCD,

[10] See section 4.4.6 for a description of those energy corrections.

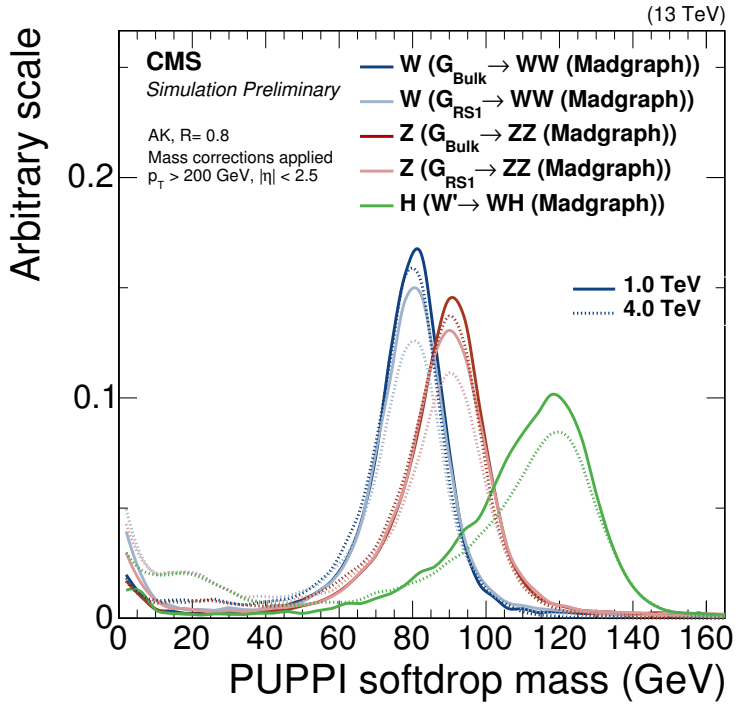

Figure 4.6: Mass of W, Z and H jets for 1 TeV jets (solid) and 4 TeV (dashed) after applying the mass corrections. Both curves peak at the same mass. Figure taken from Ref. [144].

W, and top jet. The color corresponds to the initial particles forming the jet. They confirm the expected behavior.

To quantify the likelihood that a jet originates from N initial particles the algorithm calculates the quantity

$$\tau_N = \frac{1}{d_0} \sum_k p_{Tk} \cdot \min(\Delta R_{1,k}, \Delta R_{2,k}, ..., \Delta R_{N,k}), \tag{4.6}$$

with

$$d_0 = \sum_k p_{Tk} \cdot R_0. \tag{4.7}$$

ΔR is the distance in the η-ϕ space and R_0 the distance parameter of the jet. The sum runs over all particles associated with the jet, and the axes are determined by minimizing τ_N. In figure 4.7, the square, circle, and x-mark indicate the result for $N = 1$, 2, and 3.

τ_N will be close to zero if a jet has less or equal than N axes. If the jet has more than N axes, the quantity will be significantly larger than zero because the algorithm has to place one axis between the individual energy clusters. Therefore, the quantity τ_N / τ_{N-1} is a sensitive discriminator to test if a jet aligns along N axes.

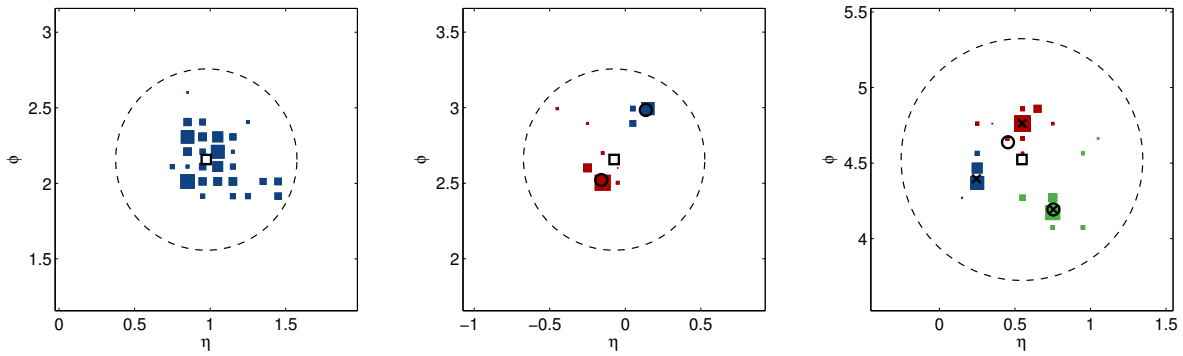

Figure 4.7: Event display of a clustered jet for (a) a QCD jet, (b) a W jet, and (c) a top jet. The size of the square is proportional to the energy deposit, while the color indicates the origin of the cluster. A QCD jet originates from a single quark or gluon, a W jet from the two quarks of its decay, and a top jet from the b-quark and the two quarks from the W decay. The square, circle, and x-marks indicate the axes for a one, two, and three axes hypothesis. Figure taken from [142].

4.4.6 Jet Energy Corrections

Jet energy corrections are the final calibration[11] applied to the jets to correct the energy to their actual value. They use a multi-stage factorized approach. The stages are performed sequentially on data and simulation. Ref. [146] describes them in detail.

In the first step, a pileup correction is applied to data and MC separately. It removes energy coming from pileup by using a function depending on η, p_T, and the energy density ρ. Residual differences between data and simulation are corrected using a function depending on η. The function is determined using a random cone method on zero-bias events[12]. The corrections remove any dependence on the luminosity of the data. After that, response differences in η and p_T are removed by analyzing the difference between the reconstructed and generated p_T in dijet simulation. Third, we correct in data for residual differences between data and simulation by analyzing dijet and $Z \to ee/\mu\mu$ events exploiting the p_T balance between both sides.

Additionally, the momentum of the jet is smeared in simulation as the resolution was found to be worse in data than in simulation. By applying Gaussian smearing to the jet momentum, we match the resolution in simulation to the one observed in data. Ref. [146] explains this method in greater detail.

Uncertainties stemming from these corrections need to be propagated through the analysis.

4.4.7 b-Tagging of Jets

Using the excellent tracker of the CMS detector, it is possible to tag jets arising from b-hadron decays. This information can provide a more in-depth insight into the hard scattering event.

[11] Substructure algorithms like soft drop use the calibrated jets as input.
[12] Zero-bias events are events triggered without any bias towards the event content.

b-hadrons have a relatively long lifetime of around 1.5 ps [4]. Thus, the decay products are displaced a few mm to one cm from the interaction point and create secondary vertices.

The CSVv2 algorithm used in this analysis combines the input from secondary vertices and displaced tracks to identify b-jets. The algorithm is described in detail in reference [147]. It features a neural network to differentiate between b-jets and light jets. In total, 19 distinct variables are used to train the algorithm. The output is a value between zero and one. A value close to unity indicates a high probability to originate from a b-hadron, a value around zero indicates a regular light jet.

4.5 Particle Identification

The reconstruction algorithms reviewed in the previous sections provide a list of objects of the event. However, we cannot use them directly as input to the analysis, but we need to apply additional quality criteria.

On the one hand, this helps to suppress misreconstructed particles. On the other hand, it filters well-reconstructed particles which were not produced promptly, i.e., during the hard interaction. Jets, for example, can contain muons produced by meson decays. We should not treat such muons like prompt muons created at the hard interaction, but rather as part of the jet. Electrons and photons are also frequently produced by pion decays. Similar to muons inside jets, we should not treat them as individual objects.

CMS developed IDs for all types of particles. A proper ID is highly efficient and has a low misidentification rate. Often, CMS provides different working points. Loose IDs are more efficient at the cost of an increased misidentification rate. Tight working points have more stringent requirements leading to less efficiency but higher purity. This analysis also takes advantage of specialized high-p_T IDs. They have an enhanced performance for high-energetic objects compared to the "normal" IDs.

Normally, IDs perform slightly different in data and simulation. We measure efficiencies in both data and simulation and derive a *scale factor*, which we apply to the simulation. The scale factor is a weight defined as

$$\mathrm{SF} = \frac{\varepsilon_{\mathrm{data}}}{\varepsilon_{\mathrm{simulation}}}. \tag{4.8}$$

Applying this weight re-scales the ID efficiency to the one observed in data. Such scale factors are applied per particle. The total scale factor is the product of all individual scale factors. Uncertainties of efficiency measurement are propagated to the efficiency and have to be applied in the analysis.

The following sections discuss the individual IDs for electrons, muons, and jets since the presented analysis features only these objects.

4.5.1 Muon Identification

This thesis utilizes the high-p_T muon ID. The primary sources for misreconstructed or non-prompt muons are muons from meson decays or hadronic punch-through (c.f. section 4.1.1). The following requirements are suited to separate such muons from prompt ones [130, 148].

- The muon needs to be a **global muon**.[13]
- The **global fit needs to include at least a single hit** in the muon system.
- **At least two reconstructed segments** in the muon system need to be matched to the muon. This requirement additionally suppresses accidental matches of segments to tracks and makes the ID consistent with the trigger logic.
- The **relative p_T uncertainty** of the TuneP fit has to be **below 30%.** This is a general requirement to ensure a decent fit quality.
- It is necessary that the **transverse impact parameter** of the track is **smaller than 2 mm** and the **longitudinal impact parameter smaller than 5 mm.** Both requirements help to get rid of cosmic muons as well as muons from decays. The latter requirement also suppresses muons from pileup. The impact parameter is the distance of the track extrapolated to the primary vertex in the beampipe. The transverse impact parameter is the distance perpendicular to the beam pipe (in the x-y-plane). The longitudinal impact parameter is the distance along the beam pipe (in z-direction).
- **At least one pixel hit** needs to be included in the fit to suppress non-prompt muons.
- **A minimum of six tracker hits** are used by the fit to ensure a decent p_T measurement.

Moreover, isolation criteria are applied to filter muons inside jets. This analysis uses the loose working point of the tracker isolation. The relative isolation is defined by the **sum of all tracks around the muon** in a cone with a size[14] of $\Delta R = 0.3$ **divided by the momentum of the muon.** The quantity needs to be **below 10%.**

The efficiency of the high-pt ID in data is measured as a function of η and p_T and is above 95% [149, 150]. The scale factor between data and simulation ranges between 97 and 99%. The isolation efficiency is measured on top of the ID and is between 95 and 100% increasing with the p_T of the muon. The isolation efficiencies in data and MC agree within 1% [149, 150].

4.5.2 Electron Identification

The *HEEP* (high energy electron pairs)[15] ID used in this analysis is also specifically tuned to identify high-energy electrons efficiently. It suppresses electrons from hadron decays, photon conversions, and misidentified jets [131, 153]. The following criteria must be fulfilled:

- The **transverse energy** must be **above 35 GeV**.

[13] See section 4.1.1 for an explanation.
[14] See chapter 3.3.1 for an explanation of ΔR.
[15] Different names exist for this acronym. The two main ones are the one presented above and *High energy electrons and photons*. Both were used interchangeably in various publications, e.g., references [151, 152].

- The electron reconstruction is required to be **driven by the ECAL** (c.f. section 4.1.1), because the energy measurement of the ECAL is more precise than the tracker measurement at large energies.
- The **distance between** the extrapolated **track and the ECAL cluster** must be **below 0.004 (0.006)** in the barrel (endcap) **in η and below 0.06 rad in ϕ** to reject photons.
- The **fraction of energy deposited in HCAL and ECAL** has to be **below $1\,\text{GeV}/E + 0.05 (5\,\text{GeV}/E + 0.05)$** in the barrel (endcap). Electron showers should be contained in the ECAL and only a small amount energy can leak into the HCAL. In contrast, jets deposit their energy mainly in the HCAL.
- The **energy spread in η direction** is measured by $\sigma^{5\times5}_{i\eta i\eta}$. I refer to the literature [131] for the exact definition. It must be **smaller than 0.03** in the endcap. In the barrel a different requirement is used (see next bullet point). An electromagnetic shower is typically narrower than a hadronic shower. The energy spread in ϕ is not sensitive because the energy is more spread because bremsstrahlung photons are scattered in ϕ due to the magnetic field.
- In the barrel another shower shape variable is used. Either the **ratio of the energy contained in a $1x5$ or a $2x5$ array** around the seed **and the $5x5$ array** needs to be **above 0.94 ($1x5$) or 0.83 ($2x5$).**
- Prompt electrons should be isolated from other energy deposits in the calorimeters. The requirement on the **relative isolation in the ECAL and the first readout section of the HCAL** is given by

  $$\text{Rel. Iso.} < 2\,\text{GeV} + 0.03 E_T + 0.28\rho \tag{4.9}$$

  in the barrel and

  $$\text{Rel. Iso.} \begin{cases} < 2.5\,\text{GeV} + 0.28\rho & E_T < 50\,\text{GeV} \\ < 2.5\,\text{GeV} + 0.28\rho + 0.03(E_T - 50\,\text{GeV}) & E_T > 50\,\text{GeV} \end{cases} \tag{4.10}$$

  in the endcap. ρ is the average energy density in the event and is estimated using the median of the energy density distribution in clustered jets [131].
- The **total energy of tracks** in a cone with radius of 0.3 **around the electron** is required to be **below 5 GeV.** This isolation criteria suppresses mis-identified hadrons.
- To differentiate between converted photons and prompt electrons, **at most one hit** in the inner tracking is allowed to be **missing**.
- Finally, the **transverse impact parameter** must be **below $2\,\text{mm} (5\,\text{mm})$** in the barrel (endcap).

The HEEP ID efficiency is measured to be around 87% in Drell-Yan events [154, 155]. The scale factor has no p_T dependence and is provided separately for barrel and endcaps. They are in the order of 96 to 97%. In 2017 the efficiency degraded towards the end of the year by a few percent because of the issues of the new pixel detector. These issues are summarized in section 3.3.3. The ID scale factor corrects for the observed inefficiencies and increases up to 94%.

4.5.3 Jet Identification

The main task of the jet ID is to suppress jets arising from noise. The tight working point of the jet ID is 99% efficient and rejects more than 98% of the background for $|\eta| < 3$ [156, 157]. It features requirements on the energy fraction of electrons, hadrons and muons, as well as multiplicities of particles, and thereby profits heavily from the particle flow reconstruction. The criteria are listed below:

- **Less than 90% neutral hadron energy fraction.** Real jets are a mixture of neutral and charged hadrons and should not purely be made up by neutral hadrons.
- **Less than 90% neutral electro-magnetic energy fraction.** The same argument is true for the electromagnetic component of the jet.
- **Jets must be made up of at least two components.** A jet is the result of a hadronic shower, which is composed of many particles.
- **The charged hadron energy fraction must be above zero** and a jet must have **at least one charged particle**.

b-jets are identified using the CSVv2 algorithm described in section 4.4.7. They are used in the W channel to suppress events from top-quark induced backgrounds. The analysis utilizes the tight working point. The b-tag efficiency is around 40% with a mistag-rate of 0.1% for light flavor jets.

The analysis applies also a scale factor to correct for different responses of data and simulation to the algorithm. Every event is weighted by a factor which is defined as the ratio of the probability to observe a given configuration of jets in data and MC simulation:

$$w = \frac{P(\text{Data})}{P(\text{MC})}, \tag{4.11}$$

with

$$P(\text{MC}) = \prod_{i=\text{tagged}} \varepsilon_i \prod_{j=\text{not tagged}} (1 - \varepsilon_j) \tag{4.12}$$

and

$$P(\text{Data}) = \prod_{i=\text{tagged}} \text{SF}_i \varepsilon_i \prod_{j=\text{not tagged}} (1 - \text{SF}_j \varepsilon_j). \tag{4.13}$$

ε is the tagging efficiency measured in MC simulation for the analysis specific final state. SF is the scale factor which is determined by measuring the efficiency in data. I refer to the literature [147] for the exact methods to measure the efficiencies and mistag-rates. Both quantities depend on η, p_T, and the jet flavor. The uncertainty on the scale factor needs to be propagated through the analysis.

4.6 Summary

This chapter discussed the reconstruction and identification algorithms to convert the raw data recorded by the detector into physical objects. The next section of this thesis examines the characteristic signature typical signal events leave in the detector.

5 | Signal Properties

This chapter introduces the expected kinematic properties of an excited lepton signature. It aims to convey a feeling of the signal to the reader and to motivate the kinematic requirements described in chapter 7. I begin the discussion with a section explaining the general simulation procedure (section 5.1). Following that, I examine features that are common for all channels, in section 5.2. Then, I discuss the three different channels presented in the thesis separately, starting with the CI channel (section 5.3), the Z channel (section 5.4), and ultimately the W channel (section 5.5). The decays are described in detail in section 2.3.3. I will summarize the most important information for the discussion.

5.1 Signal Simulation

The excited lepton signal is simulated using Pythia8 [37]. Pythia8 is a standard simulation tool for collisions of high-energy particle beams. It can calculate cross sections for several SM and BSM processes, generate physical events, decay particles, hadronize jets, simulate initial- and final-state radiation, and much more.

The excited lepton signature is simulated for different excited lepton masses in the range of 200 GeV to 7 TeV. Table 5.1 documents the exact signal points for all three channels and their respective cross sections. A common value for Λ was chosen and set to 10 TeV, f and f' are set to unity. We can rescale the cross section for different values of Λ, f and f' using the formulae provided in sections 2.3.2 and 2.3.3 under the assumption that the shape of the distribution is invariant under changes of these parameters. This assumption is only approximately correct, as these parameters affect the width of the resonance. However, these effects are negligible compared to the detector resolution and, thus, can be ignored. Also, the final search variable will not try to reconstruct the excited lepton and make use of the resonance width.

All decay channels are simulated separately from each other. For example, only the CI decay into two leptons and two jets is allowed for the simulation of the CI channel. This procedure eases the posterior variation of Λ, f and f' since we can trivially incorporate branching fraction variations into the result. Possible interferences with the Standard Model are not simulated.

All distributions presented in this chapter are obtained using parton-level information, i.e., without any simulation of the detector response. Specifically, they do not include the detector resolution. I use the muon channel for this study. On generator level, both electrons and muons behave nearly identical, so the distributions for excited electrons are similar. Hence, the results of this study are valid for the electron channel as well.

Table 5.1: Simulated signal masses for all three channels and the respective cross section for $\Lambda = 10\,\text{TeV}$ and $f = f' = 1$.

Mass / TeV	σ / fb [37]		
	CI channel	Z Channel	W Channel
0.2	0.22	-	-
0.25	-	4.23	24.8
0.5	0.68	2.87	14.9
0.75	0.99	1.76	9.33
1.0	1.12	1.11	5.79
1.5	0.99	0.44	2.28
2.0	0.69	0.17	0.86
2.5	0.40	$6.4 \cdot 10^{-2}$	0.32
3.0	0.22	$2.4 \cdot 10^{-2}$	0.12
3.5	0.11	$8.8 \cdot 10^{-3}$	$4.6 \cdot 10^{-2}$
4.0	$5.3 \cdot 10^{-2}$	$3.2 \cdot 10^{-3}$	$1.6 \cdot 10^{-2}$
4.5	$2.4 \cdot 10^{-2}$	$1.2 \cdot 10^{-3}$	$6.0 \cdot 10^{-3}$
5.0	$1.1 \cdot 10^{-2}$	$4.3 \cdot 10^{-4}$	$2.2 \cdot 10^{-3}$
5.5	$5.0 \cdot 10^{-3}$	-	$8.4 \cdot 10^{-4}$
6.0	$2.4 \cdot 10^{-3}$	-	-
6.5	$1.2 \cdot 10^{-3}$	-	-
7.0	$6.9 \cdot 10^{-4}$	-	-

5.2 Common Kinematic Features

This section discusses features which are common to all decay channels, i.e., properties which are only depending on the production of the excited lepton and not its decay. I chose the CI channel to produce the plots presented in this section. All channels share the production method. Hence, the results can be transferred to the other channels as well.

Figure 5.1a displays the mass of the generated signal. It does not include detector resolution effects. All four signal points peak at their expected mass i.e. 200 GeV, 1 TeV, 3 TeV and 6 TeV. I will use these mass points throughout this section to display how signal properties change under the mass hypothesis. The width of the peak increases towards higher masses, and for the heaviest signal mass point, a fraction of events is produced *off-shell*. In other words, the excited lepton is not produced with its nominal mass, but with a lower mass because the energy of the parton system is not sufficient to produce it on its mass shell. Figures 5.1b and 5.1c show the pseudorapidity and ϕ distributions. Excited leptons are produced in the central part of the detector and uniformly in ϕ.

All channels have a common production method: An excited lepton is produced in conjunction with an associated SM lepton. Since the production is a basic $2 \to 2$ process, the excited lepton and the SM lepton are produced back-to-back. Therefore, their $\Delta\phi$ is exactly π. A longitudinal boost of the initial system can result in different pseudorapidities.

The angular distribution of the decay products depends on the boost of the excited lepton. The

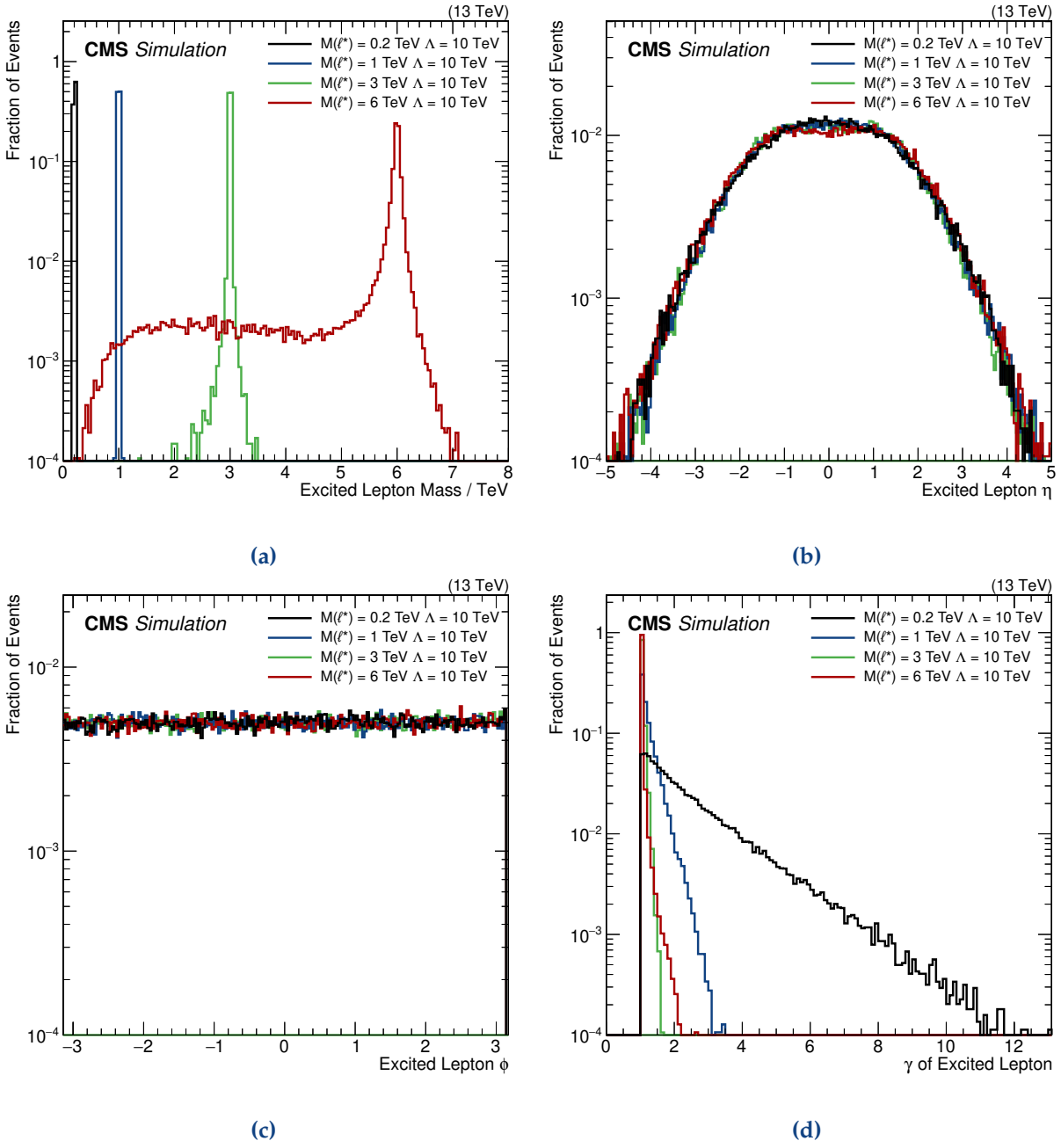

Figure 5.1: Basic kinematic properties of excited leptons with different masses produced in proton-proton collisions at $\sqrt{s} = 13\,\text{TeV}$. (a) shows the invariant mass distribution of the produced $\ell^\star$, (b) the η distribution, (c) the ϕ distribution, and (d) the distribution of the relativistic γ factor of the $\ell^\star$. All excited leptons have their mass peak at the expected position, are produced mainly in the central part of the detector and uniformly in ϕ. Light excited leptons have a more considerable boost than heavy ones.

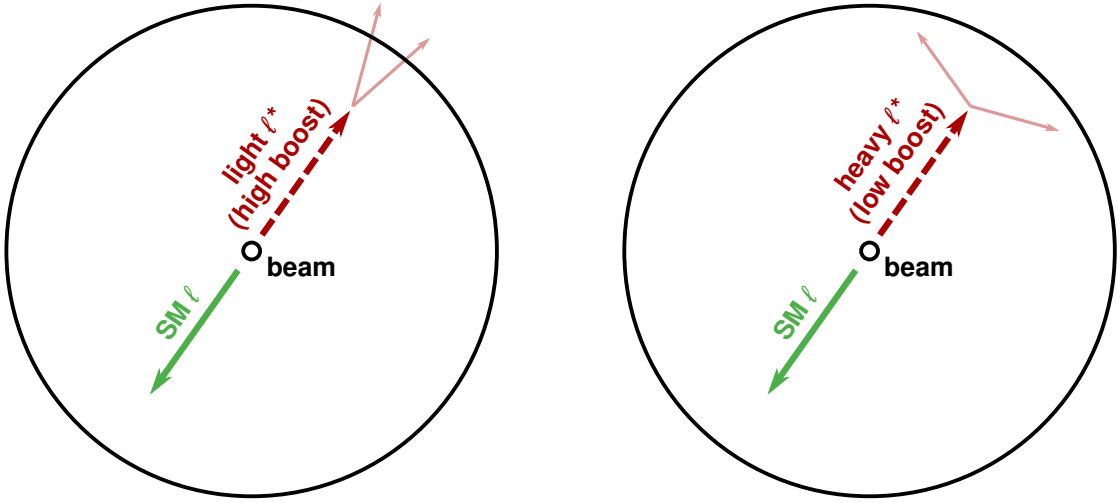

(a) (b)

Figure 5.2: Sketches illustrating typical topologies for (a) light excited leptons and (b) heavy excited leptons. In the former case, the decay products are boosted and have a small spatial distance; in the latter case, the boost is smaller and the decay closer to a back-to-back topology. The excited lepton and the associated lepton are always back-to-back. The beam is perpendicular to the drawing plane.

relativistic γ factor of the $\ell^\star$ is displayed in figure 5.1d. As expected, the boost is substantially larger for light excited leptons than for heavy ones because the total amount of energy is fixed by the center-of-mass energy of the parton system. In the rest frame of the excited lepton, the decay products are produced back-to-back for two-body decays. Three-body decays are not realized by nature.[1] It is simulated by Pythia as two successive two-body decays. The mass of the intermediate particle is not fixed and determined randomly. For light signals, the decay products are boosted into the direction of the excited lepton.

If the initial boost is large, the decay products have a small angle between each other. Figure 5.2a draws a sketch of typical kinematic distributions: The decay products all have a small angle between each other and are back-to-back to the associated lepton. Contrary, heavy excited leptons typically lead to wide-spread decay products since the boost is small. Here, we expect the decay products to be back-to-back, and hence not necessarily back-to-back with the associated lepton, as the sketch 5.2b illustrates.

5.3 The CI Channel

The CI channel analyzed in this thesis leads to a final state of two leptons and two jets. Final states with four leptons, or two leptons and two neutrinos are also possible but neglected since their branching fraction is significantly lower. Figure 5.3 displays the Feynman diagram. I chose signal masses of 200 GeV, 1, 3, and 6 TeV for this comparison, as in the previous section.

[1] The weak interaction was assumed to be a three-body decay before the W boson was discovered. For energies below the W mass an effective four-Fermi vertex description of this interaction provides good results. At energies at or above the W mass the intermediate particle can be resolved and the four-Fermi vertex description is not valid anymore. Contrary, the CI of the excited leptons does not have an intermediate particle with a given mass.

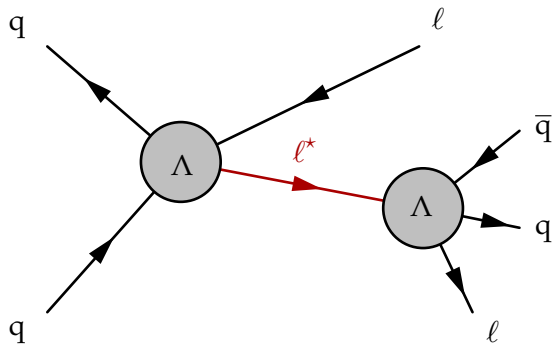

Figure 5.3: Feynman diagram of the CI channel. For more information see section 2.3.3.

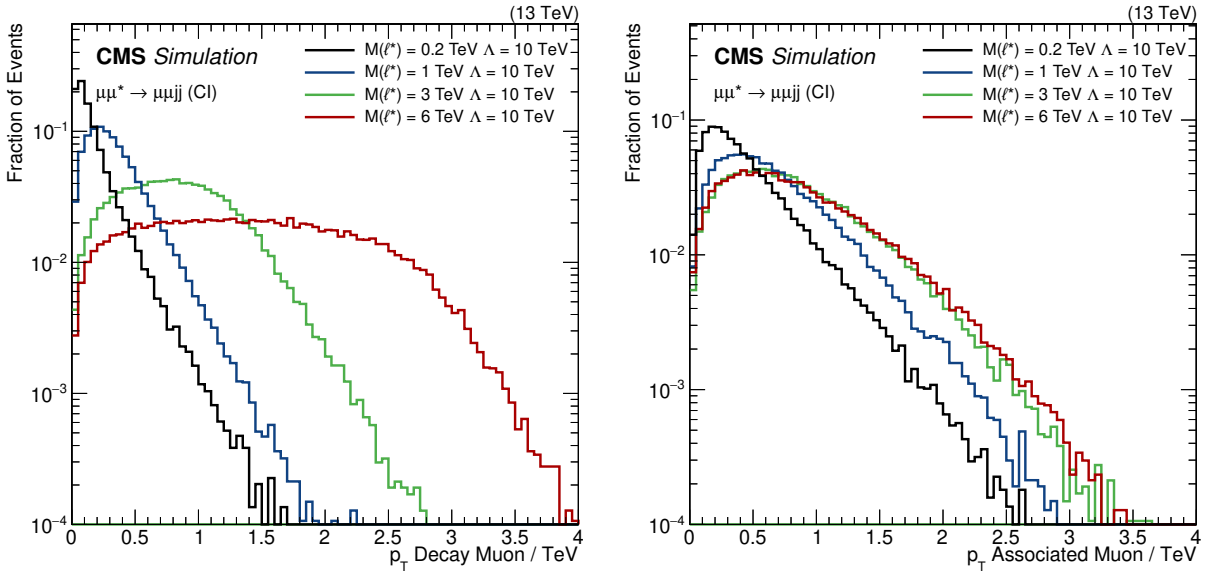

(a) **(b)**

Figure 5.4: Transverse momentum distribution of (a) the lepton originating from the decay of the excited lepton and (b) the associated lepton. For light excited leptons, the spectrum of the associated lepton is much softer than for the one coming from the decay. For massive signals, it is the other way around. The p_T of the leptons covers a wide range from 100 GeV to multiple TeV. The average p_T increases with the signal mass.

Figure 5.4 shows the transverse momentum of both leptons. They range from around 100 GeV for light excited leptons up to multiple TeV for heavy ones. On generator level, the information which lepton originates from the decay and which is the associated one is available. Without this information, there is no a priori way to determine the origin of the lepton. Figure 5.5 shows the probability that the leading[2] lepton originates from the excited lepton decay. For light signals, the leading lepton is most probably the associated one, while it is the other way around for heavy excited leptons. The reason is the conservation of the total energy and momentum during the collision. The excited lepton will recoil against the associated lepton with roughly the same momentum. The energy of the excited lepton is then split across the three bodies of the decay

[2]Leading means the lepton with the highest p_T. Sub-leading means second-highest p_T.

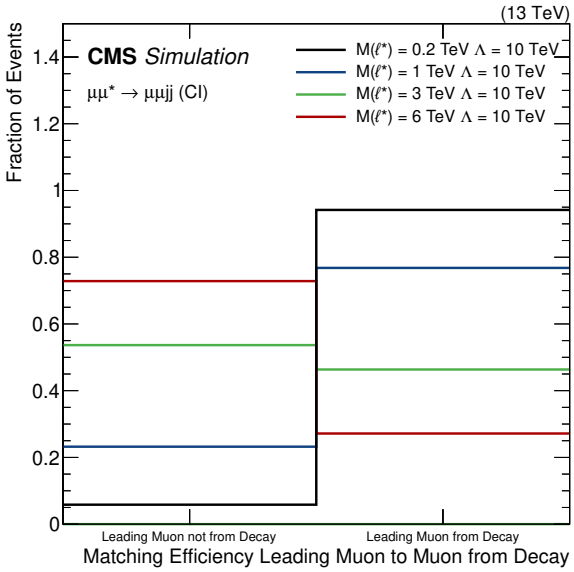

Figure 5.5: Probability that the lepton stemming from the $\ell^\star$ decay corresponds to the leading lepton, i.e., the one with larger p_T. For low signal masses, this probability is substantial, for heavy excited leptons it is rather unlikely.

while the associated lepton keeps its entire momentum. For heavy excited leptons, the mass is much larger part of the total energy, and the momentum of the excited lepton is much lower. The decay products gain their momentum due to the mass of the excited lepton and not due its initial momentum as for light excited leptons. In these cases, the leading lepton more likely stems from the excited lepton decay.

Figure 5.6 presents the transverse momenta of the two quarks matched to the decay of the excited lepton. At tree level, there are only two quarks present in the interaction. In reality, not only these two quarks will produce jets but also initial- and final-state radiation (ISR and FSR) as well as pileup. These additional jets can lead to more ambiguities in the matching of objects to the decay products of the $\ell^\star$, especially for light excited leptons where the p_T of the jets is relatively small.

For sufficiently massive excited leptons, all objects are expected to pass acceptance requirements of the transverse momentum, which will be in the order of 20 to 50 GeV. For light excited leptons, we expect an efficiency loss if two leptons and two jets are required, and ambiguities in the assignment of jets can arise due to ISR and FSR jets.

Figure 5.7 displays the pseudorapidity distribution of the leptons and the two quarks matched to the decay of the excited lepton. All objects are mostly inside the detector acceptance of $|\eta| < 2.4 - 2.5$.

Another essential quantity is the angular distance between the objects.[3] If objects are not well separated, modified isolation criteria need to be applied. If both jets are close to each other, we can use substructure techniques to differentiate between signal and background.[4] Figure 5.8a

[3] See section 3.3.1 for a definition of the distance of two particles to each other.
[4] See sections 4.4.4 and 4.5.1 for more information about isolation and substructure.

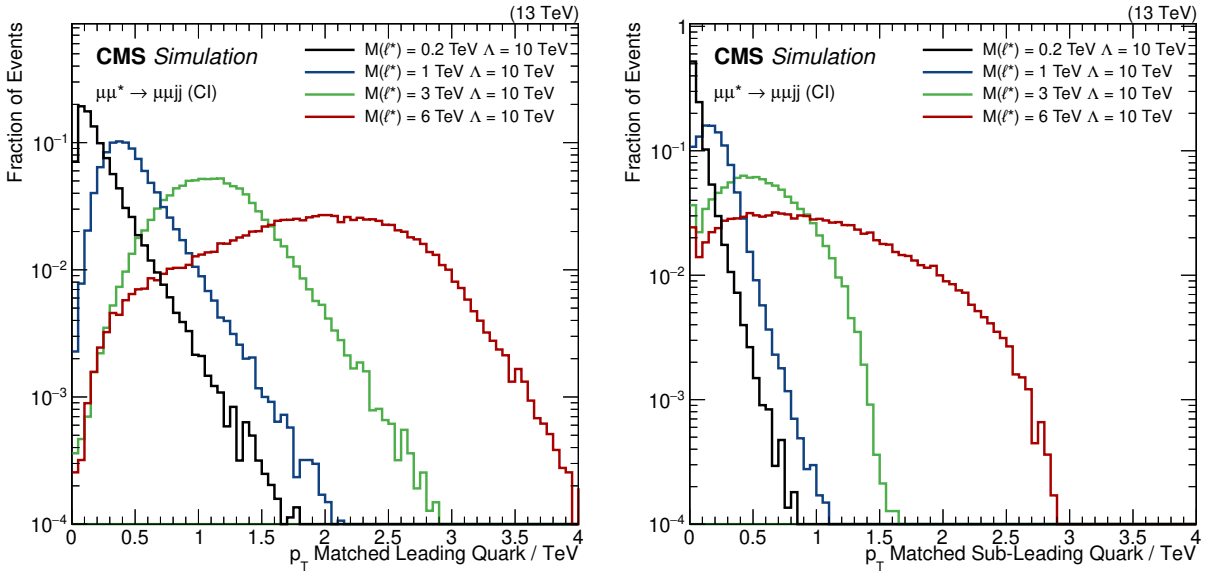

(a) **(b)**

Figure 5.6: Transverse momentum distribution of the quarks originating from the decay of the excited lepton. (a) shows the leading quark and (b) the sub-leading one. As expected, the average p_T of a quark increases to more massive excited leptons, and extends above 3 TeV for an excited lepton mass of 6 TeV.

displays the distance between the two quarks of the decay. Only for light excited leptons, both quarks would merge into a single jet with a distance parameter of 0.8. As this channel is especially sensitive for massive excited leptons[5], I decided to use two jets with a distance parameter of 0.4. Figure 5.8b shows exemplarily the distance between the lepton from the decay to the leading quarks. Again, both objects are well separated for sufficiently heavy signals. The reason for the smaller distance for light excited leptons is their boost, as discussed in the previous section.

Furthermore, the mass of the di-lepton pair shown in figure 5.9 is of interest. As there is no intermediate boson in the decay chain, the di-lepton mass spectrum does not feature a peak but is rather flat. This property can later be exploited to differentiate between signal and background.

The last figure of this section, figure 5.10, compares the flavors of the quarks from the decay. For massive signals, all six quark flavors are equally likely. Light excited leptons cannot decay into two top quarks because not enough energy is available. Both quarks always have the same flavor.

[5]See section 2.3.3.

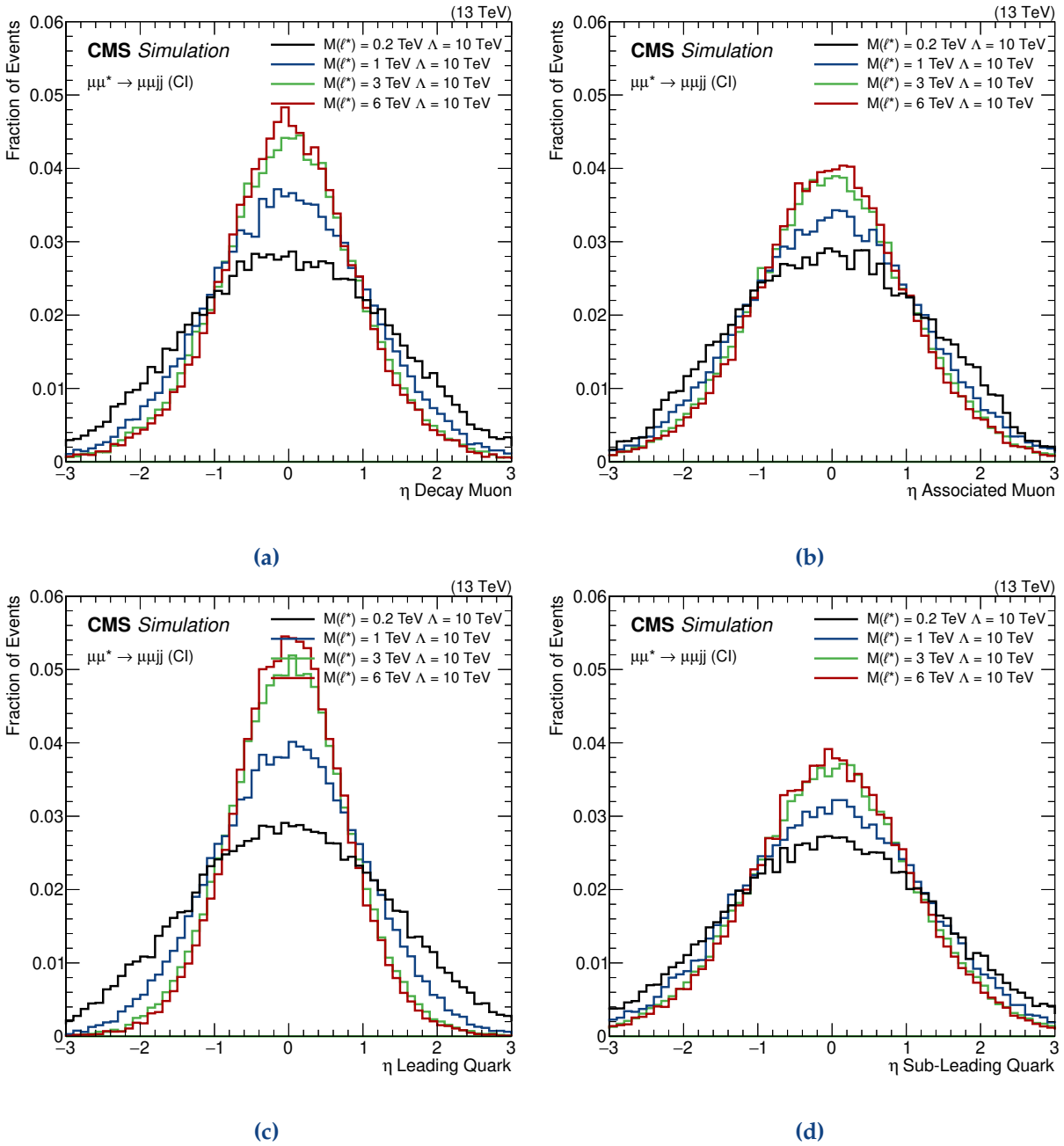

Figure 5.7: Normalized pseudorapidity distribution of (a) the lepton from the decay, (b) the associated lepton, (c) the leading and (d) the sub-leading quark.

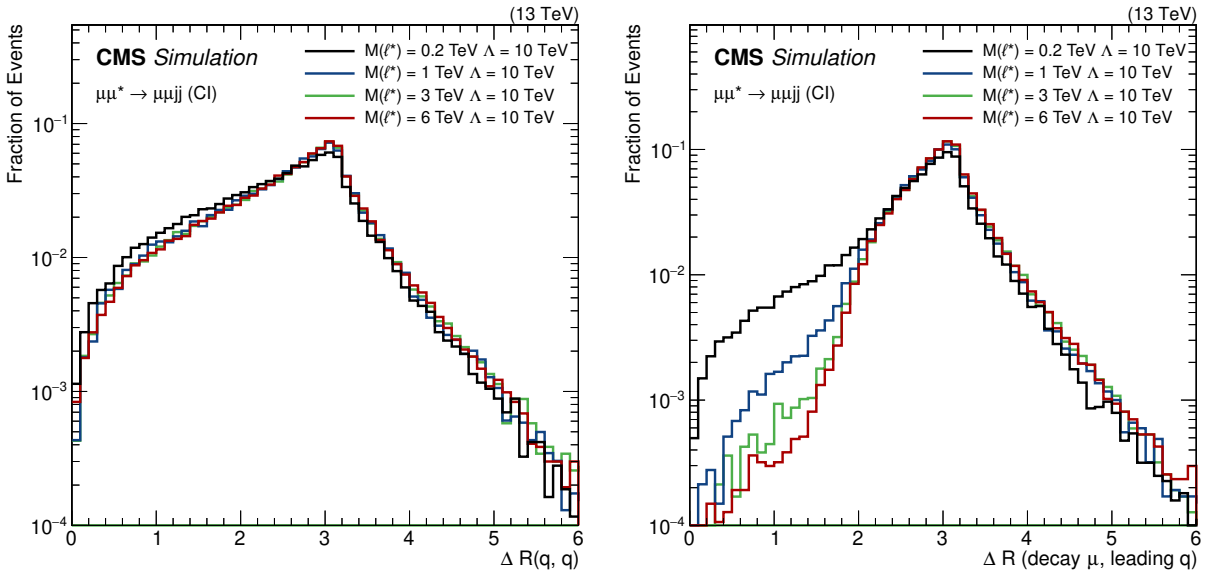

(a) **(b)**

Figure 5.8: Distribution of the spatial distance in the η-ϕ-plane between (a) both quarks of the decay and (b) the leading quark and the lepton coming from the decay. Both distributions exhibit a sufficient separation between the objects to use standard reconstruction and isolation methods. The distribution on the right-hand side peaks slightly stronger because the leading jet is more likely to be back-to-back to the muon as the sub-leading jet.

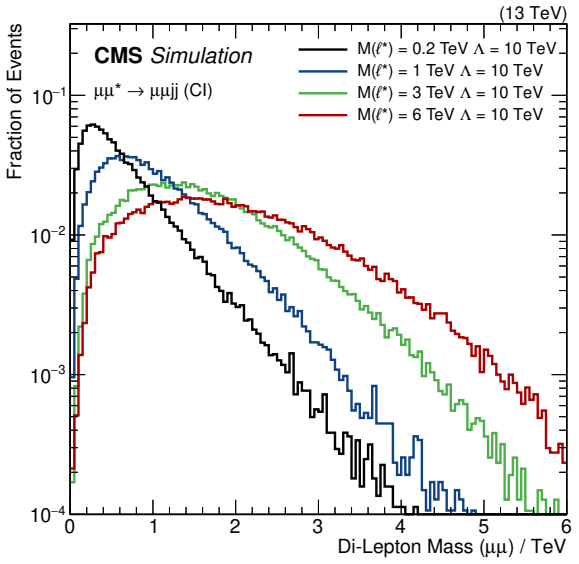

Figure 5.9: Di-lepton invariant mass distribution of the CI decay. The mass distribution does not feature a peak but is rather flat over a broad mass range.

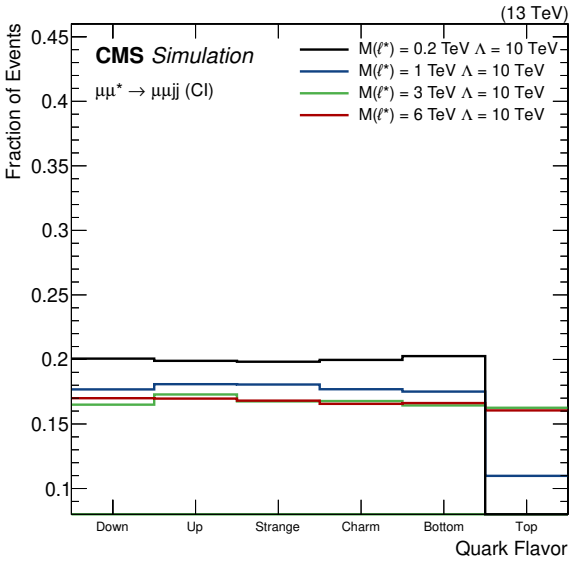

Figure 5.10: Flavor of the quarks from the $\ell^\star$ decay. Light signals cannot decay into top quarks because of their mass, while heavy excited lepton decays show no preference to any quark flavor. Both quarks of the decay always have the same flavor.

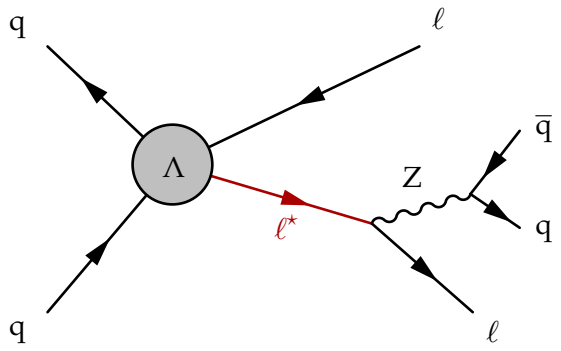

Figure 5.11: Feynman diagram of the Z channel. For more information see section 2.3.3.

5.4 The Z Channel

I will examine the Z channel in a very similar way to the previous one and highlight differences. Figure 5.11 depicts the Feynman diagram for this process. The final state is composed of two leptons and a hadronically decaying Z boson. The simulated mass range of the Z channel is slightly different compared to the CI channel. Signal masses of 250 GeV, 1, 3, and 5 TeV are chosen to compare the different kinematic distributions.

Figures 5.12a–5.12c show the transverse momenta of both leptons and the Z boson, and figure 5.12d displays the matching efficiency of the leading lepton to the one stemming from the excited lepton decay. The findings are mostly similar to the one of the CI channel. The p_T distributions change slightly because the $\ell^\star$ decays only in two particles and not to three. The η distributions of all final state particles roughly correspond to the ones of the CI channel and are not repeated here.

The angular distances between the final-state particles are different to the ones of the CI channel. The reason is the intermediate Z boson in the excited lepton decay chain. Figure 5.13a shows the distance between the two quarks of the Z boson decay. For the 250 GeV mass point, the distribution looks similar to the one of the CI channel (c.f. figure 5.8a) because the initial momentum of the excited lepton dominates the topology. For more massive excited leptons, where the momentum of the excited lepton is small, the distance between the quarks becomes smaller. This behavior is in sharp contrast to the CI channel, where the distance rises. The boost of the Z boson increases due to the substantial mass of the excited lepton and causes the smaller distances between the quarks. In this channel, the analysis uses a single large-cone jet containing both quarks instead of two separated jets.

Figures 5.13b–5.13d illustrates the distances between the lepton stemming from the decay of the excited lepton and the Z boson, the associated lepton and the Z boson, and both leptons. They match the expectations postulated in section 5.2. Light excited leptons lead to back-to-back kinematics of the leptons, and collinearity of the Z boson and the lepton matched to the decay. Heavy excited leptons have a back-to-back signature between these two particles and, therefore, a smaller distance between both leptons and between the associated lepton and the Z boson.

The di-lepton mass distribution is similar to the one of the CI channel.

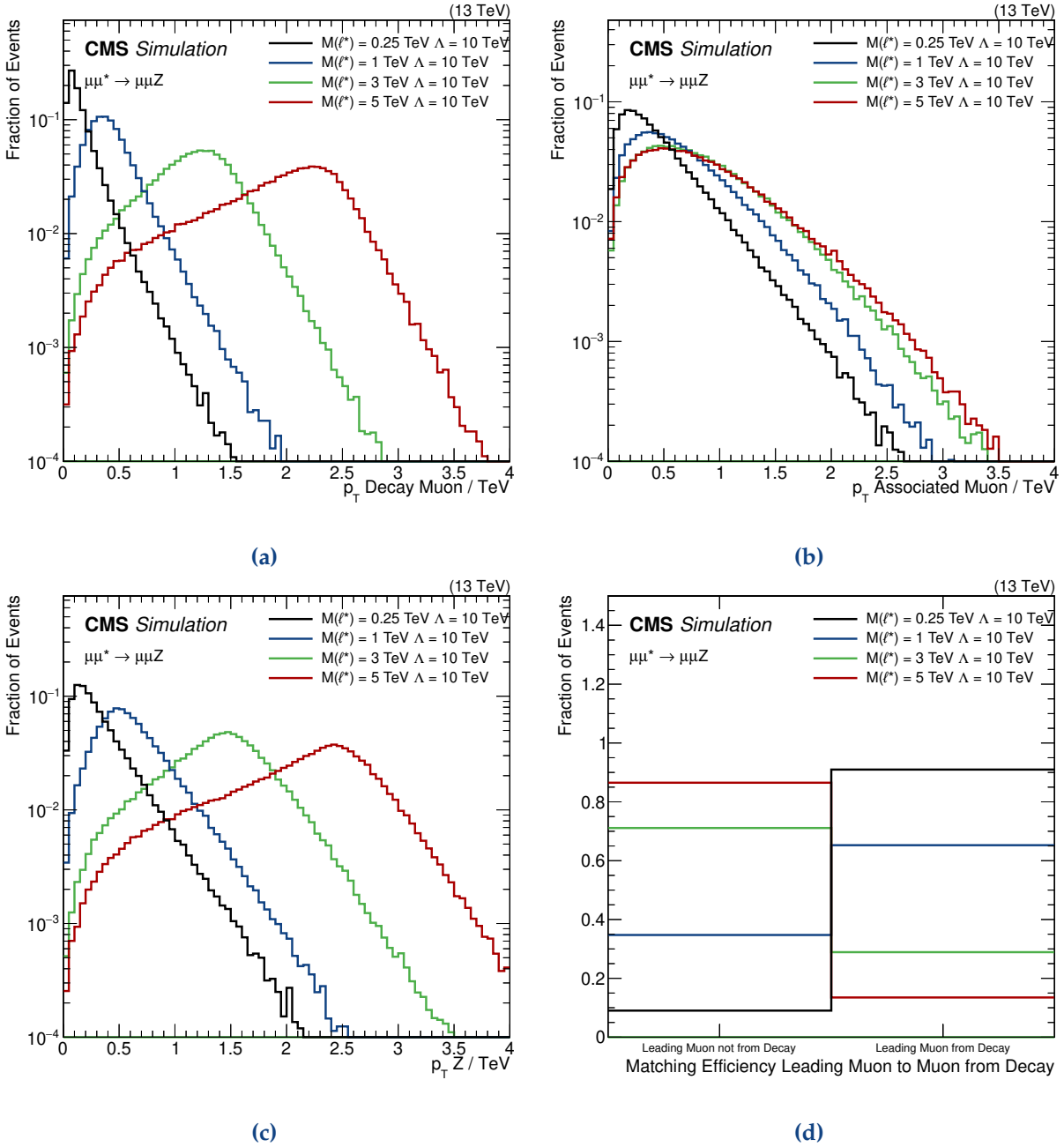

Figure 5.12: Transverse momentum distribution of (a) the lepton from the $\ell^\star$ decay, (b) the associated lepton, and (c) the Z boson. (d) shows the probability that the lepton stemming from the $\ell^\star$ decay corresponds to the leading lepton, i.e., the one with larger p_T. For light excited leptons this probability is substantial, for heavy excited leptons it is rather unlikely.

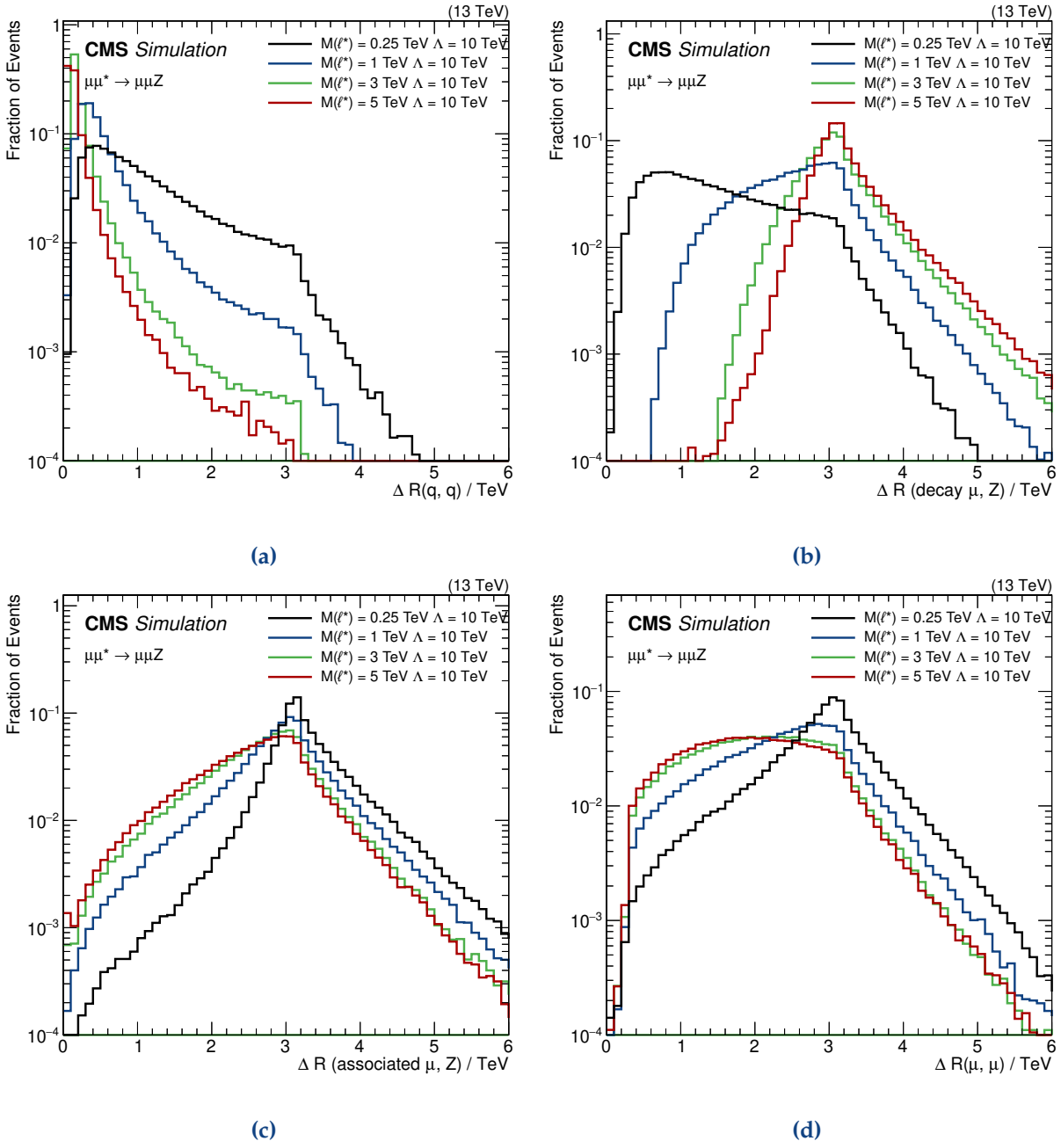

Figure 5.13: Distribution of the spatial distance in the η-ϕ-plane between (a) the quarks of the Z decay, (b) the lepton from the decay and the Z boson, (c) the associated lepton and the Z boson, and (d) the two leptons. For sufficiently heavy excited leptons, the boost is strong enough to reconstruct both jets in a single large-cone jet. For light excited leptons the decay products are boosted in the direction of the excited lepton and are back-to-back to the associated lepton.

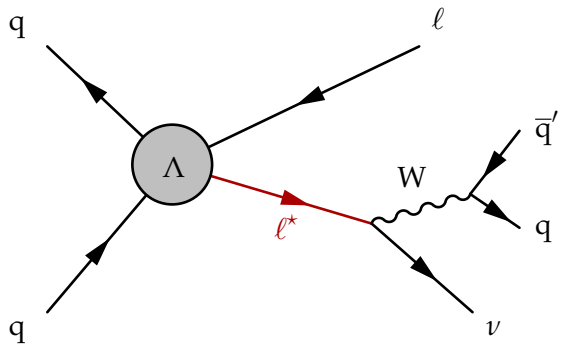

Figure 5.14: Feynman diagram of the W channel. For more information see section 2.3.3.

5.5 The W Channel

The description of the W channel follows the one of the CI and Z channels closely as well. Figure 5.14 shows the Feynman graph. I use signal masses of 250 GeV, 1, 3, and 5 TeV for this study. The final state consists only of a single charged lepton, a hadronically decaying W boson, and a neutrino that escapes detection. It will only show up as missing transverse momentum in the detector. On generator level, the $\boldsymbol{p}_T^{\text{miss}}$ is identical to the p_T of the neutrino. The kinematics of the W channel are very similar to the Z channel because the decay chains mimic each other. The W boson substitutes the Z boson and a neutrino the lepton from the decay.

Therefore, the p_T and η distributions are almost identical to the ones of the Z channel and are not repeated here. The spectrum of the charged lepton corresponds the one of the associated lepton in the Z channel, the W boson spectrum matches the one of the Z, and the missing transverse momentum spectrum the one of the lepton matched to the decay. Since only a single charged lepton is present in the decay chain, the W channel is the only channel without ambiguities in the assignment of the particles to the decay chain.

The spatial distance between both quarks of the W decay is shown in figure 5.15. Again, the distance is small for heavy excited leptons due to the boost of the W boson. The other angular distributions match the ones of the Z channel as well and are not repeated here.

Figure 5.16 shows the transverse mass distribution of the charged lepton and the neutrino. I show the transverse mass distribution since the longitudinal momentum of the neutrino cannot be measured and remains unknown without generator information. The transverse mass is defined similarly to the invariant mass using only the transverse component of energy and momentum. The distribution does not have a characteristic peak but behaves equivalent to the di-lepton distributions of the earlier channels.

5.6 Summary

To summarize, signal events are expected to manifest themselves at high energies. The observable objects are expected in the central region of the detector and have enough momentum to pass the trigger requirements of the analyses. The events have a distinct kinematic signature, which can be exploited to differentiate between signal and background.

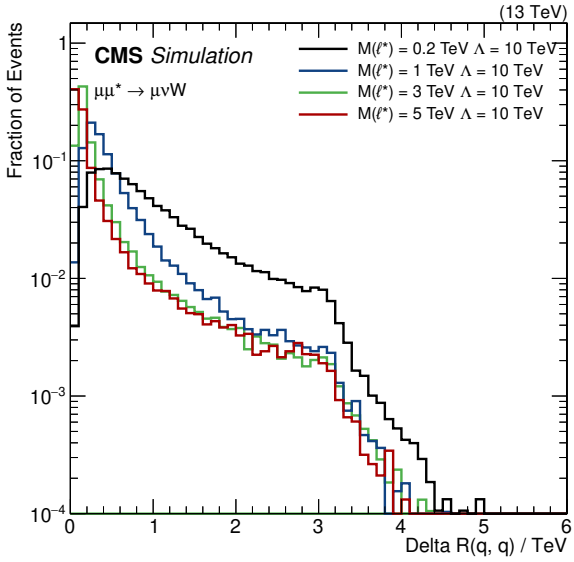

Figure 5.15: Distance between the quarks of the W decay. For sufficiently heavy excited leptons, the boost is strong enough to reconstruct both jets in a single large-cone jet.

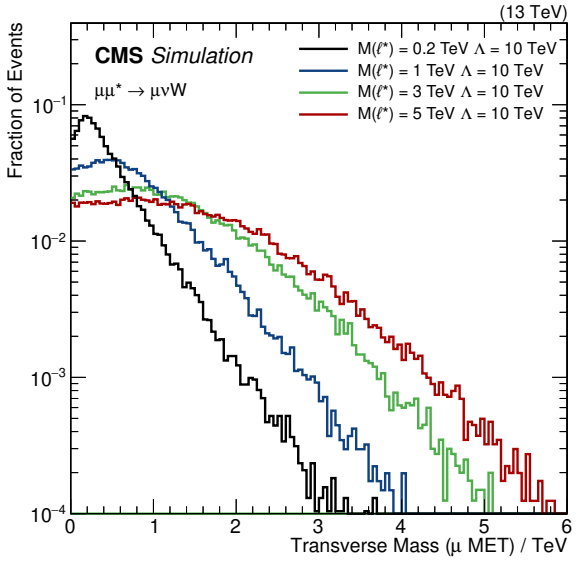

Figure 5.16: Transverse mass distribution of the lepton and the neutrino. The mass distribution does not feature a peak but is rather flat over a wide mass range.

Before I discuss the analysis strategies, I will present the different Standard Model processes which produce similar signatures to the signal.

6 Simulation of Standard Model Backgrounds and Signal Processes

This chapter focuses on the description of the simulation of inelastic proton-proton collisions. The simulation defines our expectation, both for the signal, as presented in the previous chapter, and for SM processes mimicking signal-like events.

First, I discuss the fundamentals of the simulation procedure in section 6.1. The discussion follows a review of all relevant SM processes leading to final states with the same signature as excited leptons, in section 6.2. Section 3.3.8 already described the analyzed CMS data.

6.1 Simulation of Proton-Proton Collisions

6.1.1 Simulation of Deep-Inelastic Scattering

A proton-proton collision is a stochastic process. The probability of observing a given event depends on the cross section of the process compared to the total cross sections of a proton-proton collision. Monte Carlo (MC) simulation of theses processes provides both the cross section and physical events. The latter can be handled just like real data events and allows us to apply kinematic requirements after the simulation of the process.

Several Monte Carlo generators exist to simulate high-energy pp collisions. This thesis uses MadGraph5_aMC@NLO [158] in LO and NLO mode, Powheg [159–165] and Pythia8 [37]. MadGraph5_aMC@NLO and Powheg only simulate the hard interaction of the process but do not take care of showering and hadronizing produced quarks and gluons. Instead, they use Pythia8 to perform this task. Pythia8 accepts different settings summarized in *tunes*. The MC samples for the simulation of 2016 data use the tune `CUETP8M1` [166] (`CUETP8M2T4` [167] for top-quark production), while they use `CP5` [168] for the 2017 simulation. The PDF sets used for simulation vary between 2016 and 2017, and the different generators as well. Table 6.1 summarizes the utilized PDF sets.

MC generators can simulate processes in different orders of α_s in the perturbation theory. Pythia8 and MadGraph5_aMC@NLO LO simulate events at leading order (LO) of the QCD perturbation theory. MadGraph5_aMC@NLO in NLO mode and Powheg are capable of simulating events at next-to-leading order (NLO), adding one additional vertex or loop to the Feynman graph. An example is shown in figure 6.1. It is also possible to simulate processes in higher-orders of the electro-weak (EWK) perturbation theory. However, all MC generators used in this thesis generate events in LO of the EWK perturbation theory. For this reason, I will use NLO as a synonym for NLO QCD and mention NLO EWK corrections explicitly.

Table 6.1: PDF sets used in 2016 and 2017 for all generators. All PDF sets are provided by NNPDF [94, 169, 170].

Generator	2016	2017
MadGraph5_aMC@NLO LO	NNPDF30_lo_as_0130	NNPDF31_nnlo_hessian_pdfas
MadGraph5_aMC@NLO NLO	NNPDF30_nlo_nf_5_pdfas	NNPDF31_nnlo_hessian_pdfas
Powheg	NNPDF30_nlo_as_0118	NNPDF31_nnlo_hessian_pdfas
Pythia8	NNPDF23_lo_as_0130_qed	NNPDF31_nnlo_as_0118_luxqed

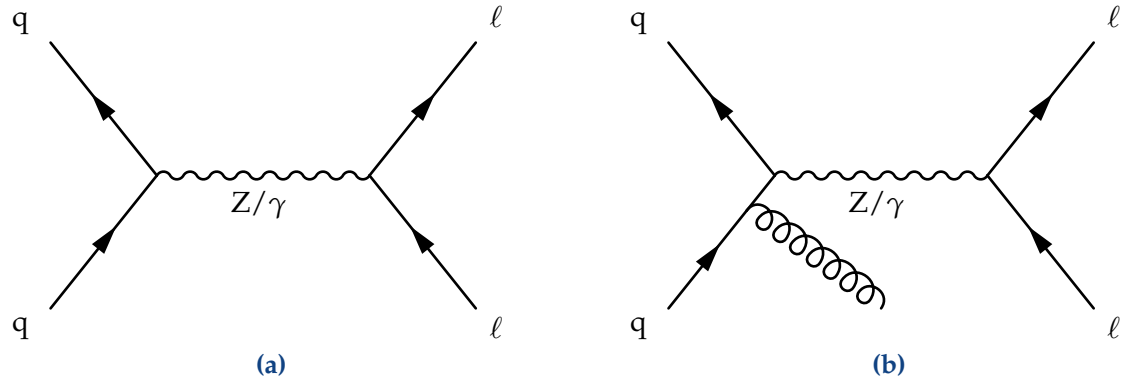

Figure 6.1: Feynman diagrams for the Drell-Yan process. (a) shows the LO diagram while (b) shows one of the NLO diagrams.

Simulating a process at NLO has several advantages: First, the overall cross section is more accurate than the LO prediction. Therefore, the distribution compares better to data in normalization and shape.

That being said, we can gain the same advantages also by using a LO generator and applying a correction factor often called *k-factor*. k-factors correct for the difference of the LO cross section to the higher-order one. They are computed either inclusively for the entire process or depending on a single quantity. Computing them inclusively improves the normalization of a distribution but does not correct the shape of a distribution. Uncorrected shapes often lead to discrepancies in the tails of distributions. Variable k-factors can also correct the shape but still have shortcomings compared to directly simulating events at a higher-order: They do only change the relative weight of the event but not the kinematics of it. Thus, they do not necessarily correct the shape of other distributions besides the one used to calculate them. For example, a di-lepton mass binned k-factor does not guarantee to correct the p_T spectrum of both leptons. Nonetheless, they still have use-cases. Up to date, MC generators are not able to generate events at a higher precision than NLO, so k-factors are often used to apply NNLO corrections or EWK NLO corrections on top of the NLO QCD prediction of the generator. The disadvantages are less severe in these cases, as the impact of higher-order corrections diminishes with every order of the perturbation theory.

Despite that, NLO generators have drawbacks, too. The computation time per event is much larger, and more events need to be generated than with a LO generator to achieve the same statistical uncertainty, especially when using MadGraph5_aMC@NLO. The cross section calculation at NLO involves some negatively interfering terms. The total cross section is still positive, but a fraction of the events simulated by MadGraph5_aMC@NLO has negative weights. With

an infinite number of generated events, the calculation would be precise. However, their finite number can lead to issues if not enough events with positive weight are present to balance the ones with negative weights. In extreme scenarios, this can even lead to a total prediction below zero, which is unphysical. Then, we need to bin the distribution more coarsely to increase the number of generated events per bin and to receive a physically accurate description of the process. The number of generated events is usually referred to as *Monte Carlo statistics*.

Jets coming from initial- or final-state radiation often accompany collision events. Pythia8 adds jets after the event generation according to the distribution observed in data and re-balances the event to maintain momentum- and energy conservation. MadGraph5_aMC@NLO can generate additional jets on the matrix-element level and matches them using the MLM [171] or FXFX [172] matching scheme in LO and NLO mode, respectively, to the ones added by Pythia8.

Additionally, the simulation procedure adds soft proton-proton interactions to the event following an approximated distribution of pileup.[1] It will later be re-weighted to the actual pileup density.

6.1.2 Simulation of the Detector Response

Up to this point, we only simulated the hard scattering event, the pileup, and the showering and hadronization of jets. The next step is to model the response of the CMS detector. The CMS collaboration uses the GEANT4 simulation toolkit [173] for this task. Provided the geometry and material budget of the full CMS detector, the tool can simulate how the particles traverse the different detector layers, which signatures they leave, and how their tracks are bent in the magnetic field of the solenoid. Defects in the description of the detector such as a misaligned detector can lead to a mismodeling of the detector response with effects on the momentum scale and resolution of the particles.[2]

6.1.3 Using Monte Carlo Events in the Analysis

As mentioned earlier, we can analyze MC events similarly to data events. The MC generator provides events with a physical description of the kinematic properties, and the detector simulation models the detector response to such an event. Even so, for an accurate description of the process, we need to apply the correct event weight because the number of generated events does not necessarily match the number of events produced during data taking.[3] The event weight is provided by

$$w = \frac{\sigma \mathcal{L} w_{\text{gen}}}{N}, \tag{6.1}$$

[1] We only know the experimental distribution after having finished the data taking. As we need the MC simulation already during data taking, we need to estimate it.

[2] Chapter 4 explains the reconstruction algorithms and introduces the sources of systematic uncertainties and their measurements.

[3] Typically, we want to have more MC events than CMS data events of this process to obtain a decent description in regions with only a few expected events. In the high-energy tail of a narrow-binned distribution, the expectation for a given process is often below one. Therefore, not every bin contains data events; some are empty. The simulation cannot predict which bins will be empty in data but should reflect that the probability density is smoothly decreasing, resulting in an expectation of below unity per bin. This smooth description is only possible if the number of generated events is larger than the number of observed events.

with the cross section σ of the process, the integrated luminosity $\mathcal{L}$, the generator weight w_{gen} and the total number N of simulated events for this sample. w_{gen} is a weight computed by the generator and needs to be incorporated for a correct description of the process. For example, MadGraph5_aMC@NLO uses negative event weights to simulate the correct NLO shape of a process as described in section 6.1.1.

Many processes have a steeply falling spectrum towards higher energies. For example, the Drell-Yan process, describing the s-channel production of a Z/γ and the decay into two fermions[4], has the largest cross section for the mass of the di-lepton system ($M(\text{ff})$) equal to the mass of the Z boson. The cross section in the high-mass tails at $M(\text{ff}) \approx 1\,\text{TeV}$ is much lower. This dependence will lead to a strong preference for the MC generator to simulate events near the Z-peak. Hence, CMS produces dedicated *tail samples* to boost the number of generated events in the high-mass tails of the sample. For these samples, a requirement is set at generator level on the mass $M(\text{ff})$, to only accept events with high masses. When using these dedicated tail-samples with the samples without requirement (called *bulk sample*), we need to carefully clean both samples against each other to avoid double counting. All events in the bulk sample which would pass the requirement of the tail sample need to be removed.

6.2 Relevant Background Processes

For a new physics search, we need to simulate both, the signal in order to know what we are looking for and the SM background. The background consists of all SM processes which can mimic a signal-like signature. The simulation of the SM background defines our expectation if no signal is present. The signal would lead to an excess of events over the background.[5]

We do not need to simulate the entire Standard Model but only the relevant processes for the analysis. The relevant processes are mainly defined by the number of leptons and the kinematic selection. Two of the search channels for excited leptons have two leptons; the W channel has only one. In general, this search is focused on the high energy regime, so we do not need to simulate low mass resonances like the J/ψ.

We differentiate between two distinct kinds of backgrounds: Prompt backgrounds and *fake* backgrounds. The former includes processes containing the required number of particles from the prompt interaction, while the latter includes processes that do not produce the required objects promptly but only due to misidentification.[6] The following sections present the relevant backgrounds for all three search channels: Drell-Yan, $t\bar{t}$, Multiboson, Single top, W+jets, and QCD. The background description of the presented analysis relies completely on the MC simulation.

6.2.1 Drell-Yan Background

The Drell-Yan process is the annihilation of two quarks into a virtual Z/γ, which decays into two charged leptons. Figure 6.2 presents the Feynman graph. This process is relevant for this search

[4] See section 6.2.1.

[5] In principle, interference between signal and SM processes can also lead to deficits, which can hint to new physics. However, this thesis does not investigate such effects.

[6] See section 4.5.

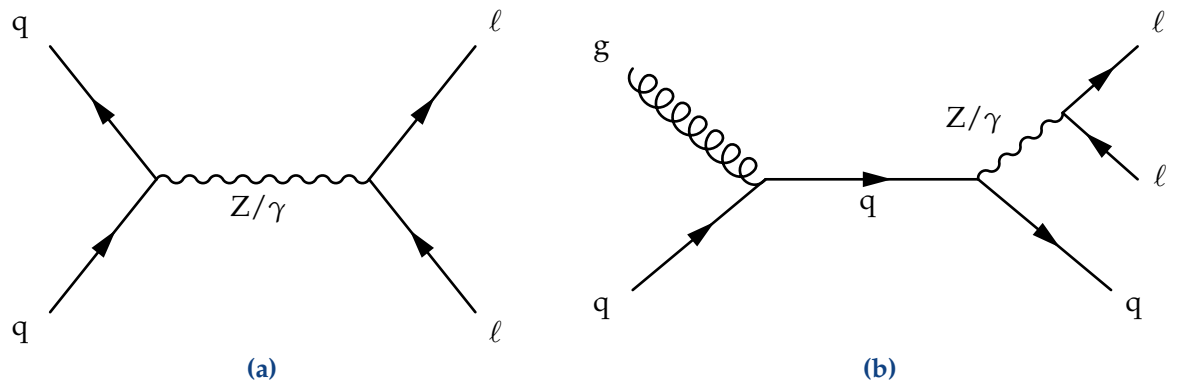

Figure 6.2: Feynman diagrams for the Drell-Yan process. (a) shows the LO diagram while (b) shows one of the many NLO diagrams leading to additional jets.

due to the production of two prompt leptons with a relatively large cross section. Additional jets can be produced by initial-state radiation or in diagrams like the one illustrated in figure 6.2b. While the signature is identical to the signal, if at least two jets are produced, the kinematics are different. The cross section peaks at the Z mass while the excited lepton production is flat over the di-lepton mass. We can remove a large portion of the events by imposing a lower bound on this variable.

For this reason, we are interested in events with heavy Z/γ. As the cross section peaks at the Z mass, most of the generated events will be concentrated in this region. To increase the number of generated events at high masses, we can use high-mass tail samples, as discussed in section 6.1.3. The event yield can be increased even more by adding another tail sample for events with a large p_T of the Z/γ because such events have a higher probability of containing high-p_T jets since the Z/γ needs something to recoil against to conserve momentum. The composition of the Drell-Yan samples is depicted in figure 6.3. The bulk sample is used for di-lepton masses below 400 GeV and $p_T(Z) < 50\,\text{GeV}$, and the $p_T(Z)$ tail-samples above this p_T threshold. For masses above 400 GeV, I use the mass-binned tail samples independently of the p_T of the boson. This composition of samples does not change the physical spectrum of the Drell-Yan process but increases the event yield to obtain a more accurate description.

For the W channel, this background can be suppressed by applying a veto on the second lepton since the Drell-Yan process produces them always in pairs.

The cross section is normalized to NNLO QCD and NLO EWK using a di-lepton mass-dependent k-factor [174, 175] for the CI channel as high-mass Drell-Yan is the dominant background process. The Z- and W channel both use a constant NNLO QCD k-factor. The samples are generated by MadGraph5_aMC@NLO.

6.2.2 Top Pair Production Background

The $t\bar{t}$ process can lead to a variety of final states. Figure 6.4 illustrates a possible Feynman diagram. It features the production of a pair of top quarks by gluon fusion. The top quarks subsequently decay into a bottom quark and a W boson. The W boson can decay either hadronically or leptonically. When both W bosons decay leptonically (*full-leptonic decay*) into two

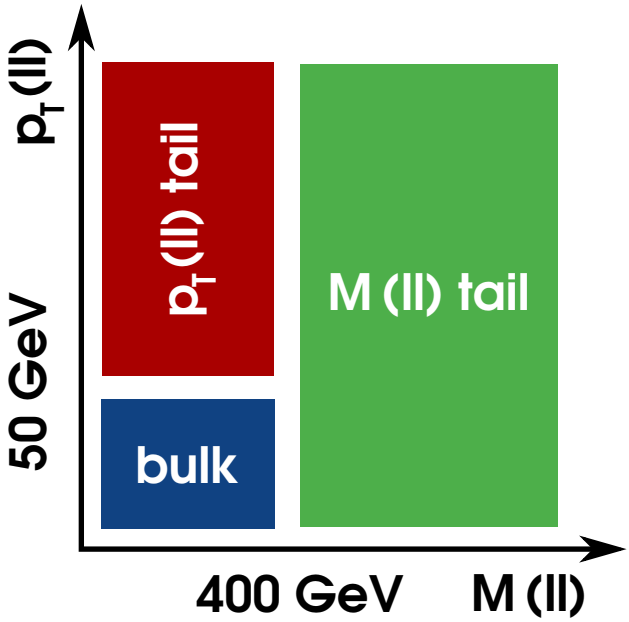

Figure 6.3: Composition of the Drell-Yan samples. This analysis uses the bulk, $p_T(Z)$- and mass-binned samples.

same-flavor leptons, the process resembles the signature of an excited lepton in the CI and Z channel. Since both leptons do not originate from the same boson, the cross section does not peak at a certain value, unlike the Drell-Yan process. It does, however, fall much more steeply compared to the high-mass excited lepton signatures, so a requirement on the di-lepton mass can still be very effective. Also, the total $t\bar{t}$ cross section is one order of magnitude smaller than the one of the Drell-Yan process.

If only one W boson decays leptonically (*semi-leptonic decay*), it produces a final state with only a single lepton, which resembles the excited lepton signature in the W decay channel.

I use dedicated high-mass tails to enhance the number of generated events in the high-mass region of the analysis. The cross section is normalized to NNLO by a flat k-factor [176]. All samples are generated by Powheg.

6.2.3 Multiboson Backgrounds

Multiboson is a hypernym for multiple different processes involving two or more bosons. The most important ones are the WW, WZ, and ZZ production. Triple boson productions are also possible but have a negligible cross section compare to other processes. All three di-boson processes can lead to final states with at least one prompt lepton if the W or Z-bosons decay leptonically. Final states with at least two leptons are also frequent. Figure 6.5 shows an example of a WZ process leading to a final state with two leptons and two jets.

While capable of producing signatures similar to excited lepton decays, the cross sections are relatively small, and we can remove a lot of the background by imposing a requirement on the di-lepton mass or the transverse mass of the lepton and missing transverse momentum.

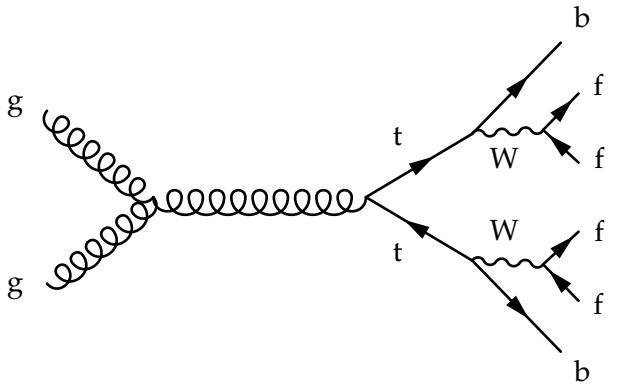

Figure 6.4: $t\bar{t}$ production via gluon fusion with subsequent decay.

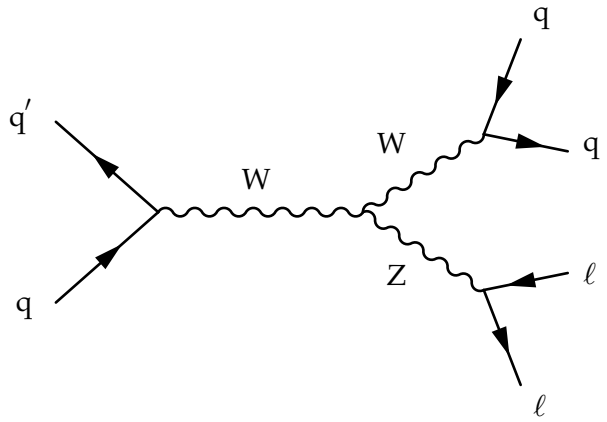

Figure 6.5: WZ process into a two-lepton-two-jet final state.

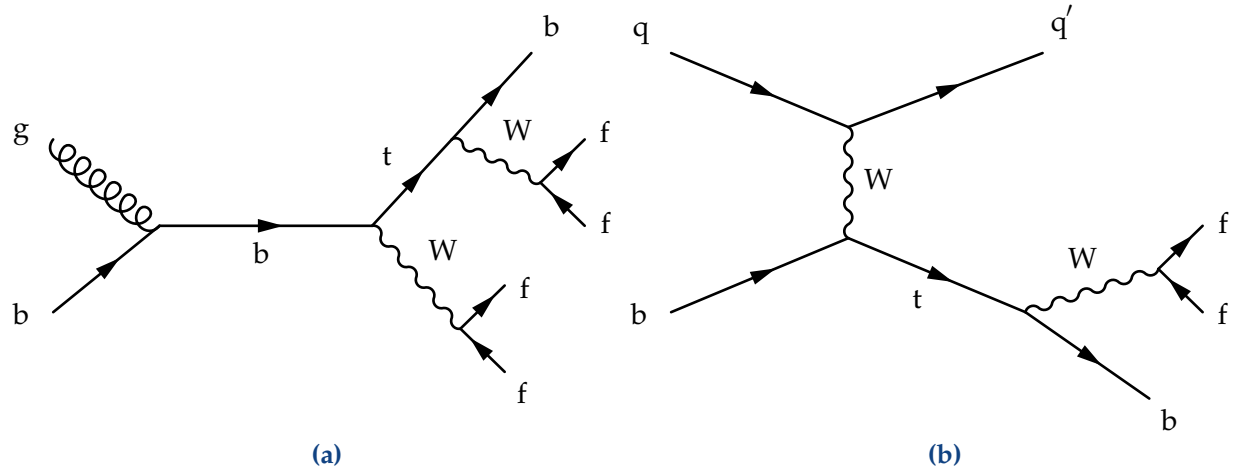

Figure 6.6: Single top production in (a) the tW channel and (b) the *t*-channel.

All multiboson processes are simulated at NLO precision. Powheg simulates the WW process, MadGraph5_aMC@NLO the others. Additionally, a flat NNLO k-factor further improves the precision of the WW cross section which is the multiboson process with the largest cross section.

6.2.4 Single Top Backgrounds

Single top is a collective term for three different processes, all including the production of a single top-quark: The production of a top-quark in association with a W boson and productions via *s*- and *t*-channel. Figure 6.6 shows the Feynman diagrams for the tW channel and the *t*-channel production. The *s*-channel diagram has a much lower cross section. Both the *t*- and the *s*-channel can only produce a single lepton while the tW can produce two prompt leptons.

Similar to the multiboson backgrounds, Powheg and MadGraph5_aMC@NLO simulate the single top processes at NLO precision. Powheg simulates the tW and *t*-channel, and MadGraph5_aMC@NLO the *s*-channel diagram at NLO precision. For the process with the largest cross section – tW – a flat NNLO k-factor is applied.

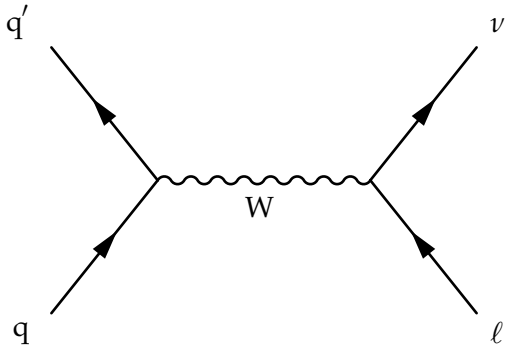

Figure 6.7: Feynman diagram for W production. Jets can be added in the same ways as for the Drell-Yan process (c.f. figure 6.2b)).

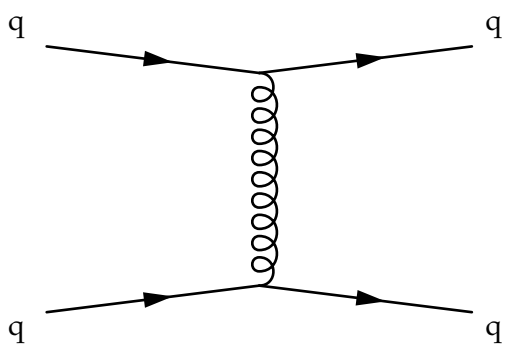

Figure 6.8: Feynman diagram for a QCD di-jet event.

6.2.5 W+Jets Backgrounds

The W+jets process is the process with the highest cross section at LHC, that produces at least a single prompt lepton. This significant cross section makes it the dominant background for the search for excited leptons in the W channel. As it cannot produce a second prompt lepton, it can only contribute to the CI and Z channels by misidentification. Figure 6.7 illustrates the Feynman diagram: The annihilation of two quarks produces a W boson which subsequently decays leptonically. Jets can be added in the same way as for the Drell-Yan process.

Since the lepton and the missing transverse momentum stems from the same W boson, we can remove a significant fraction of events by imposing a lower bound on the transverse mass of the lepton and the $\boldsymbol{p}_T^{\text{miss}}$.

MadGraph5_aMC@NLO simulates this process at NLO for the W channel and at LO for the CI and Z channels. For those two channels, I use the LO simulation of MadGraph5_aMC@NLO since it contains a higher number of simulated events. The W+jets process can only contribute via misidentified objects to the CI and Z channel. Therefore, the correct NLO shape of the background is less critical because the contribution will be dominated by the accuracy of the misidentification rate.

Additionally, the W channel uses dedicated high-mass tails simulated by Pythia8 at LO precision for off-shell W bosons above 500 GeV.

A flat NNLO k-factor is applied to the MadGraph5_aMC@NLO simulation. The high-mass Pythia8 samples utilize a flat NNLO k-factor which is calculated for their respective mass window.

6.2.6 QCD Backgrounds

While the W+jets process is the one with the highest cross section containing at least a single lepton, the QCD process is the one with the highest cross section of all processes. As the exemplary Feynman diagram in figure 6.8 shows, it does not produce prompt leptons. Hence, it can only contribute via misidentified objects. As the probability of misidentifying two objects as

leptons is minimal, it can be neglected for the CI and Z channel. For the W channel, it is still relevant due to its extensive cross section.

The QCD multijet background is still only simulated at LO by state of the art MC generators. This thesis utilizes the simulation from MadGraph5_aMC@NLO.

6.3 Summary

For the CI and Z channel, we expect the Drell-Yan and $t\bar{t}$ backgrounds to dominate. The W+jets process will play a subdominant role because it only produces a single lepton at the hard interaction. Contrary to that, it will overshadow all other Standard Model backgrounds in the W channel because its final state features only a single charged lepton, and the W+jets process has an enormous cross section compared to other Standard Model processes.

With this chapter, all prerequisites for the analysis are explained. This lays the foundation for the description of the search for excited leptons.

7 | Analysis

This chapter describes the analysis of the contact interaction (CI) channel, Z channel, and W channel. The channels share large parts of the analysis chain. Thus, I will describe the CI channel first and highlight the differences in the explanation of the other two channels.

Chapter 5 discussed the kinematic properties of the different decay channels and chapter 6 the simulation of the signal and the SM background. This chapter will present the analysis of all three channels while the next chapter compares the sensitivity of the different channels.

7.1 The Contact Interaction Channel

The CI channel defines the reference for the other channels. Therefore, I will describe it in great detail. Its final state consists of two leptons (two electrons or two muons assuming flavor conservation) and two well-isolated jets.

An analysis consists of multiple steps. At first, I will describe the event selection including, e.g., the trigger (section 7.1.1). The next sections explain the object selection, i.e., the identification of electrons, muons, and jets (section 7.1.2). The following section 7.1.3 presents analysis specific requirements to distinguish between signal and background before section 7.1.4 exhibits the resulting distributions. Section 7.1.5 contains a summary of all relevant systematic uncertainties. After that, section 7.1.6 shows the signal efficiency before section 7.1.7 summarizes the statistical analysis. Finally, section 7.1.8 presents the exclusion limits.

7.1.1 Event Selection

The event selection consists of the trigger selection, the *missing transverse energy filters* for data, the certification, the pre-selection, and further requirement to differentiate between signal and background. This section explains the first three steps.

Trigger Selection

CMS does not record all data but relies on a trigger system (c.f. section 3.3.6). This analysis makes use of two different trigger paths: The electron channel uses a trigger that selects events containing at least a single electron or photon above a certain transverse momentum threshold. The trigger of the muon channel requires at least one muon above a p_T threshold.

The expected sensitivity of the analysis drives the trigger choice for the electron channel. The CI channel ought to be sensitive for heavy excited leptons (c.f. section 2.3.3). Topologies containing heavy excited leptons typically feature high-p_T leptons because of the available energy during the decay of the $\ell^\star$ (c.f. section 5.3). The trigger of the electron channel is primarily designed

to trigger events containing high-energetic photons. However, it has the highest efficiency for selecting high-energetic electrons as well [177]. The reason is the simplicity of the trigger: It only relies on the electromagnetic calorimeter and not on the tracker. Since both, electrons and photons, leave similar clusters in the ECAL, the single-photon trigger accepts electrons equally efficiently as photons. The downside of the highly efficient single-photon trigger is the increased p_T threshold compared to dedicated electron triggers. However, the effect on the final selection efficiency is minor[1], since the selection is optimized for the high-mass region, as mentioned earlier. Therefore, this analysis can profit from the high trigger efficiency.

The HLT path used for this analysis is called `HLT_Photon175` and `HLT_Photon200`. The 2016 analysis uses the former trigger while the 2017 analysis uses the latter. The number corresponds to the p_T threshold of the photon. The trigger with the lower threshold was not available in 2017 to cope with the increased instantaneous luminosity (c.f. section 3.1).

The trigger efficiency depends on the momentum of the triggering particle. It is typically not a perfect step function which is zero below the p_T threshold and unity above. Instead, the efficiency has a smeared-out *turn-on* at the threshold. This turn-on is challenging to simulate correctly. Therefore, substantial *scale factors* arise in this region.[2] Scale factors are the ratio of the efficiency in data and MC simulation. Requiring a larger p_T threshold of the triggering object above the nominal trigger threshold avoids such substantial scale factors. For the electron channel, this threshold is set to 230 GeV for the leading electron. At this value, the efficiency of the `HLT_Photon200` trigger is at 99 and 94% in the barrel and endcap region, and the scale factor between 95 and 99% [177].

The rate of muons is much lower than the rate of electrons and photons. The lower rate allows reducing the p_T threshold of muon triggers significantly. The lowest not pre-scaled[3] single muon trigger has a threshold of 50 GeV. The trigger path is called `HLT_Mu50`. It is available in 2016 and 2017. In 2016 the trigger had an inefficiency due to the dynamic strip inefficiency (c.f. section 3.3.3), which was compensated by another trigger called `HLT_TkMu50` with the same momentum threshold. Using a logical OR between both triggers maximizes the efficiency. Figure 7.1 shows the trigger efficiency which is stable for muons above 53 GeV. Thus, this value defines the p_T threshold for the leading muon in the analysis. Above this value, the efficiency varies between 93 and 79% decreasing towards the outer edges of the endcaps [149, 150].

The single-lepton triggers provide better performances compared to double-lepton triggers because of the higher efficiency at high transverse momenta. A double-lepton trigger provides lower p_T thresholds than single-lepton triggers, but the analysis does not gain sensitivity from those because of the optimization for the high-mass region. Using a single-lepton trigger provides two possible candidates to trigger because the final state contains two leptons.

As mentioned before, scale factors correct differences in the trigger efficiency between data and MC simulation. They are weights that shift the MC efficiency on an event-by-event basis to the one measured in data. Although the scale factors for individual leptons are as high as 95%, the total scale factor applied in the analysis is typically much smaller because the final state contains

[1] Section 7.1.6 will present the final selection efficiency.

[2] Figure 7.1 shows an example for the muon channel.

[3] A pre-scaled trigger does not trigger every event passing the trigger criteria but only every x-th events when x is the pre-scale of the trigger. Pre-scaled triggers enable studies at lower energies but limit the size of the dataset.

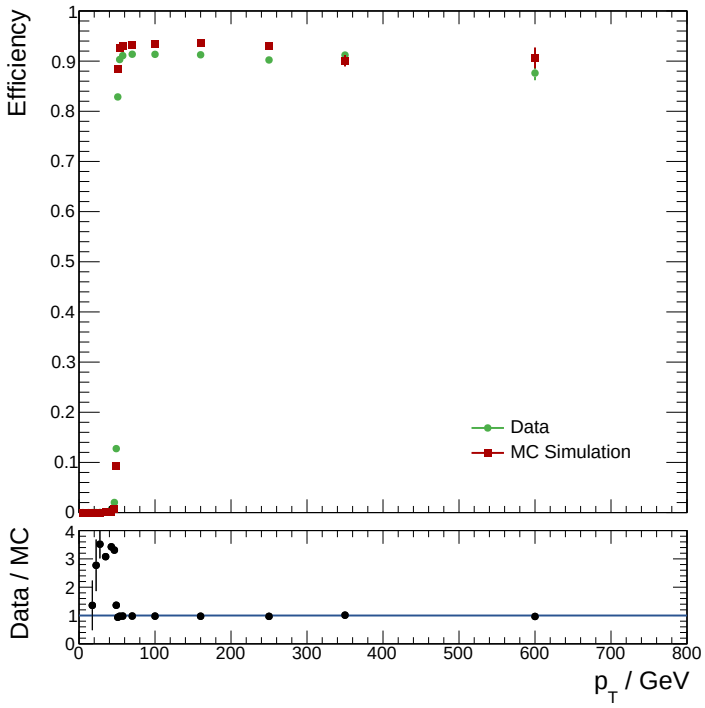

Figure 7.1: Muon trigger efficiency for the combination of the `HLT_Mu50` and the `HLT_TkMu50` trigger paths in 2016. The green curve shows the efficiency measured in data and the red one in MC simulation. The ratio is flat above 53 GeV, with scale factors below 5%. The trigger efficiency is defined by the ratio of muons which are inside the detector acceptance of $|\eta| < 2.4$, pass the high-p_T ID, and are triggered over all muons inside the detector acceptance passing the high-p_T ID. Data taken from reference [149, 150].

two leptons which can both trigger the event. If both leptons are above the trigger threshold, the scale factor derives as

$$\mathrm{sf} = \frac{1 - (1 - \varepsilon_1^{\mathrm{data}}) \cdot (1 - \varepsilon_2^{\mathrm{data}})}{1 - (1 - \varepsilon_1^{\mathrm{MC}}) \cdot (1 - \varepsilon_2^{\mathrm{MC}})}. \tag{7.1}$$

If only one lepton passes the trigger threshold this equation simplifies itself to

$$\mathrm{sf} = \frac{\varepsilon_{\mathrm{data}}}{\varepsilon_{\mathrm{MC}}}. \tag{7.2}$$

If both leptons pass the trigger requirement, an individual scale factor of 95% would reduce itself to less than 99%.

Missing Transverse Energy Filter

Missing transverse energy filters (MET filters) remove single problematic events, such as events suffering from detector issues. Problematic events often manifest themselves in the p_T^{miss} distribution as momentum conservation enforces balanced momenta of the reconstructed event in

Table 7.1: Acceptance requirements for electron, muons, and jets for the CI channel. The p_T requirement of the trigger is included for the leading leptons.

	Electron	Muon	Jet
p_T	> 35 GeV (leading: 230 GeV)	> 25 GeV (leading: 53 GeV)	> 50 GeV
$\|\eta\|$	< 2.5	< 2.4	< 2.4

the transverse plane. If an event assigns a wrong momentum to one particle, the reconstruction algorithm must increase the $\boldsymbol{p}_T^{\text{miss}}$ to keep the momenta balanced.[4]

This analysis uses the MET filters recommended by the CMS collaboration [178]:

- **HCAL filters** eliminate events with unusual noise in the HCAL readout or from interactions of particles with light guides.
- **ECAL filters** remove events suffering from anomalous energy deposits caused by noise in the ECAL readout and events with significant energy deposits in crystals with malfunctioning readout. While the crystal-by-crystal readout is not working in some crystals, the trigger primitive information is still available. The filter uses this information to tag and remove events with significant energy deposits in these crystals.
- The **beam halo filter** suppresses events containing machine-induced background. Beam halo particles are created by interactions of the beam with external particles in the LHC and travel parallel to the beam. If they interact with the detector, they induce spurious missing transverse energy.
- **Reconstruction filters** remove events affected by poorly reconstructed high-p_T muons, which induce irregular missing transverse energy.
- Finally, the **primary vertex filter** discards events without a proper reconstructed primary vertex to suppress events not originating from hard proton-proton interactions.

All filters are applied on data, and all filters except the beam halo filter on the MC simulation.[5]

Certification

The certification ensures that we only analyze well-recorded data without any detector issues, as described in section 3.3.8. This step does not apply to the MC simulation.

7.1.2 Object Selection

After the event selection, we can identify individual objects in those events. This section describes the selection of electrons, muons and jets. The identification criteria are listed in sections 4.5.2, 4.5.1, and 4.5.3 respectively. Table 7.1 lists the acceptance requirements on η and p_T.

[4] The $\boldsymbol{p}_T^{\text{miss}}$ increases naturally, since $\boldsymbol{p}_T^{\text{miss}}$ is the negative vectorial sum of all particle momenta.
[5] No beam halo effects are simulated in MC simulation.

Both the electron and the muon channel require a minimum of two leptons of the corresponding flavor and at least two jets, meaning at least two electrons and two jets in the electron channel and two muons and two jets in the muon channel. This requirement is motivated by the expected signal topology. The final state consists of two leptons and two jets. While we do not expect additional leptons in signal-like events, a requirement on the number of leptons does not improve the discrimination between signal and background because only rare multi-boson processes can result in final states with more than two leptons. However, we do expect more than two jets in the final state because of initial or final-state radiation, as well as the presence of pileup interactions. If more than two leptons or jets pass the object selection, the two particles with the highest transverse momentum are selected.

Event weights are used to correct the lepton identification efficiency in simulation to match the one observed in data (c.f. section 4.5.1 and 4.5.2).

7.1.3 Analysis Specific Selection

Pre-Selection

This section presents several distributions on the pre-selection level, i.e., only applying the event and object selection but no further background-suppressing requirements. These distributions help to judge the agreement between data and MC simulation and to understand the kinematic properties of selected events. All distributions share a common color code: A colored stack of histograms displays the Standard Model expectation with the smallest background at the bottom and the largest on top. The Drell-Yan process uses a dark red, $t\bar{t}$ a dark blue, Multiboson processes a light blue, Single top a dark green, and W+jets a light green. Lines with different shades of purple present various signal hypotheses. The data are superimposed in black. The ratio panel below shows the ratio of the data and the Standard Model expectation. If the expectation in a single bin is below one event, the ratio summarizes multiple bins into a single bin until the bin contains at least a single expected event or the end of the spectrum is reached. This procedure makes it easier to assess the agreement between data and expectation in the high-energy tails of a spectrum. Two bands show the uncertainties on the expectation: The orange band represents the statistical uncertainty, and the grey band the combination of statistical and systematic uncertainties.[6] The bins become broader towards higher energies as both the detector resolution and the number of generated MC events diminish. With variable bin widths, the shape of the histogram can become misleading as broader bins naturally contain more events than narrow bins. This issue is resolved by normalizing the height of the bins to the width of the smallest bin. The actual number of events is obtained by multiplying the value of the bin with its width divided by normalization given on the y-axis.

The pre-selection for this channel includes the selection of two leptons and two jets. Additional particles are allowed in the event but not included in the calculation of any physical quantities. The electron channel has $1.2 \cdot 10^4$ events after preselection and the muon channel $6.6 \cdot 10^5$. The MC prediction is normalized to cross section and luminosity.

Figure 7.2 shows the distribution of the leading lepton in the electron and the muon channel. The MC simulation describes both spectra within its uncertainties. In the high-mass tail some events

[6] Section 7.1.5 summarizes the sources of the systematic uncertainties.

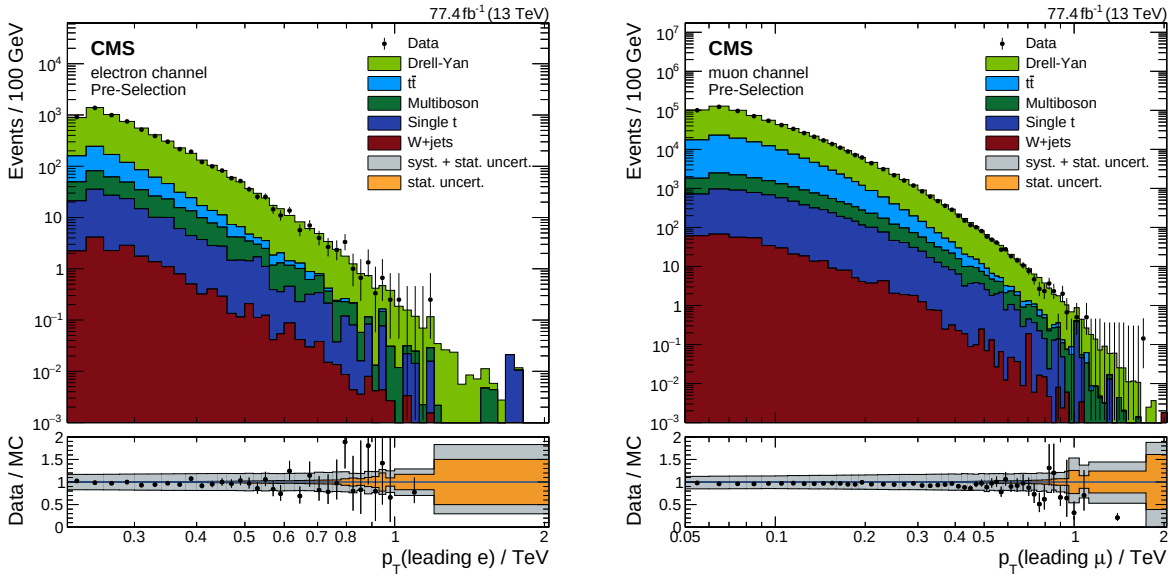

(a) **(b)**

Figure 7.2: p_T distributions of the triggering leptons. (a) shows the electron and (b) the muon channel. The simulation describes both channels within 10%. The colored stacked histograms visualize the background. Lines with different shades of purple present various signal hypotheses. The data are superimposed in black. The ratio panel below shows the ratio of the data and the Standard Model expectation. If the expectation in a single bin is below one event, the ratio summarizes multiple bins into a single bin until the bin contains at least a single expected event or the end of the spectrum is reached. This procedure makes it easier to assess the agreement between data and expectation in the high-energy tails of a spectrum. Two bands show the uncertainties on the expectation: The orange band represents the statistical uncertainty, and the grey band the combination of statistical and systematic uncertainties. The simulation is normalized to the luminosity of the dataset.

are not covered by the systematic uncertainty but are scattered randomly around unity and have no systematic trend. Drell-Yan is the dominant background. The electron spectrum starts only at 230 GeV since the trigger threshold is higher for the electron channel than for the muon channel. The event yield of the electron channel is more than two orders of magnitude lower compared to the muon channel due to the higher trigger threshold. Both spectra end around 1.1 TeV. The muon channel features one additional high-p_T event at 1.7 TeV. The statistical uncertainty of the MC simulation starts to dominate above 1 TeV.

Other relevant quantities are the invariant mass of both, the di-lepton system and the four-body system. We can utilize the di-lepton mass spectrum to differentiate between signal and background, as indicated in section 5.3. The reason is the lack of an intermediate particle in the decay chain of both leptons compared to processes like Drell-Yan, where both leptons originate from a common particle. For this purpose, we must verify the agreement between data and simulation. Figure 7.3 shows the distribution for both channels. The Drell-Yan process shows a clear peak at the Z mass, while the signal is roughly flat over a large mass range. Data and simulation agree within their uncertainties. The muon channel shows a deficit of less than 10% for masses between the Z peak and 500 GeV. It originates from the 2016 dataset and was also observed by other analyses [174]. The events in the high-mass tails are randomly distributed around the expectation and show no systematic shift. The high trigger threshold of the electron

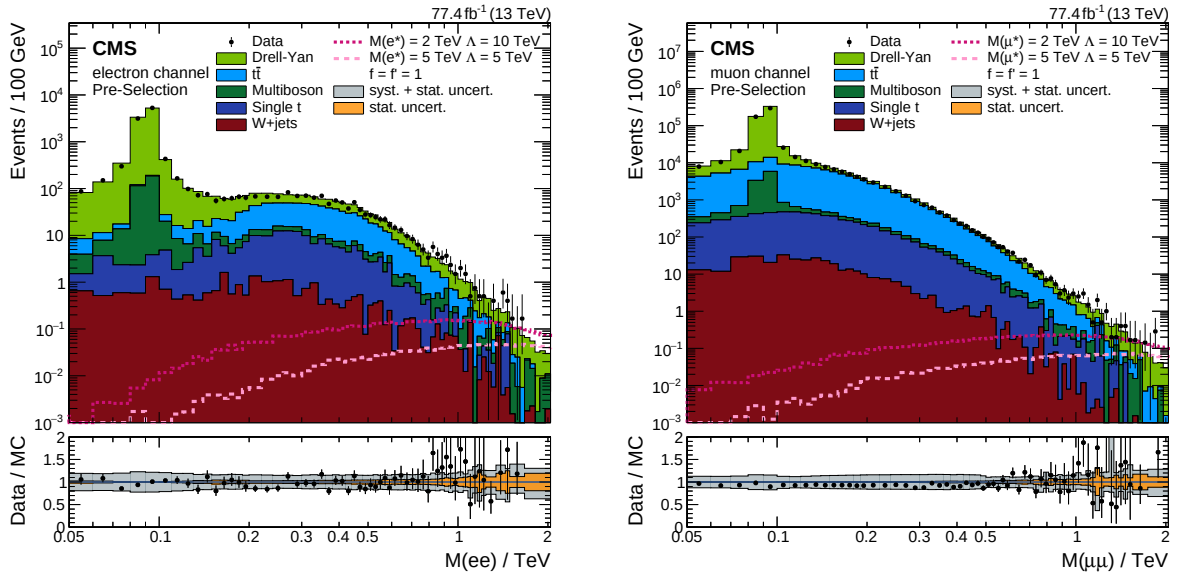

(a) (b)

Figure 7.3: Invariant mass spectrum of the di-lepton system. (a) shows the electron and (b) the muon channel. The background has a sharp peak at the Z mass while the signal is rather flat over a broad mass range.

channel explains the dip above the Z peak. Drell-Yan events with an invariant di-lepton mass below $\approx 200\,\text{GeV}$ require a boosted Z boson to fulfill the kinematic requirement of the trigger.[7] Such a boosted topology is possible if the Z boson recoils against a jet. However, such events are less likely than events with a small boost; hence we can observe events below this threshold, but with a lower frequency. The muon channel does not have this feature since the trigger threshold is much lower.

The other relevant quantity – the mass of the four-body system – is presented in figure 7.4. This variable will be the final search variable as motivated in section 7.1.4. Both spectra are smoothly falling and the data extend up to 5.5 and 7 TeV in the electron and muon channels, respectively. The muon channel shows a small excess at high masses; however, the sizeable statistical uncertainty limits the quality of the background description. The two signal lines indicate excited lepton signatures for masses of 2 and 5 TeV. f and f' are set to unity for both curves and Λ to 10 and 5 TeV, respectively. The 2 TeV signal is buried under the background and cannot be observed without additional requirements. This spectrum would already be sensitive for a 5 TeV excited lepton, but further requirements can still increase the sensitivity. Both channels show equally good agreement between data and MC simulation as the prior distributions besides the highest mass bins which lack simulated SM events.

Final Selection

The invariant mass of the di-lepton spectrum does not only create a region with suppressed background and enriched signal but also two independent control regions. These control regions

[7] An on-shell Z boson decaying at rest cannot produce a lepton with a p_T larger than 230 GeV which is the trigger threshold of the electron channel since the mass of 90 GeV is equally shared by both leptons.

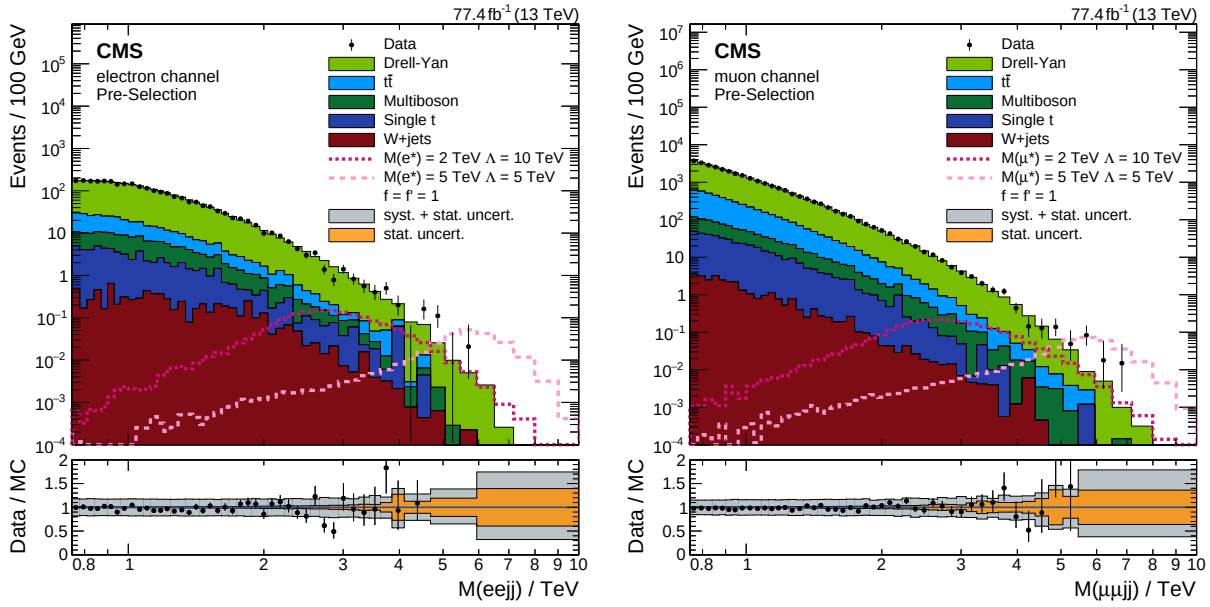

(a) (b)

Figure 7.4: Invariant mass spectrum of the four-body system containing both leptons and the two leading jets. (a) shows the electron and (b) the muon channel. The two signal hypotheses do not emerge strongly from the background warranting further selection steps.

can be used to validate the agreement between data and simulation further. Figure 7.5 depicts the definition of the two control regions as well as the signal region. Events with an invariant di-lepton mass below 200 GeV are sorted into the *low-mass control region (CR)*. This region includes the Z peak; hence it is dominated by the Drell-Yan process. The *medium-mass control region* is defined between masses of 200 and 500 GeV. This region does contain less Drell-Yan events, and the $t\bar{t}$ process dominates it. Finally, the mass window above 500 GeV defines the signal region.

For heavy excited leptons only 5% of the signal contributes to the medium-mass control region and less than one percent to the low-mass control region. The signal region contains 500 events in the electron channel and 1136 events in the muon channel.

Validation of the Background Description

Low-Mass Control Region The low-mass control region contains events with an invariant di-lepton mass below 200 GeV. Drell-Yan dominates it since it contains events with on-shell Z bosons. Figure 7.6 shows the invariant mass spectrum of the four-body system for both channels. I chose the coarse binning to limit the impact of the statistical uncertainty on the MC simulation and to be consistent with the binning used in the signal region. Data and simulation agree within the systematic uncertainties. The last bin features an excess in both distributions. It cannot be explained by an excited lepton signal as indicated by the two lines because the di-lepton mass requirement suppresses the signal strongly. The local significance is below two sigma for both channels.

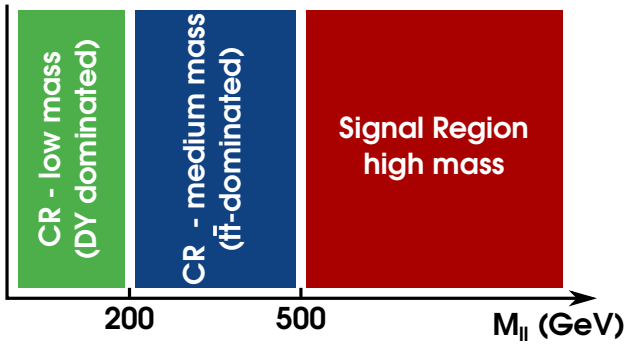

Figure 7.5: Sketch indicating the final selection requirement to differentiate between the Standard Model and signal. A minimum invariant di-lepton mass of 500 GeV defines the signal region. Below two control regions (CR) are defined: The low-mass CR below 200 GeV dominated by Drell-Yan and the medium-mass region between 200 and 500 GeV dominated by $t\bar{t}$.

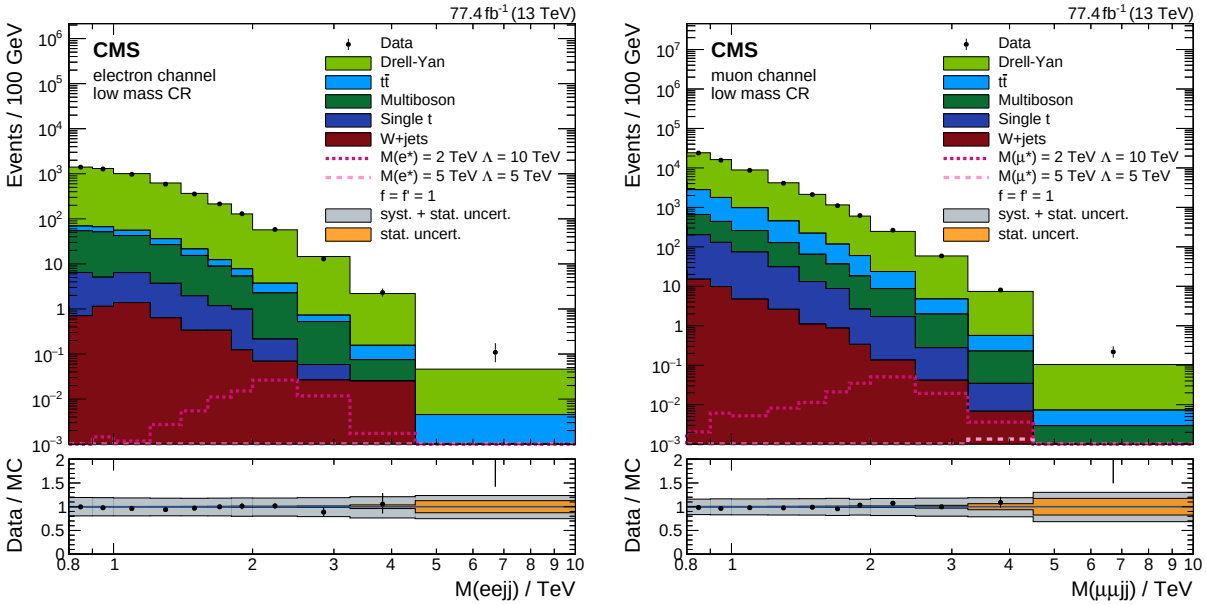

(a) **(b)**

Figure 7.6: Invariant mass spectrum of the four-body system containing both leptons and the two leading jets, in the low-mass control region ($m_{\ell\ell} < 200$ GeV). (a) shows the electron and (b) the muon channel. The Drell-Yan process dominates both spectra. The control region is virtually signal-free.

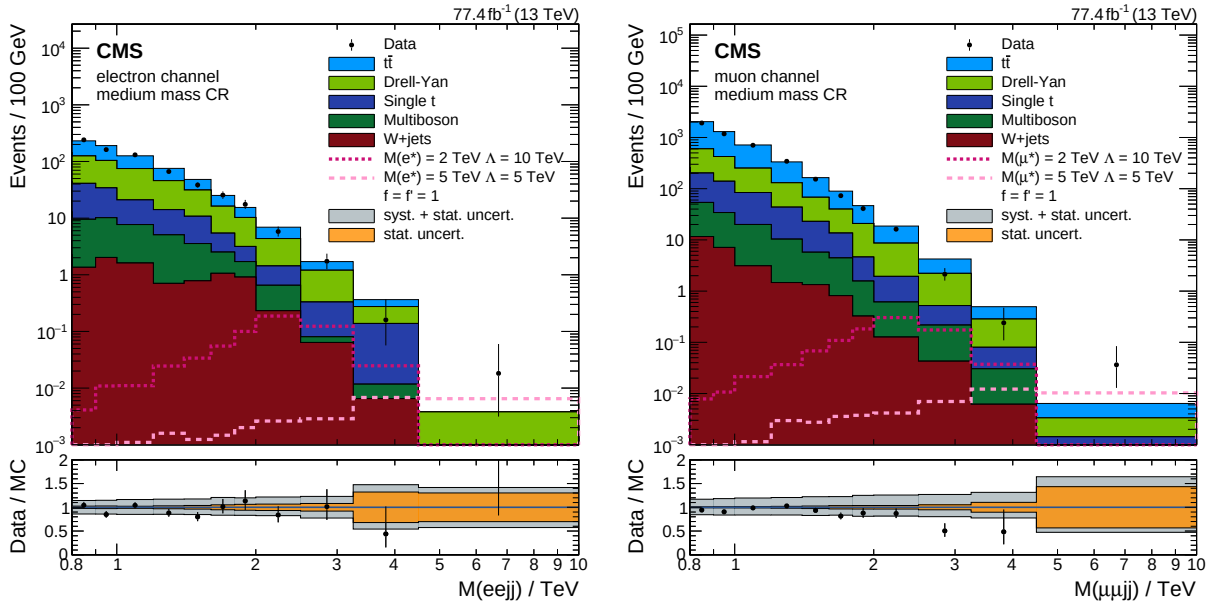

(a) (b)

Figure 7.7: Invariant mass spectrum of the four-body system containing both leptons and the two leading jets in the medium-mass control region (200 GeV $< m_{\ell\ell} <$ 500 GeV). (a) shows the electron and (b) the muon channel. The $t\bar{t}$ process dominates the spectrum. This control region contains only a small amount of the hypothetical signal.

Medium-Mass Control Region Figure 7.7 shows the medium-mass control region. It reaches from invariant di-lepton masses of 200 to 500 GeV, and $t\bar{t}$ is the dominant background. The binning is similar to the one in the low-mass control region. The electron channel generally shows good agreement between data and simulation. The data are randomly distributed around the expectation and mostly contained in its uncertainty. The relative statistical uncertainty on the last two bins is already very sizable, with more than 30%. The muon channel has a deficit in the bins between 2.5 and 4.5 TeV. The last bin shows an excess over the background estimation. However, the statistical uncertainty is around 40% for this bin. In the electron channel, the data agree with the prediction within the systematic uncertainties and show no systematic trend. Overall, the simulation describes the spectrum well enough to continue the analysis. The $t\bar{t}$ process is further validated in the next paragraph.

Mixed-Flavor Validation Region The excited lepton signal always contains two leptons of the same flavor. Contrary, the $t\bar{t}$ background can contain leptons with mixed flavor. We can use this feature to define another signal-free validation region for the $t\bar{t}$ background. The selection is generally similar to the standard selection with the difference that it contains one electron and one muon instead of either two electrons or two muons. Jets are selected similar to the main analysis, and at least two jets are required per event. I chose to use the muon trigger for this validation region since the threshold is far below the one of the electron trigger. We can apply the same di-lepton mass requirement as well to validate the $t\bar{t}$ specifically in the signal region of the search.

Figure 7.8 shows the distribution of the invariant mass of the four-body system containing the

electron, the muon, and the two leading jets. It is, as expected, dominated by the $t\bar{t}$ process and shows excellent agreement within 10% between data and simulation.

Summary I validated the quality of the MC simulation in several quasi signal-free regions and final states. All distributions show good agreement between data and expectations. This agreement strengthens the trust in the simulation and validates that it provides an accurate description of the Standard Model expectation also in the signal region.

7.1.4 Final Distribution

Typically, the search variable attempts to reflect the mass of the resonant particle – the excited lepton. The excited lepton decays into one lepton and two quarks. However, the second lepton from the associated production adds an ambiguity in which lepton corresponds to the excited lepton. Additional jets from initial state radiation can add more ambiguities if they have a larger p_T than the jets of the excited lepton decay. Section 5.3 discussed the probabilities that the leading lepton corresponds to the lepton of the decay. It showed that this probability highly depends on the signal hypothesis. Thus, there is no a priori handle to assign one of the leptons to the decay.

It is still possible to attempt to reconstruct the excited lepton by using the *minimal* or *maximal* mass. First, we calculate the masses of both combinations of the leptons with the leading two jets. The smaller one is the minimal, and the larger the maximal mass. The distributions for the muon channel are shown in figure 7.9. The electron channel behaves similarly. The minimal mass shows a sharp peak for the 2 TeV signal. However, it is mostly below the background expectation. The 5 TeV signal is flatter than the 2 TeV signal, and a significant part of the signal is shifted to small masses. Another issue is the background description. The statistical uncertainty of the background prediction in the last two bins reaches 100%. A significantly wider binning would be needed, which would further limit the sensitivity. The excess in the second to last bin in the minimal mass is not significant as both neighboring bins are empty as can be seen in the ratio.

The maximal mass shifts the 5 TeV signal events to higher masses. However, most of the 2 TeV signal is still below the background. The uncertainty of the last bin reaches 100% as well.

The best compromise is the use of the *four-body mass*, i.e., the invariant mass of both leptons and both quarks. At 1 TeV it is 25 to 40% more sensitive than both three-body mass options. At higher masses, the differences become smaller as the signal gets shifted away from the background for all mass reconstruction techniques. Figure 7.10 shows the spectrum for the electron and muon channels. Both the 2 and the 5 TeV signal ascend visibly above the background. Drell-Yan is the relevant background, especially at high masses. The event yield in the muon channel is larger than in the electron channel because of the lower trigger threshold. The uncertainties reach up to 100% in the last bin.

Both channels show no significant excess compared to the expectation. The electron channel has an excess in the second-highest bin, but no event in the highest bin. The highest mass

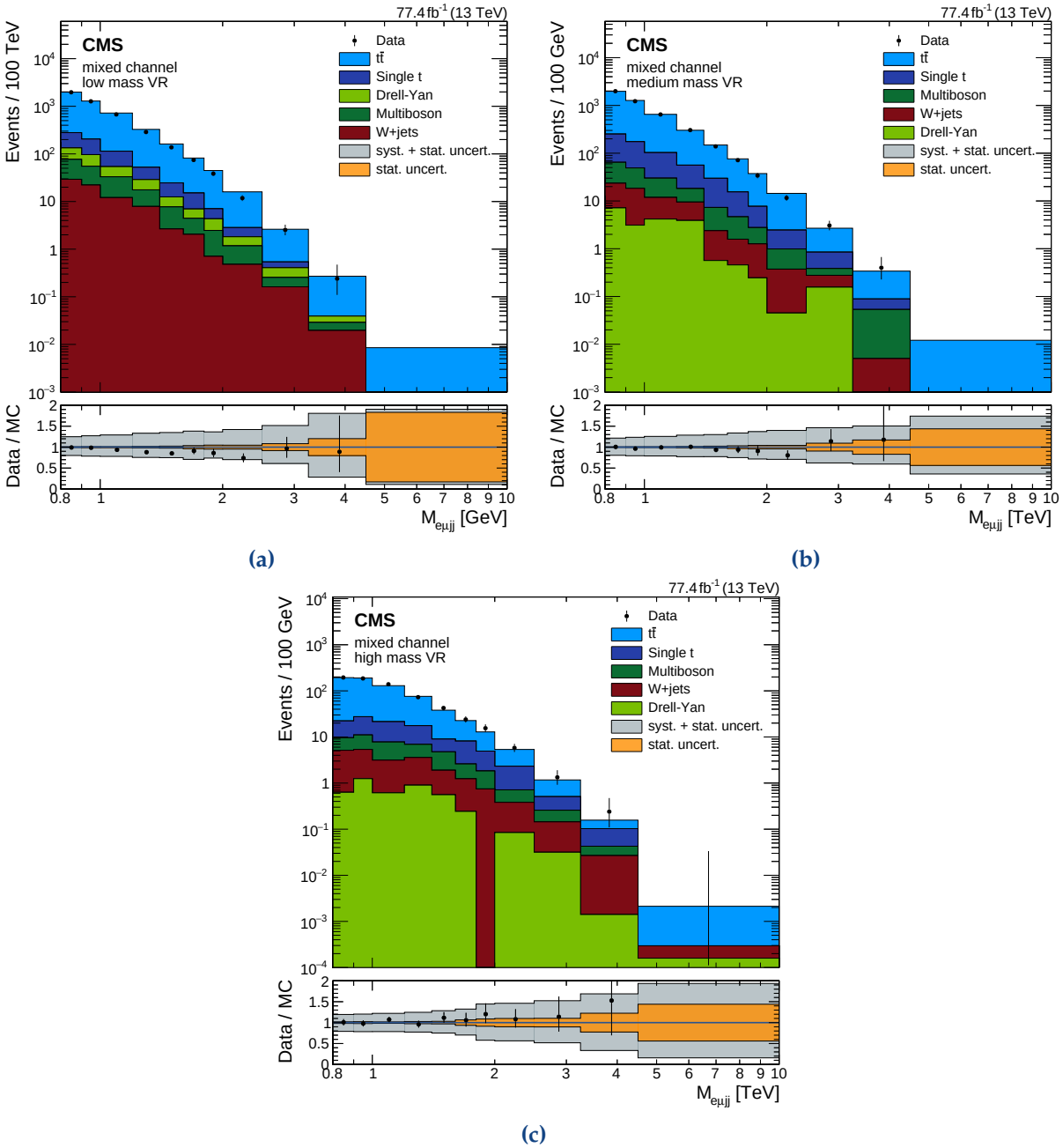

Figure 7.8: Invariant mass spectrum of the four-body system containing the leading electron, leading muon, and the two leading jets in the mixed-flavor validation region. (a) shows the distribution in the low-mass region for $M_{e\mu} < 200\,\text{GeV}$ matching the usual requirement of the analysis. (b) shows the spectrum in the medium-mass region, and (c) in the high-mass region, which corresponds to the signal region of the CI analysis ($M_{e\mu} > 500\,\text{GeV}$). The spectra are dominated by $\text{t}\bar{\text{t}}$ as Drell-Yan can only produce a pair of same-flavor leptons. All spectra, especially the spectrum in the high-mass region, are described by the simulation within its uncertainties.

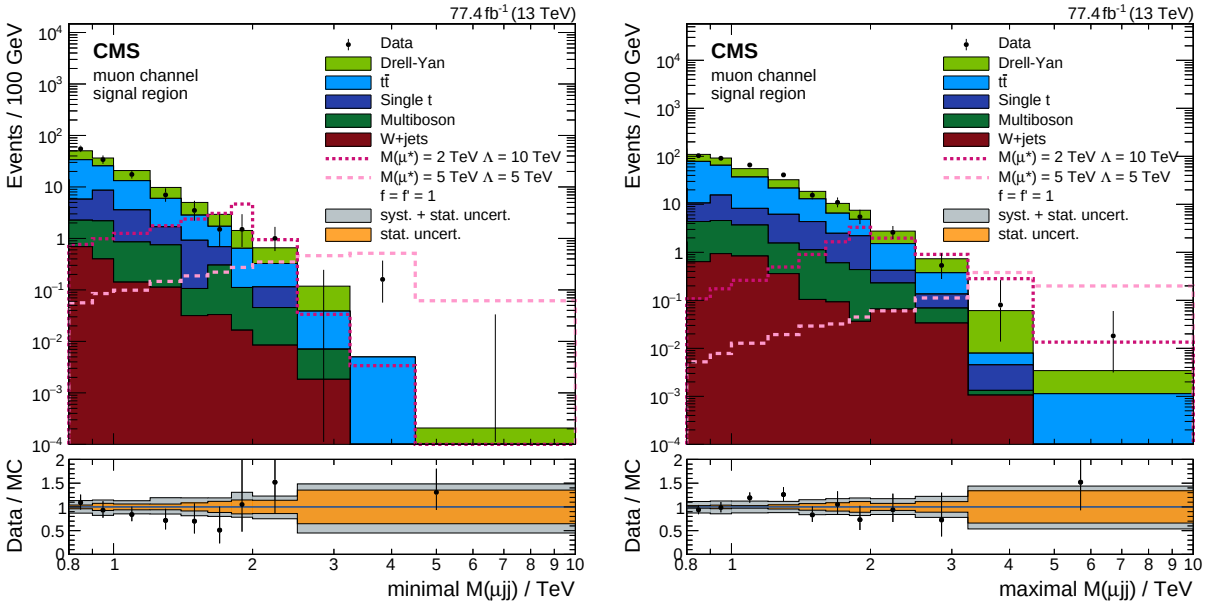

(a) (b)

Figure 7.9: Invariant mass spectrum of the three-body system containing the two leading jets and one lepton in the signal region of the muon channel. (a) shows the selection of the lepton which maximizes the mass and (b) of the one which minimizes it. Both distributions are not ideal to differentiate between signal and background. The minimal mass spectrum would also need to use a coarser binning.

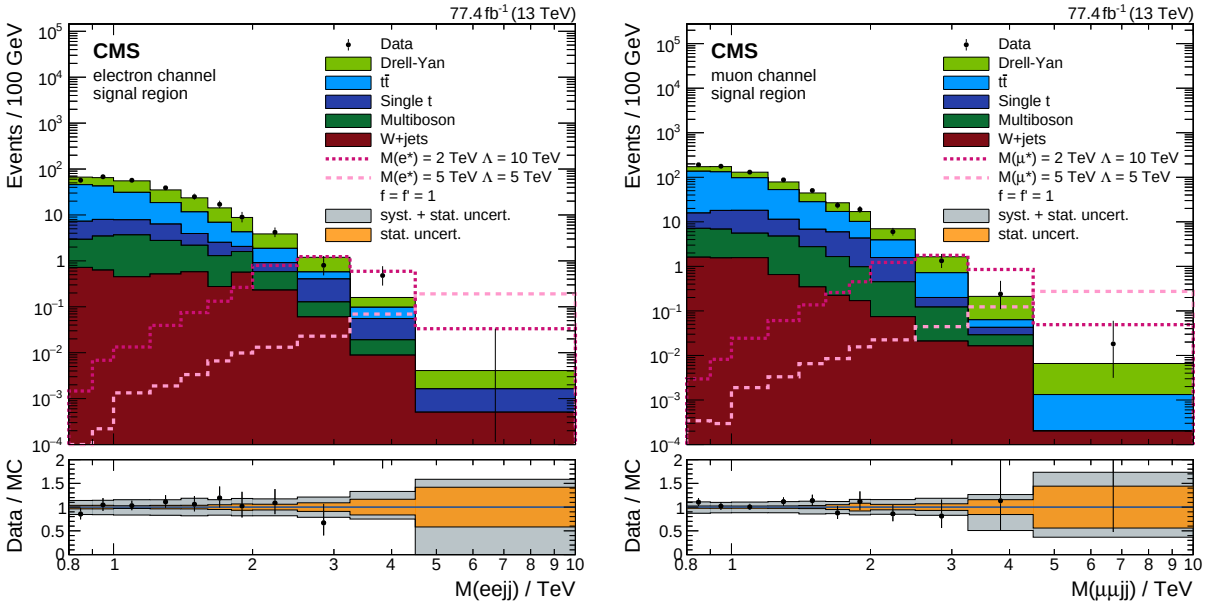

(a) (b)

Figure 7.10: Invariant mass spectrum of the four-body system containing both leptons and the two leading jets in the signal region. (a) shows the electron channel and (b) the muon channel. The lines represent two signal hypothesis of a 2 and 5 TeV excited lepton. The cross section corresponds to values of $f = f' = 1$ for both hypotheses and $\Lambda = 10$ and 5 TeV for the electron and muon channel respectively. No significant excess of data over the expected background is observed.

events are at 4.4 and 5.9 TeV, respectively. Figure 7.11 presents a display of the events.[8] It shows the measured energy deposits and hits in the detector as well as the reconstructed high-level objects. The event of the electron channel contains two electrons – one in the central part of the detector and one in the forward region of the detector. The two highest energetic jets are also in the forward region. The leading jet contains a non-isolated muon. The highest mass event in the muon channel contains one very high energetic muon and one with a smaller transverse momentum of 200 GeV. Both jets have more than 1 TeV transverse momentum. The event displays do not raise any concerns about potential reconstruction issues.

7.1.5 Systematic Uncertainties

There are two categories of systematic uncertainties: Experimental uncertainties and theoretical uncertainties. The sources for theoretical uncertainties were described in section 3.2 and the ones for experimental uncertainties in chapter 4. Both categories will be quickly summarized here:

PDF: The primary source of theoretical uncertainties is the description of the parton distribution functions (PDFs). This analysis uses the MC replica method for the simulation of the 2016 dataset and the Hessian method for the simulation of the data taken in 2017 following the NNPDF recipe [94].[9] The PDF sets are accessed using LHAPDF6 [179].

α_s: The choice of the strong coupling constant α_s introduces an additional theoretical uncertainty in the cross section calculation. It is estimated by varying α_s up- and downwards by 2% in the PDF estimation.

Renormalization- and Factorization Scale: The renormalization- and factorization scale uncertainty estimates the uncertainty of the cross section evaluation of a process due to missing higher orders. The uncertainty itself is evaluated by simultaneously varying both scales up- and downwards by a factor of two.[10]

Object Energy Scale and Resolution: These uncertainties belong to the group of experimental systematic uncertainties. They are related to the measurement of the detector. Energy scale uncertainties are treated by shifting the transverse momentum of a particle[11] according to the measured uncertainty as described in sections 4.3, 4.2.1, and 4.4.6 for electrons, muons, and jets, respectively. Energy resolution uncertainties account for an over-estimated energy resolution in simulation compared to data. The momentum of the particle is smeared to match the resolution observed in data.[12] Both uncertainties do not impact the normalization of the distribution but shift or smear the measured spectrum. They can only affect the normalization by shifting events outside of the acceptance.

Luminosity: The uncertainty on the luminosity measurement is 2.5 and 2.3% in 2016 and 2017, respectively [180, 181]. This uncertainty impacts the normalization of the spectrum directly.

[8] The presented event in the electron channel is the event with the seconds-highest mass. The highest mass event display was not available for technical reasons. The masses of the leading events are less than 3 GeV apart from each other – much less than the detector resolution.

[9] Section 3.2 describes both the MC replica and the Hessian method.

[10] Section 3.2 contains an explanation of the physical meaning of these quantities.

[11] For muons $1/p_T$ is shifted as the transverse momentum is measured by the curvature of the track.

[12] Sections 4.2, 4.3, and 4.4.6 explain the method and the size of the uncertainty.

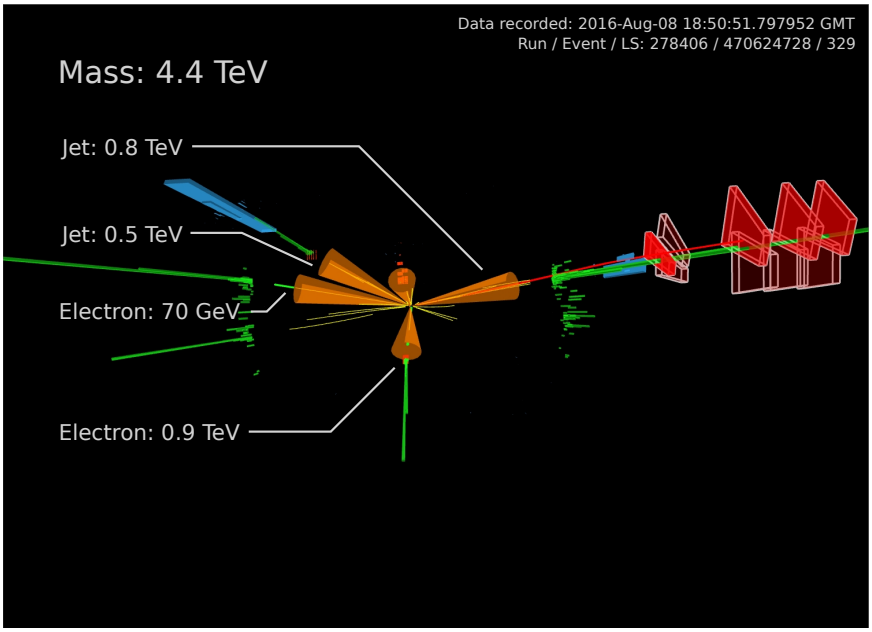

(a)

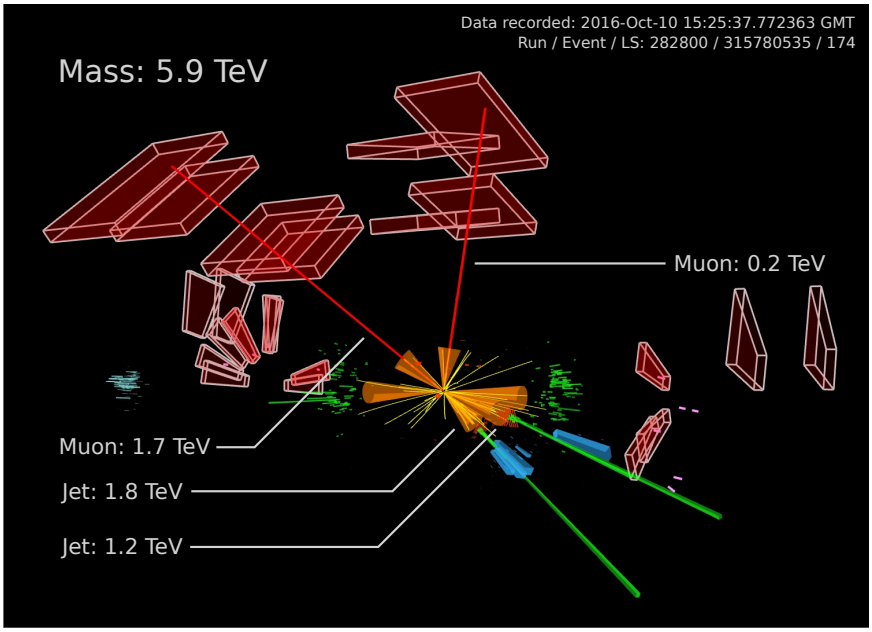

(b)

Figure 7.11: Event displays of the highest mass event in the signal region of (a) the electron and (b) the muon channel. Green bars visualize energy deposits in the ECAL, blue bars deposits in the HCAL, and white bars in the forward region correspond to measurements of the HF. The length of the bar corresponds to the measured energy. The yellow lines represent reconstructed tracks above 2 GeV, and red lines depict reconstructed global muons. The muon chambers which are hit by reconstructed muons are highlighted. The orange cones indicate jets. The beam axis is in the horizontal plain in the middle of the figure. The mass corresponds to the four-body invariant mass of both leptons and the two leading jets and the value provided for each particle to its p_T.

Pileup: Shifting the total inelastic pp cross section by 5% up-and downwards assesses the uncertainty on the pileup distribution. The impact of this uncertainty is small compared to the other sources.

Misidentification Rate of Leptons: The misidentification rate is not well described by Monte Carlo simulation. I assign an additional uncertainty of 100% to events contributing to the W+jets background due to the imprecise modeling of misidentified objects in MC simulation. While the size of this uncertainty is large, its total impact is expected to remain small because the process only contributes to a small amount of the entire Standard Model expectation in this analysis.

top-p_T Spectrum: The MC simulation of the $t\bar{t}$ process does not describe the p_T spectrum of the top-quark well [182–185]. This analysis does not apply a correction because the source of the disagreement is unknown. The difference between the simulated and the measured spectra is used as an uncertainty on the $t\bar{t}$ background.

Drell-Yan k-Factor: As the dominant background source, the Drell-Yan process uses a differential NNLO QCD + EWK NLO k-factor as described in section 6.2.1. The difference between the NLO shape of the generator and this di-lepton mass dependent k-factor is added as a systematic uncertainty.

Efficiencies: Identification, reconstruction, and trigger efficiencies differ slightly between data and simulation. Scale factors are used to mitigate different efficiencies as described in section 4.5. The systematic uncertainties on the efficiency measurement influence the normalization on the spectrum directly.

Prefiring: The uncertainties on the corrections for the prefiring issue of the ECAL[13] have direct impact on the normalization of the spectrum as well. The uncertainty as well as the correction increases towards the endcaps of the detector.

MC Sample Size: The final systematic uncertainty arises from the statistical uncertainty of the MC simulation.

We treat all uncertainties as fully correlated between both data taking periods. The only exceptions are the luminosity and muon scale uncertainty. The MC sample size uncertainty is uncorrelated between different processes, data taking periods, and bins of the distribution. For one data taking period, all other uncertainties are fully correlated between different bins and different distributions.

Figure 7.12 illustrates the relative contribution of all systematic uncertainties. The uncertainty caused by MC sample size, the PDF uncertainty, and the object energy scales dominate at high masses. At low masses, the renormalization and factorization scale uncertainty is dominant. The muon scale uncertainty for the 2016 data taking period is determined on the 2017 MC by applying the 2016 uncertainty map because it is one of the most important uncertainties. The obtained relative uncertainty is then applied to the 2016 SM expectation. This method provides a more accurate description of the uncertainty due to the increased number of generated MC events in 2017.

[13] c.f. section 3.3.4.

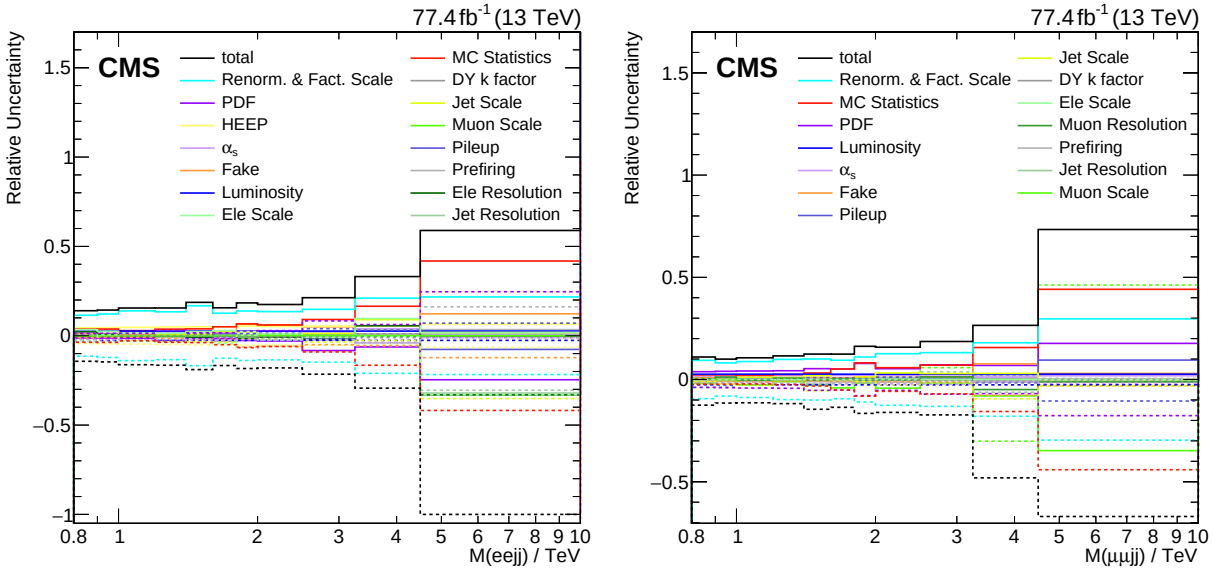

(a) **(b)**

Figure 7.12: Relative contribution of the uncertainties to the total systematic uncertainty of the background expectation in the signal region. (a) shows the electron channel and (b) the muon channel. The most important uncertainties are the statistical uncertainty of the MC simulation, the PDF uncertainty, and the object energy scales of electrons, muons, and jets. At low masses, the factorization and renormalization scale uncertainty dominates.

7.1.6 Signal Efficiency

A large signal efficiency is paramount for a good sensitivity of the analysis. It is important to remember the expected sensitive region in the parameter space of the model: The contact interaction channel has a large signal branching fraction and hence sensitivity for heavy excited leptons.

Figure 7.13 shows the signal efficiency of the pre-selection and the final selection. For the lowest signal mass hypothesis of 200 GeV, the efficiency is only at 5 to 10%. It rises, however, quickly to 50 and 65% for the electron and muon channels, respectively and reaches a stable plateau above 2 TeV. The efficiency is slowly declining to the highest masses due to off-shell produced excited leptons.[14] The di-lepton mass requirement leads to an efficiency loss of only 5%. The efficiency at low masses is lower because of the relatively high acceptance requirements and the high-p_T trigger requirement.

The uncertainties presented in figure 7.13 correspond only to the statistical uncertainty. Figure 7.14 illustrates the effect of the systematic uncertainties on the signal efficiency. The efficiency correction factors have the most significant impact on the signal efficiency. Other uncertainties like the object energy scale uncertainties have a more substantial impact on the shape but a minor effect on the normalization. The PDF uncertainty considers only the uncertainty on the acceptance.[15]

[14] See figure 5.1a in section 5.2.

[15] In 2017, the sample was produced using the `NNPDF31_nnlo_as_0118_luxqed` PDF set, which yields unphysical

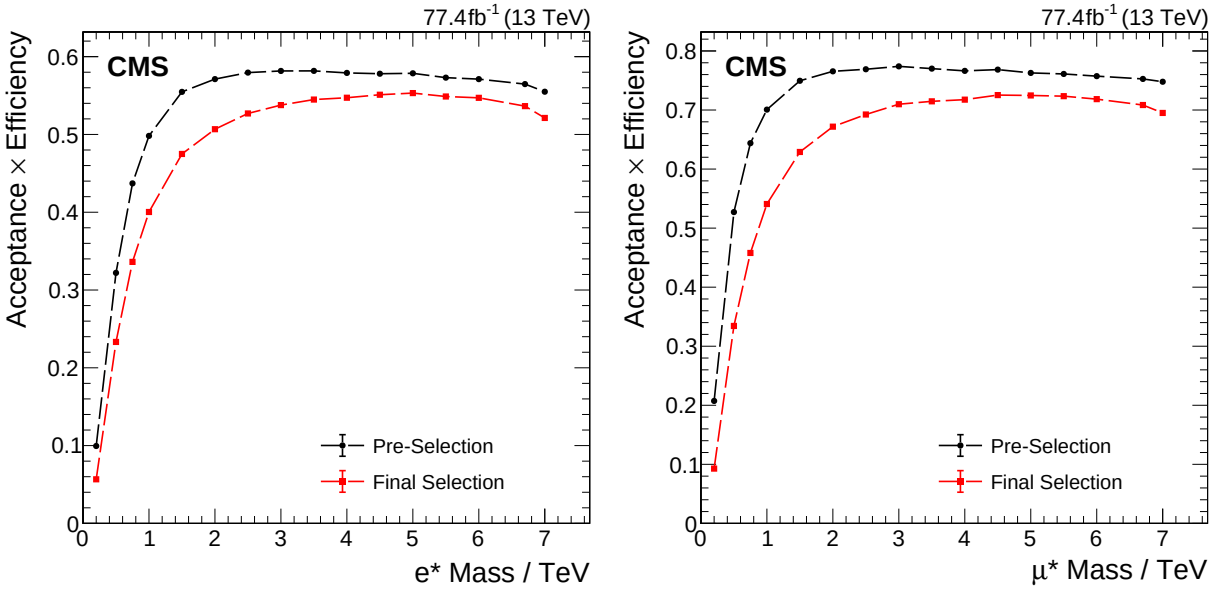

(a) (b)

Figure 7.13: Signal efficiency for (a) the electron channel and (b) the muon channel. The pre-selection is shown in black and the final selection in red. The efficiency becomes stable above 2 TeV at 50% and 65% for the electron and muon channels, respectively.

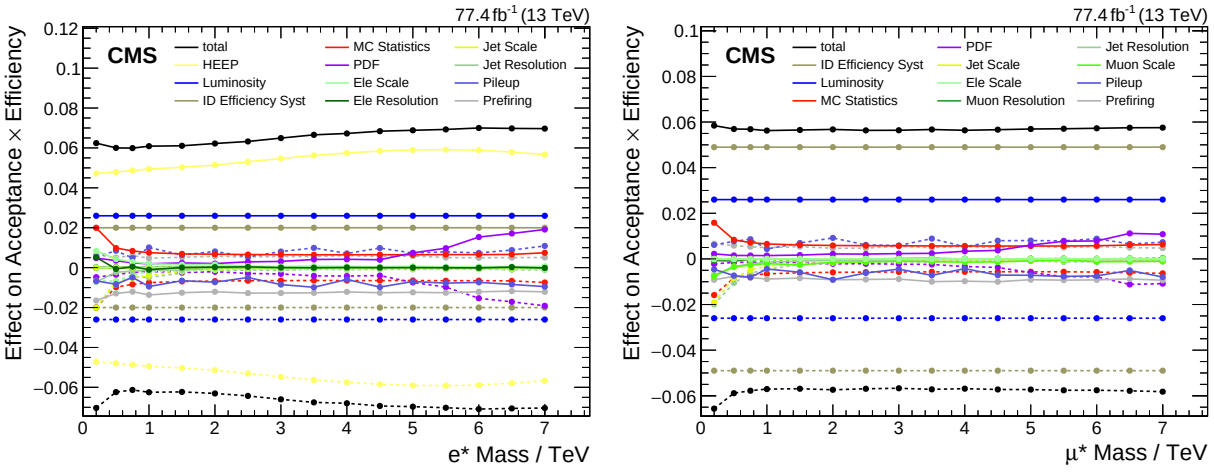

(a) (b)

Figure 7.14: Effect of the systematic uncertainties on the signal efficiency for (a) the electron channel and (b) the muon channel. The efficiency corrections have the largest impact since they directly influence the normalization of the signal. Object energy scale uncertainties, on the other hand, have a stronger impact on the shape of the signal but a small impact on the normalization. This distribution contains only the uncertainty on the acceptance of the PDF.

7.1.7 Statistical Analysis

The final distribution helps to identify deviations between expectation and data but does not quantify the sensitivity. For this purpose, we need a statistical analysis which can quantify the significances of excesses, and to set exclusion limits. The foundation of the statistical analysis is the optimization of a profiled likelihood. Reference [186] describes this method. This thesis uses the *combine* tool developed by the CMS collaboration [122].

The likelihood is defined as follows:

$$\mathcal{L}(\text{data}|\mu,\theta) = \prod_{i\,\in\,\text{bins}} \frac{(\mu s_i + b_i)^{n_i}}{n_i!} \mathrm{e}^{-\mu s_i + b_i} \cdot \prod_{j\,\in\,\text{nuisnaces}} p(\tilde{\theta}_j|\theta_j). \tag{7.3}$$

The first term is the Poisson probability to observe n_i events given the expectation $\mu s_i + b_i$. $\mu = \sigma_{\text{signal}}/\sigma_{\text{theory}}$ is the signal strength modifier, s_i the number of expected signal events, and b_i the number of expected background events. Both, s_i and b_i are provided by simulation, n_i is the number of data events, and the signal strength modifier is the parameter of interest. The product multiplies the individual probabilities of all bins in the distribution.

As described in section 7.1.5, the number of expected signal and background events have an associated systematic uncertainty. This uncertainty is split into several sources, which are either assumed to be fully correlated across all bins of all distributions and all data taking periods or entirely uncorrelated. Section 7.1.5 describes all uncertainty sources and their correlations. Statistical Monte Carlo uncertainties are implemented using the Barlow-Beeston approach [187, 188].

The uncertainties are described by the parameters θ_j, and both s_i and b_i depend on those ($s_i = s_i(\theta), b_i = b_i(\theta)$). $\tilde{\theta}$ represents the best estimate for this uncertainty and $p(\tilde{\theta}|\theta)$ describes the degree of belief that a value θ for an uncertainty is compatible with the input value $\tilde{\theta}$. A *log-normal* function[16] parametrizes this probability. A log-normal distribution has the advantage that it is positive definite, while a Gaussian can have tails to negative hence unphysical values for large uncertainties. For small uncertainties, both probability density functions are asymptotically equal.

The test statistic is defined as the profile likelihood ratio:

$$\tilde{q}_\mu = -2\ln\frac{\mathcal{L}(\text{data}|\mu,\hat{\theta}_\mu)}{\mathcal{L}(\text{data}|\hat{\mu},\hat{\theta})}, \tag{7.4}$$

with the values $\hat{\theta}$ and $\hat{\mu}$ that maximise the likelihood and $\hat{\theta}_\mu$ which maximizes the likelihood for a given μ.

We can obtain the limit by comparing the observed value $\tilde{q}_\mu^{\text{obs}}$ with the distribution of the test statistic. The test statistic is built by performing pseudo-experiments randomizing the nuisance parameters according to their probability density function. This step is performed separately for the *signal + background* hypothesis for a given value of μ and the *background-only* hypothesis setting

values for the uncertainty calculation. Therefore, I use the `NNPDF31_nnlo_hessian_pdfas` set to calculate the PDF uncertainty on the signal yield. The background production already used the latter PDF set.

[16] A log-normal function behaves like a Gaussian in logarithmic space.

μ to zero. Depending on the sensitivity of the analysis, a large number of pseudo-experiments might be required. This statistical analysis of the searches presented in this thesis performed up to 10^4 pseudo-experiments.

Using the distribution of the test statistic, we can calculate the probability to observe a deviation larger than observed in data for both the non-zero signal hypothesis (p_μ) and the background-only hypothesis (p_b):

$$p_\mu = P(\tilde{q}_\mu \geq \tilde{q}_\mu^{\text{obs}} | \text{signal+background}) = \int_{\tilde{q}_\mu^{\text{obs}}}^{\infty} \mathrm{d}\tilde{q}_\mu f(\tilde{q}_\mu|\mu), \tag{7.5}$$

$$1 - p_b = P(\tilde{q}_\mu \geq \tilde{q}_\mu^{\text{obs}} | \text{background-only}) = \int_{\tilde{q}_0^{\text{obs}}}^{\infty} \mathrm{d}\tilde{q}_\mu f(\tilde{q}_\mu|0). \tag{7.6}$$

The ratio of both quantities defines the CL_s value [189, 190]:

$$\mathrm{CL}_s(\mu) = \frac{p_\mu}{1 - p_b}. \tag{7.7}$$

A signal is excluded at a confidence level (CL) α if $\mathrm{CL}_s < 1 - \alpha$. To obtain the exact CL_s value for a given α, we sample several CL_s values for different values of μ close to the expected exclusion limit. The combine tool uses a quadratic fit to interpolate between the tested signal strengths to increase the precision of the limit further. This analysis follows the general guideline of high energy particle physics analyses using a confidence level of 95%.

The expected limit is calculated by drawing pseudo-data for the background-only hypothesis and calculating the exclusion limits μ^{excl}. The pseudo-data are treated precisely as real data. The 50% quantile of the cumulative distribution of μ^{excl} defines the median expected limit. The ± 1 and $\pm 2\sigma$ bands are defined by their respective quantile of the cumulative μ^{excl} distribution.

7.1.8 Results

Simultaneously fitting the signal region and both the low- and medium-mass control regions yields the 95% confidence level exclusion limits since there is no evidence for excited leptons. The electron and muon channel are fitted independently from each other. The mixed-flavor validation region is not used for fitting to avoid correlations between both channels.

Figure 7.15 shows the exclusion limit for the electron and the muon channel. The expected and observed limits coincide within their uncertainties. In the electron channel, the observed limit is above the expected one and not contained in the one-sigma variation for excited leptons between 2 and 4 TeV. This is consistent with the excess in the 4 TeV bin in figure 7.10a. The muon limit coincides with the expected limit inside the one-sigma band with a minor exception around signal masses of 5 TeV. The slight excess in the highest mass bin in figure 7.10b explains this deviation.

Both limits follow the same shape and reach values around 0.1 fb and a mass limit of 5.6 TeV in both channels for $\Lambda = M_{\ell^\star}$ and $f = f' = 1$. Because of the better signal efficiency[17], the limit of

[17] See section 7.1.6.

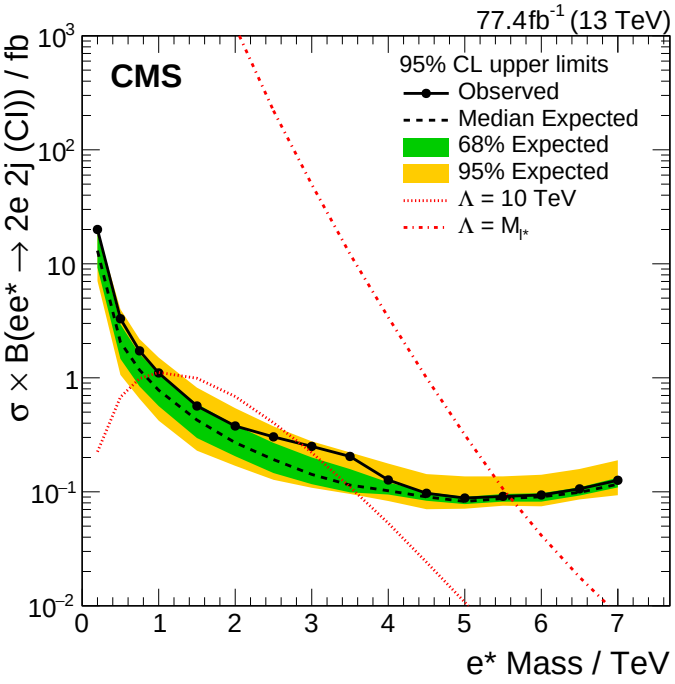

(a)

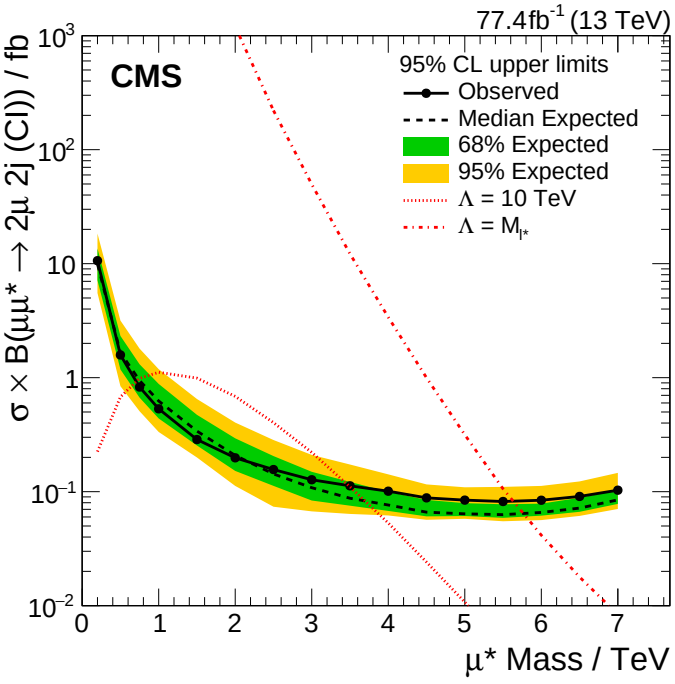

(b)

Figure 7.15: Cross section limits for (a) the electron channel and (b) the muon channel. The dashed line presents the expected limit with the $\pm 1\sigma$ band in green and the $\pm 2\sigma$ band in yellow. The solid black line indicates the observed limit. It is compatible with the expected limits as no significant deviations were observed. The two red, dotted curves correspond to signal hypotheses of $\Lambda = 10\,\text{TeV}$ and $\Lambda = M_{\ell^\star}$ for the lower and upper curve. For both curves, f and f' are equal to unity. The crossing point of the theory curve with the limit marks the maximal excluded signal mass. This limit is at 5.6 TeV for both channels.

the muon channel is generally more stringent compared to the electron channel. The limit rises above 6 TeV due to increasing off-shell production and decreasing signal efficiencies.

Figure 7.16 illustrates the impact of the uncertainties on the limit for a 5.5 TeV signal mass. The impacts are calculated using the Asimov dataset instead of real data.[18] The signal strength is set to 0.1 and the cross section corresponds to $\Lambda = 5.5\,\text{TeV} = M_{\ell^\star}$ and couplings of unity. This cross section is close to the expected exclusion limit. $\hat{r}$ denotes the obtained signal strength. The central value is equal to 0.1 because the Asimov dataset is used with a signal strength of 0.1. The middle section of the figure shows the relative shift of the post-fit uncertainty relative to the pre-fit value and the size of the bar corresponds to the obtained constraint. No uncertainty is shifted because no real data entered the fit. The theory uncertainties seem to be too conservative, as they can be constrained by fitting the Asimov dataset. The right hand column corresponds to the impact of the systematical uncertainty on the extracted signal strength. The red bar shows the impact when the uncertainty is shifted by $+1\sigma$ and the blue one when it is shifted by -1σ. The impact does not have to be symmetric and can even point in the same direction for both shifts. In the electron channel, the statistical uncertainty on the last bin of the signal region has the most impact on the signal strength. The renormalization and factorization scale uncertainties of the two dominating background processes have the second and third largest impact. The muon channel has similar impactful uncertainties.

The result of the fit using the actual data is shown in figures 7.17 and 7.18. Most uncertainties cannot be constrained strongly due to the small number of bins going into the fit. This figure assumes an excited leptons with a mass of 1 TeV, $\Lambda = 10\,\text{TeV}$ and $f = f' = 1$. The result of the fit depends only minorly on the choice of the signal hypothesis since the fit of the *signal+background* fit is very similar to the *background-only* fit.

Two goodness-of-fit tests ensure the quality of the fit: The Kolmogorov-Smirnov test [191, 192] and the Anders-Darling test [193]. The resulting p-values are mostly between 0.35 and 0.65, which indicates an excellent fit quality. Some signal points show p-values down to 0.14, which still indicates a reasonable fit quality.

[18] The Asimov dataset is the dataset for which all observed quantities are set to their expected value.

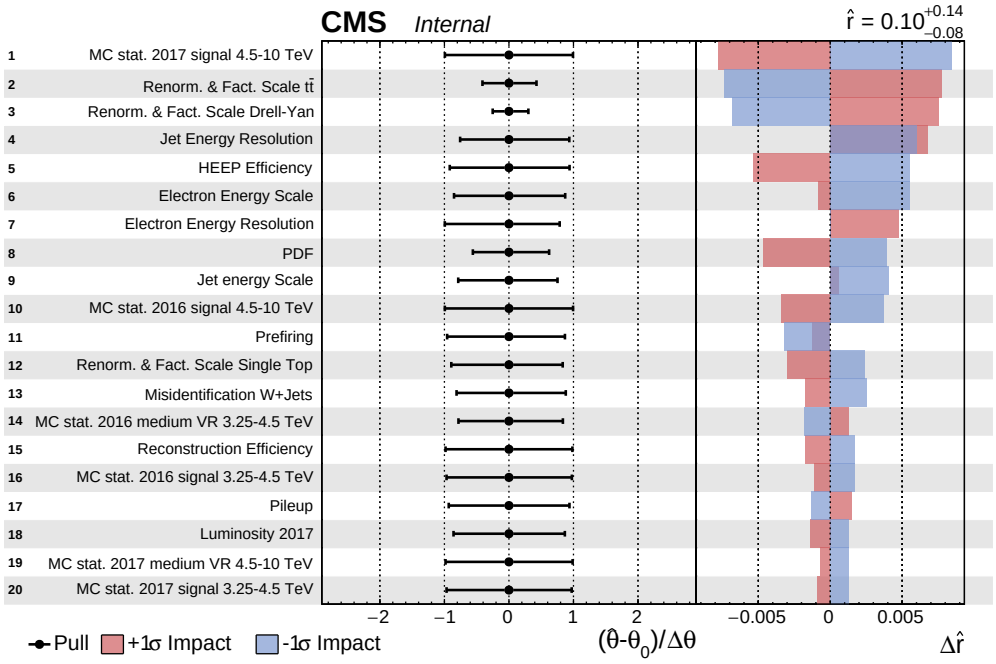

(a)

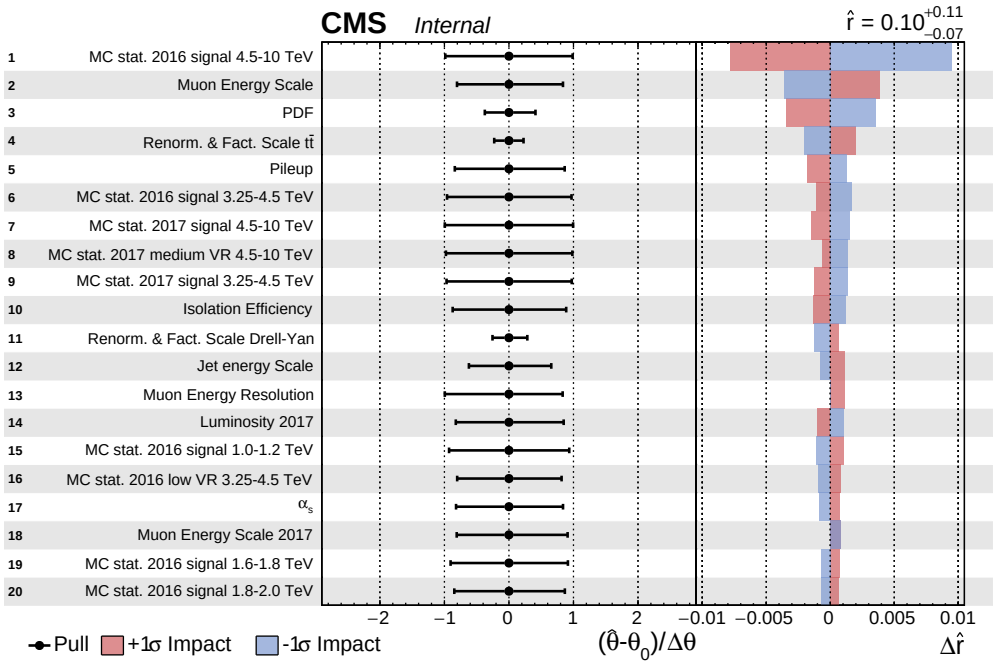

(b)

Figure 7.16: Impact of systematic uncertainties on the exclusion limit for a 5.5 TeV mass point for (a) the electron channel and (b) the muon channel. The cross section corresponds to model parameters $\Lambda = 5.5\,\text{TeV}$ and couplings f and f' of unity. The signal strength is fixed to $\mu = 0.1$. The Asimov dataset is used to calculate the impacts instead of real data. The most impactful uncertainties are the statistical MC uncertainty, theory, and object-related uncertainties.

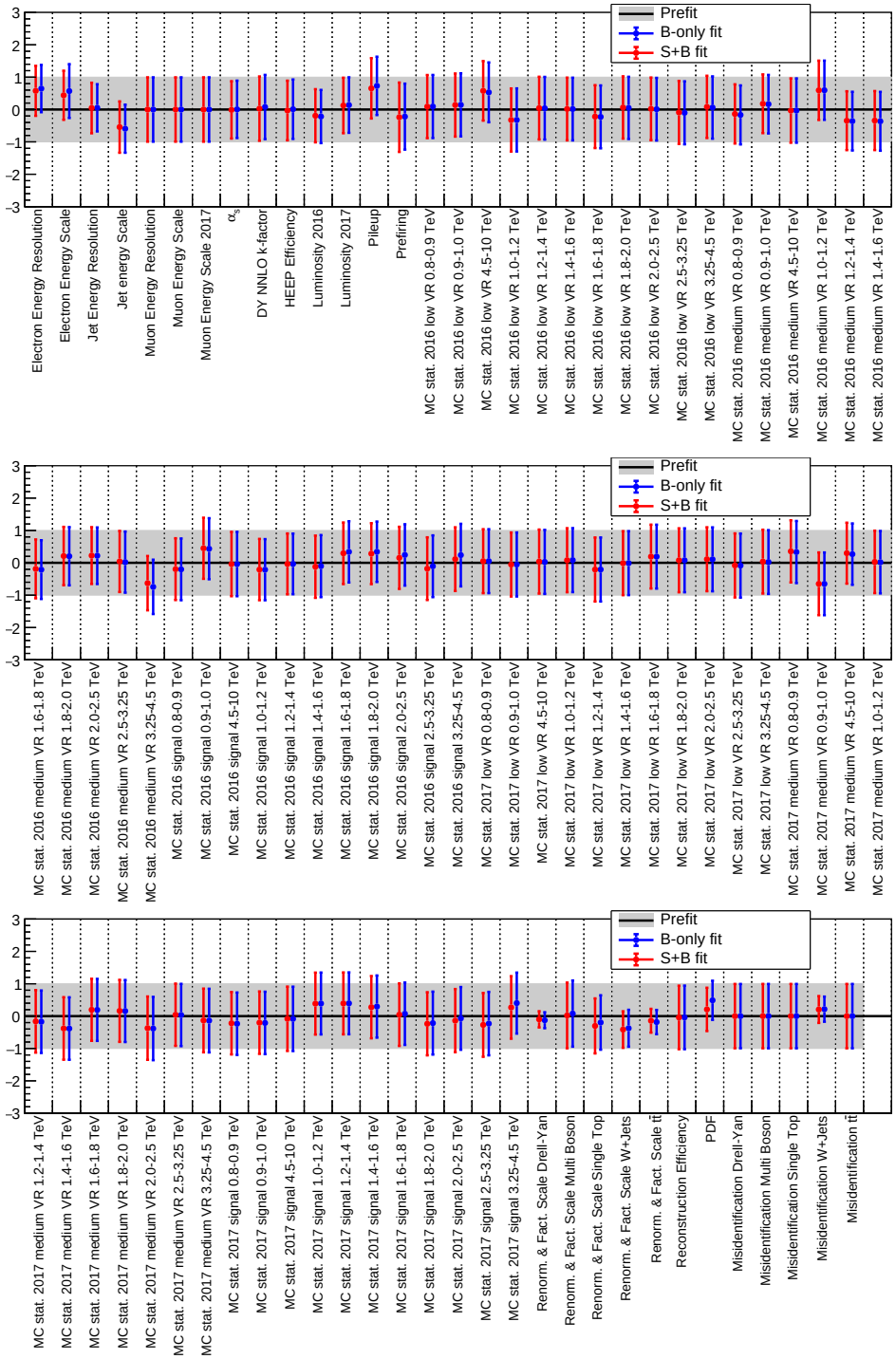

Figure 7.17: Pulls and constrained uncertainties of the fit using the actual data in the electron channel. The x-axis shows the shift relative to the pre-fit value. The size of the error bar corresponds to the relative constraint. A value of 1 ± 0.5 would correspond to an upshift by one sigma and a reduction by a factor of two. The red points show the combined fit of signal and background, and the blue ones the background-only fit. Both coincide well as no significant deviations were observed. This figure uses a 1 TeV signal hypothesis.

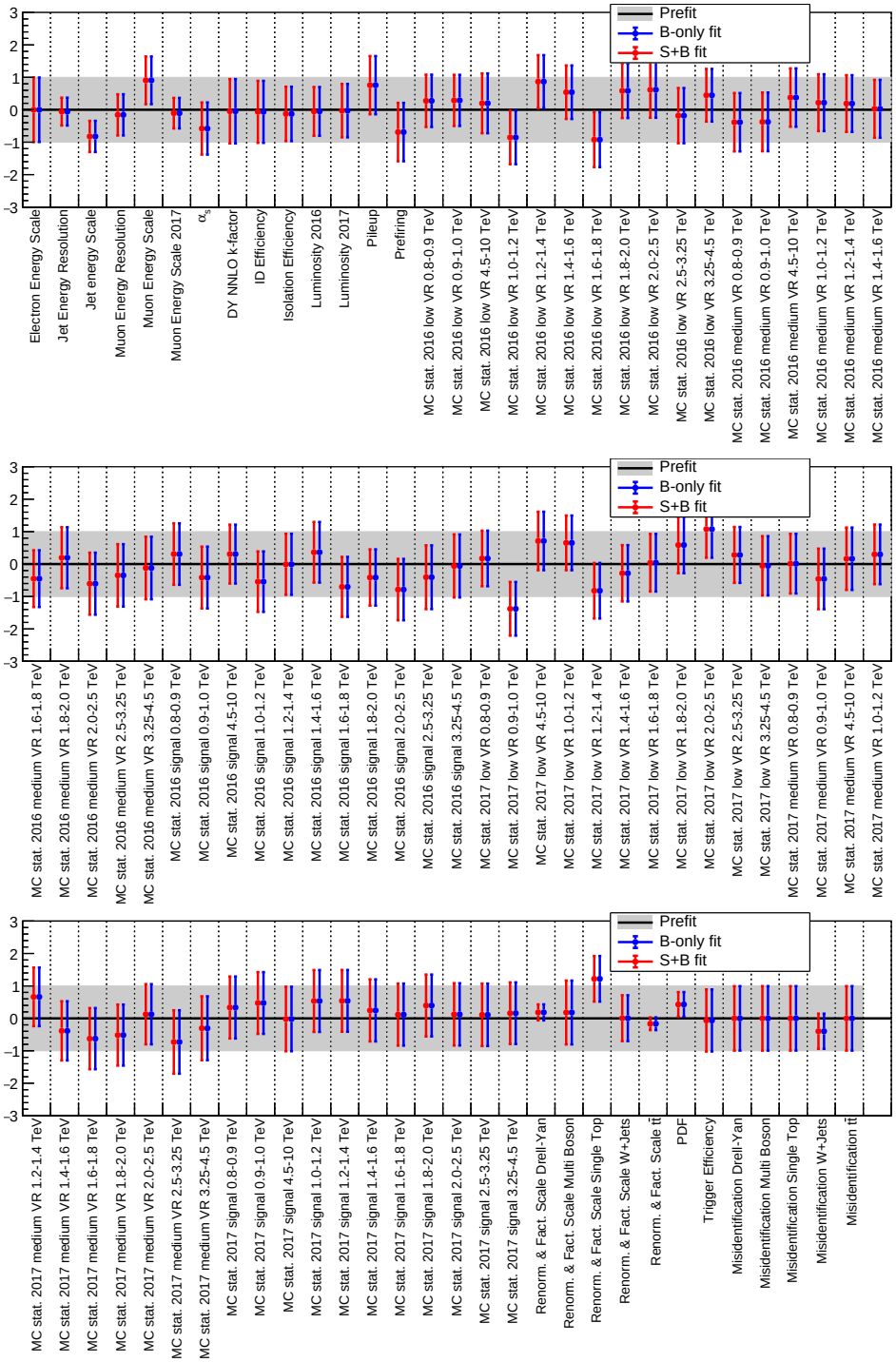

Figure 7.18: Pulls and constrained uncertainties of the fit using the actual data in the muon channel. The x-axis shows the shift relative to the pre-fit value. The size of the error bar corresponds to the relative constraint. A value of 1 ± 0.5 would correspond to an upshift by one sigma and a reduction by a factor of two. The red points show the combined fit of signal and background, and the blue ones the background-only fit. Both coincide well as no significant deviations were observed. This figure uses a 1 TeV signal hypothesis.

Table 7.2: Acceptance requirements for electron, muons, and jets for the Z channel. The p_T requirement of the trigger is included for the leading leptons.

	Electron	Muon	Jet
p_T	> 50 GeV	> 25 GeV (leading: 53 GeV)	> 200 GeV
$\|\eta\|$	< 2.5	< 2.4	< 2.4

7.2 The Z Channel

The Z channel follows the same guidelines as the contact interaction channel as it uses a similar selection for large parts of the analysis. I will highlight relevant differences in this chapter. The structure is similar to the CI chapter.

The final state of the Z channel consists of two leptons and one wide-cone jet containing two jets from the hadronic decay of a Z boson. The kinematic properties of the signal are described in detail in section 5.4.

7.2.1 Event Selection

Trigger Selection

While the muon channel uses the same trigger as the CI channel (c.f. section 7.1.1), the electron channel uses a different one. Instead of the "single-photon trigger" with a high threshold, it utilizes a double-electron trigger with lower p_T thresholds on both objects to avoid an efficiency loss at low energies. In contrast to the CI channel, the branching fraction of the Z channel is large for light excited leptons. A high-p_T trigger would remove most potential signal events for lighter resonances. The threshold of the muon trigger is with 53 GeV already low enough to probe light excited leptons. Switching to a double-muon trigger would not increase the efficiency by a large margin and might even reduce it since the double-muon trigger efficiency is lower than for the single muon trigger efficiency if both leptons pass the trigger threshold.

The HLT path of the double-electron trigger is `HLT_DoubleEle33_CaloIdL_MW` for both data taking periods.[19] The trigger is fully efficient above 50 GeV for both electrons [154]. Thus, both electrons are required to be above this threshold.

Table 7.2 summarizes the acceptance requirements on η and p_T.

Missing Transverse Energy Filter

The same missing transverse energy filters as in the CI channel are applied (c.f. section 7.1.1).

[19] In 2016, the trigger was substituted for a small run period by the backup trigger named `HLT_DoubleEle33_CaloIdL_GsfTrkIdVL` because of a misconfiguration which led to increased trigger rates. This issue had no impact on the physics performance.

7.2.2 Object Selection

As in the CI channel, we select only events with at least two electrons or two muons. Instead of two jets with a distance parameter of 0.4 and a p_T above 50 GeV, a single wide-cone anti-kt jet using a distance parameter of 0.8 with a transverse momentum above 200 GeV is requested. The PUPPI algorithm reduces the contribution of pileup to the large-cone jet.[20]

The identification and isolation criteria, as well as their efficiency correction factors, are similar to the CI channel (c.f. section 4.5.1 and 4.5.2).

7.2.3 Systematic Uncertainties

The systematic uncertainty sources are similar to the CI channel (c.f. section 7.1.5) as their final states are mostly similar.

7.2.4 Analysis Specific Selection

Pre-Selection

This section presents several distributions on the pre-selection level, i.e., after applying trigger, missing transverse energy filters, and the selection of at least two leptons and one wide-cone jet called *fat jet*. Furthermore, the soft drop mass of the fat jet is required to be above 40 GeV because the simulation of light jets is known to not reproduce the observed spectrum well at low masses [194]. The figures use the same color code as in the previous section.[21] Two signal hypotheses for masses of 1 and 3 TeV represent possible excited lepton signatures. The masses are lower than in the CI channel because the Z channel has a better sensitivity at low masses. The structure of this section follows the contact interaction channel as well: First, I present a few basic kinematic properties of the triggering particles before going over to high-level quantities used to differentiate between signal and background.

Figures 7.19a and 7.19b show the p_T spectrum of the leading and sub-leading electron. In the Z channel, both electrons trigger the event in order to significantly lower the p_T threshold compared to the single-photon trigger used in the CI analysis. The Monte-Carlo simulation describes both spectra within its uncertainties and without a visible systematic trend. The Drell-Yan process contributes most to the SM background, followed by $t\bar{t}$, multi-boson processes, single top production, and W +jets, which can only contribute via misidentified leptons. The spectrum of the leading lepton is not steadily falling. Instead, it rises to a maximum around 150 GeV and then continues to decline. The reason is the additional fat jet on the pre-selection level. It requires the Z boson of the Drell-Yan process to recoil against the jet to balance the event. The resulting boost of the Z boson makes events with a larger transverse momentum of the leading lepton more probable.

Figure 7.19c presents the analogous figure of the muon channel. The muon channel uses the same single muon trigger as the CI channel; hence, I present only the p_T spectrum of the leading

[20] Section 4.4 provides more information about the reconstruction, clustering of jets, and pileup rejection.
[21] The beginning of section 7.1.3 explains the color code.

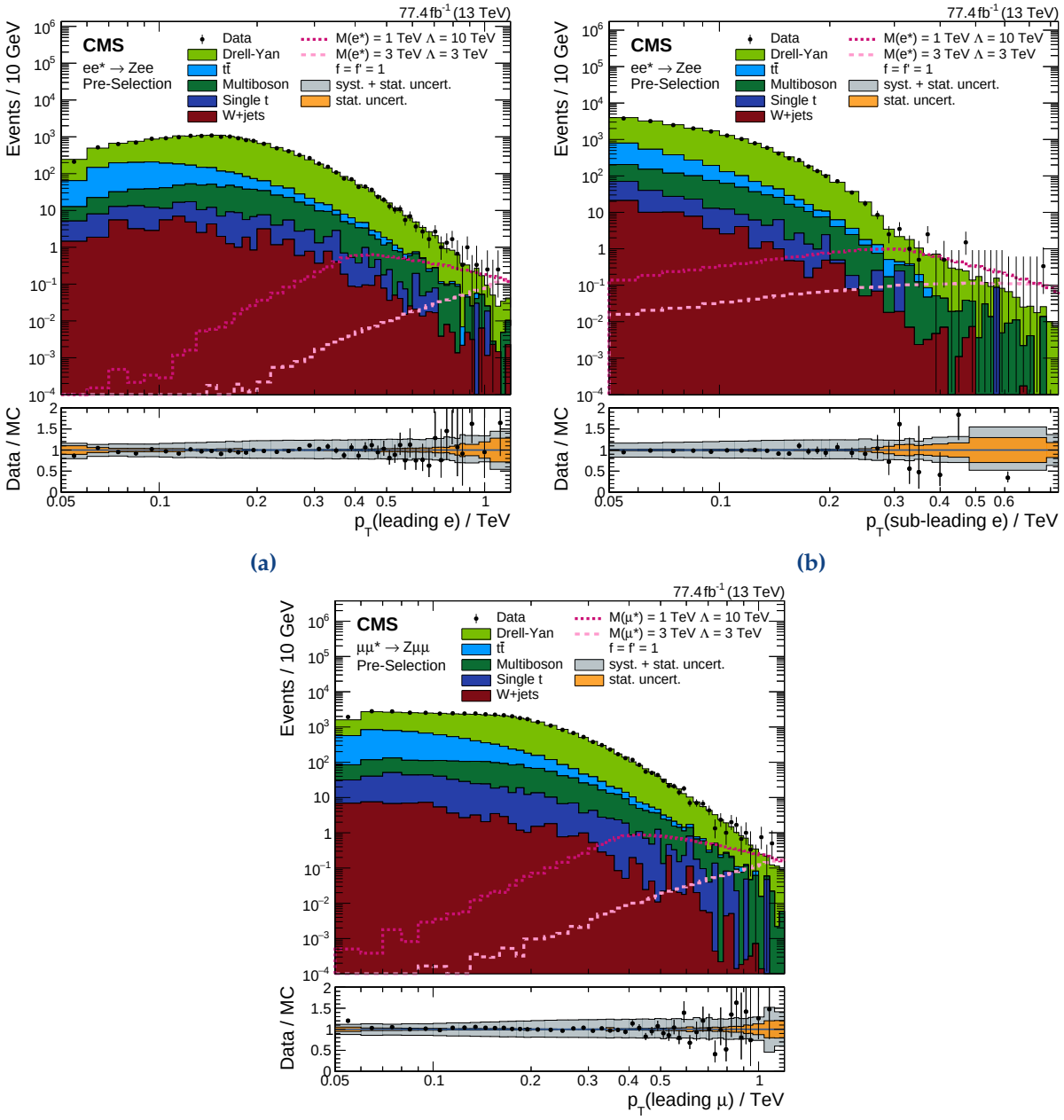

Figure 7.19: p_T distributions of the leading leptons. (a) and (b) show the leading and sub-leading electrons in the electron channel electron while (c) shows the leading muon in the muon channel. The simulation describes all spectra well. The colored stacked histograms visualize the background; the orange and grey bands represent the statistical and the total systematic uncertainties, respectively. The data are shown on top using black dots. The two pink lines represent two signal hypotheses. The p_T spectrum of the leading electron rises at the beginning due to the high p_T thresholds of the fat jet and the second electron.

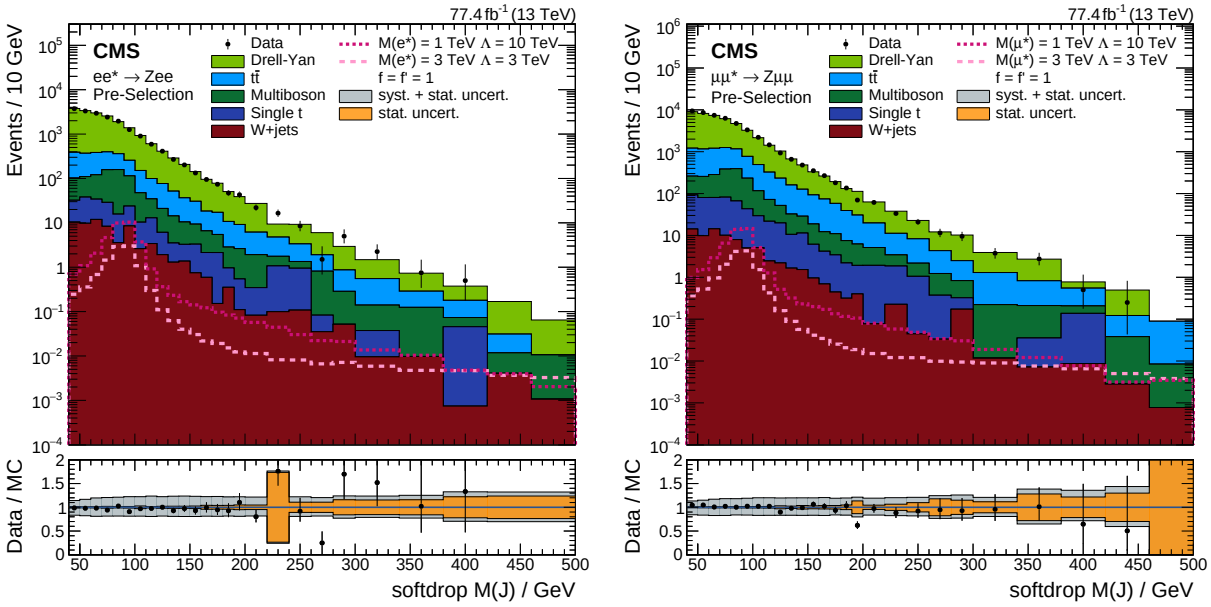

(a) (b)

Figure 7.20: Soft-drop mass distribution of the selected leading fat jet in (a) the electron and (b) the muon channel. The background is smoothly falling while the signal peaks at the Z mass.

lepton. The simulation of the SM background describes the data well, and the background composition is similar to the electron channel too. This spectrum has no rising edge at low p_T because the second muon is allowed to have a significantly lower p_T of only 25 GeV compared to the 50 GeV of the sub-leading electron. Only the first bin is below the second one because the trigger threshold is at 53 GeV instead of 50 GeV. The muon channel contains more events because of the lower p_T threshold of the second lepton as well.

As described in section 4.4.4, substructure information of the jet can help to differentiate between QCD jets and the two jets of a hadronically decaying boosted Z boson. The dominating backgrounds do not have any hadronically decaying heavy vector bosons in their decay chain. They are required to decay leptonically to provide both leptons. Therefore, this quantity can be utilized to suppress the SM background. Figure 7.20 shows the soft drop mass spectrum of the leading fat jet in the muon channel and in the electron channel. The spectrum of the SM background is smoothly falling while both signal hypothesis peak sharply at 90 GeV.

The final three distributions are the same as in the CI channel with a single addition: The invariant mass spectrum of the di-lepton system (figure 7.21), the p_T spectrum of the di-lepton system (figure 7.22), and the three-body mass spectrum of both leptons and the wide-cone jet (figure 7.23).

The invariant mass spectrum of the di-lepton system is very similar to the one of the CI channel. The electron channel has no dip above the Z peak because of the lower trigger thresholds. The simulation describes the spectra in both the peak region and the high-mass tails within its uncertainties. The muon channel has a small excess at high masses above 600 GeV. The electron channel has several bins above the expectation as well but they are balanced by the empty bins in between as the ratio panel shows.

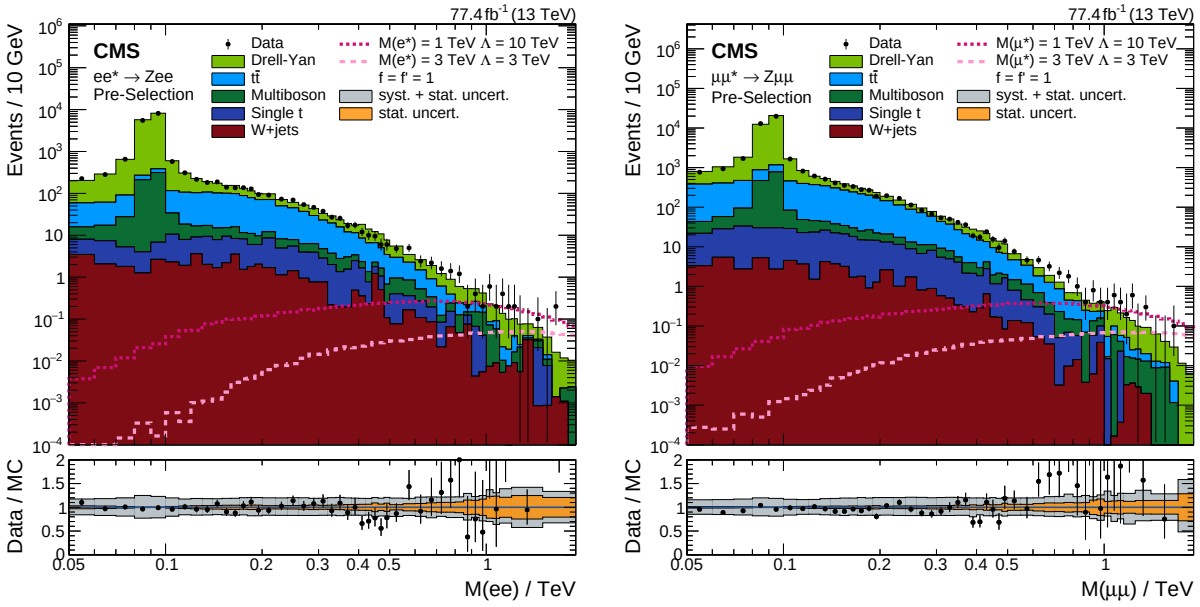

(a) (b)

Figure 7.21: Invariant mass spectrum of the di-lepton system. (a) shows the electron and (b) the muon channel. The background has a sharp peak at the Z mass while the signal is rather flat over a broad mass range.

The di-lepton p_T spectrum (figure 7.22) is also adequately described by MC simulation: The data are randomly distributed around the expectation and agree within 10% for large parts of the spectrum. At hight masses single bins fluctuate by more than 10% but are mostly covered by the systematic uncertainty and show no systematic trend. The spectrum peaks at 200 GeV because both leptons can then balance out the wide-cone jet without requiring additional objects. The signal contribution differs from the background. Its maximum is shifted towards higher values making this variable a powerful tool to differentiate between signal and background.

Finally, the invariant mass spectrum of the three-body system (figure 7.23) shows equally good agreement between observation and expectation in both channels as the last distribution. Both signal hypotheses do not significantly elevate above the SM expectation. Further analysis steps are required to improve the sensitivity of the analysis.

Final Selection

In contrast to the CI channel, the strength of the Z channel is the sensitivity for light excited leptons due to the higher branching fraction. This feature complicates the selection because possible signatures of light excited leptons blend into the distribution of the background, which is also located mainly at low energies. Thus, more advanced and carefully tuned selection steps are required to differentiate the signal from the background. While the CI channel relies on a single requirement on the invariant mass of the di-lepton system, the Z channel uses an approach featuring requirements on three uncorrelated kinematic properties: The soft-drop mass of the wide-cone jet, the invariant mass of the di-lepton system, and its transverse momentum. Splitting up the requirements on independent variables allows for smaller threshold values. The

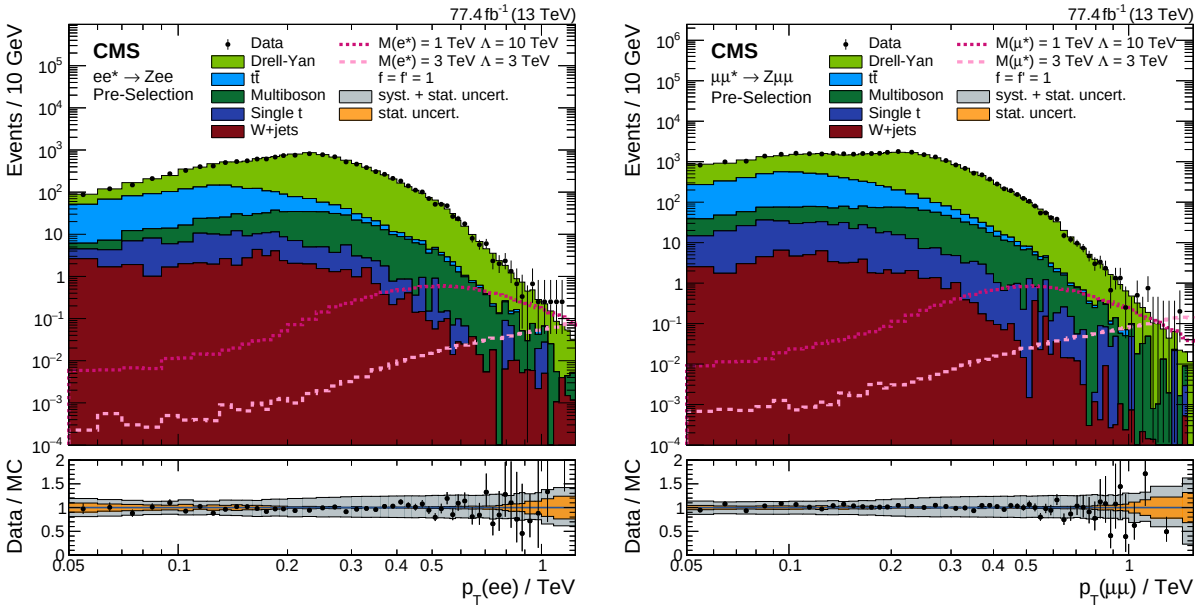

(a) (b)

Figure 7.22: Transverse momentum spectrum of the di-lepton system. (a) shows the electron and (b) the muon channel. Both spectra peak at 200 GeV to balance the associated fat jet. The signal generally favors larger values than the SM background.

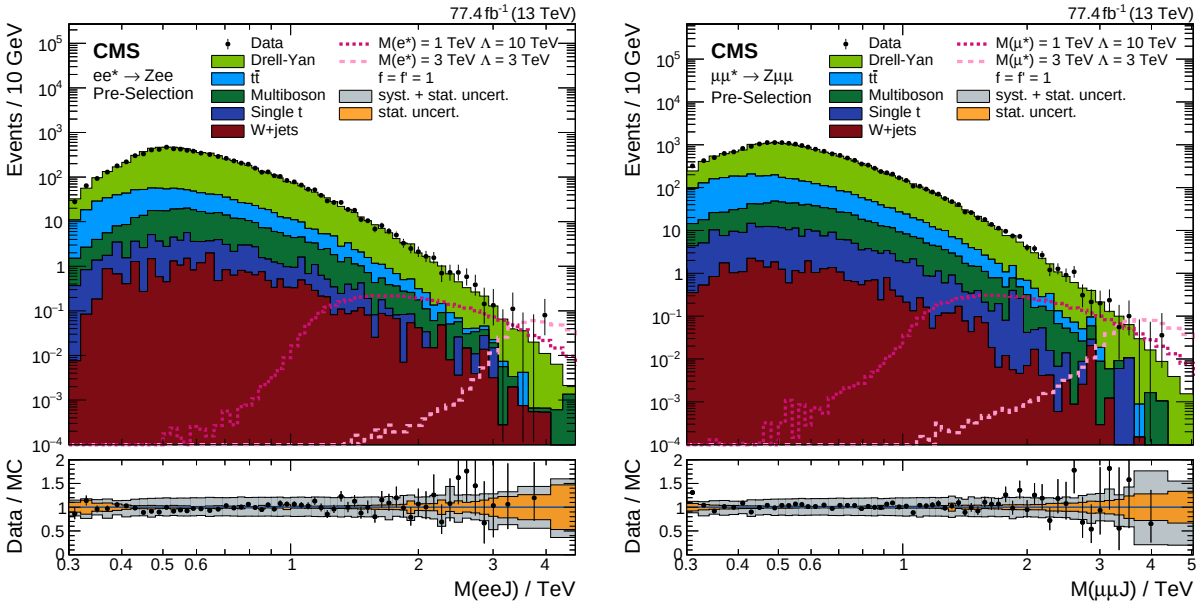

(a) (b)

Figure 7.23: Invariant mass spectrum of the three-body system containing both leptons and the leading fat jet. (a) shows the electron and (b) the muon channel. The two signal hypotheses do not emerge strongly from the background warranting further selection steps.

signal efficiency can be kept effectively high even for light excited leptons while suppressing the background.

The requirements are applied in three stages.[22] The first stage requires the soft-drop mass of the wide-cone jet to be between 65 and 105 GeV. The second stage demands on top of the first requirement a di-lepton mass of at least 200 GeV. The third and final stage puts a constraint of at least 400 GeV on the transverse momentum of the di-lepton system. The choice of these threshold values was driven by a compromise of background suppression and keeping enough generated events in the signal region to ensure an accurate description of the Standard Model.

Similar to the CI channel, we can utilize the kinematic requirements to define several control regions (CR). Applying three independent requirements leads to a maximum of eight independent regions. One of those is the signal region where events pass all requirements and seven unique control regions where events fail one or more requirements. Every event is only sorted into exactly one of those regions to avoid any correlations between the regions. Figure 7.24 provides a graphical representation of those regions as well as the three stages.

The previous chapter (figure 7.20) already presented the distribution of the soft-drop mass of the jet. The mass of the selected jet peaks exactly at the mass of the Z boson for the signal while the background is smoothly falling. The mass of the signal hypothesis does not influence the peak position.

Figure 7.25 shows the distribution of the di-lepton invariant mass spectrum after the application of the soft-drop mass requirement. The number of background events is already reduced compared to the distribution on the pre-selection level. The number of generated MC events in the high-mass tail starts to degrade. Therefore, the lower threshold is kept at 200 GeV.

Figure 7.26 presents the distribution of the di-lepton p_T spectrum after the application of the first two requirements. MC simulation describes the spectra still well. The uncertainties are larger compared to the pre-selection level and the event yield reduced to roughly 10 events per bin. Hence, the bin-by-bin fluctuations increase but the data are still randomly distributed around the expectation and show no systematic trend. A requirement of $p_T(\ell\ell) > 400\,\text{GeV}$ eliminates most of the SM background without removing many signal events.

Analysis exploiting sub-structure quantities of fat jets often apply a threshold on the *N-subjettiness* variable.[23] Figure 7.27 illustrates the distribution of this quantity. While displaying a different shape for signal and background, it is not powerful enough to enhance the sensitivity of this search because the other requirements already remove most background events from the signal region. Thus, this analysis uses no requirement on this variable.

In conclusion, figure 7.28 depicts the number of events of the SM background, the two signal hypotheses, and data for all stages. The background is reduced by nearly three orders of magnitude, while the signal efficiency decreases by less than a factor of two.

The next section presents the distributions in all seven control regions before section 7.2.5 reveals the signal region.

[22] The order of the stages does not matter for the final selection but eases the explanation.
[23] See section 4.4.5 for more information.

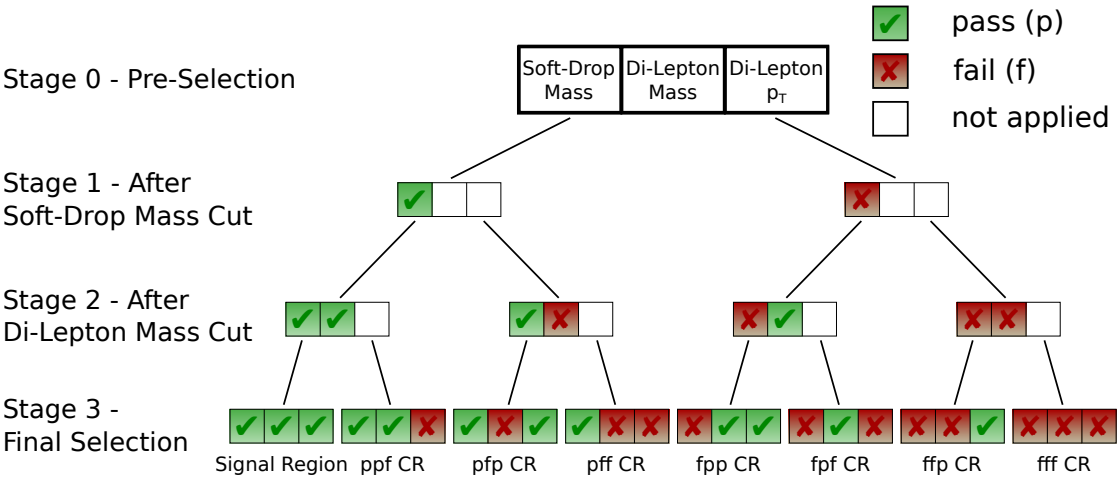

Figure 7.24: Scheme of the different stages of the kinematic selection and the naming of the control regions. Green boxes denote that the requirement is passed (p) and red boxes that it is failed (f). The left box corresponds to the first requirement – the soft-drop mass window of the wide-cone jet, the middle box to the di-lepton mass, and the right box to the di-lepton p_T requirement. The box on the lower left with the three green check marks represents the signal region, and the other seven boxes the control regions. The name (ppf, pfp, etc.) corresponds to the passed or failed selection criteria in the order of the three stages.

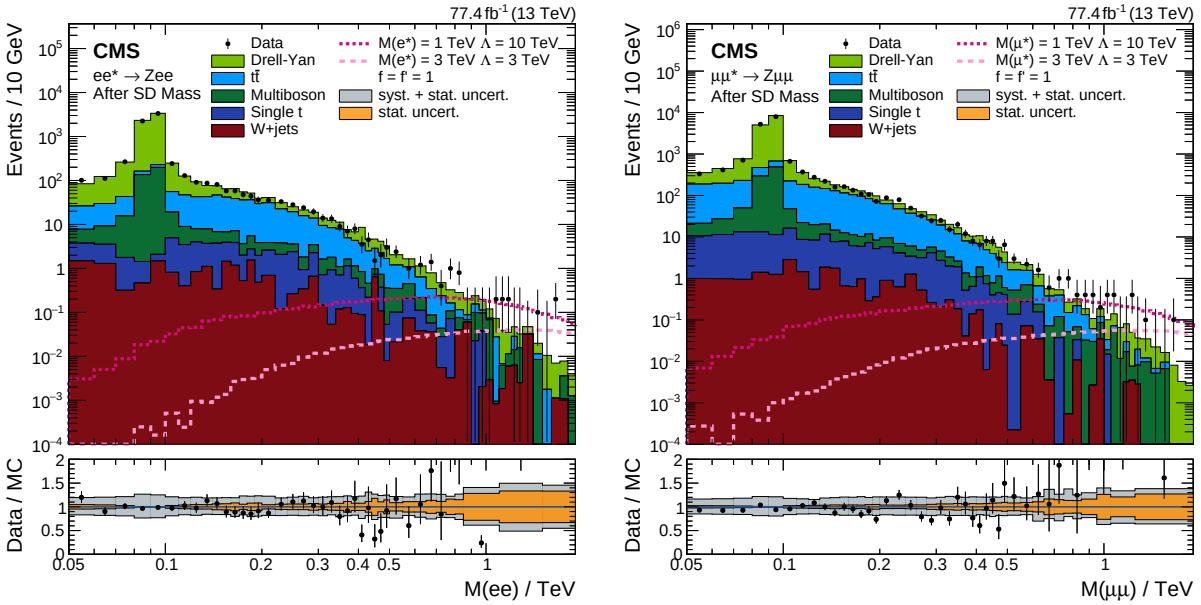

(a) **(b)**

Figure 7.25: Invariant mass spectrum of the di-lepton system after the application of the soft-drop mass window. (a) shows the electron and (b) the muon channel. The background has a sharp peak at the Z mass, while the signal is rather flat over a broad mass range. Hence, a threshold of 200 GeV can differentiate between signal and background.

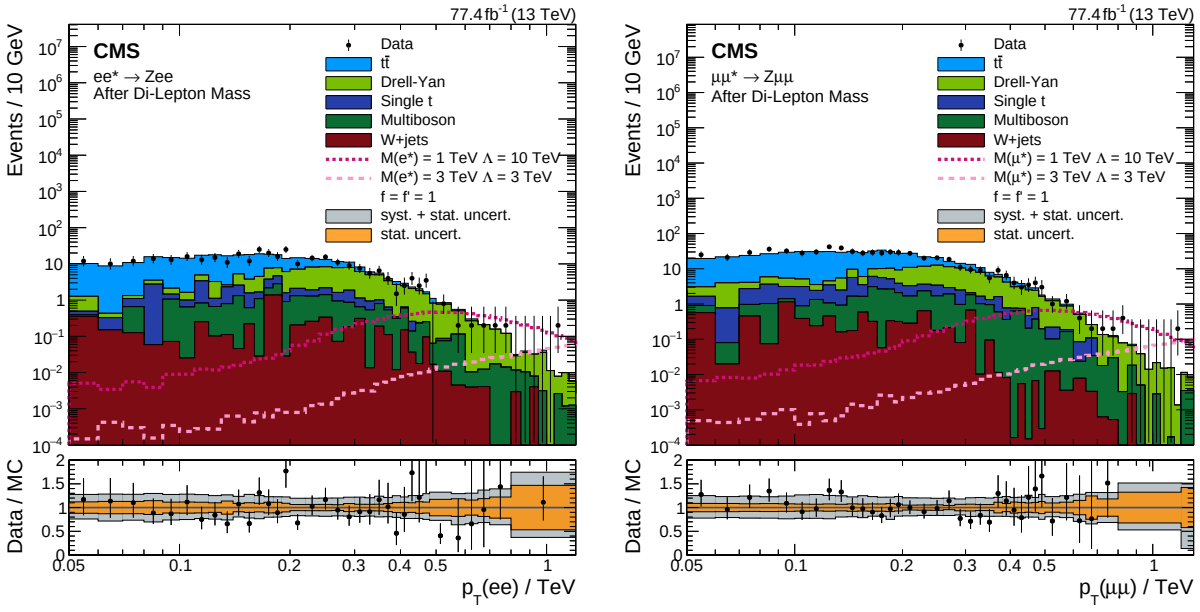

(a) (b)

Figure 7.26: Transverse momentum spectrum of the di-lepton system after the application of the soft-drop mass window and the di-lepton mass requirement. (a) shows the electron and (b) the muon channel. The p_T threshold for the signal region is set to 400 GeV.

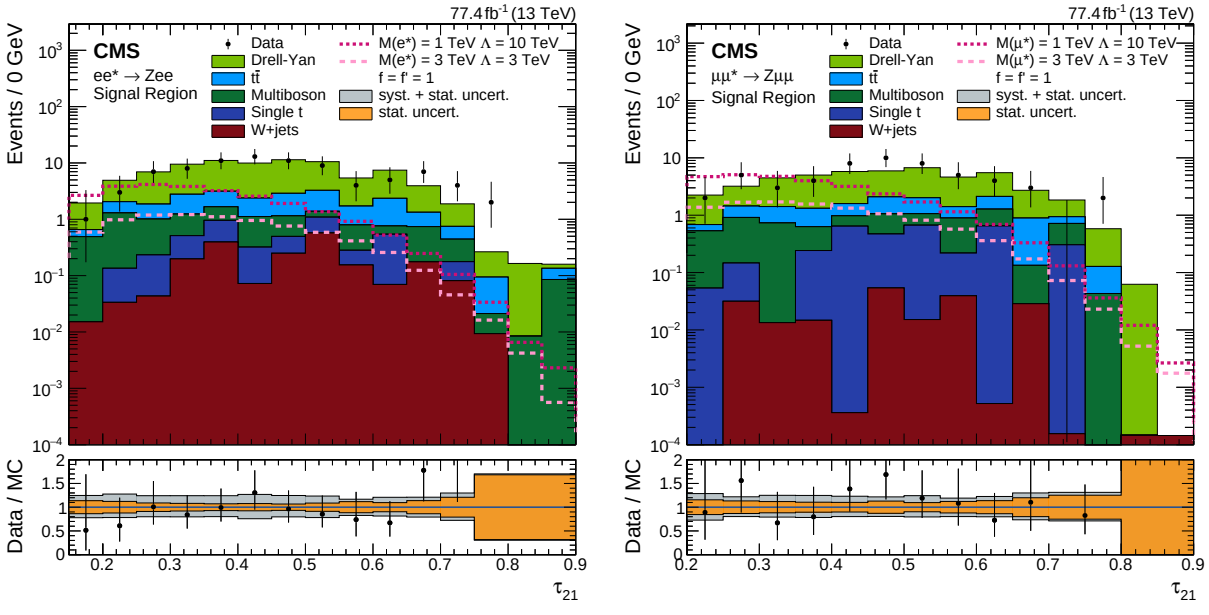

(a) (b)

Figure 7.27: *N-Subjettiness* of the selected fat jet for (a) the electron and (b) the muon channel after the full selection. The shapes for signal and background are different, but the variable is not powerful enough to enhance the sensitivity of this search. Therefore, it is not used.

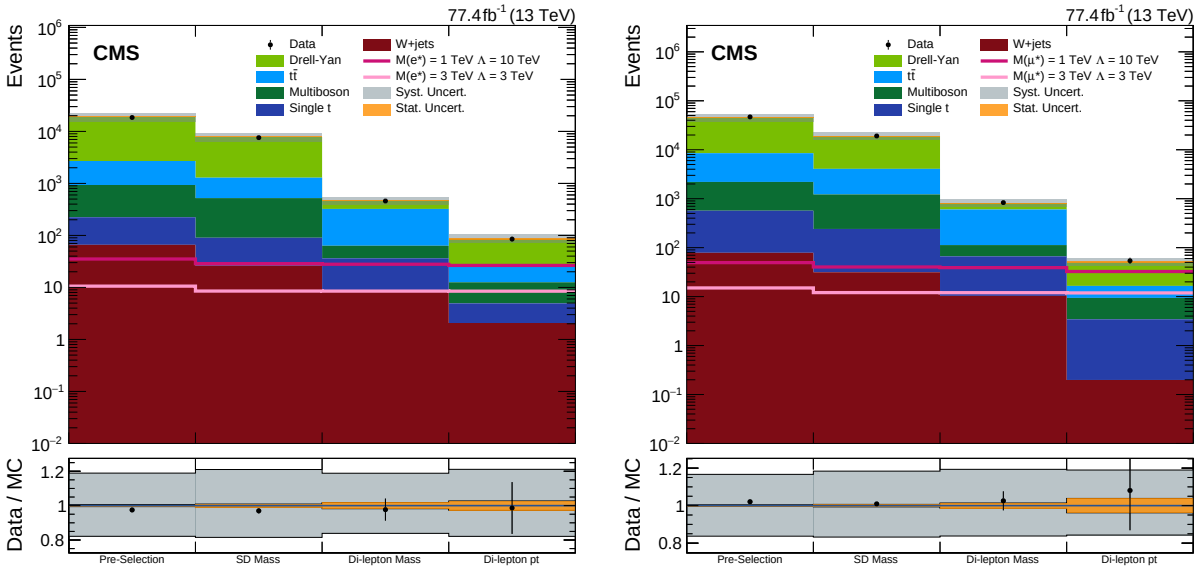

(a) (b)

Figure 7.28: Number of background, data, and expected signal events for (a) the electron and (b) the muon channel for each selection stage. The number of background events gets diminished by three orders of magnitude, while the number of signal events is not even halved.

Validation of the Background Description

The naming of the control regions (CR) is explained in figure 7.24. The first letter corresponds to the first stage, the second letter to the second stage, and the third accordingly. *f* is short for failed and *p* for passed. Hence, *fff* denotes the region where events fail all three requirements, i.e., $m_{\mathrm{SD}} < 65\,\mathrm{GeV}$ or $m_{\mathrm{SD}} > 105\,\mathrm{GeV}$, $M_{\ell\ell} < 200\,\mathrm{GeV}$, and $p_T(\ell\ell) < 400\,\mathrm{GeV}$. Events passing the soft-drop mass requirement and the di-lepton p_T but not the di-lepton mass requirement are sorted into the *pfp* CR. *ppp* denotes the signal region.

Figure 7.29 shows the three-body mass spectra of the control regions for the electron channel and figure 7.30 the ones of the muon channel. The MC simulation is normalized to the luminosity. The Drell-Yan process dominates most control regions, except the *fpf* and *ppf* regions. They can be used to validate the $\mathrm{t\bar{t}}$ description as Drell-Yan is sub-dominant here. In the electron channel, the data agree to the expectation in most regions within the expected uncertainties and show no systematic trend. Regions *fff* and *fpp* have a 30% deficit at high masses while region *ppf* shows an excess. In the muon channel all distributions agree within their uncertainties, except region *fpp*, which has a small event yield and no systematic trend.

The control regions do not just verify a proper description of the Standard Model background. They are also used in the statistical analysis by simultaneously fitting them together with the signal region to constrain the systematic uncertainties and recover lost signal efficiency as for the CI channel.

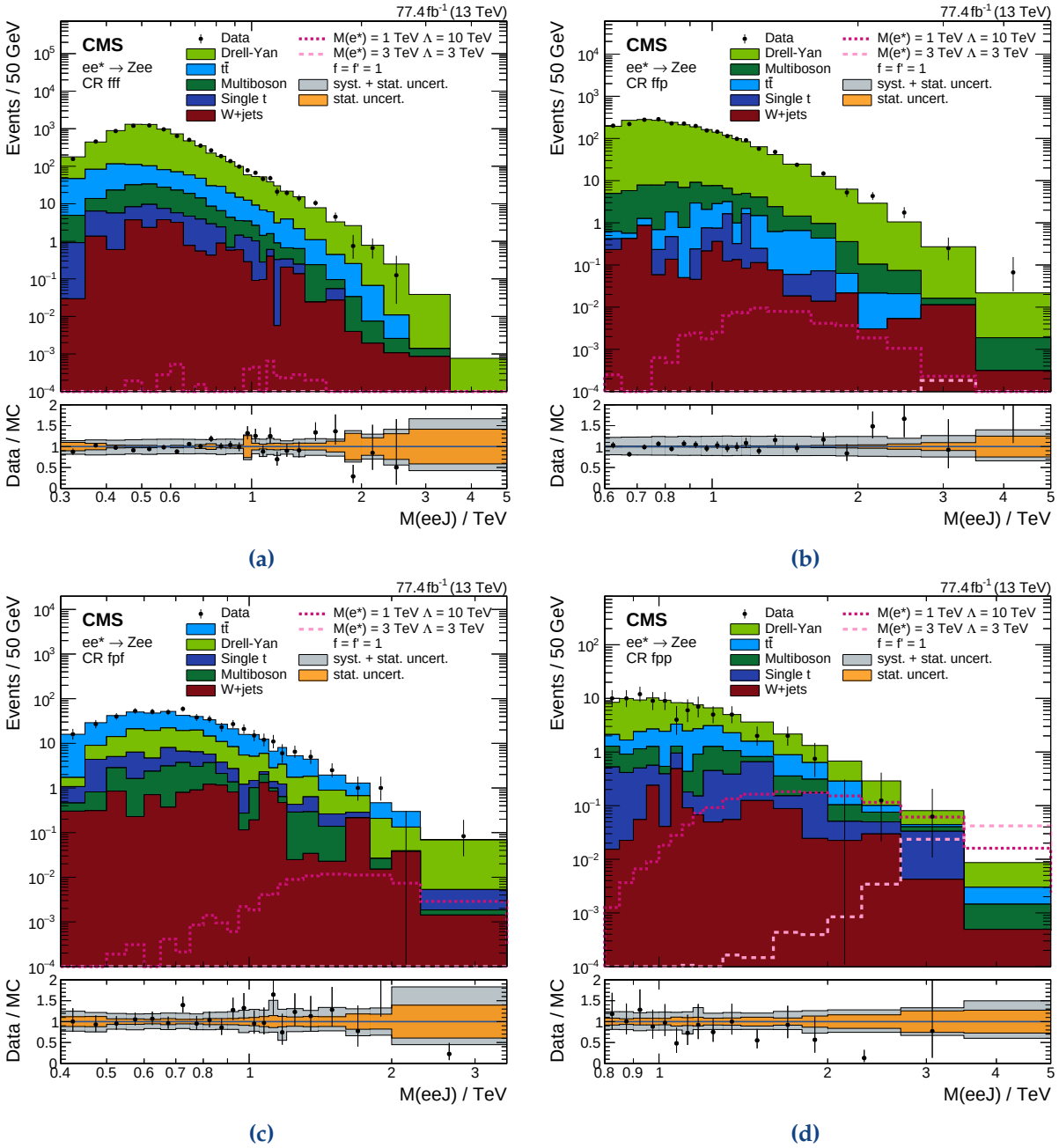

Figure 7.29: Three-body mass spectra of all control regions of the electron channel. The naming scheme is explained in figure 7.24. Continued on next page.

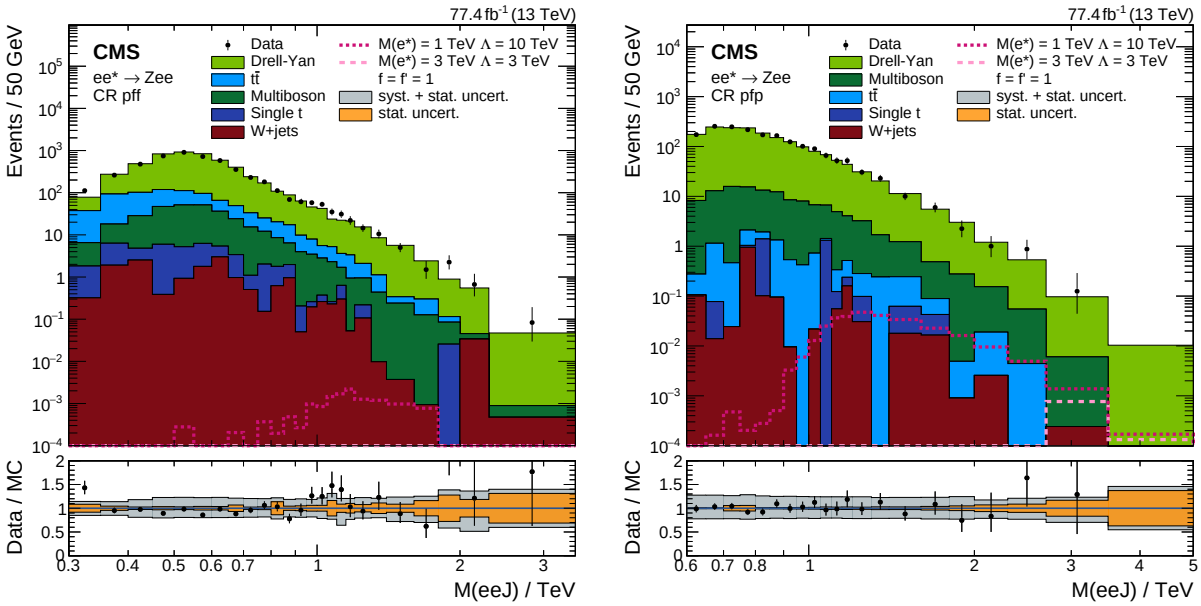

(e) (f)

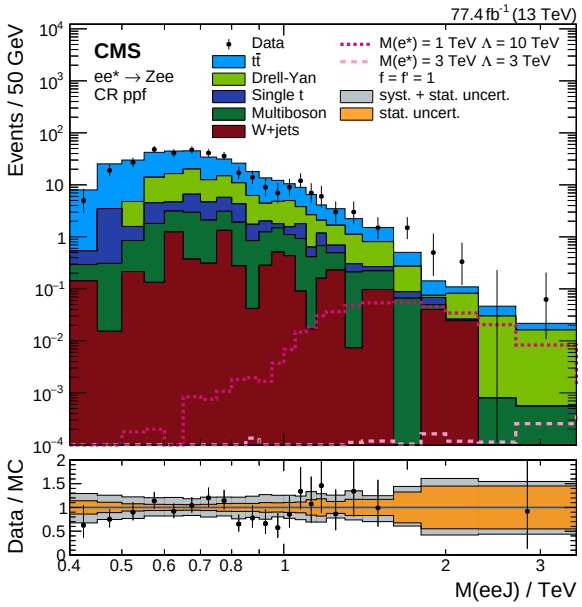

(g)

Figure 7.29 (cont.): Three-body mass spectra of all control regions of the electron channel. The naming scheme is explained in figure 7.24.

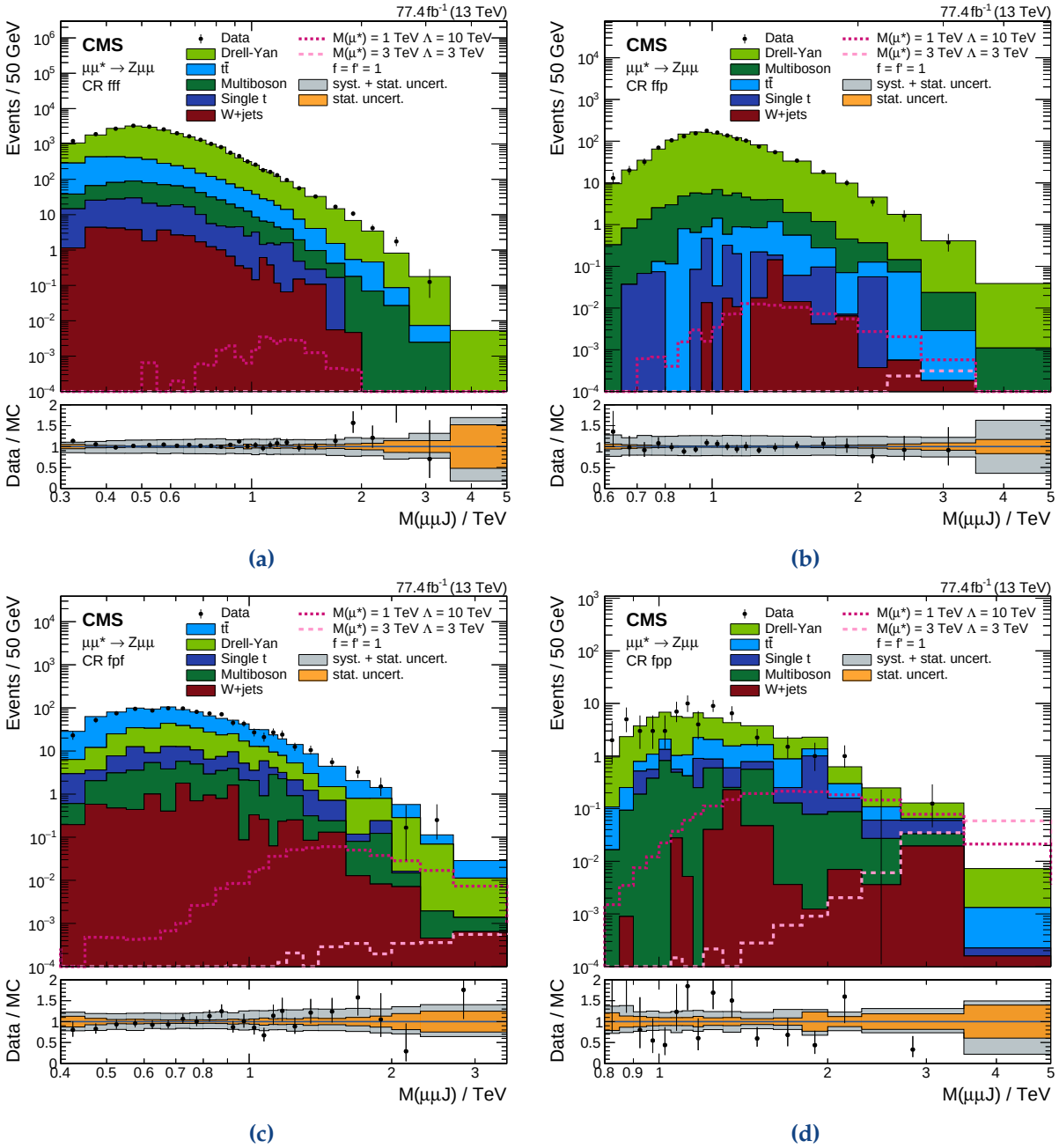

Figure 7.30: Three-body mass spectra of all control regions of the electron channel. The naming scheme is explained in figure 7.24. Continued on next page.

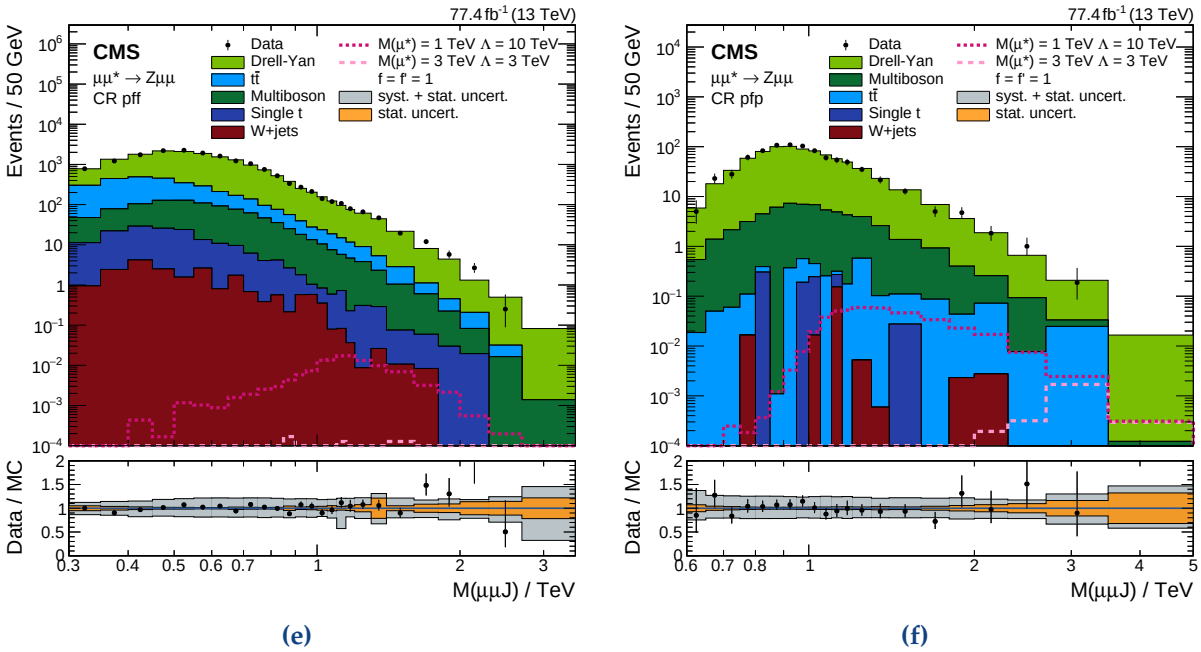

(e) (f)

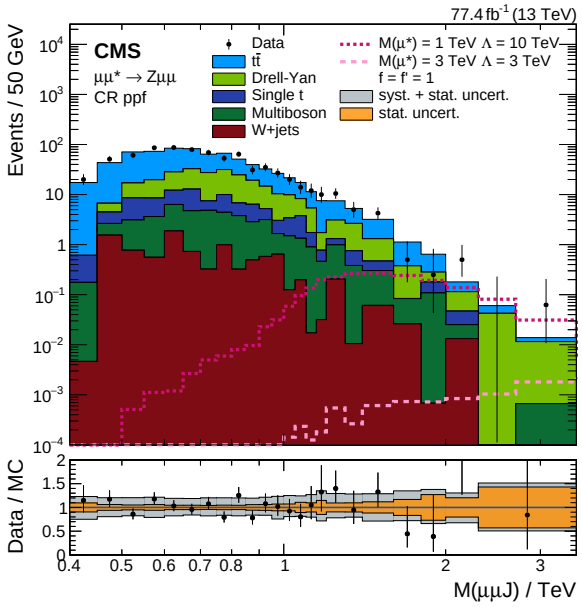

(g)

Figure 7.30 (cont.): Three-body mass spectra of all control regions of the muon channel. The naming scheme is explained in figure 7.24.

7.2.5 Final Distribution

The discussion about the choice of the final distribution follows the same arguments as in the CI channel. We cannot reconstruct the excited lepton because we do not know which lepton originates from the excited lepton decay. Hence, we have the choice between the same combinations as in the CI channel: The minimal mass, using the lepton, which gives the smallest reconstructed $\ell^\star$ mass when paired with the wide-cone jet, the maximal mass, and the three-body mass of both leptons and the jet.[24] Figure 7.31 shows the distributions for the muon channel. The electron channel behaves analogously. The minimal mass exhibits a narrow peak at the respective signal hypotheses. However, the background description has large statistical uncertainties, even with the wide binning chosen for this distribution. The maximal mass displays an expected excess in the last bin for both signal hypotheses and has lower statistical uncertainties. The three-body mass has even lower statistical uncertainties as figure 7.32 displays for both channels. The larger number of simulated events in the tail of the distribution allows using a finer binning at lower masses. The signal would manifest itself by excesses in the last bins, but also at lower masses above the SM background. Therefore three-body mass distribution is chosen as input for the statistical analysis.

Figure 7.33 depicts the relative contribution of the systematic uncertainties to the total uncertainty. The total uncertainty is smaller than in the CI channel as the high energy tail is contained in a single large bin. This does not affect the sensitivity of the analysis negatively since the strength of the Z channel is the low-mass region.

We do not observe a significant excess over the Standard Model expectation. The highest mass events of the electron and muon channel have an invariant mass of 2.1 and 4.3 TeV, respectively. Figure 7.34 displays the reconstructed objects of the events inside the detector. The electron channel event has one electron with a transverse momentum of 700 GeV and another one with 200 GeV in the forward direction. The jet recoils against the di-electron system on the lower right side. The muon channel event has a much higher mass despite all objects being in the 300 to 400 GeV p_T range. The mass of the three-body system is still substantial since all three objects are located in the forward region. The di-muon system is strongly boosted to the right with the jet recoiling against this system on the left. The event contains another jet on the upper left side, which is softer than the selected jet and, therefore, not considered for the calculation of kinematic properties.

7.2.6 Signal Efficiency

Figure 7.35 presents the selection efficiency of the signal for the different selection stages. The pre-selection efficiency is stable above 1.5 TeV and does not, contrary to the CI channel, decline to high masses because signal hypotheses are only tested up to 5 TeV and not 7 TeV due to the smaller sensitivity for heavy excited leptons. The off-shell production comes only into play at very high masses, which are not tested here.

The first selection step – the soft-drop mass window on the fat-jet – shows the most significant efficiency drop of approximately 10%. The efficiency declines by about 2% towards the highest

[24] In principle, two-dimensional distributions would combine the benefits of the different mass calculations. However, the MC statistics is not sufficient for this approach.

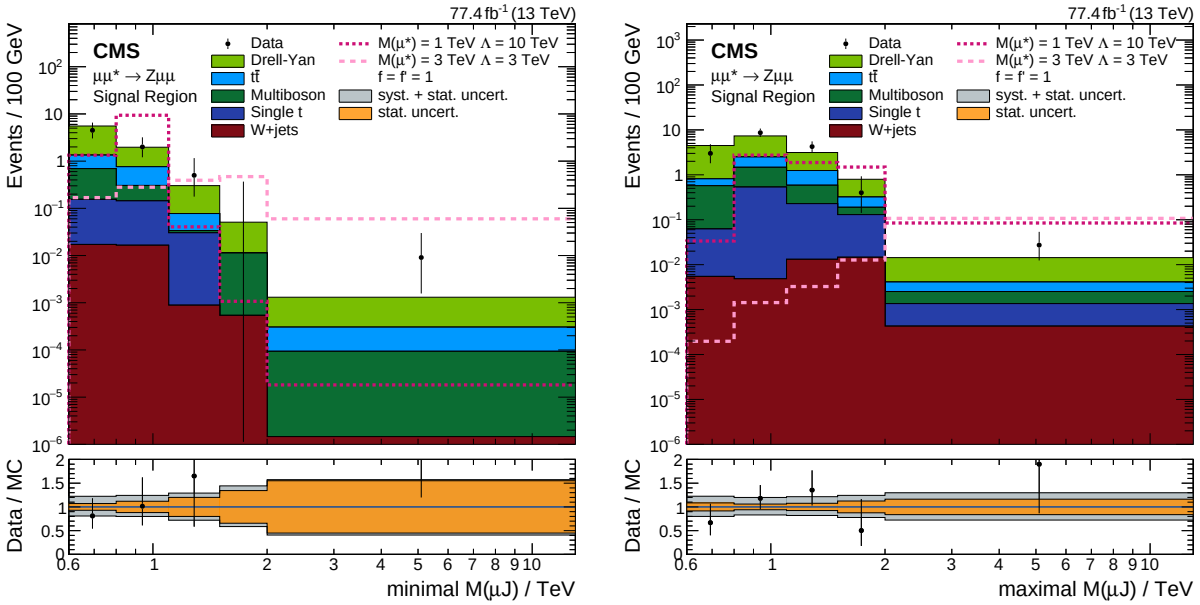

(a) (b)

Figure 7.31: Invariant mass spectrum of the two-body system containing the leading fat jet and one lepton in the signal region of the muon channel. (a) shows the selection of the lepton, which minimizes the mass and (b) of the one, which maximizes it. Both distributions are not ideal to differentiate between signal and background.

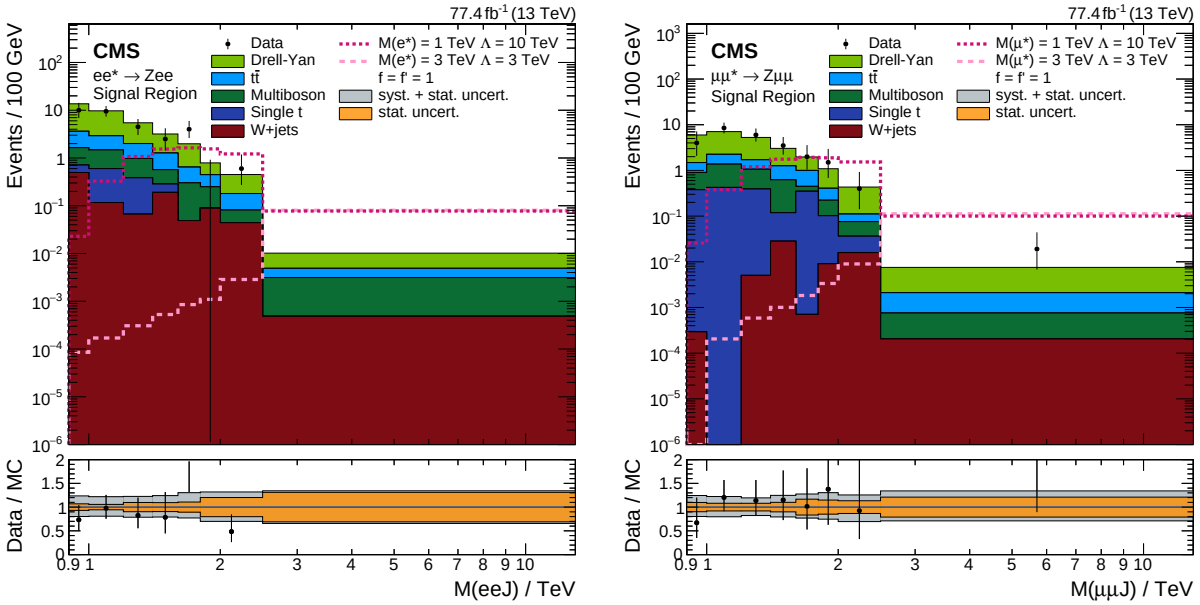

(a) (b)

Figure 7.32: Invariant mass spectrum of the three-body system containing both leptons and the leading fat jet in the signal region. (a) shows the electron channel and (b) the muon channel. The lines represent two signal hypothesis of a 1 and 3 TeV excited lepton. The cross section corresponds to values of $f = f' = 1$ for both hypotheses and $\Lambda = 10$ and 3 TeV for the electron and muon channel respectively. No significant excess of data over the expected background is observed.

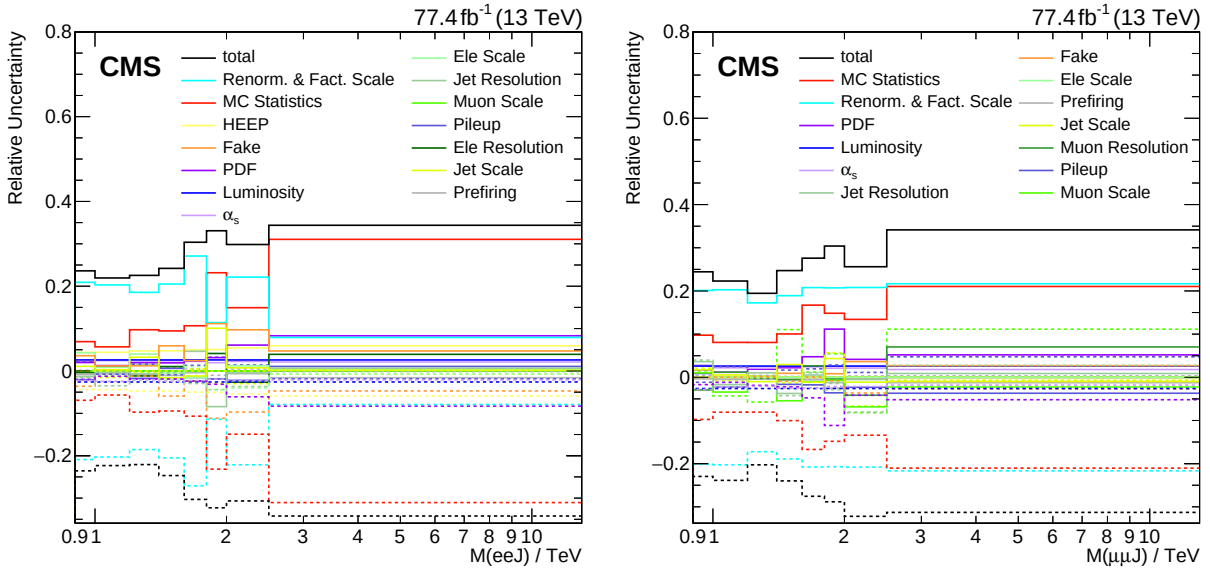

(a) (b)

Figure 7.33: Relative contribution of the uncertainties to the total systematic uncertainty of the background expectation in the signal region. (a) shows the electron channel and (b) the muon channel. The dominant uncertainties are the statistical MC uncertainty, the renormalization and factorization scale uncertainty, the PDF uncertainty, and the muon energy scale uncertainty in the muon channel.

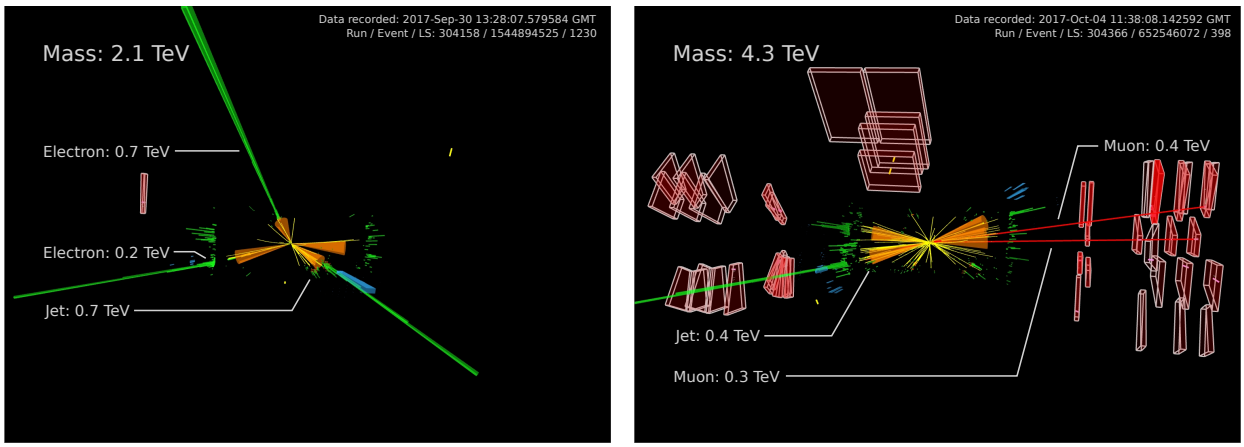

(a) (b)

Figure 7.34: Event displays of the highest mass event in the signal region of (a) the electron and (b) the muon channel. Green bars visualize energy deposits in the ECAL, blue bars deposits in the HCAL, and white bars in the forward region correspond to measurements of the HF. The length of the bar corresponds to the measured energy. The yellow lines represent reconstructed tracks above 2 GeV, and red lines depict reconstructed global muons. The muon chambers which are hit by reconstructed muons are highlighted. The orange cones indicate jets. The beam axis is in the horizontal plain in the middle of the figure. The mass corresponds to the three-body invariant mass of both leptons and the leading wide-cone jet and the value provided for each particle to its p_T.

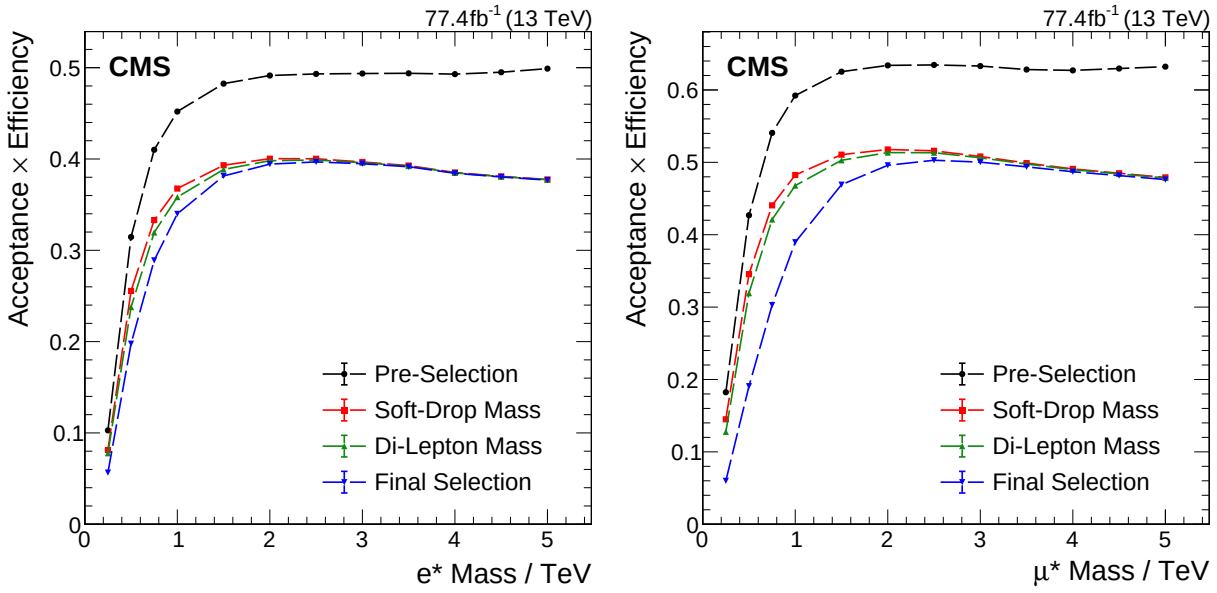

(a) (b)

Figure 7.35: Signal efficiency for (a) the electron channel and (b) the muon channel. The black curve corresponds to the pre-selection, the red curve to the soft-drop mass selection, the green to the di-lepton mass, and the blue to the final selection. The efficiency becomes stable above 1.5 TeV at 40% and 50% for the electron and muon channels, respectively.

masses. This decline indicates that the soft-drop algorithm performs slightly worse for high energetic jets. However, with a variance of only 2%, it is still remarkably stable over a broad energy range.

The di-lepton mass requirement costs nearly no signal efficiency since the threshold value is chosen relatively low in this analysis.

Finally, the di-lepton transverse momentum selection reduces the signal efficiency between 5 and 10% for light excited leptons. Massive excited leptons are not affected since the p_T of di-lepton spectrum is shifted towards higher energies.

The signal efficiency can be compared directly to the background rejection shown in figure 7.28. The two latter selection steps depending on the di-lepton system have the most potent background rejection while also preserving a high signal efficiency. The soft-drop mass requirement rejects only smaller parts of the background while reducing the signal efficiency by 10%. However, simultaneously fitting all control regions, which includes all events which did not pass the soft-drop mass selection, recovers this lost signal efficiency. The control regions have some discrimination power as well since the other two requirements are still applied. The expected exclusion limit improves by roughly 10% compared to a fit of the signal region only. The limit of the lowest mass point improves by more than 30%.

The impact of the uncertainties on the signal efficiency is similar to the CI channel. The distribution is shown in figure 7.36. The ID efficiencies have the largest effect on the signal efficiency since they directly influence the normalization of the process.

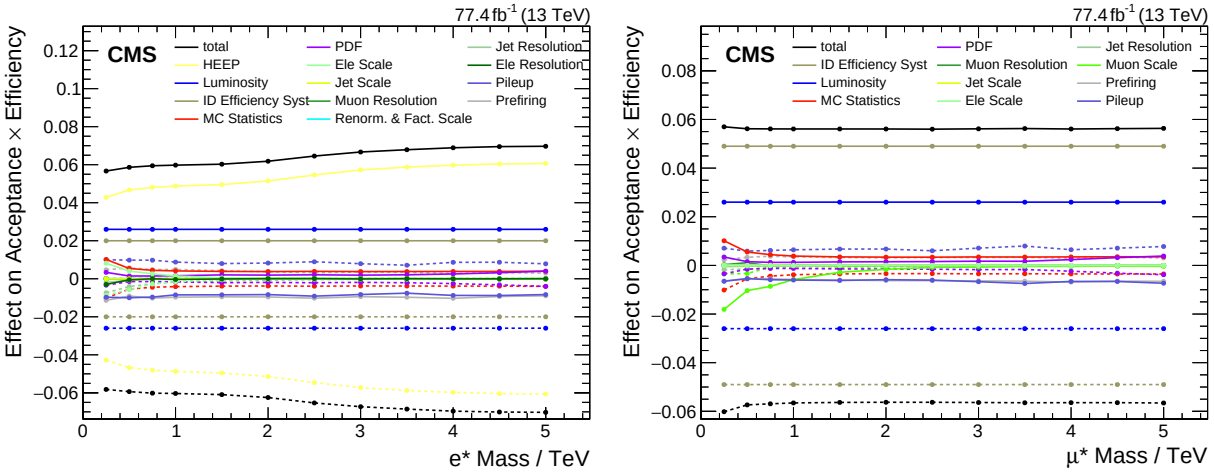

(a) (b)

Figure 7.36: Effect of the systematic uncertainties on the signal efficiency for (a) the electron channel and (b) the muon channel. The efficiency corrections have the highest impact since they directly influence the normalization of the signal. Object energy scale uncertainties, on the other hand, have a more substantial impact on the shape of the signal but a small impact on the normalization. This figure only includes the uncertainty on the acceptance of the PDF.

7.2.7 Results

Figure 7.37 presents the cross section limit for the electron and muon channel. The statistical analysis is identical to the CI channel. Both channels can exclude cross sections down to around 0.1 fb for masses above 2 TeV. The limit worsens for smaller masses because of the increased background and the smaller signal efficiency. Above 2 TeV the limit is constant as the signal efficiency is constant and most of the signal events contribute to the last bin of the distribution. The limit is slightly better for the muon channel as the signal efficiency is higher for this channel.

The observed limit is below the expected limit in the electron channel because the signal region shows a slight deficit with the exception of a single bin. Especially, the last bin has no observed event. Contrary, the muon channel has a higher observed limit due to the single event in the last bin of the signal region.

The cross section line for $\Lambda = M_{\ell^\star}$ intersects the observed limit at $M_{\ell^\star} = 3.6$ and 3.5 TeV for the electron and muon channel, respectively. The expected limit behaves vice-versa with 3.5 and 3.6 TeV, respectively. The mass limit is much smaller compared to the CI channel because the branching fraction of the Z channel is much smaller for $\Lambda = M_{\ell^\star}$. Contrary, the cross section curve for $\Lambda = 10$ TeV extends much further above the exclusion limit indicating a better sensitivity for large values of Λ.

Figure 7.38 depicts the impact of the systematic uncertainties. The findings are similar to the CI channel. The statistical Monte Carlo uncertainty on the last bin of the signal regions dominates, followed by theory uncertainties. They are calculated using a 2 TeV excited lepton mass hypothesis. Λ is equal to 10 TeV and both couplings are equal to unity. The signal strength is fixed to 0.1. The results are representative for other signal hypotheses as well.

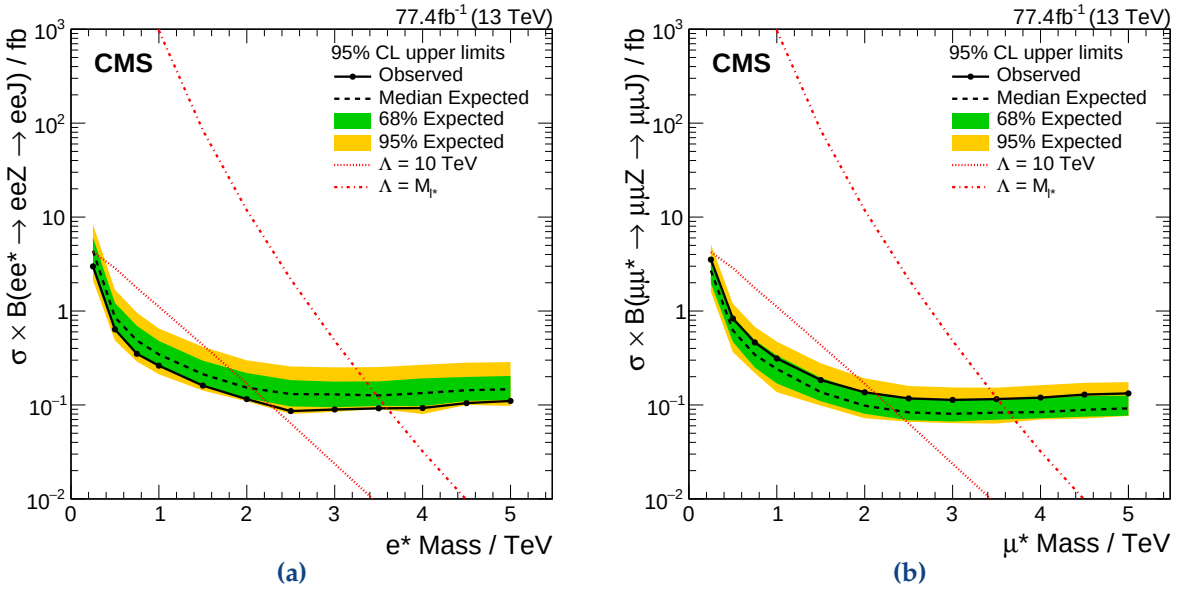

Figure 7.37: Cross section limits for (a) the electron channel and (b) the muon channel. The dashed line presents the expected limit with the $\pm 1\sigma$ band in green and the $\pm 2\sigma$ band in orange. The solid black line indicates the observed limit. It is compatible with the expected limits as no significant deviations were observed. The two red, dotted curves correspond to signal hypotheses of $\Lambda = 10\,\text{TeV}$ and $\Lambda = M_{\ell^*}$ for the lower and upper curve. Both couplings are equal to unity. The crossing point of the theory curve with the limit marks the maximal excluded signal mass. This limit is at 3.6 and 3.5 TeV for electron and muon channel, respectively.

Finally, figure 7.39 shows the result of the maximum likelihood fit. I decided to not show the pulls of the statistical uncertainties due to the enormous number of bins (more than 300) going into the fit. The *signal+background* fit uses the same signal point as described in the last paragraph. No uncertainty gets pulled by more than one standard variation. Due to the larger number of bins, the fit is able to constrain some uncertainties. The fit results for the *background-only* and the combined fit of signal and background are identical because no signs of an excited lepton signal are observed in data.

The p-values of the goodness-of-fit tests are around 0.2 and 0.4 for the electron and muon channel indicating a reasonable quality of the fit.

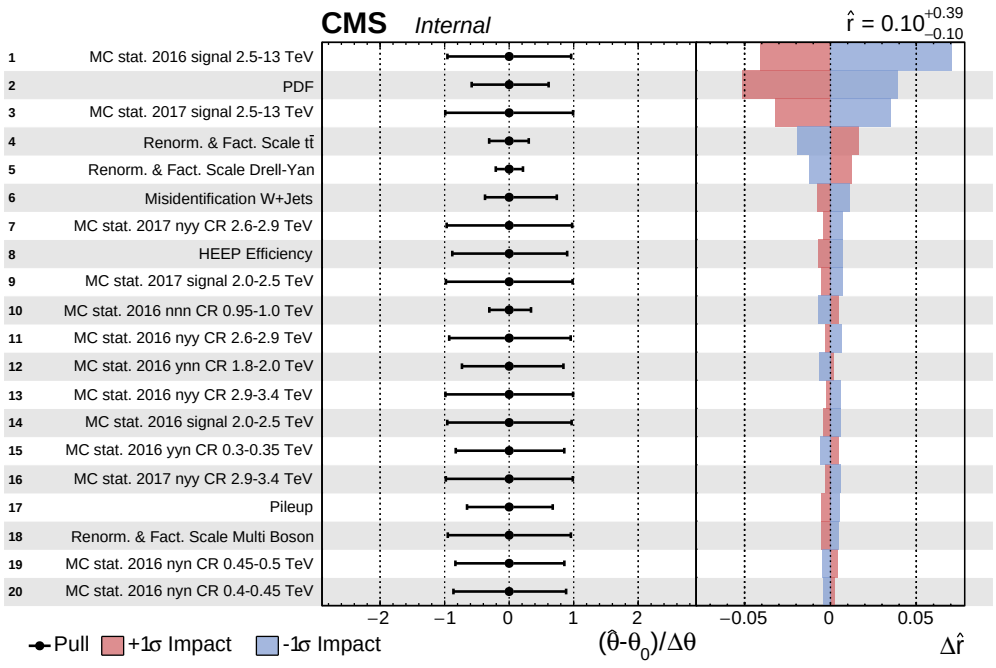

(a)

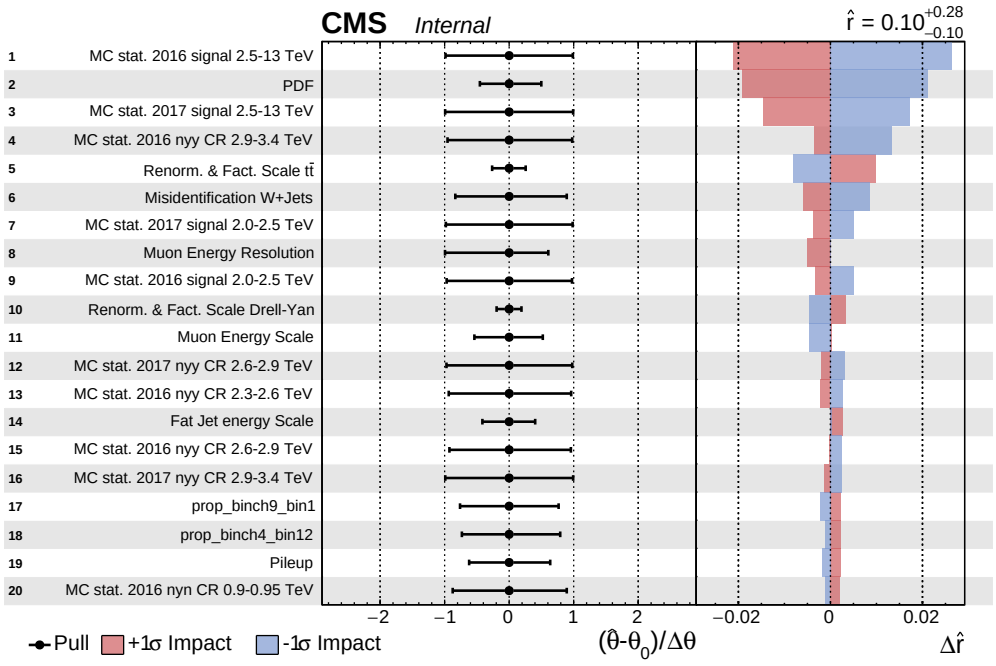

(b)

Figure 7.38: Impact of systematic uncertainties on the exclusion limit for a 2 TeV mass point for (a) the electron channel and (b) the muon channel. The cross section corresponds to model parameters $\Lambda = 10$ TeV and couplings of unity. The signal strength is fixed to 0.1. The Asimov dataset is used to calculate the impacts instead of real data. The most impactful uncertainties are the statistical MC uncertainty, and theory uncertainties.

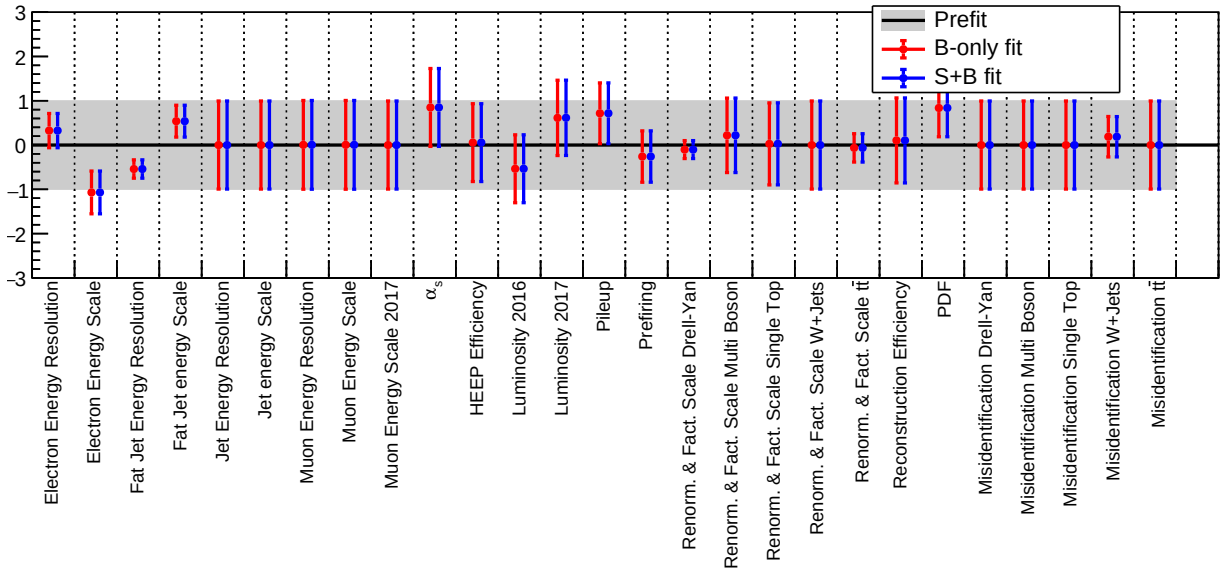

(a)

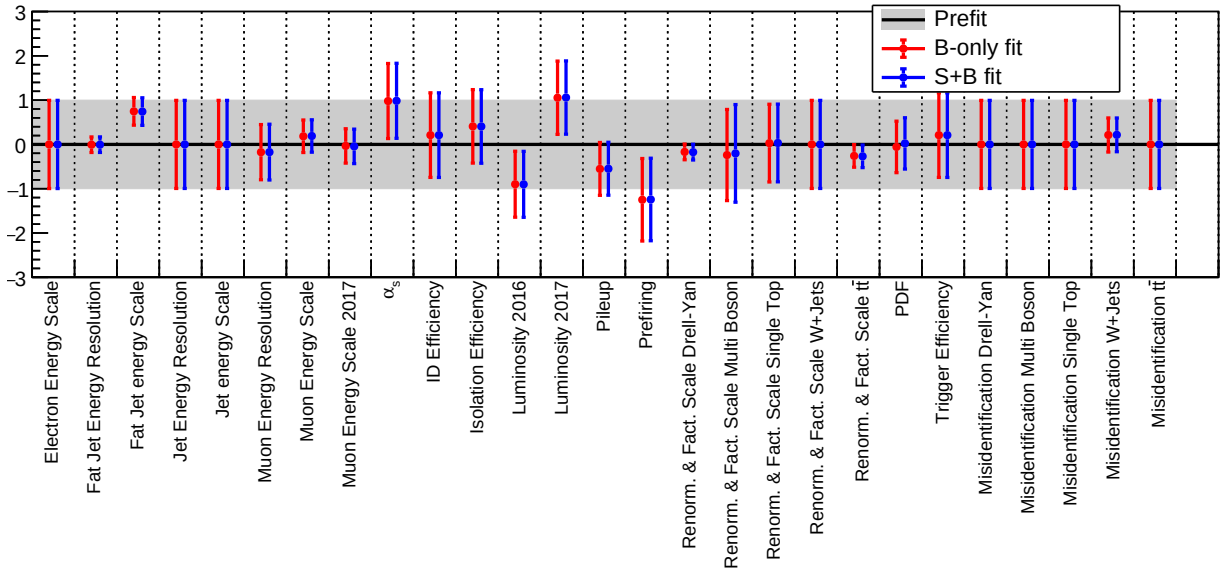

(b)

Figure 7.39: Pulls and constrained uncertainties of the fit using the actual data in (a) the electron and (b) the muon channel. The x-axis shows the shift relative to the pre-fit value. The size of the error bar corresponds to the relative constraint. A value of 1 ± 0.5 would correspond to an upshift by one sigma and a reduction by a factor of two. The red points show the combined fit of signal and background, and the blue ones the background-only fit. Both coincide well as no significant deviations were observed. This figure uses a 2 TeV signal hypothesis and does not show the pulls of the statistical uncertainties because of the large number of bins.

7.3 The W Channel

The W channel differs significantly from the two previously described channels. Its final state contains only a single charged lepton instead of a lepton pair. A neutrino and a hadronically decaying W boson accompany the lepton. Similar to the Z channel, a single wide-cone jet contains the two quarks of the W decay for sufficiently boosted W bosons.

The different final state changes the background composition significantly. Drell-Yan is no longer the dominant background process, and W+jets becomes a prompt background. Additionally, we have to consider misidentified QCD events where the reconstruction algorithms mistake a jet for a prompt lepton. The $t\bar{t}$ process gains importance as well because semi-leptonic decays can contribute directly to the final state. The semi-leptonic decays greatly enhance the number of $t\bar{t}$ events in this final state compared to the CI and Z channel.

In total, the different final state leads to an increase of more than one order of magnitude of selected SM events on pre-selection level, making the W channel the most challenging one for excited lepton searches. Therefore, this thesis does not present a complete analysis of this channel. Instead, it outlines possible background mitigation techniques but also challenges in the background description. In contrast to the other channels, this one analyses only the 2016 dataset and only the muon channel. However, kinematic requirements to suppress the SM background should behave similarly in the electron channel. The background description might become even more difficult as the misidentification rate of jets to electrons is more substantial than for muons.

The structure of this section is similar to the other channels. I will refer to the corresponding sections of the other channels whenever the selection is similar to the previously described channels.

7.3.1 Event Selection

Trigger Selection

As the final state of this analysis comprises only a single charged lepton, double-lepton triggers are not applicable for this channel. Thus, the W channel uses the same single-muon trigger as the other two channels.

This section does not discuss possible electron triggers since this thesis only presents the muon channel.

Missing Transverse Energy Filter

The same missing transverse energy filters as in the CI and Z channel are applied (c.f. section 7.1.1).

Table 7.3: Acceptance requirements for electron, muons, and jets for the W channel. The p_T requirement of the trigger is included for the leading leptons.

	Electron	Muon	Jet
p_T	> 35 GeV	> 25 GeV (leading: 53 GeV)	> 200 GeV
$\|\eta\|$	< 2.5	< 2.4	< 2.4

7.3.2 Object Selection

The selection of electrons[25] and muons is similar to the other channels (c.f. section 7.1.2). The wide-cone jet is selected similarly to the Z channel (c.f. section 7.3.2).

A new addition is the missing transverse momentum ($\boldsymbol{p}_T^{\text{miss}}$). The pre-selection puts a requirement of 50 GeV on the missing transverse momentum of the event. This threshold reduces the number of events where mismeasurements of the energy of other particles generate the $\boldsymbol{p}_T^{\text{miss}}$ and not neutrinos.[26]

Table 7.3 summarizes the acceptance requirements on η and p_T.

7.3.3 Systematic Uncertainties

The systematic uncertainties are similar to the other channels (c.f. section 7.1.5) with two exceptions. First, the misidentification uncertainty of 100% applies to QCD instead of W+jets events since this is a prompt background for this channel.

Second, an additional uncertainty arises from the usage of flavour tagging. Sections 4.4.7 and 4.5.3 describe the method in detail.

7.3.4 Analysis Specific Selection

Pre-Selection

The pre-selection requires at least one muon and one wide-cone jet passing the acceptance and identification requirements. Additionally, at least 50 GeV $\boldsymbol{p}_T^{\text{miss}}$ have to be present in the event, the event needs to be triggered, and all event filters passed.

Figures 7.40a-7.40c show the transverse momenta for all three objects. All three spectra show a clear trend of an overestimation of the background at high momenta of 10 – 20%. At low momenta, the $t\bar{t}$ process dominates; at high momenta, the W+jets background takes over. Figure 7.40d shows the soft-drop mass spectrum of the leading wide-cone jet. The signal has a visible peak around the mass of the W boson. The SM background prediction is smoothly falling. The Multi-boson, Drell-Yan, and $t\bar{t}$ processes peak at 80-90 GeV because they have either W or Z

[25] While this thesis only analysis the muon channel, it still selects electrons and leverages the number of electrons per event to suppress SM events.

[26] Every event needs to preserve a balance of transverse momenta. If the energy of one object is measured imprecisely, the reconstruction algorithm needs to add $\boldsymbol{p}_T^{\text{miss}}$ to compensate for the mismeasured momentum.

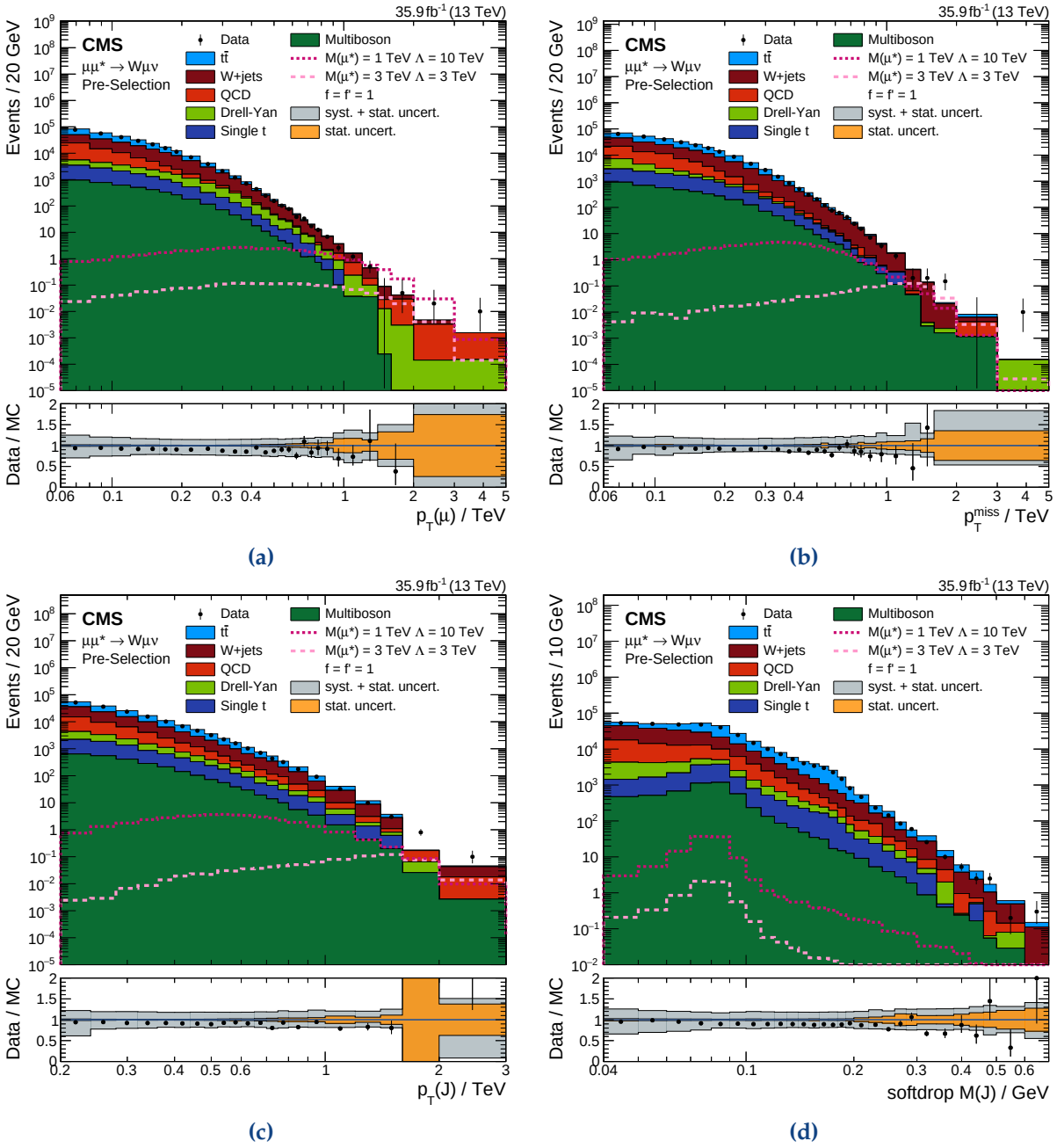

Figure 7.40: Elemental kinematic distributions on the pre-selection level. (a) shows the transverse momentum spectrum of the muon, (b) the $\boldsymbol{p}_T^{\text{miss}}$ spectrum, (c) the p_T spectrum of the leading wide-cone jet, and (d) its soft-drop mass spectrum. The colored stacked histograms visualize the background; the orange and grey bands represent the statistical and the total systematic uncertainties, respectively. The data are shown on top using black dots. The two pink lines represent two signal hypotheses. The p_T spectra for all particles are smoothly falling. The soft-drop mass spectrum is smoothly falling for the SM background, while the signal is peaking around the W mass.

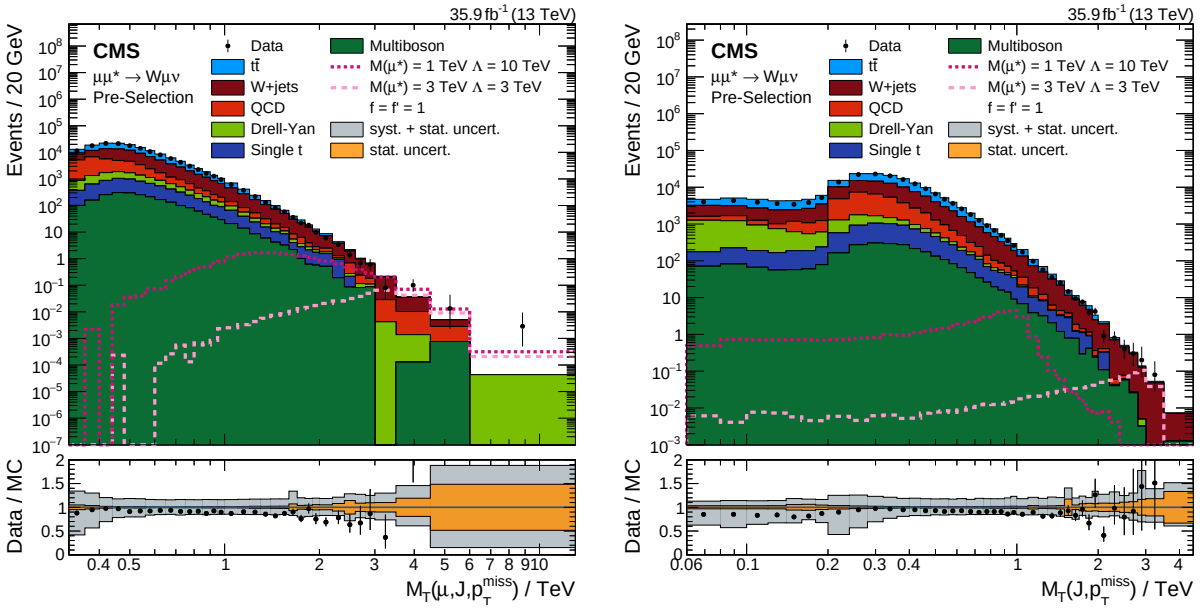

(a) (b)

Figure 7.41: Transverse mass spectrum of (a) all three objects and (b) only the leading wide-cone jet and the missing transverse momentum. The second spectrum attempts to reconstruct the excited lepton. Both signals peak at their respective mass. They have long tails to lower energies because we can only use the transverse component of the mass. In (b), the background rises towards 200 GeV because of the kinematic requirements on the objects.

bosons in their decay chain. The $t\bar{t}$ process also has a small bump around the mass of the top-quark at 173 GeV.

Figure 7.41 shows the transverse mass spectrum of all three objects on the left-hand side and the wide-cone jet and the $\boldsymbol{p}_T^{\text{miss}}$ on the right-hand side. We can only compute the transverse mass as the longitudinal component of the missing momentum is unknown. Both spectra show the same trend as the previous figures towards higher masses. The transverse mass of the wide-cone jet and the $\boldsymbol{p}_T^{\text{miss}}$ attempts to reconstruct the excited lepton. The W channel is the only channel without ambiguities in the assignment of the decay products. The spectrum of the signal rises up to their mass hypothesis and falls rapidly afterward. The background suddenly rises above ≈ 200 GeV because of the kinematic threshold of the jet. The jet and the $\boldsymbol{p}_T^{\text{miss}}$ must be collinear to produce masses below 200 GeV.

The next section will show additional kinematic distributions on both pre-selection level and after kinematic requirements.

Final Selection

The W channel has more additional selection steps than the other two channels together. I moved some distributions from the previous section into this section to have the distribution closer to the description of the requirement.

Figure 7.42: Overview over all stages of the final selection of the W channel. The order of the requirements does not influence the final result but reflects the order in which this thesis presents them.

Figure 7.42 illustrates the applied requirements. After the pre-selection, the analysis applies a total of eight additional requirements to separate the signal from the SM background.

The first requirement forbids additional leptons in the event. Figure 7.43 shows the number of muons and electrons per event. The signal favors exactly one muon and zero electrons as expected. Prohibiting additional muons suppresses mainly the Drell-Yan background, which has two prompt same-flavor leptons. Disallowing the presence of electrons in events eliminates $t\bar{t}$ events in which one W boson decays into a muon and the other into an electron. The MC simulation shows large deficits for bins with at least three leptons[27] because the background description does not include all relevant processes for these bins, e.g., multiboson processes containing three or four leptons. The missing background contributions are not an issue for the analysis since their number is minimal compared to the other bins.[28] This requirement also removes them. While being very efficient, this requirement does not remove a significant fraction of the background events.

The next requirement uses the transverse momentum spectrum of the remaining muon. Figure 7.44 shows the spectrum after the application of the first requirement. It is very similar to the p_T spectrum of the pre-selection level shown in figure 7.40a. The SM background is steeply falling while the signal disfavors low p_T muons. A requirement of at least 200 GeV removes a significant fraction of background events without strongly impacting the signal efficiency.

We can use the distribution of the $\boldsymbol{p}_T^{\text{miss}}$ to suppress the background too. Figure 7.45 presents the distribution after the first two requirements. The background is again steeply falling. The signal rises until roughly half the mass of the signal hypothesis. Requiring at least 200 GeV missing

[27] In the figure showing the number of electrons, events in the third bin (i.e., two electrons) mean that at least three leptons are present because one muon must be present to pass the pre-selection.

[28] The number of data events is four orders of magnitude below the first bin.

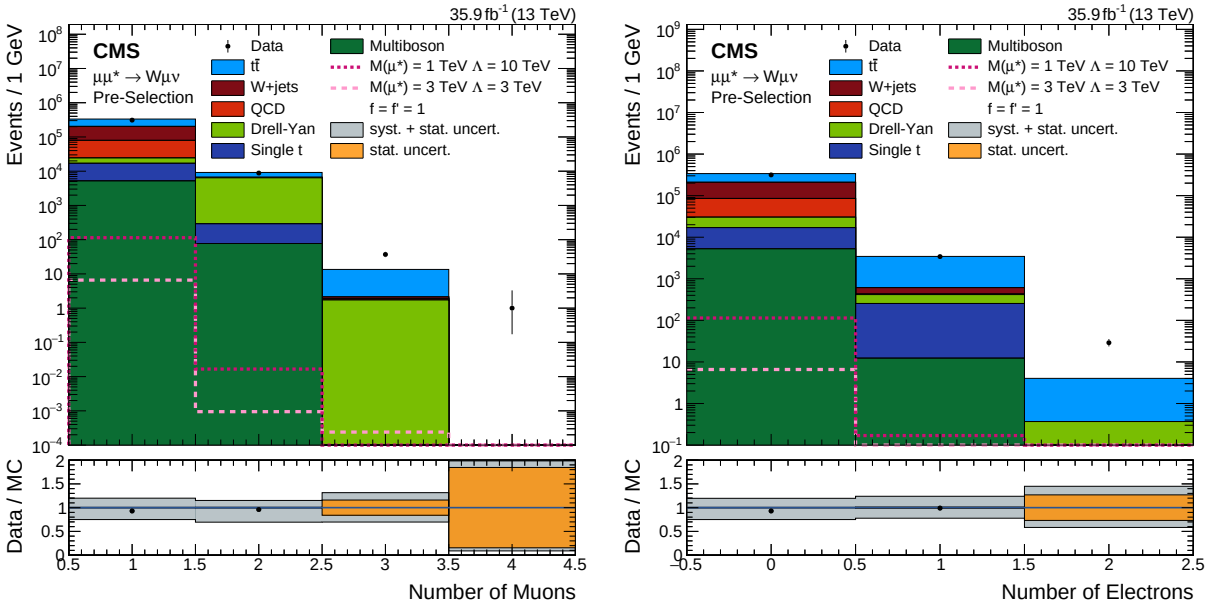

(a) (b)

Figure 7.43: Distribution of the number of (a) muons and (b) electrons per event. The signal has mostly exactly one muon and zero electrons. Removing events with more leptons eliminates most of the Drell-Yan contribution, which has two prompt leptons and some full-leptonic $t\bar{t}$ where the second lepton can have either flavor. The left-hand figure has no bin at zero because the pre-selection requires at least a single muon in the event. This analysis does not contain some background processes contributing to the three and four-lepton bins. The contributions of these bins to the total event yield are completely negligible.

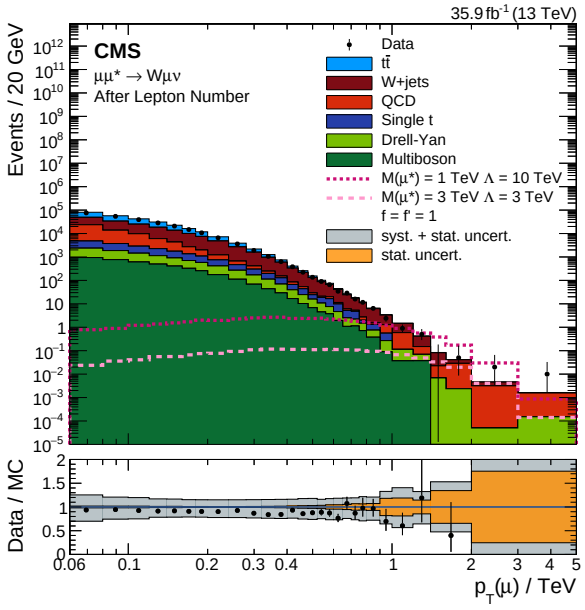

Figure 7.44: Transverse momentum of the muon after applying the requirement on the number of leptons per event. The background is smoothly falling while the signal tends to favor events with larger transverse momenta. The threshold is set to 200 GeV.

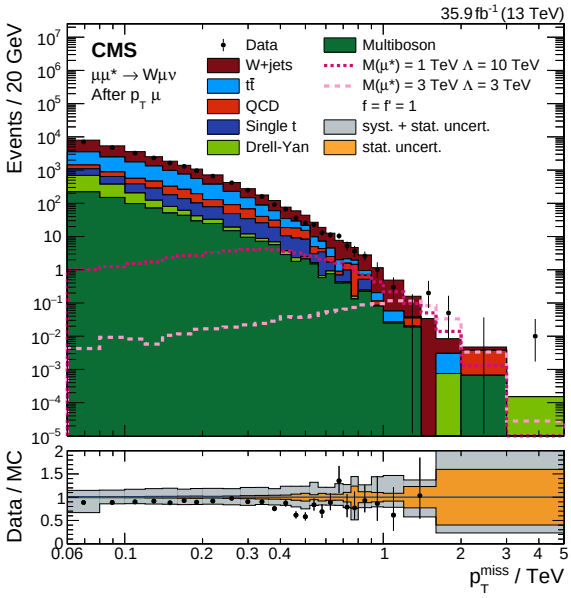

Figure 7.45: Spectrum of the missing transverse momentum after the application of the first two requirements of figure 7.42. The background is steeply falling while the signal rises until roughly half of its mass. The threshold is set to 200 GeV. Figure 7.40b presents this distribution at the pre-selection level.

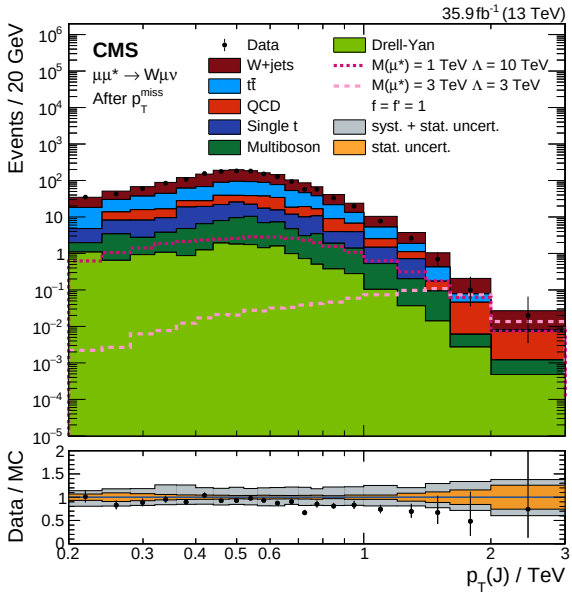

Figure 7.46: Transverse momentum spectrum of the leading wide-cone jet after the first three requirements of figure 7.42. The background rises towards 500 GeV before starting to decline. The signal has a similar shape for light excited leptons. Heavy excited leptons have a broader spectrum. The threshold is set to 400 GeV to boost the sensitivity for heavy excited leptons. Figure 7.40c shows this distribution at the pre-selection level.

transverse momentum decreases the background by another order of magnitude and removes only signal events for very light excited leptons.

The fourth requirement on the p_T spectrum of the selected wide-cone jet is less sensitive because the applied requirements already shape the spectrum as figure 7.46 illustrates. Nonetheless, a requirement of at least 400 GeV can remove some additional background events without impacting the signal efficiency for heavy excited leptons.

Following the requirements on the p_T of the objects, we can remove events containing b-jets. Figure 7.47 shows the number of b-jets per event on the pre-selection level and after applying all previous requirements. The signal does not contain b-quarks, so most of the signal contributes to the first bin. W+jets also contains mostly zero b-tagged jets. $t\bar{t}$, however, has two b-quarks in its decay chain. Therefore, a veto on any b-tagged jets removes a significant fraction of $t\bar{t}$ events.

Similar to the Z channel, we can leverage the soft-drop mass distribution of the selected wide-cone jet to differentiate between signal and background. Figure 7.48 exhibits the distribution after the application of all previous requirements. The last section (figure 7.40d) showed the distribution on the pre-selection level. The signal peaks at the W mass of 80 GeV while the background is flat up to 200 GeV and falls steadily after. Requiring the mass to be in a 20 GeV window around the W mass reduces the SM background by roughly a factor of three.

The next requirement is also related to both other channels. The CI and the Z channel put a

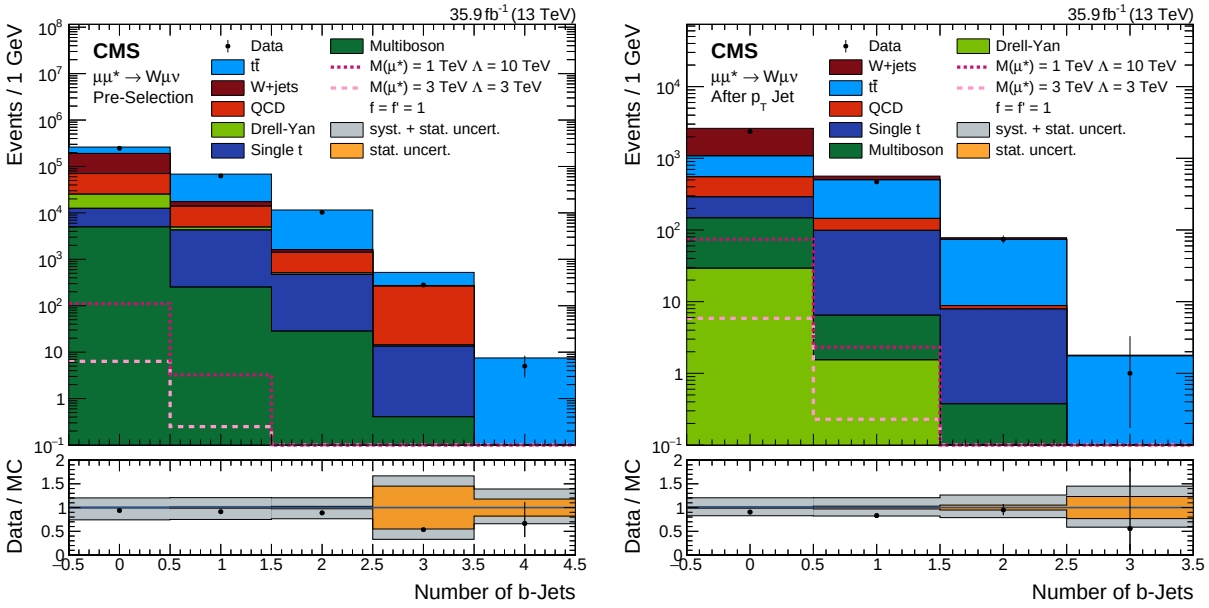

(a) (b)

Figure 7.47: Number of b-tagged jets (a) on the pre-selection level and (b) after the application of all previous requirements. The signal does not contain b-quarks since the W boson decay into b-quarks is highly suppressed. The $t\bar{t}$ background contains at least two b-jets.

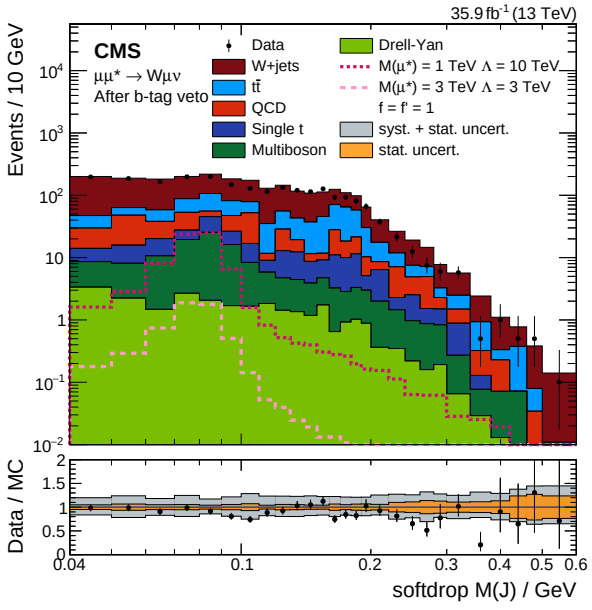

Figure 7.48: Soft-drop mass distribution of the selected wide-cone jet after applying all previous requirements. Figure 7.40d shows the spectrum on pre-selection level. The signal is peaking around 80 GeV while the background is flat. Events in a window of ±20 GeV around the mass of the W boson pass this requirement.

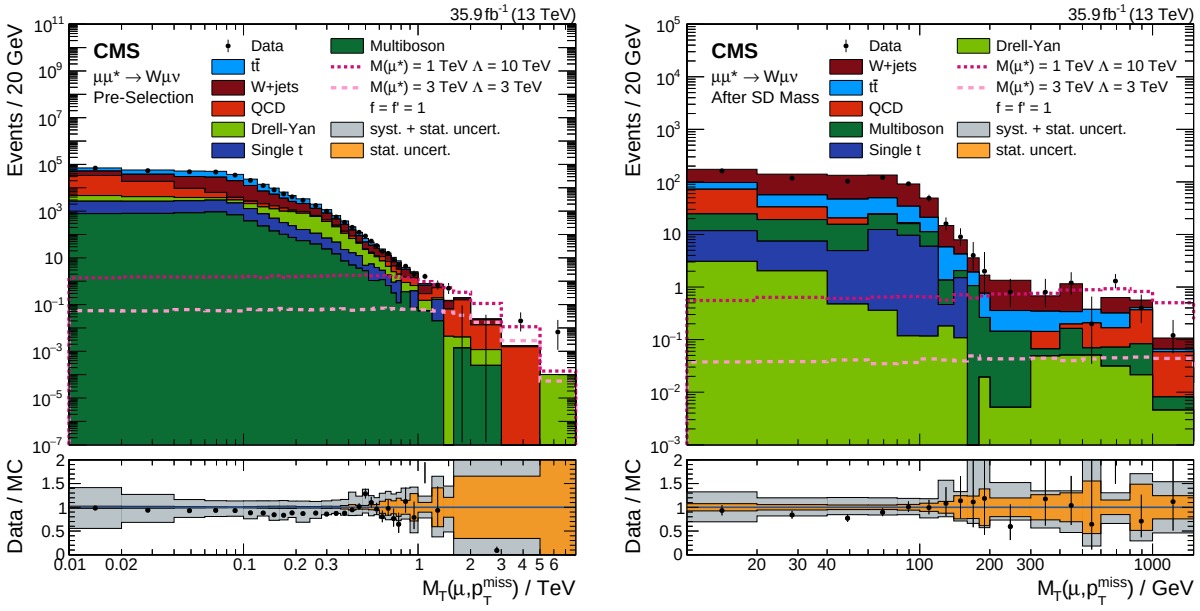

(a) (b)

Figure 7.49: Transverse mass spectrum of the muon and the p_T^{miss}. (a) shows the spectrum on the pre-selection level and (b) after the application of all previous requirements. The signal is flat over an extensive mass range while the SM background is located primarily at low masses. The threshold is placed at 250 GeV.

requirement on the di-lepton mass. This channel has only a single charged lepton, but we can substitute the second lepton with the p_T^{miss}. For the W+jets background, this quantity reconstructs the transverse mass of the W boson.[29] Figure 7.49 shows the distribution of the transverse mass of the muon and the p_T^{miss}. The signal is flat over a broad mass range while the background is primarily located at low masses. A requirement of at least 250 GeV transverse mass diminishes the background by more than one order of magnitude.

The final requirement exploits the N-subjettiness variable τ_{21}.[30] Figure 7.50 features its distribution. A clear separation between signal and background is visible in figure 7.50b. I chose an upper threshold of 0.6 to maintain a good signal efficiency.

To summarize the selection, figure 7.51 presents the event yield for data, SM prediction, and two signal hypothesis for each selection step. The SM background gets diminished by four orders of magnitude, leaving only 20 events after the final selection. The most potent requirements are the transverse mass of the lepton and the p_T^{miss}, the transverse momentum of the muon, the p_T^{miss}, and the soft-drop mass window.

The background description using pure MC simulation does not work as well as in the other channels. A clear trend is visible in many distributions. However, the agreement after the soft-drop mass window improves and is mostly within 10%. As mentioned earlier, this analysis does not aim to understand all features of this channel fully but to judge the sensitivity and possible

[29] The transverse mass will always be smaller than the invariant-mass. It also does not peak as sharp but has a longer tail towards lower masses.

[30] Section 4.4.5 contains more information about this variable.

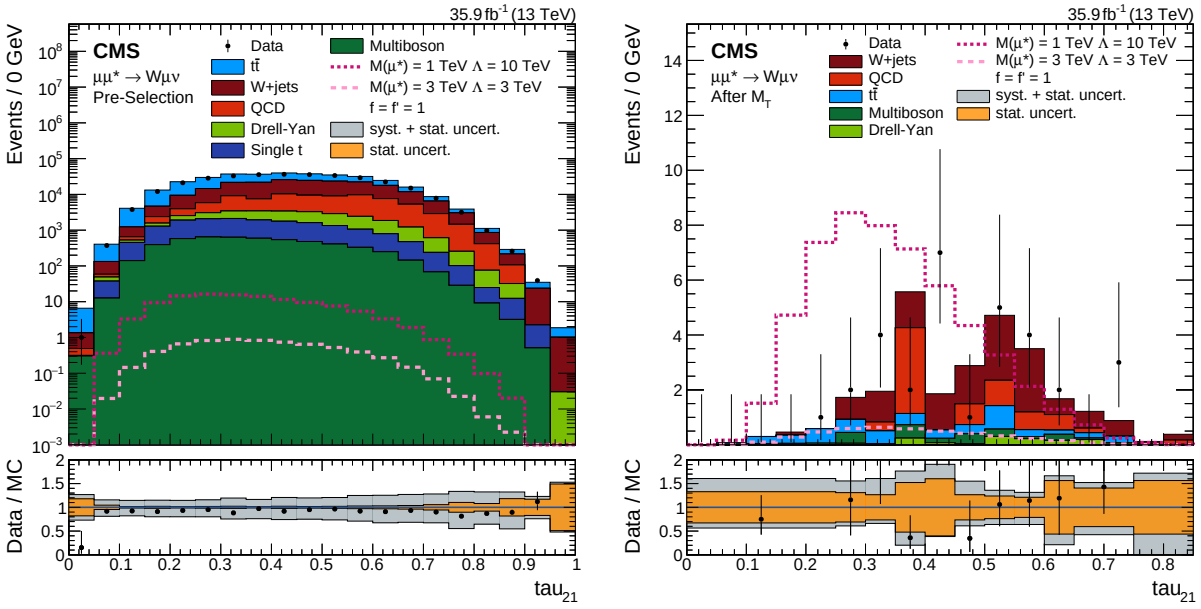

(a) (b)

Figure 7.50: Distribution of the N-subjettiness variable (a) on the pre-selection level and (b) after the application of all previous requirements. The signal prefers smaller values than the background. The threshold is set to 0.6.

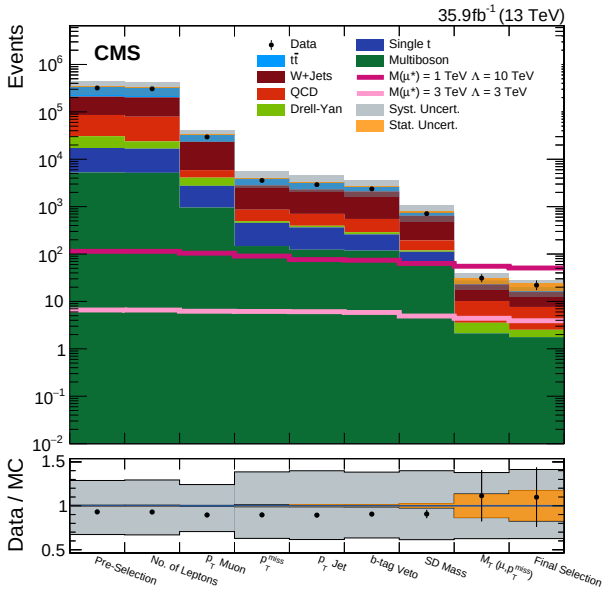

Figure 7.51: Number of background, data, and expected signal events for each selection stage. The number of background events gets diminished by four orders of magnitude.

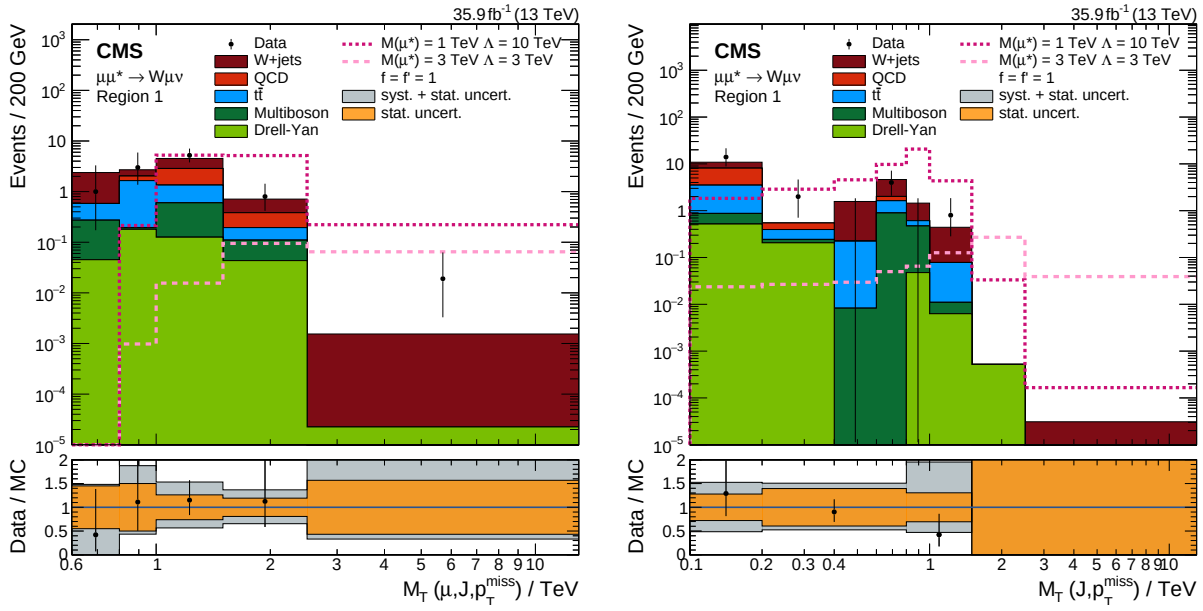

(a) (b)

Figure 7.52: Distribution of the transverse mass of (a) all three selected objects and (b) the selected wide-cone jet and the p_T^{miss} after all selection steps. The second distribution attempts to reassemble the excited lepton. Indeed, it has a clear peak at the expected value. The transverse mass distribution of all objects shifts the signal generally to higher masses into a background-free region. This shift enhances the sensitivity especially for light excited leptons.

gain by analyzing this channel. The background description is sufficiently good to achieve this goal. Therefore, this thesis continues the analysis of the W channel using the presented background description and leaves the analysis of all its features for future work.

7.3.5 Final Distribution

As for the other channels, we can choose a final distribution to differentiate between signal and background. The difference of the W channel is that there is no ambiguity about the decay products of the excited leptons. The down-side is the poor experimental mass resolution for the combination of a jet and missing transverse momentum. The second disadvantage is that we can only compute the transverse mass and not the full invariant mass. Both of these issues will lead to longer tails and broad peaks. Similar to the other channels, we can calculate the mass of all selected objects, i.e., the muon, the leading wide-cone jet, and the p_T^{miss}.

Figure 7.52 presents both distributions after applying all requirements described in the previous section. The transverse mass spectrum of the wide-cone jet and the p_T^{miss} indeed show a clear peak at the respective signal masses. However, the signal events still distribute themselves over multiple bins. The background has a peak in the first bin due to events with collinear jets and missing transverse momentum.

The transverse mass of all three bodies does not show a clear peak for the signal. Nevertheless, it shifts most of the signal prediction towards higher masses into a relatively low background

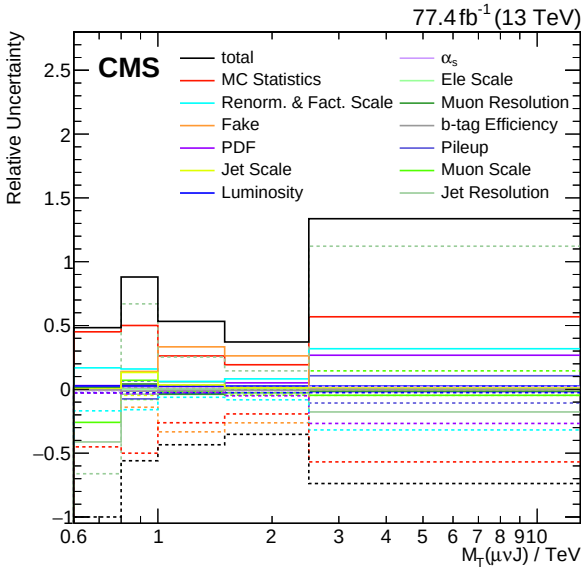

Figure 7.53: Composition of the systematic uncertainties for the final transverse mass distribution. The energy resolution uncertainty of the wide-cone jet becomes the dominant uncertainty at high masses. The statistical uncertainty reaches 50% as well.

region. Using this distribution for the statistical analysis significantly boosts the sensitivity for very light excited leptons with masses below 1 TeV by a factor three. The two-body transverse mass distribution yields maximally 10% better limits for medium-mass excited leptons, but the advantages for light excited leptons outweigh this insignificantly better limit at medium masses around 2 TeV. Combining both methods could improve the sensitivity in a future, more thorough, iteration of this analysis.

Figure 7.53 breaks down the composition of systematic uncertainties. At the highest masses, the energy resolution uncertainty of the wide-cone jet dominates. The statistical MC uncertainty reaches 50%. The misidentification uncertainty of QCD events contributes significantly to the total uncertainty as well, especially at moderate masses around 1 to 2 TeV. This substantial contribution warrants a better description of the misidentification background.

We can increase the sensitivity of the analysis by not only analyzing the distribution passing all requirements but by also taking distributions into account where single requirements were not passed. This way, we can recover signal events lost by a single requirement while the other requirements can still suppress the background. The two other channels use all possible distinct regions. With eight requirements, the number of distinct regions would reach 256. An analysis of all regions would be computationally challenging due to the number of independent bins entering the fit. Regions with next-to-none signal contributions would also only minorly improve the limit by better constraining the background. On the flip side, the regions containing a significant fraction of signal events can directly improve the limit. Therefore, I chose to simultaneously fit the ten regions with the best signal to background ratio. Table 7.4 presents these ten regions and introduces a naming scheme.

Figure 7.54 shows all nine additional region while figure 7.52b presents the region where all selection requirements are passed. The data agrees in most regions with the background

Table 7.4: Summary of the ten regions used as input to the statistical analysis.

No. Leptons	$p_T(\mu)$	$\boldsymbol{p}_T^{\text{miss}}$	$p_T(J)$	No. b-jets	SD Mass	$M_T(\mu, \boldsymbol{p}_T^{\text{miss}})$	τ_{21}	Name
✔	✔	✔	✔	✔	✔	✔	✔	Region 1
✔	✔	✔	✔	✔	✔	✔	✘	Region 2
✔	✔	✔	✔	✔	✘	✔	✔	Region 3
✔	✔	✔	✘	✔	✔	✔	✔	Region 4
✔	✔	✔	✘	✔	✔	✔	✘	Region 5
✔	✔	✔	✘	✔	✘	✔	✔	Region 6
✔	✔	✘	✔	✔	✔	✔	✔	Region 7
✔	✔	✘	✔	✔	✔	✔	✘	Region 8
✔	✔	✘	✔	✔	✔	✘	✔	Region 9
✔	✘	✔	✔	✔	✔	✔	✔	Region 10

prediction within the systematic uncertainties. Some regions show an excess in the high-mass tails where the uncertainties get close to 100% and some background processes are missing because no events were generated in the high-mass tails. The number of generated MC events in the high-mass tails is always limited, leading to very wide bins. As mentioned before, the background description of the W channel clearly leaves room for future improvement. Region 3 shows a clear excess in the last bin of the distribution with two observed events. One of those events has a transverse mass of 7.8 TeV. It features a jet with a transverse momentum of 400 GeV, a muon with $p_T = 3.7$ TeV, and 3.7 TeV missing transverse momentum as well.

A closer look at the event reveals that two reconstructed muons are very close nearby: One with a transverse momentum below 100 GeV and one with 3.7 TeV. In the original reconstruction, only the low energetic muon was present. This signature is typical for events which were misreconstructed due to the mitigation algorithms deployed to recover events suffering from the dynamic silicon strip inefficiency in 2016.[31] The missing transverse energy filters eliminate most of these events, but do not recognize this specific event. The statistical analysis does not take this event into account because we can confidently tag it as misreconstructed.

Figure 7.55 illustrates the remaining highest mass events in regions one and three. The highest mass event in the region passing all requirements is very clean with a 1.4 TeV muon in the upper half and a 1.2 TeV jet on the lower right. The missing transverse momentum barely passes the requirement of 200 GeV. The total mass adds up to 3.3 TeV.

The remaining event in the last bin of region three has a muon with a transverse momentum of 2.1 TeV in the lower half of the picture. The jet with a p_T of 600 GeV is very well aligned to the missing transverse energy of 1.8 TeV. The event features another jet in the forward direction. The mass of the three selection objects is 4.6 TeV. The first event does not raise any concerns regarding the reconstruction quality. The muon in the second event looks slightly suspicious; it has many close by tracks and scattered energy deposits in the HCAL. There are also some reconstructed segments in the DT system which do not match the track of the muon. A high-p_T muon can produce showers in the iron of the magnet return yoke, explaining the reconstructed segments. It can also leave energy deposits in the HCAL, but they would be expected to be aligned with the muon itself and not scattered around it. Therefore, this muon might be a misidentified

[31] c.f. section 3.3.3

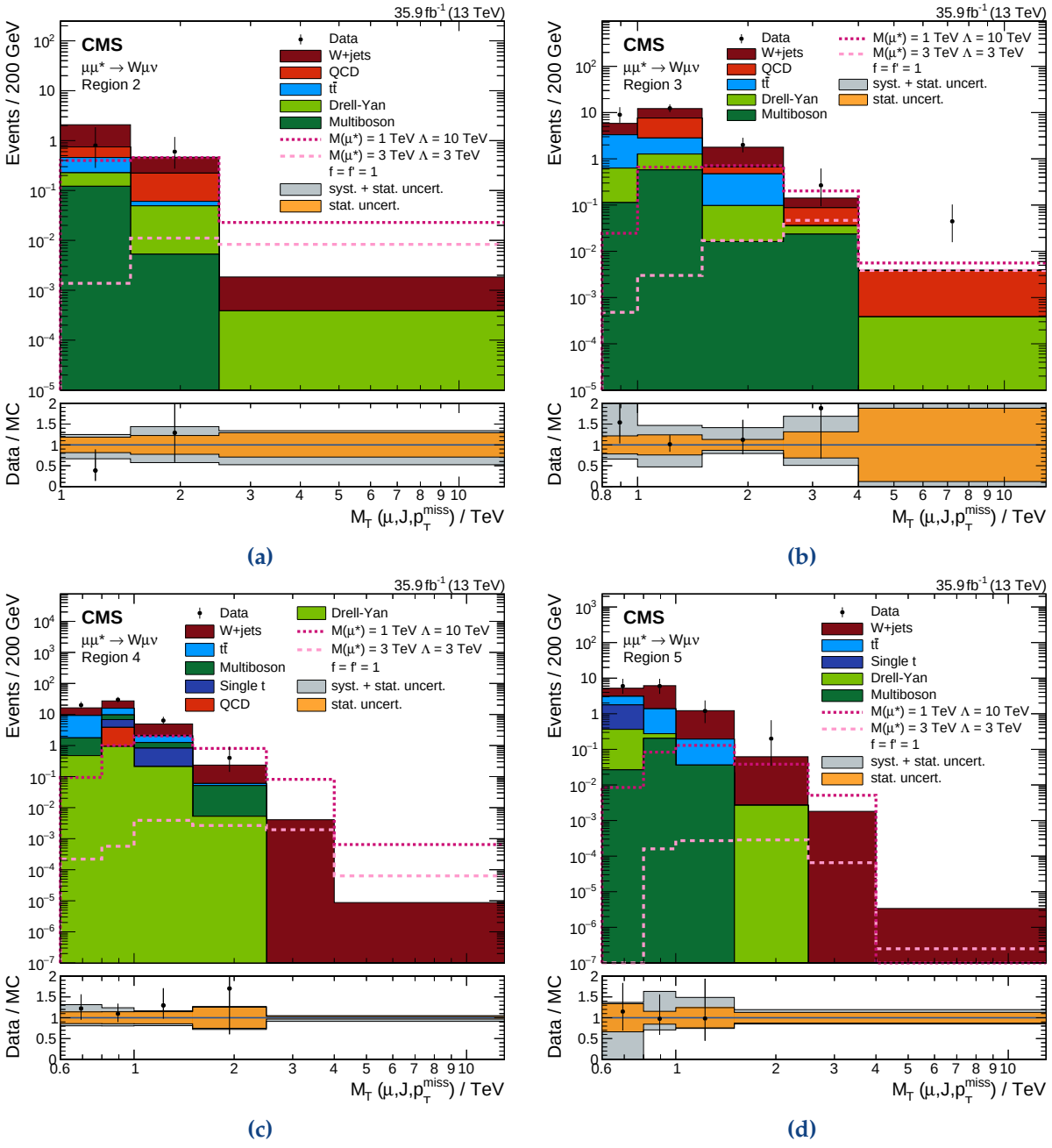

Figure 7.54: Distribution of the transverse mass of all three selected objects for the nine regions used as input for the statistical analysis in addition to the distribution where all selection requirements were passed. Table 7.4 explains the naming scheme. Continued on next page.

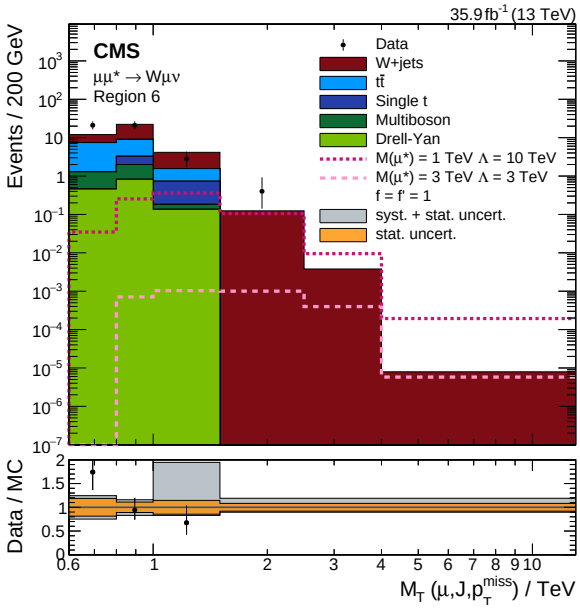

(e)

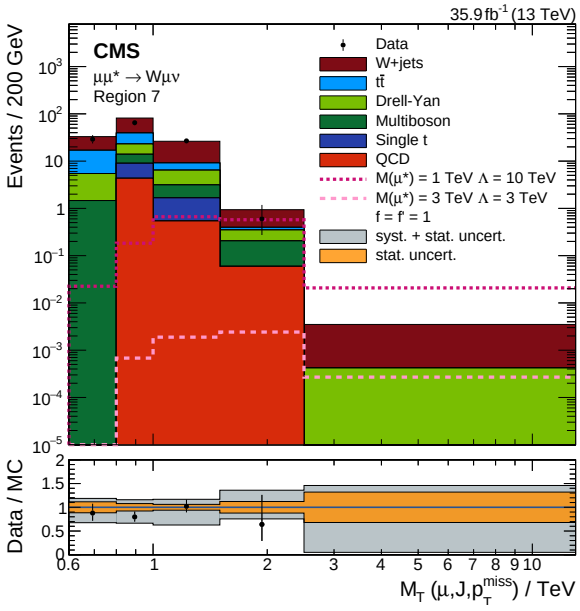

(f)

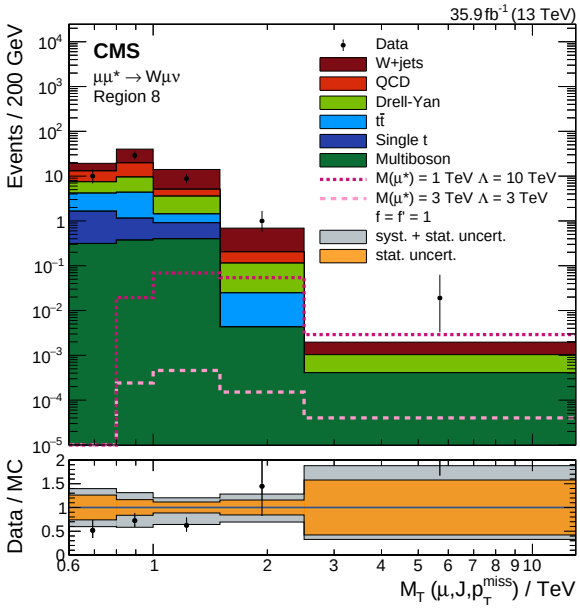

(g)

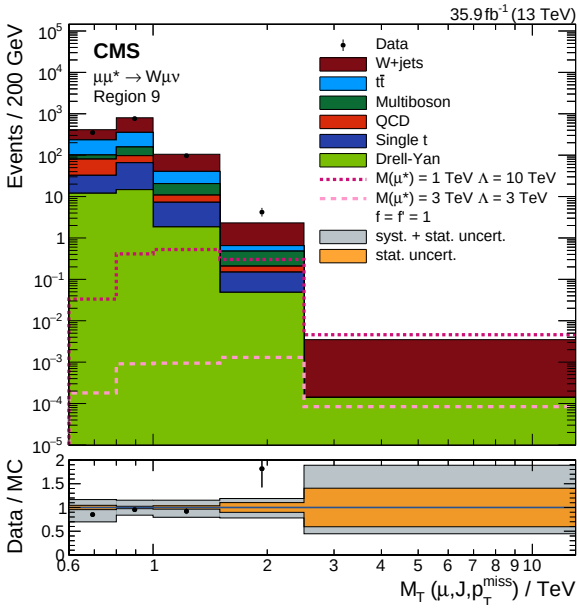

(h)

Figure 7.54 (cont.): Distribution of the transverse mass of all three selected objects for the nine regions used as input for the statistical analysis in addition to the distribution where all selection requirements were passed. Table 7.4 explains the naming scheme. Continued on next page.

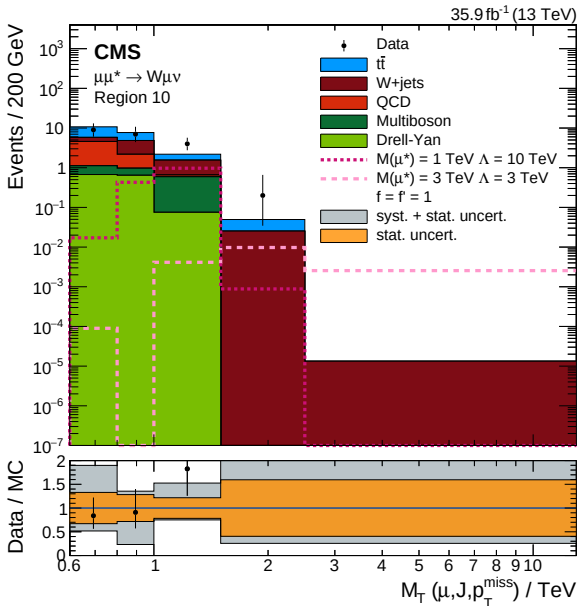

(i)

Figure 7.54 (cont.)**:** Distribution of the transverse mass of all three selected objects for the nine regions used as input for the statistical analysis in addition to the distribution where all selection requirements were passed. Table 7.4 explains the naming scheme.

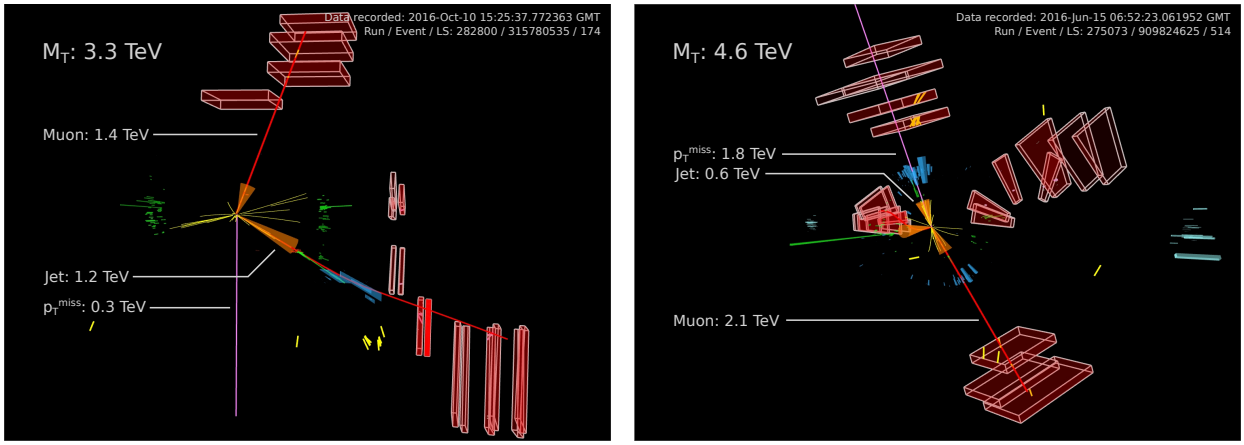

(a) (b)

Figure 7.55: Event displays of the highest mass event in (a) region 1 and (b) region 3. Green bars visualize energy deposits in the ECAL, blue bars deposits in the HCAL, and white bars in the forward region correspond to measurements of the HF. The length of the bar corresponds to the measured energy. The yellow lines represent reconstructed tracks above 2 GeV, and red lines depict reconstructed global muons. The muon chambers which are hit by reconstructed muons are highlighted. The orange cones indicate jets. The beam axis is in the horizontal plain in the middle of the figure. The mass corresponds to the three-body transverse mass of the lepton, the leading wide-cone jet, and the $\boldsymbol{p}_T^{\text{miss}}$. The value provided for each particle to its p_T.

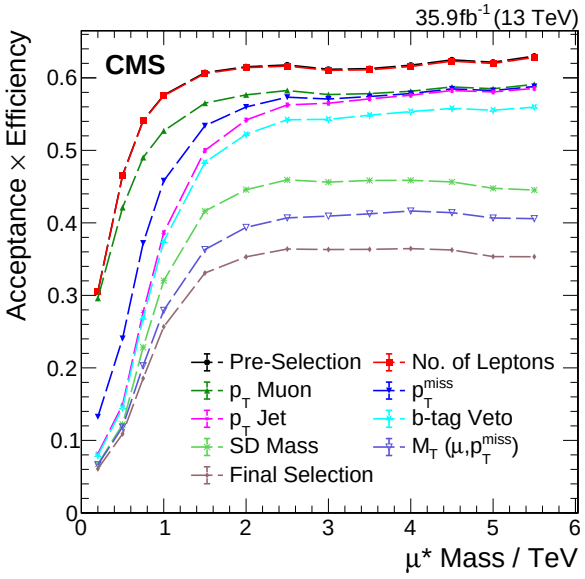

Figure 7.56: Signal efficiency for each selection step. The pre-selection efficiency flats out at 60% above 1.5 TeV. After the final selection, the signal efficiency drops to a maximum of 30%.

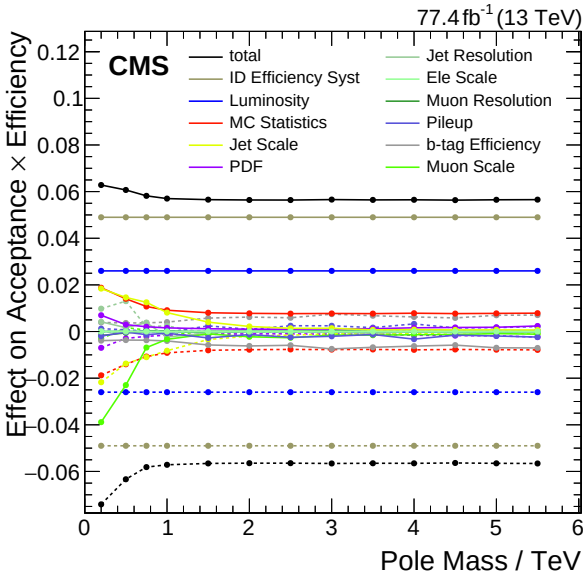

Figure 7.57: Impact of the systematic uncertainties on the signal efficiency after the full selection. The ID efficiency uncertainty has the most significant impact.

jet. We still consider this event for the statistical analysis, since we cannot confidently tag it as misreconstructed.

Signal Efficiency Suppressing the background is one important component of the selection. The other one is maintaining a high signal efficiency. Figure 7.56 presents the efficiency after each stage of the selection. The efficiency of the pre-selection rises from 30 to 60%, topping out at 1.5 TeV. The muon p_T requirement does not cost any efficiency for light excited leptons and around 4% for heavy excited leptons. Both, the jet p_T and the $\boldsymbol{p}_T^{\text{miss}}$ requirement cost efficiency for light excited leptons but not for heavy ones. For low masses, the $\boldsymbol{p}_T^{\text{miss}}$ requirement costs up to 15%. The b-tag veto rejects around 2% of the signal events. The following requirements behave similarly over the full mass range. The soft-drop mass requirement diminishes the signal efficiency by 10%, while the transverse mass and N-subjettiness requirements cost 5% of the signal events each. In total, the additional selection steps bisect the signal efficiency. Analyzing the nine additional regions recovers most of this lost efficiency.

Figure 7.57 illustrates the impact of the systematic uncertainty on the signal efficiency after the full selection. As for the other channels, the ID efficiency uncertainty has the most substantial effect. For low masses, the muon scale uncertainty shifts a significant amount of events outside the p_T requirement of the muon.

7.3.6 Results

Figure 7.58 presents the cross section limit for the W channel. The statistical analysis is identical to the other channels. The expected limit decreases towards higher masses and reaches 0.2 fb

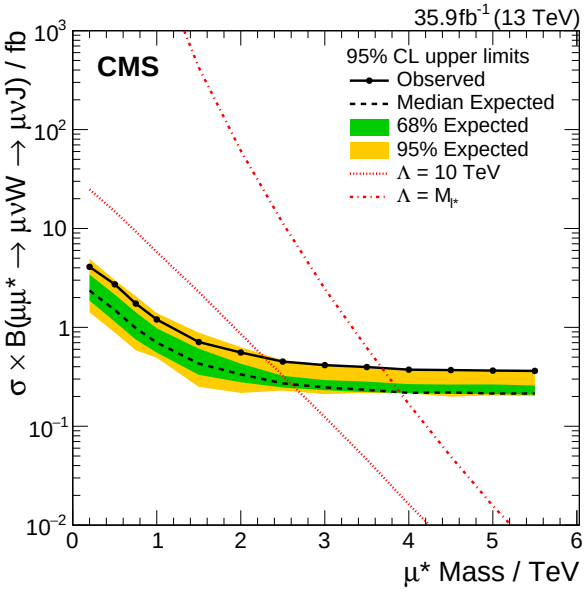

Figure 7.58: Cross section limits for the W channel. The dashed line presents the expected limit with the $\pm 1\sigma$ band in green and the $\pm 2\sigma$ band in orange. The solid black line indicates the observed limit. It is compatible with the expected limits as no significant deviations were observed. The two red, dotted curves correspond to signal hypotheses of $\Lambda = 10\,\text{TeV}$ and $\Lambda = M_{\ell^\star}$ for the lower and upper curve. For both curves, f and f' are equal to unity. The crossing point of the theory curve with the limit marks the maximally excluded signal mass. The observed lower mass limit is at 3.7 and the expected one at 3.9 TeV.

above 3 TeV. At smaller masses, the expected background is larger, and the signal efficiency worse than for heavy excited leptons. For high masses, the signal efficiency becomes flat, and the signal contributes mostly to the last wide bin of the distributions. Therefore, the limit is constant at masses above 3 TeV.

The observed limit is at the edge of the two sigma band of the expected limit, pointing to an underestimation of the background or an excess in data. The single data events in the last bin of region one and three explain this behavior. The second data event in the last bin of region three has been removed as described in section 7.3.5.

The crossing point of the cross section line for $\Lambda = M_{\ell^\star}$ with the limit marks the maximal excluded mass. The expected mass limit is at 3.9 TeV, while the observed limit is 200 GeV below due to the small observed excess. Compared to the other analyses, this value slots in between the Z and the CI channel. This ordering matches the branching fraction of the decays for those channels for $\Lambda = M_{\ell^\star}$.

Figure 7.59 illustrates the impact of the systematic uncertainties on the limit using an example of the 2 TeV mass point and a signal strength of 0.1. The findings match the expectations from figure 7.53. The limited number of MC events in region one and six has the largest impact on the limit, followed by the jet resolution uncertainty. The artificial misidentification uncertainty on QCD events has the fifth-largest impact.

Finally, figure 7.60 shows the result of the maximum likelihood fit. I decided to not show the

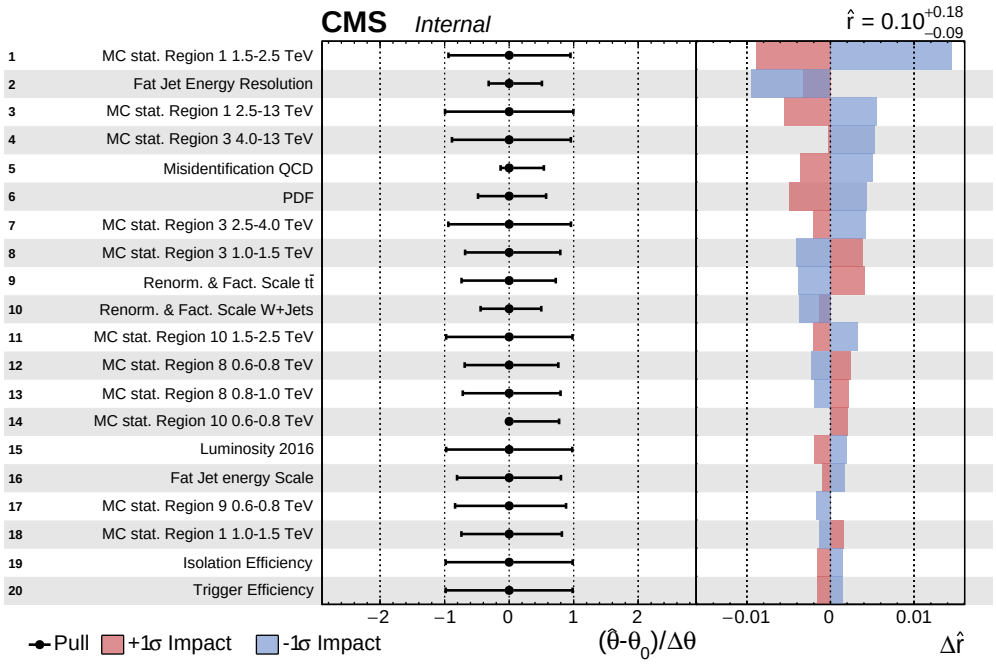

Figure 7.59: Impact of systematic uncertainties on the exclusion limit for a 2 TeV excited lepton signal. The cross section corresponds to model parameters $\Lambda = 10$ TeV and couplings of unity. The signal strength is fixed to 0.1. The Asimov dataset is used to calculate the impacts instead of real data. The most impactful uncertainties are the MC statistics and the jet energy resolution uncertainty.

pulls of the statistical uncertainties due to the large number of bins (50) going into the fit. The *signal+background* fit assumes a 2 TeV excited lepton. No uncertainty gets pulled by more than one standard variation. Due to the larger number of regions, the fit can constrain some uncertainties. The fit results for the *background-only* and the combined fit of signal and background are identical because no signs of an excited lepton signal are observed in data.

The p-values of the goodness-of-fit tests yield good values between 0.3 and 0.6.

7.4 Summary

This chapter presented the selection, results and exclusion limits of the CI, W, and Z channel. No signs for excited leptons were found. The CI achieves the best high-mass limits of 5.6 TeV for excited electrons and muons. The Z channel yields smaller limits of only 3.5 and 3.6 TeV. The W channel is in between both channels with an observed limit of 3.7 TeV and an expected one of 3.9 TeV for excited muons. The next chapter compares the results of these three channels and the photon channel in more detail.

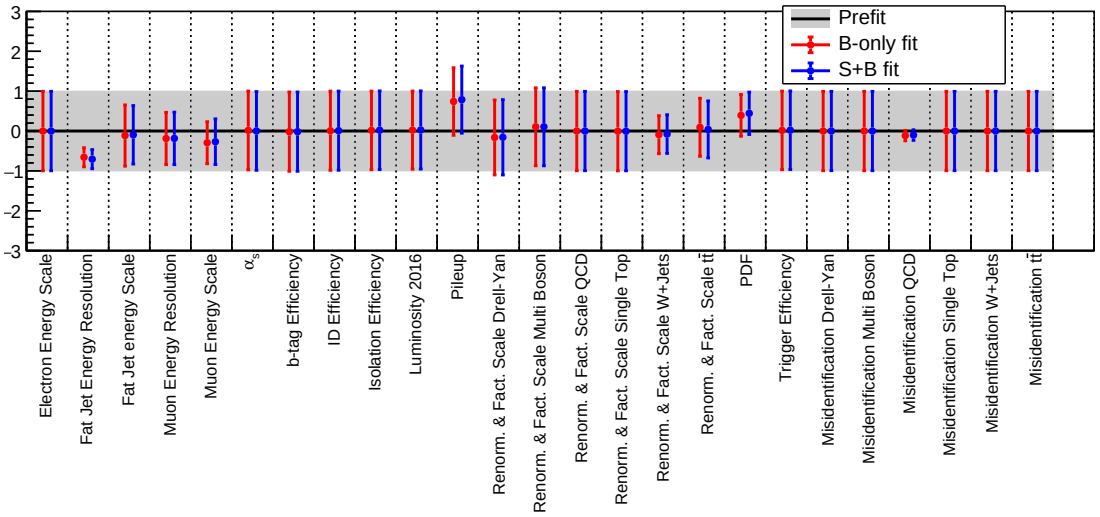

Figure 7.60: Pulls and constrained uncertainties of the fit using the actual data. The x-axis shows the shift relative to the pre-fit value. The size of the error bar corresponds to the relative constraint. A value of 1 ± 0.5 would correspond to an upshift by one sigma and a reduction by a factor of two. The red points show the combined fit of signal and background, and the blue ones the background-only fit. Both coincide well as no significant deviations were observed. This figure uses a 2 TeV signal hypothesis and does not show the pulls of the statistical uncertainties because of the large number of bins.

8 Comparison of the Sensitivity of All Channels

The last chapter discussed the analysis of the contact interaction channel, the Z channel, and the W channel. The results show no significant signs of excited leptons. The analysis of the CI and the Z decay channels searched for excited electrons and muons; the W channel only for excited muons.

This chapter analyzes the sensitivity of these decay channels for different signal parameter hypotheses. It utilizes a recent CMS analysis of the photon channel using the 2016 dataset to examine the sensitivity of this channel as well. This analysis was performed by a group from the Seoul National University and reference [5] reports the details of it. The inclusion of the photon channel allows a complete overview of all possible decay channels of excited electrons and muons.

First, I discuss the predicted branching fractions for different sets of model parameters (section 8.1). The underlying theory has four independent model parameters, as described in the theory chapter (section 2.3.1).

It is difficult to visualize the exclusion limit as a function of more than two model parameters. Thus, the following sections contain a series of two-dimensional exclusion limits depending on two of the four parameters mass, interaction scale Λ, and couplings f and f', while fixing the other two.

8.1 Branching Fractions

This section continues the discussion started at the beginning of the thesis in section 2.3.3. The theory chapter introduced the branching fractions of the four channels depending on the quotient of mass and interaction scale Λ. Figure 8.1 summarizes the findings. The CI channel dominates for $\ell^\star$ masses in the same order as Λ, while the gauge mediated channels are more sensitive for $\Lambda \ll m^\star$. This quantity does impacts all gauge mediated channels in a similar way. For $f = f' = 1$ the W channel is always the dominant GI channel, followed by the photon and the Z channel.

The next sections explore the dependence of the branching fractions of the couplings f and f'.

8.1.1 Dependence on the Scale of Couplings

First, we investigate the dependence of the branching fraction on the size of the couplings (see figure 8.2). The value of $m^\star/\Lambda$ is set to 0.1 for this study, hence the values at $f = f' = 1$ correspond to the values for $m^\star/\Lambda = 0.1$ in figure 2.6.

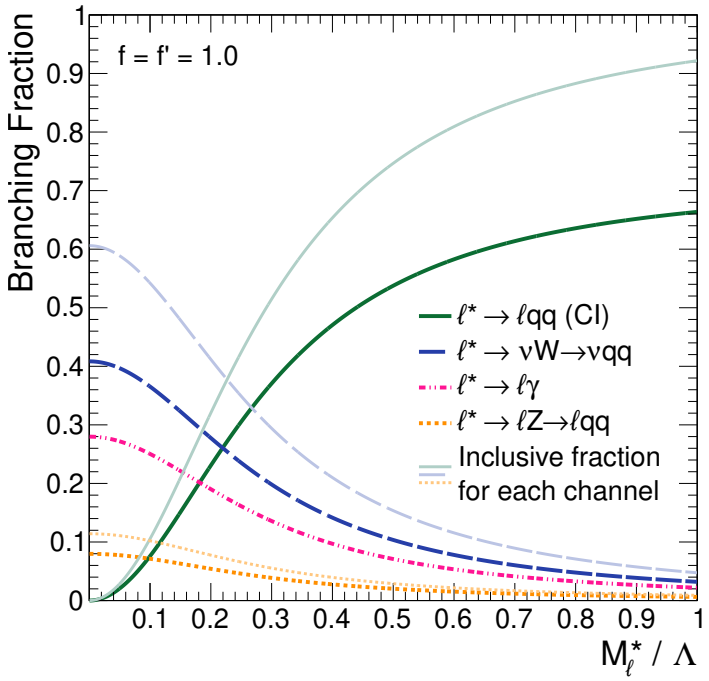

Figure 8.1: Branching fractions of GI decays (W- blue, γ- pink, Z- yellow) and CI decay (green) over m^*/Λ for hadronic decay chains. The couplings are set to unity. The light lines indicate the inclusive branching fraction of the decay, i.e., not just the hadronic fraction.

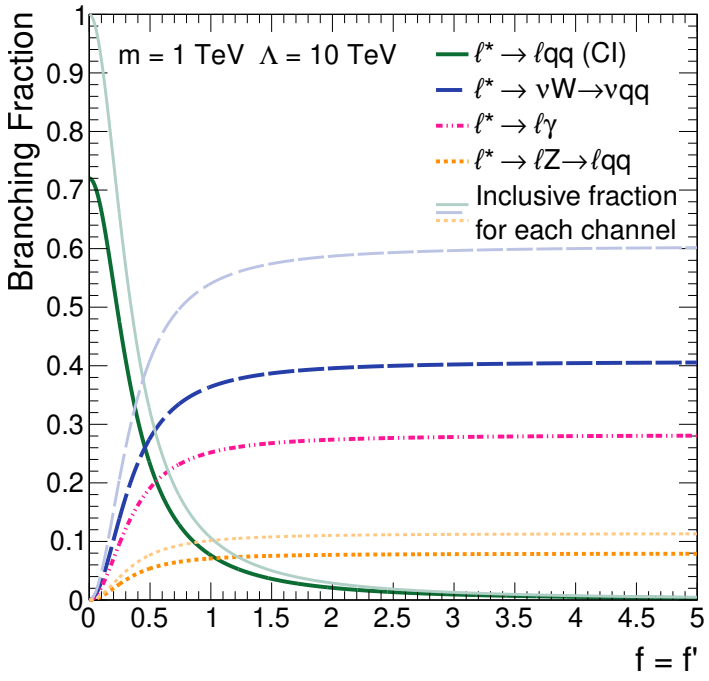

Figure 8.2: Branching fractions of GI decays (W- blue, γ- pink, Z- yellow) and CI decay (green) over $f = f'$. m^*/Λ is set to 0.1. The light lines indicate the inclusive branching fraction of the decay, i.e., not just the hadronic fraction.

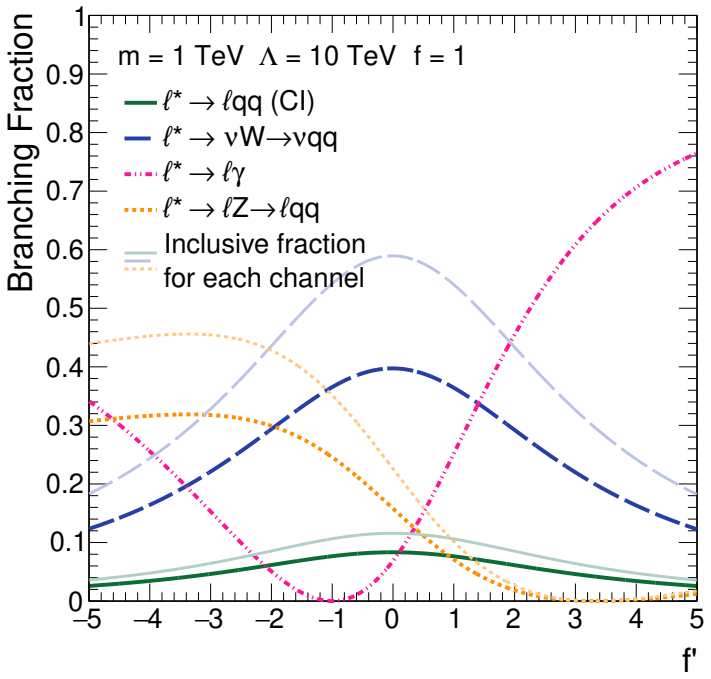

Figure 8.3: Branching fractions of GI decays (W- blue, γ- pink, Z- yellow) and CI decay (green) over f'/f. $m^\star/\Lambda$ is set to 0.1 and f to unity. The light lines indicate the inclusive branching fraction of the decay, i.e., not just the hadronic fraction.

Going back to the equations 2.8, 2.9, 2.12 and 2.13, we see that only the GI decay widths depend on f and f' while the CI decay width is invariant. As the CI mediates the production, the production cross section is also independent of the couplings.[1] The branching fractions for GI decays drop for small values of f and f' because the GI partial decay widths scale with the square of the couplings. The CI picks up the lost branching fraction of the GI channels and gains sensitivity. For $f = f' = 0$, the GI decays vanish entirely, and the contact interaction mediates the only allowed decay.

8.1.2 Dependence on the Relative Values of Couplings

The values for f and f' do not necessarily need to be equal to each other. They can even be negative. The relative sign of the couplings determines the mixing of the weak isospin and the hypercharge terms in equation 2.12.

Figure 8.3 shows the behavior of the branching fractions for different values of f'/f. Again, $m^\star/\Lambda$ is set to 0.1 and f to unity. The point at $f' = 1$ corresponds to the one for $\mathrm{m}^\star/\Lambda = 0.1$ in figure 8.1.

One can see that all three GI decay channels have different areas in which they are dominating: The photon decay channel dominates for $f' > f$, the W channel[2] for $|f'| \lessapprox 2$, and the Z channel

[1] The GI production is also possible at hadron colliders but negligible.
[2] The partial decay width depends only on f and not f'. See eq. 2.12.

Table 8.1: Datasets used for the comparison of the sensitivity of the different channels.

	Contact Interaction	W Channel	Z Channel	γ Channel
$e^\star$	2016 + 2017 ($77.4\,fb^{-1}$)	-	2016 + 2017 ($77.4\,fb^{-1}$)	2016 ($36.9\,fb^{-1}$) [5]
$\mu^\star$	2016 + 2017 ($77.4\,fb^{-1}$)	2016 ($36.9\,fb^{-1}$)	2016 + 2017 ($77.4\,fb^{-1}$)	2016 ($36.9\,fb^{-1}$) [5]

if f and f' have an opposite sign. For $f = -f'$, the branching fraction of the photon channels vanishes. The same happens for the Z channel at $f'/f = \cot^2\theta_W$.

The CI partial decay width is not influenced by f and f' (see eq. 2.13). The branching fraction only depends on this variable because the total decay width increases to larger values of the couplings. Hence, the branching fraction of the CI channel is maximal for $f'/f = 0$ as f' is effectively set to zero here.

8.1.3 Conclusion

To conclude, all decay channels have areas in the $m^\star, \Lambda, f, f'$ parameter space in which they are dominant. The CI decay is dominant for masses close to Λ and small coupling parameters f and f'. GI decays profit from masses that are small compared to the characteristic scale, and from large couplings. The Z channel favors couplings with opposite sign, while the photon channel vanishes for $f = -f'$. Large values of f' of the same sign as f are optimal for the photon channel, while the W channel benefits from large values of f and small values of f', independent of their sign. Due to the color factor, the hadronic decays have a much more significant branching fraction for the CI, Z, and W channels.

8.2 Exclusion Limits

The last section explained the theoretical strengths of each channel. This section tests if this postulation can be verified by the analysis. Table 8.1 summarizes the datasets and luminosities of the involved analyses. The contact interaction and the Z channel use the combination of the data taken in 2016 and 2017 while the photon and W channel only feature the 2016 dataset. Also, the analysis of the W channel only searches for excited muons.

The limits presented in this section can be calculated using the formulae 2.8 to 2.13. Running the Pythia8 simulation on top for the given model parameter set to iteratively find the set of parameters for which the cross section equals the cross section limit further increases the precision.

The results are presented in two-dimensional plots. The y-axis presents the scale Λ and the x-axis either the mass, the values for $f = f'$, or f'. The areas below the curves are excluded.

The black line represents the combined limit of all channels in the transition region. The envelope of the individual channels defines the combination outside the transition region. The expected limit always improves while the observed limit can deteriorate if the limit of one channel is worse compared to its expected limit than the one of the other channels.

The combined limit cannot be calculated similarly to the individual limit since different channels interfere. Instead, the cross section corresponding to a set of Λ, f, and f' of each respective channel is applied before the limit is calculated. The exclusion limit is defined by the point at which the excluded signal strength is equal to unity. A grid of different excluded signal strengths is computed for different values of Λ with fixed values of f and f'. Then a third-degree polynomial is fit to the excluded signal strength as a function of Λ. The maximally excluded values of Λ is defined by the value at which the function is equal to unity. The combined limit can only be calculated for masses which are simulated for all channels.

Since the procedure used for the individual limits of the channels is very computing intensive, the only asymptotically correct but much faster method outlined in reference [195] is used for the combined limit to save computing time.[3] The results of the asymptotic method are usually slightly too aggressive when the background prediction is close to zero events. The results of the asymptotic limit match the result of the full method still well in regions where one channel dominates. This agreement indicates that the asymptotic method provides comparable results while saving computing time.

8.2.1 Λ over Mass

$f = f' = 1$ The first set of two-dimensional exclusion limits presents the limits in terms of the mass and Λ for fixed couplings f' and f'. Figure 8.4 shows the limit for $f = f' = 1$. The green curve denotes the contact interaction (CI) channel, the pink curve the photon channel, the blue the W channel, and the yellow curve the Z channel. The shaded bands represent the one and two sigma bands, the dashed line the expected limit, and the solid line the observed limit, similar to the last chapter. The grey region where the mass is greater than Λ is theoretically forbidden.

This choice of coupling parameters marks the most common benchmark scenario for excited lepton searches for the past years. Effectively, in this scenario the interaction scales are equal to Λ for all interactions.[4]

For small masses below 2 TeV, the photon channel has the best sensitivity. It can exclude values up to 23 TeV in both channels. The limit, especially the observed one, varies strongly at low masses. The particular selection of this channel can explain this behavior. Similar to the CI and the Z channel, only one of the two leptons originates from the excited lepton decay. The other one corresponds to the associated lepton from the production. The combination of one of the leptons with the photon reconstructs the excited lepton. The photon channel analysis tests both hypotheses. For signal-like events, the mass of one of the combinations should be close to the mass of the excited lepton. This feature can be used to very efficiently suppress the SM background since it does not have any preference for the mass of both pairs. Therefore, the analysis requires the events to be in a small window around the mass of the excited leptons for at least one of the combinations, building a distinct search region for every mass hypothesis. Constructing narrow windows is possible due to the excellent energy resolution of the CMS detector for photons and leptons. If single data events are located either in- or outside of this window, the observed limit can vary strongly. The expected limit is more stable but can still vary

[3] The aysmptotic method uses formulae to calculate the distribution of the test statistics instead of toys which the method described in section 7.1.7 draw.

[4] i.e., the contact interaction and the gauge interaction coupling to the hypercharge and weak isospin

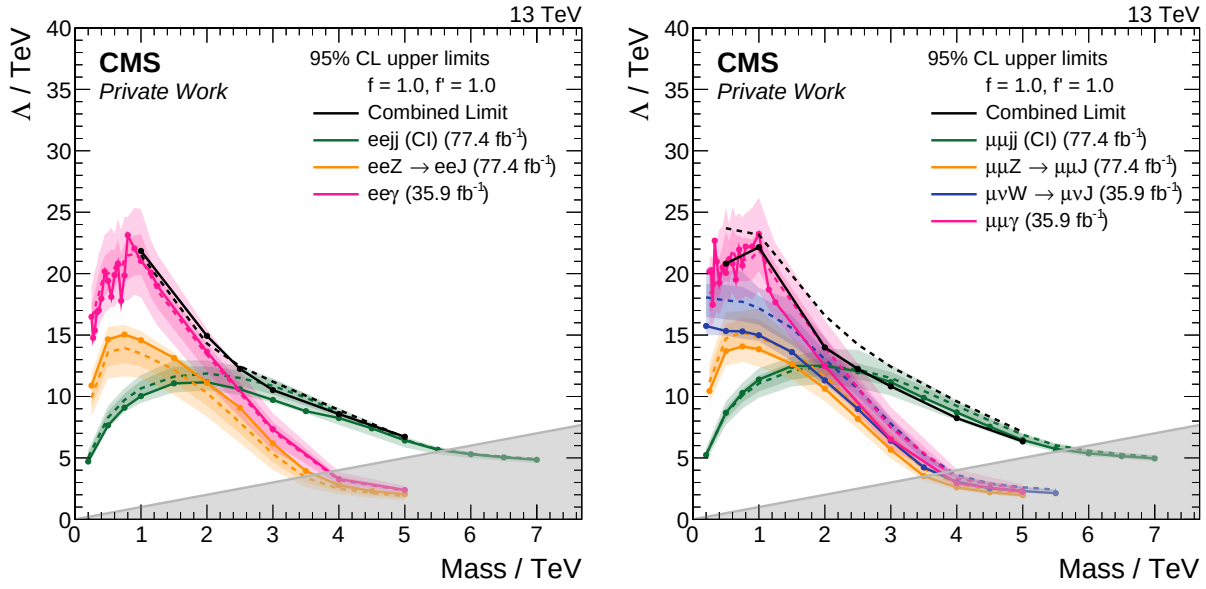

(a) (b)

Figure 8.4: Limits for excited leptons in terms of the mass and Λ. Both couplings are fixed to unity. (a) shows the electron channel and (b) the muon channel. The curves show the maximal excluded value for Λ. The solid line represents the observed limit, and the dashed line the expected limit with the one and two sigma bands in lighter shades of the corresponding color. The black lines show the combined limit. It can only be calculated for masses which are simulated for all channels and is only computed for the overlap region. Outside this region the combined limit is defined by the envelope of the individual channels. Everything below the curves is excluded, and the grey region in which the mass is greater than Λ is theoretically forbidden. The luminosity of the respective channel is provided in the legend. A capital J denotes a wide-cone jet and a lowercase j a normal jet. The contact interaction dominates at high masses while the gauge mediated decay channels govern the low-mass region. The observed limit of the W channel is below the expected limit because of the excess observed in data.

due to the finite number of simulated MC events. For masses above 1 TeV, the criterion is relaxed due to the worse mass resolution at high energies and the lower background level.

In the muon channel, the second most sensitive channel is the W channel. It has a larger branching fraction than the photon channel but also a larger background and less selection efficiency. The observed limit is below the expected limit because of the excess observed in data.[5]

The Z channel has the lowest sensitivity for this choice of f and f' because it has the smallest branching fraction. The selection is more efficient than the W channel but less efficient than the photon channel.

The CI channel takes over at high masses above 2 TeV. This behavior matches the expectation set by the branching fractions. The CI channel has low branching fractions for $\Lambda \ll m^\star$ but a high branching fraction for $\Lambda \lessapprox m^\star$. The maximum exclusion of 5.6 TeV for both channels matches the intersection of the cross section limit and the cross section line for $\Lambda = m^\star$ in figure 7.15.

[5] See section 7.3.6 at the end of the last chapter.

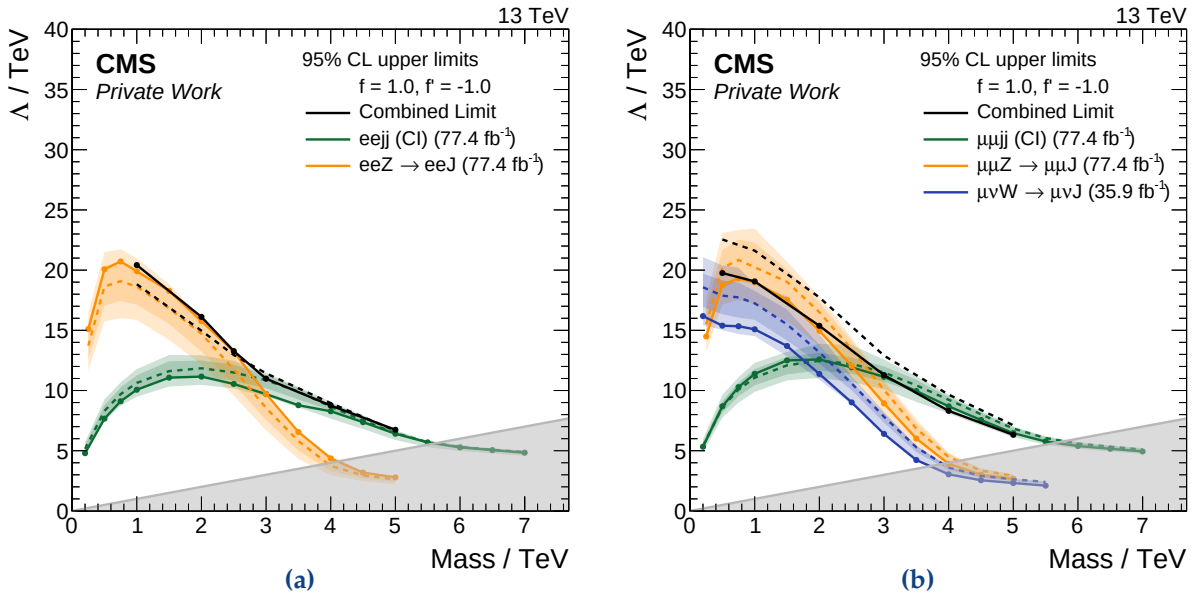

Figure 8.5: Limits for excited leptons in terms of the mass and Λ. f is set to unity and f' to -1. (a) shows the electron channel and (b) the muon channel. The curves show the maximal excluded value for Λ. The caption of fig. 8.4 explains the figure. The contact interaction dominates at high masses while the gauge mediated decay channels govern the low mass region. The photon channel vanishes while the Z channel gains sensitivity.

$m^\star/\Lambda$ does not affect the relative branching fractions of the gauge mediated channels. However, the selection efficiency for the W channel becomes competitive for more massive excited leptons, and the background level decreases. Therefore, the W channel comes closer to the photon channel at masses around 3 TeV.

f = -f' = 1 The picture changes drastically, if f' is set to minus one and f to unity as figure 8.5 shows. While the CI is barely touched, the photon channel disappears, and the Z channel is the most sensitive search channel. The cause lies again in the branching fractions. The CI and the W channel have nearly the same branching fraction as for $f = f' = 1$.[6] The decay into photons is forbidden for this configuration of the couplings as f_γ is zero.[7] The Z channel obtains the lost branching fraction and reaches now a maximum excluded Λ of 20 TeV. It does not reach the values of the photon channel for $f = f' = 1$ because its selection efficiency is lower and the background level higher. The W channel shows a small increase at very small masses of 200 GeV because the decay into W or Z bosons is suppressed for very light excited leptons since the mass is in the same order of magnitude as the mass of the bosons.

f = 1, f' = 0 If we turn off the coupling to the hypercharge and leave the coupling to the weak isospin at unity, the branching fraction of the photon channel drops below all other channels. The Z and W channel gain parts of the lost branching fraction. For the W channel, this set

[6] The total decay width is slightly smaller than for $f = f' = 1$.
[7] See equation 2.12 in the theory chapter.

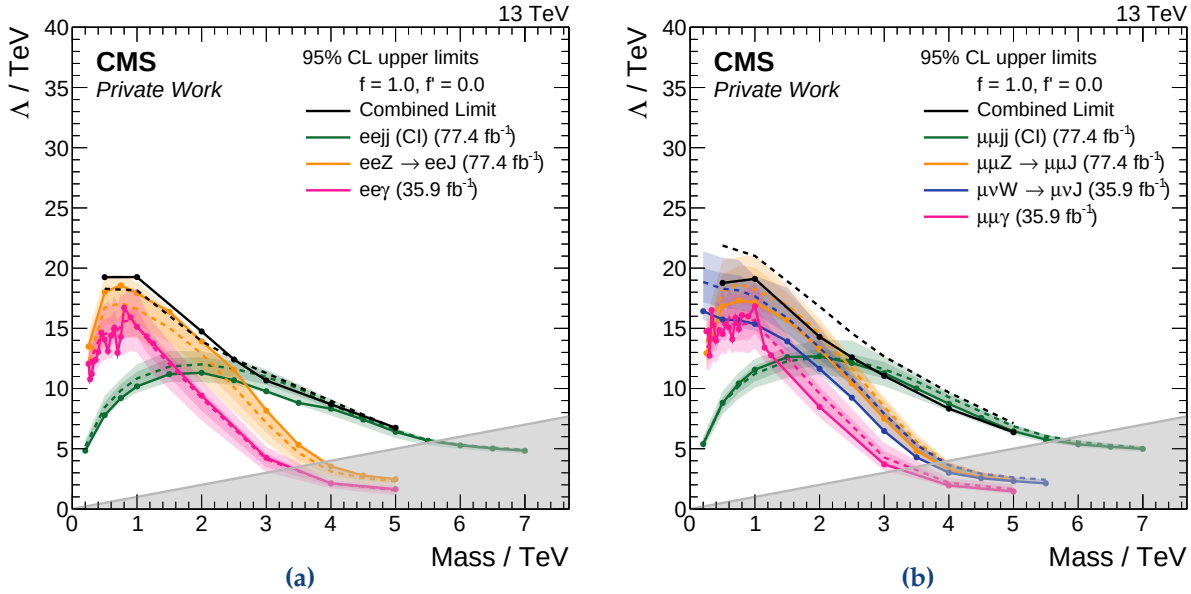

Figure 8.6: Limits for excited leptons in terms of the mass and Λ. f is set to unity, and f' is turned off. (a) shows the electron channel and (b) the muon channel. The curves show the maximal excluded value for Λ. The caption of fig. 8.4 explains the figure. The contact interaction dominates at high masses while the gauge mediated decay channels govern the low mass region. The photon channel is less sensitive while the other channels gain sensitivity.

of couplings is ideal. The CI slightly gains branching fraction because the total decay width decreases, and its partial decay width is not affected by the couplings.

Figure 8.6 illustrates the exclusion limits for this case. Both, the W and the Z channel now dominate the limit at low masses with maximal exclusion boundaries of 18 TeV. The CI limit still becomes competitive above 2 TeV.

f = 1, f' = 3.3 If we instead set f' to 3.3, which is close to $\cot^2\theta_W$, the Z channel is highly suppressed. [8] The W channel also loses importance while the CI channel is mostly unchanged. Hence, the photon channel massively gains branching fraction and is now able to exclude values of nearly up to 30 TeV as figure 8.7 indicates. The CI channel becomes competitive only above 3 TeV.

f = f' = 0.1 This time, we do not vary f' relative to f, but both couplings simultaneously. Figure 8.8 shows the exclusion limits if both are decreased by one order of magnitude. The gauge mediated decays are highly suppressed as their partial decay width scales with the square of the couplings. Contrary, the CI massively gains branching fraction. Therefore, the CI is the dominant channel except for tiny masses below 0.5 TeV. It also nearly doubles its maximal excluded value for Λ reaching 17 and 20 TeV for the electron and muon channel, respectively.

[8] c.f. equation 2.12.

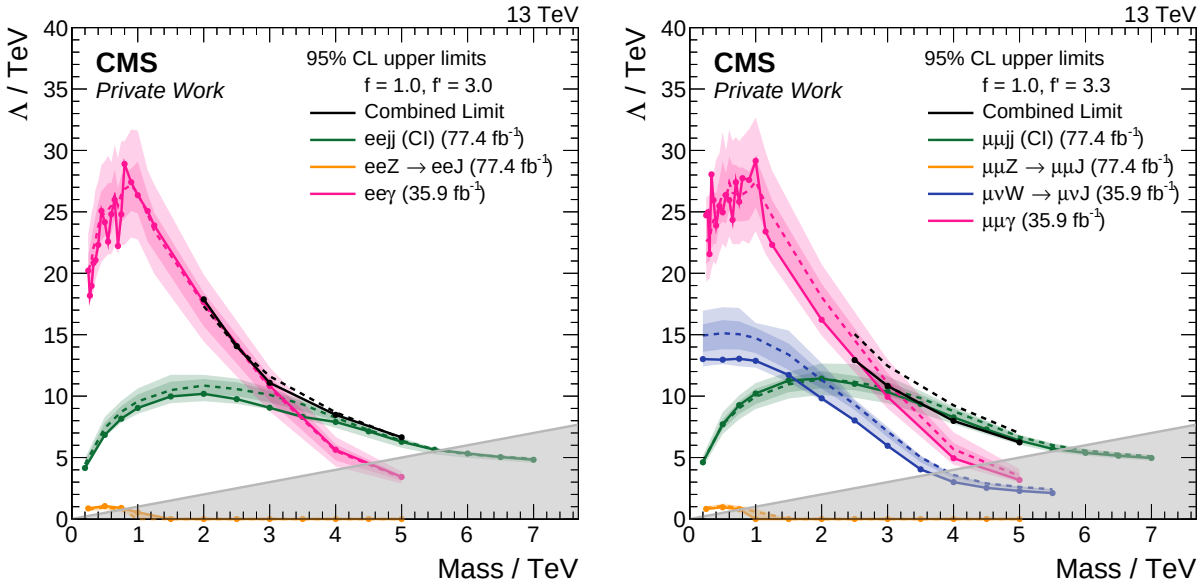

(a) (b)

Figure 8.7: Limits for excited leptons in terms of the mass and Λ. f is set to unity and f' to 3.3. (a) shows the electron channel and (b) the muon channel. The curves show the maximal excluded value for Λ. The caption of fig. 8.4 explains the figure. The contact interaction dominates at high masses while the gauge mediated decay channels govern the low mass region. The Z channel nearly vanishes, and the photon channel massively increases its sensitivity.

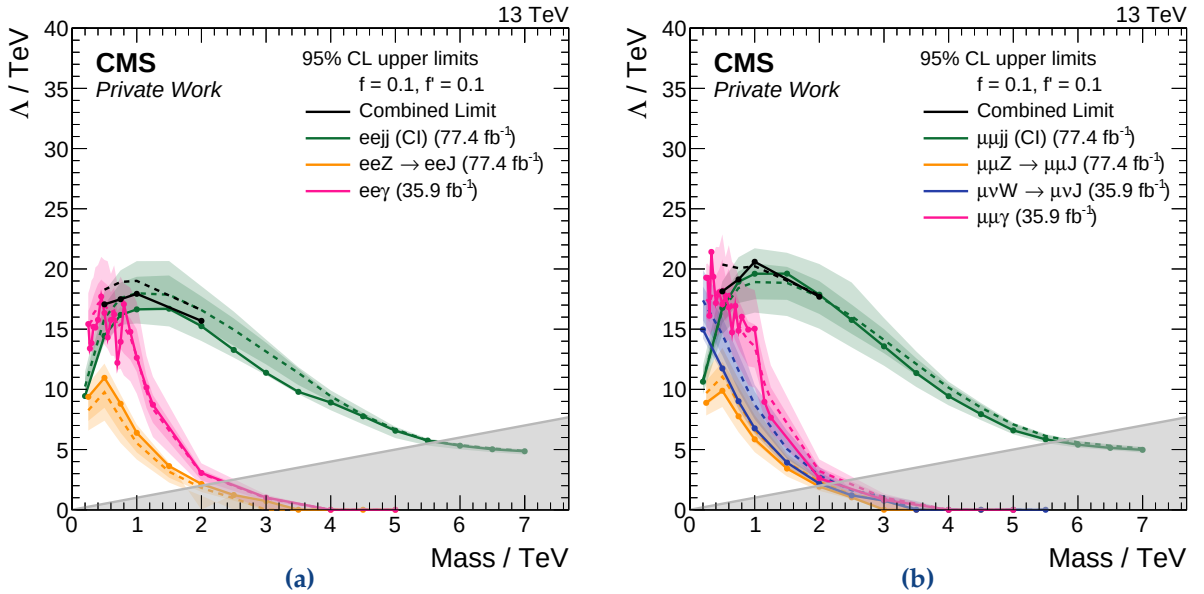

(a) (b)

Figure 8.8: Limits for excited leptons in terms of the mass and Λ. Both couplings are set to 0.1. (a) shows the electron channel and (b) the muon channel. The curves show the maximal excluded value for Λ. The caption of fig. 8.4 explains the figure. The contact interaction dominates much earlier than for couplings of unity.

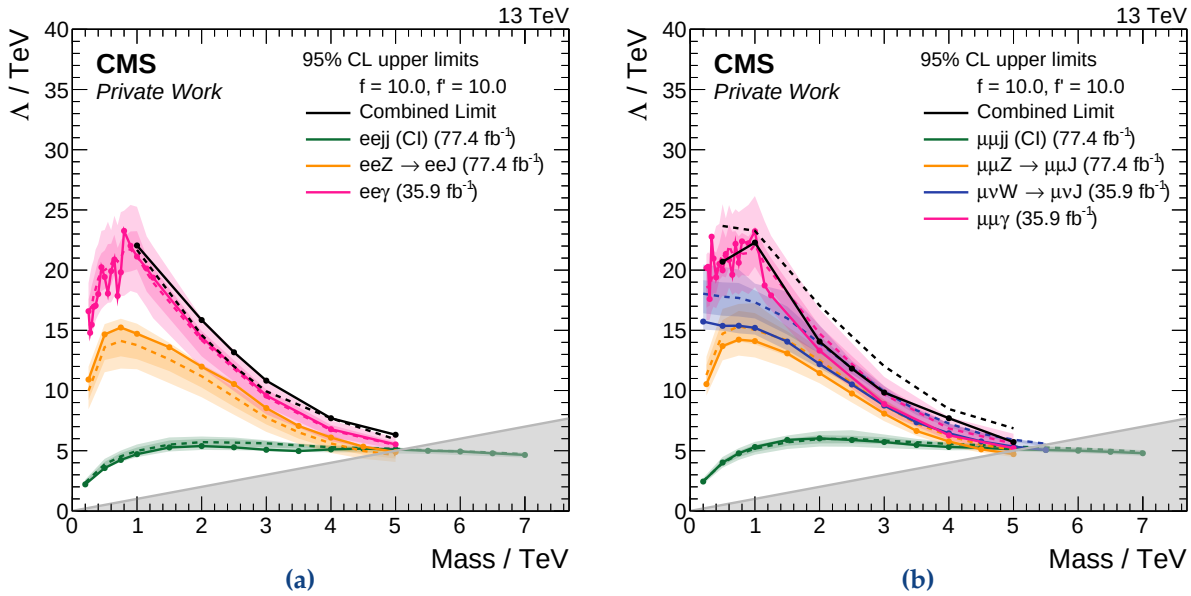

Figure 8.9: Limits for excited leptons in terms of the mass and Λ. Both couplings are set to ten. (a) shows the electron channel and (b) the muon channel. The curves show the maximal excluded value for Λ. The caption of fig. 8.4 explains the figure. The gauge interactions are now competitive up to the highest masses.

$f = f' = 10$ If decreasing both couplings by one order of magnitude decreases the strength of the gauge mediated decay channels, increasing them must improve their sensitivity, especially at high masses. Indeed, figure 8.9 shows a massive increase in the sensitivity at high masses where typically the CI dominates. The larger couplings push the point at which the CI takes over as the most dominant channel towards higher masses. For couplings $f = f' = 10$, this results in a similar mass reach for all decay channels. At low masses, the limits of the gauge mediated channels do not change because they are anyhow the dominant decay channel in this region. This study does not take into account that the gauge mediated **production** of excited leptons might become relevant for large couplings.

8.2.2 Λ over Absolute Value of Couplings

Following the last two figures of the previous section, this section investigates the dependence of the maximal excluded substructure scale on the scale of both couplings. f and f' are varied simultaneously for different fixed excited leptons masses.

Figure 8.10 presents the maximally excluded value for Λ for mass hypotheses of 0.5, 1, 2, and 4 TeV for couplings between 0.01 and ten. All figures have in common that the contact interaction dominates for weak couplings f and f' while the gauge interactions overshadow the CI for strong couplings. These findings are consistent with the previous section.

The higher the mass of the excited lepton, the higher is the crossing point at which the gauge interactions take over because the ratio of mass and maximal excluded Λ is higher for more massive excited leptons, and the CI is, in general, predominant for this configuration. Therefore, the point at which the gauge interactions take over increases from $f = f' \approx 0.5$ by one order of

magnitude to five between signal masses of 0.5 and 4 TeV. Also, the maximal reach decreases towards higher masses because the production cross section shrinks for heavy excited leptons regardless of f and f' while the cross section limit is constant.

The Z and W channel become more competitive to the photon channel for heavy and very light excited leptons. For medium-mass excited leptons, the selection of the photon channel is more efficient, while also rejecting more background, as the previous section explains.

8.2.3 Λ over Relative Values of Couplings

This section does not change the scale of the couplings but fixes f to unity and varies f' in a range of minus five to five. As for the previous section, every figure presents the maximal excluded value for Λ for fixed masses of 0.5, 1, 2, and 4 TeV.

Figure 8.11 presents all limits and shows generally similar behavior for the different mass hypotheses. The contact interaction becomes dominant for heavy excited leptons, and the maximal excluded values decrease. This behavior is consistent with the previous findings.

The contact interaction is rather unaffected by the value of f'. Its sensitivity is maximal for $f' = 0$ because it has the most extensive branching fraction since one of the couplings of the gauge interaction is turned off. The W channel shows the same behavior because its partial decay width is independent of f'. The smaller f', the more significant is the branching fraction of the W channel compared to the other gauge interaction channels.

The photon channel vanishes for $f = -f'$ as the branching fraction becomes zero. It reaches its maximum for $f' > f$. Contrary, the Z channel favors a configuration in which both couplings have an opposite sign. It vanishes for $f' \approx 3.3$. All findings are consistent with the expectation set by the branching fractions presented in section 8.1.2.

8.3 Summary

All decay channels dominate at least one part of the parameter space of the model. The CI dominates the high mass region and is generally the most sensitive channel for weak couplings. Contrary, the gauge mediated decay channels improve the sensitivity at low masses and are more sensitive than the contact interaction for strong couplings.

The W channel has the most challenging selection and cannot outperform the other gauge mediated channels at the moment. However, its sensitivity is comparable to the other gauge mediated channels for a suitable set of model parameters. This channel also offers the most room for improvements.

The photon channel has the cleanest signature and is the most sensitive channel for couplings of unity and $f > f'$. It vanishes for $f = -f'$.

The Z channel is complementary to the photon channel since it provides the best sensitivity for couplings with the opposite sign. Even for an ideal set of parameters, it does not reach the sensitivity of the photon channel since the selection efficiency is smaller because of the more challenging selection.

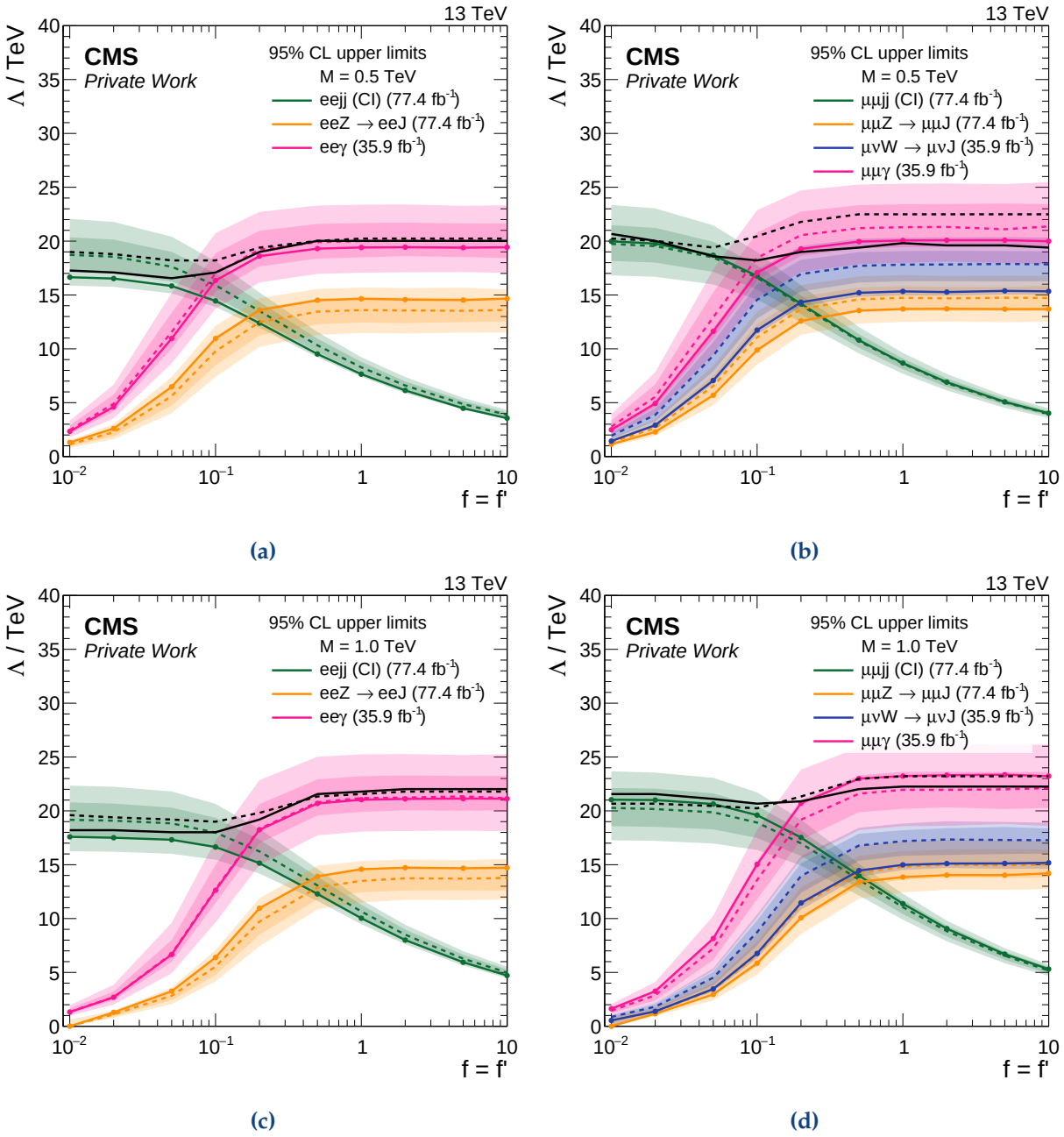

Figure 8.10: Limits for excited electrons in terms of Λ, f, and f'. Both couplings are varied simultaneously. The excited leptons mass M is set to (a) and (b) 0.5, (c) and (d) 1, (e) and (f) 2, and (g) and (h) 4 TeV. The left side shows the electron channel and the right-hand side the muon channel. The curves show the maximal excluded value for Λ. The solid line represents the observed limit, and the dashed line the expected limit with the one and two sigma bands in lighter shades of the corresponding color. The black lines show the combined limit. The luminosity of the respective channel is provided in the legend. A capital J denotes a wide-cone jet and a lowercase j a normal jet. Everything below the curves is excluded. The CI is dominant for weak couplings, and the gauge interactions for strong couplings. For higher masses the GI take over later than for light excited leptons. Continued on next page.

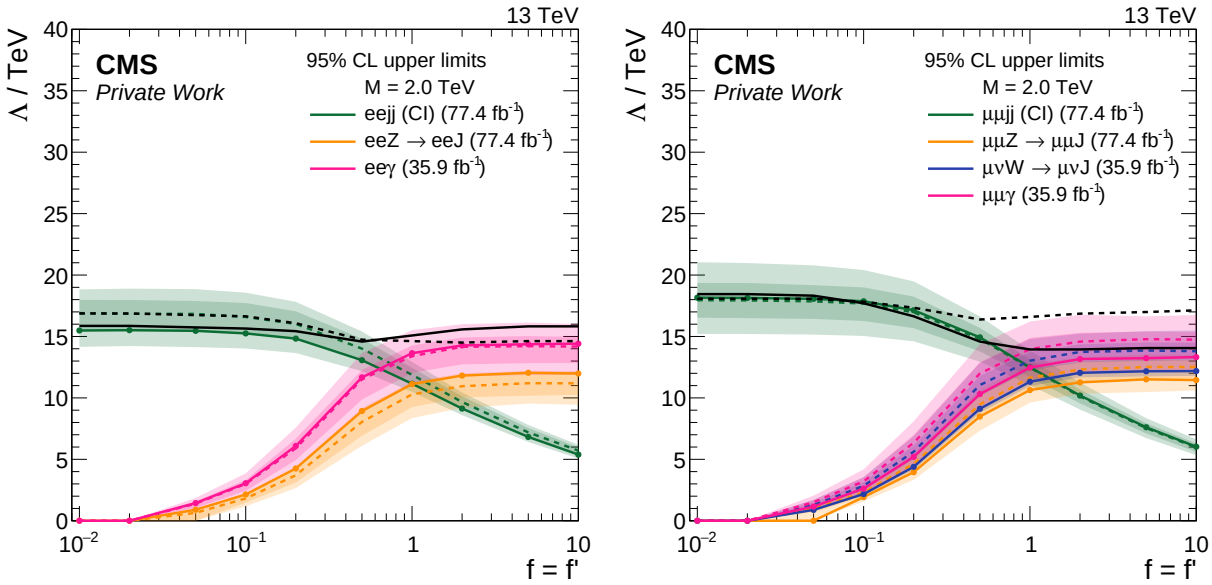

(e)

(f)

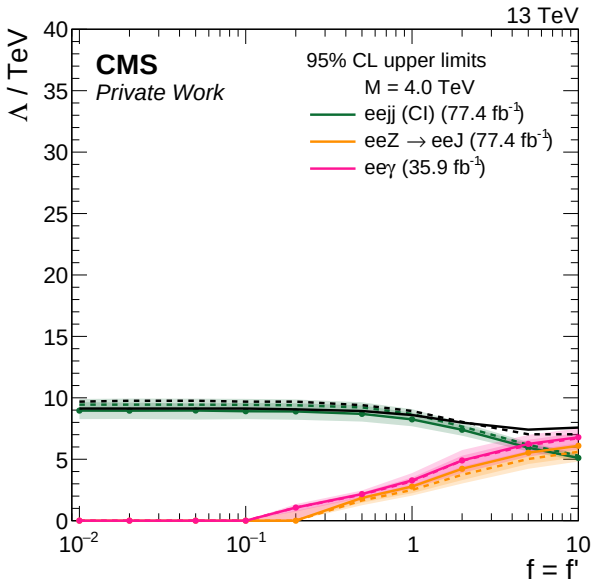

(g)

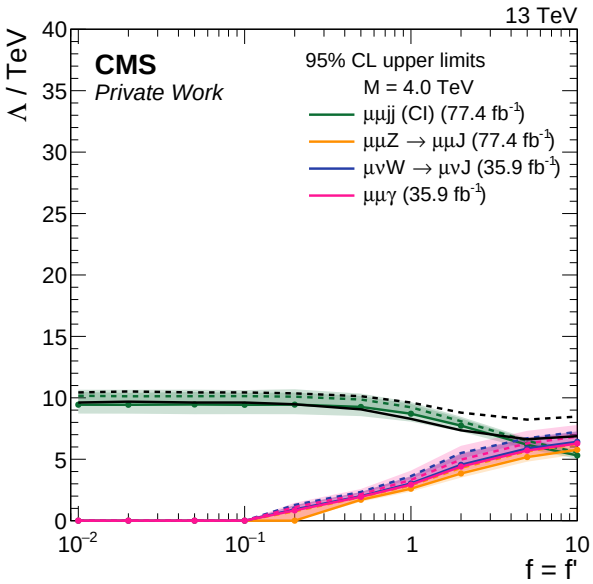

(h)

Figure 8.10 (cont.)**:** Limits for excited electrons in terms of Λ, f, and f'. Both couplings are varied simultaneously. The excited lepton mass M is set to (a) and (b) 0.5, (c) and (d) 1, (e) and (f) 2, and (g) and (h) 4 TeV. The left side shows the electron channel and the right-hand side the muon channel. The curves show the maximal excluded value for Λ. The solid line represents the observed limit, and the dashed line the expected limit with the one and two sigma bands in lighter shades of the corresponding color. The black lines show the combined limit. Everything below the curves is excluded. The luminosity of the respective channel is provided in the legend. The CI is dominant for weak couplings, and the gauge interactions for strong couplings. For higher masses the GI take over later than for light excited leptons.

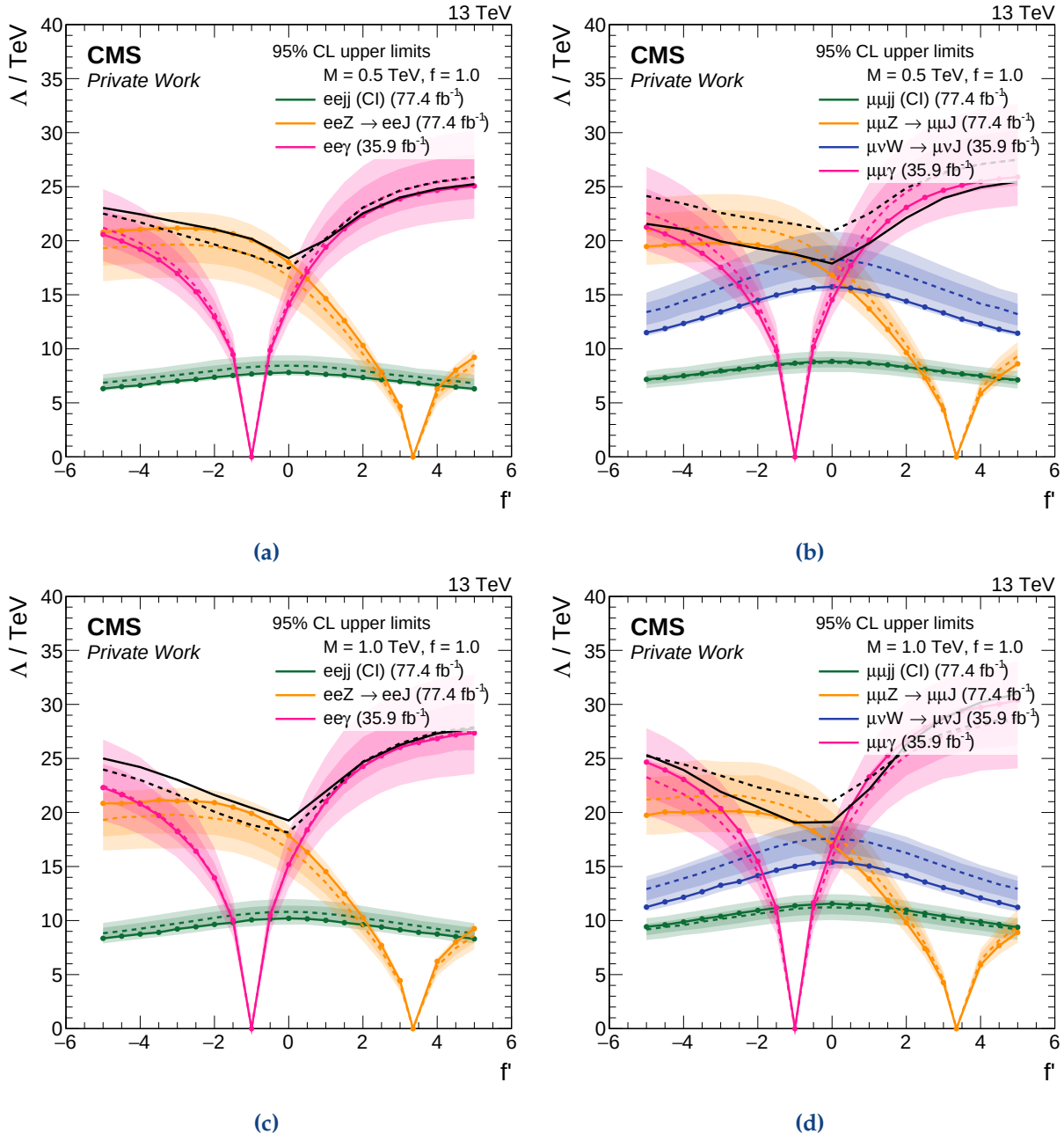

Figure 8.11: Limits for excited leptons in terms of Λ and f'. f is set to unity and the mass to (a) and (b) 0.5, (c) and (d) 1, (e) and (f) 2, and (g) and (h) 4 TeV. The left side shows the electron channel and the right-hand side the muon channel. The curves show the maximal excluded value for Λ. The solid line represents the observed limit, and the dashed line the expected limit with the one and two sigma bands in lighter shades of the corresponding color. The black lines show the combined limit. Everything below the curves is excluded. The luminosity of the respective channel is provided in the legend. The CI is stable over the entire range. Its branching fraction is maximal for $f' = 0$ because then the total decay width is minimal while the particle decay width of the CI decay is not affected. The W channel peaks at zero as well because its decay width is also not affected by f'. The photon channel favors large values of f' and vanishes at $f = -f'$. In contrast, the Z channel vanishes for $f'/f = \cot^2\theta_W$. The maximal excluded scale decreases towards heavier excited leptons because of the shrinking production cross section. The CI is naturally dominant for heavy excited leptons. Continued on next page.

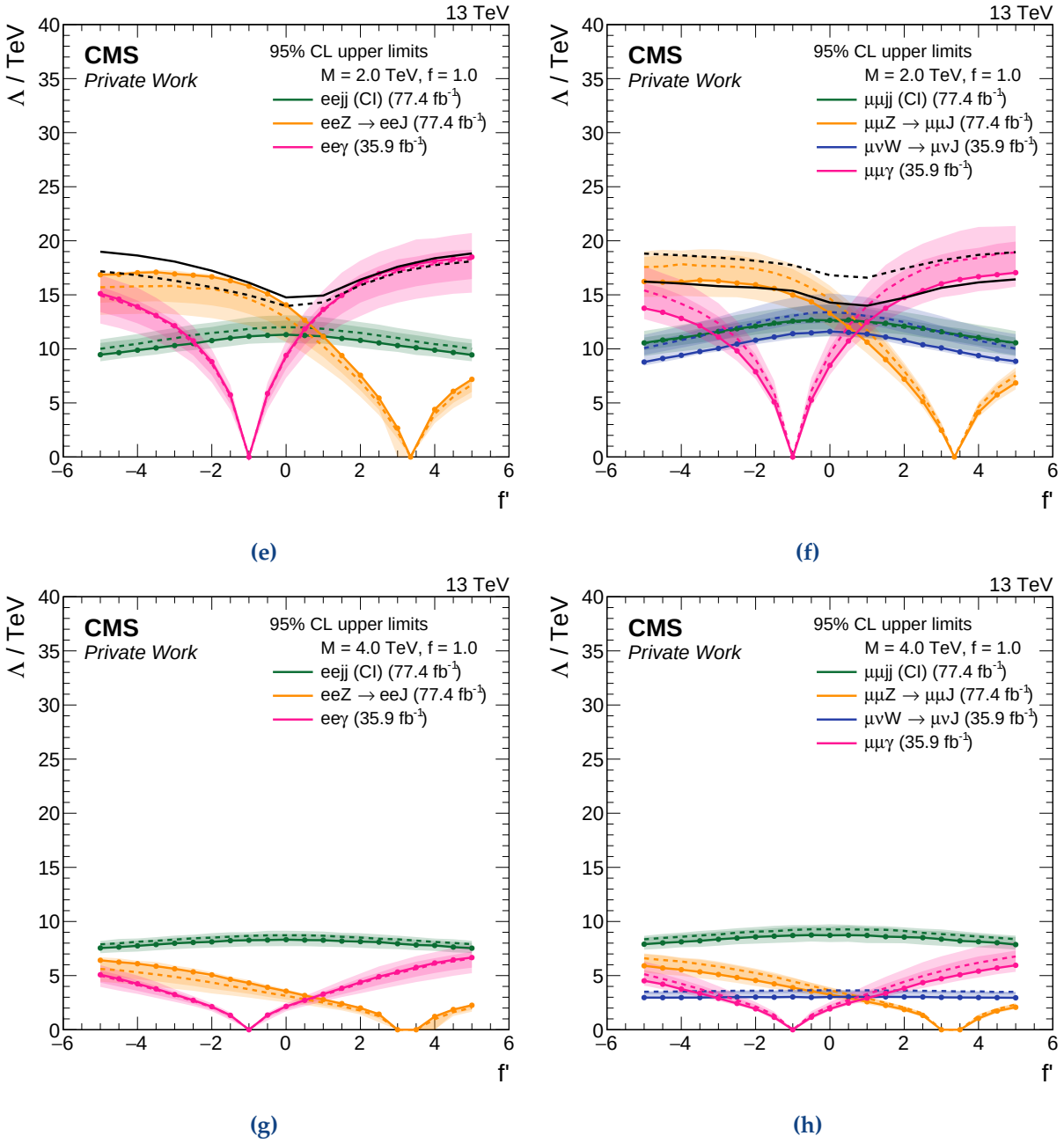

Figure 8.11 (cont.)**:** Limits for excited leptons in terms of Λ and f'. f is set to unity and the mass to (a) and (b) 0.5, (c) and (d) 1, (e) and (f) 2, and (g) and (h) 4 TeV. The left side shows the electron channel and the right-hand side the muon channel. The curves show the maximal excluded value for Λ. The solid line represents the observed limit, and the dashed line the expected limit with the one and two sigma bands in lighter shades of the corresponding color. The black lines show the combined limit. Everything below the curves is excluded. The luminosity of the respective channel is provided in the legend. The CI is stable over the entire range. Its branching fraction is maximal for $f' = 0$ because then the total decay width is minimal while the particle decay width of the CI decay is not affected. The W channel peaks at zero as well because its decay width is also not affected by f'. The photon channel favors large values of f' and vanishes at $f = -f'$. In contrast, the Z channel vanishes for $f'/f = \cot^2 \theta_W$. The maximal excluded scale decreases towards heavier excited leptons because of the shrinking production cross section. The CI is naturally dominant for heavy excited leptons.

9 | Outlook

While the LHC is in a shutdown period at the moment of writing, it has not finished its scientific program yet. Operation is planned to continue for at least fifteen more years. Following the upcoming Run 3, CERN will install several upgrades to facilitate a significant increase of the instantaneous luminosity by a factor of 2.5. The *High Luminosity LHC* (HL-LHC) is expected to deliver a luminosity of $3000\,\mathrm{fb}^{-1}$ during its operation at a center-of-mass energy of 14 TeV.

This chapter projects the expected increase of the sensitivity of excited lepton searches. The projection starts with the analysis of the Run 2 dataset, scales the luminosity to $3000\,\mathrm{fb}^{-1}$, and recalculates the signal cross section for $\sqrt{s} = 14\,\mathrm{TeV}$. The cross sections of the Standard Model prediction and all uncertainties remain unchanged. Effectively, constant uncertainties imply that the upgraded CMS detector can cope with the harsher environment equally well as the present detector with the current conditions. Optimistic estimations even predict a smaller uncertainty due to an improved understanding of the detector and the theory [196]. The Standard Model cross section will increase towards higher energies, but to a lesser extent than the signal cross section. For example, the $\mathrm{t\bar{t}}$ cross section is expected to increase by less than 20% [197]. The signal cross section increases by 20–230% over the mass range of simulated CI samples.

The photon channel follows a more sophisticated approach by calculating the appropriate background cross sections and attempting to model the expected detector response using a parametrization of the detector's efficiencies and resolutions. The same group from the Seoul National University that performed the analysis produced the HL-LHC projects as well. Ref. [198] describes their model.

This thesis' approach is less precise but can still provide a reasonable estimate of the HL-LHC's potential for excited lepton searches. The statistical methods follow precisely the description of the previous chapter. This study only provides the expected limit because the data have not been taken yet. It utilizes the 2017 MC simulation as it has more generated events than the 2016 MC.

Figure 9.1 presents the expected exclusion limit in the Λ-mass plane for couplings equal to unity. All limits show a significant improvement over the present exclusion limits. The CI channel is expected to include excited electrons up to 7 TeV and even beyond that in the muon channel – an increase of at least 25% of the mass limit. The exact mass limit cannot be calculated because no signal was simulated above a mass of 7 TeV. The photon channel only studies the high-mass region between 3.5 and 6.5 TeV. In this region, it can significantly increase its expected mass sensitivity up to 5.5 TeV for both channels compared to 3.8 TeV using the 2016 dataset.

The Z channel shows a smaller improvement. The maximal excluded mass rises from 3.5 to 4.5 TeV and the maximal excluded value of Λ for masses around 1 TeV from 14 and 15 TeV up to 22 and 24 TeV for the electron and muon channel respectively. The Run 2 analysis was competitive with the photon channel at high masses. In the HL-LHC scenario, the distance is much larger. One reason is that the Run 2 photon channel analysis only utilized the 2016 dataset and not the combination of 2016 and 2017. The other reason is the background regression: For Run 2, the selection was able to reduce the total Standard Model expectation to less than one event at high

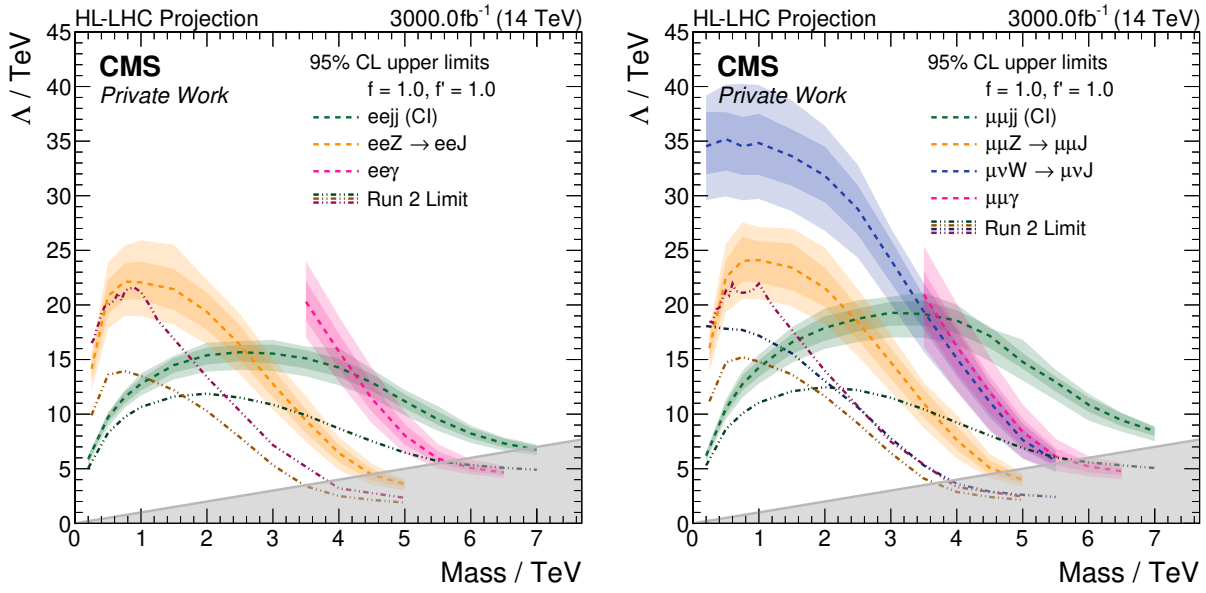

(a) (b)

Figure 9.1: Projected limits for the HL-LHC dataset for (a) excited electrons and (b) excited muons in terms of the mass and Λ. Both couplings are fixed to unity. The curves show the maximal excluded value for Λ. The dashed line the expected limit with the one and two sigma bands in lighter shades of the corresponding color. The darker dotted-dashed lines show the Run 2 limits. Everything below the curves is excluded, and the grey region in which the mass is greater than Λ is theoretically forbidden. The high-mass limit improves by 25% and the low-mass exclusion power by up to 100% compared to the Run 2 limits.

masses. With the HL-LHC dataset, the requirements are not sufficient to reduce the background by the same amount.

Finally, the W channel[1] increases its high-mass sensitivity by the same amount as the photon channel. Both Run 2 analyses used the same dataset and obtained a similar high-mass limit. In the HL-LHC projection, both channels predict again comparable values of 5.5 TeV for the high-mass limit. At low masses, the limit nearly doubles from a maximal excluded Λ of 18 TeV using the 2016 data to 35 TeV for the HL-LHC projection.

This study projected the sensitivity of the analyses using the Run 2 selection and efficiencies. The selection was optimized using the expected number of events using the Run 2 dataset. Since the expected total integrated luminosity of the HL-LHC is more than an order of magnitude higher, the Run 2 selection will not suppress the background as efficiently as for the Run 2 analysis. In Run 2, the selection decreased the expected background to less than one event in the high-mass bins of each channel. The sensitivity can increase even further if the selection can be improved to maintain such a low background level while not decreasing the signal efficiency.

The CI channel projects a background of 3.5 events in the highest mass bin. The cross section limit could improve by another factor of two if the background gets reduced to less than one event. The increase of the high-mass limit cannot be reasonable judged because no signal masses

[1] The W channel was only analyzed in the context of excited muons.

above 7 TeV were produced.[2] The Z channel has the largest projected background of all channels with 29 events. Therefore, its limit does increase by a smaller amount than the W and photon channel in the projection. Reducing the background to the current level would improve the limit at a mass of 2 TeV to roughly 35 TeV from currently 21 TeV. Finally, the W channel has a projected background of nine events in the highest mass bin. If the selection can suppress these events while maintaining the current signal efficiency, the cross section limit can improve by roughly a factor of three while the maximally excluded value of Λ rises to 45 TeV from currently 32 TeV at a $\ell^\star$ mass of 2 TeV. Further increases of the signal efficiency would improve the limit in a similar way.

This chapter concludes the work presented by this thesis. We expect the sensitivity of excited lepton searches to increase mass limit by roughly 25% and maximally excluded value of Λ by up to 100% at low masses. Other coupling scenarios impact the exclusion limits similarly to the results presented in the last chapter. The next chapter will summarize this thesis.

[2] The signals were produced for the Run 2 analysis and not with regard to the HL-LHC outlook.

10 | Summary

This thesis presented the search for excited electrons and muons. It utilized the proton-proton collision data delivered by the Large Hadron Collider (LHC) which were recorded by the Compact Muon Solenoid (CMS) detector in 2016 and 2017. The integrated luminosity of the analyzed dataset totals $77.4\,\mathrm{fb}^{-1}$.

Excited leptons are a direct consequence of compositeness in the fermion sector. If the leptons of the Standard Model are not point-like particles but composite objects, we can produce them in excited states and observe their decay products. Hypothetical excited leptons are produced in conjunction with a Standard Model lepton via a contact interaction of two quarks and can decay in four different ways: Via a contact interaction producing final states with two same-flavor leptons and two other fermions, or by radiating either a photon or a W or Z boson. This thesis analyzed the contact interaction decay channel in final states with two leptons and two jets as well as the W and Z decay channels where the boson decays hadronically. The W channel results in a final state containing a single lepton, a wide-cone jet and missing transverse momentum, and the Z channel in two same-flavor leptons and a wide-cone jet. The search in the W decay channel was carried out only for excited muons using the 2016 dataset.

Both the contact interaction as well as the W channel had not been analyzed by CMS so far because the contact interaction decay was not implemented in Pythia6 and the W channel due to the challenging final state. Together with the Z channel and the photon channel which was analyzed by a different CMS group, this thesis completed the picture of the excited lepton decays. It was the first scientific work accomplishing this for modern hadron colliders.

No significant deviation from the Standard Model prediction has been observed. 95% confidence level exclusion limits were calculated for all three channels. The sensitivity was compared for different sets of model parameters. This thesis was the first one to include an extensive study of the sensitivity regarding all model parameters.

The contact interaction is the most sensitive channel for heavy excited leptons and weak couplings. Its high-mass exclusion limit for the normal benchmark scenario of couplings equal to unity and the interaction scale Λ equal to the mass of the excited lepton is the best limit to date with an exclusion range of up to 5.6 TeV. Below masses of 2.5 TeV the gauge mediated channels provided a better sensitivity than the contact interaction channel and were able to exclude larger values for the interaction scale Λ of up to 15 TeV. The photon channel remained the most sensitive channel for light excited leptons for couplings of unity. The Z channel became the dominant channel for couplings of opposite sign while the W channel became competitive for $f' = 0$. For weaker couplings of 0.1, the contact interaction started to dominate at 1 TeV.

With these unrivaled exclusion limits, this thesis marks the culmination of the almost forty-year long endeavor of excited leptons searches. But it will not be the end of it as the High Luminosity LHC (HL-LHC) will start operation after the upcoming final run period of the LHC. This thesis provided a projection of the sensitivity of all decay channels for the HL-LHC. The high-mass limit is expected to increase by 25% up to 7 TeV and the excluded values for Λ low masses even by up to 100%.

Bibliography

[1] S. Berryman, "Ancient Atomism", in *The Stanford Encyclopedia of Philosophy*, E. N. Zalta, ed. Metaphysics Research Lab, Stanford University, winter 2016 edition, 2016.

[2] ALEPH, DELPHI, L3, OPAL, LEP Electroweak Collaboration, "Electroweak Measurements in Electron-Positron Collisions at W-Boson-Pair Energies at LEP", *Phys. Rept.* **532** (2013) 119–244, arXiv:1302.3415. doi:10.1016/j.physrep.2013.07.004.

[3] ALEPH, DELPHI, L3, OPAL, SLD, LEP Electroweak Working Group, SLD Electroweak Group, SLD Heavy Flavour Group Collaboration, "Precision electroweak measurements on the Z resonance", *Phys. Rept.* **427** (2006) 257–454, arXiv:hep-ex/0509008. doi:10.1016/j.physrep.2005.12.006.

[4] Particle Data Group Collaboration, "Review of Particle Physics", *Phys. Rev. D* **98** (2018), no. 3, 030001. doi:10.1103/PhysRevD.98.030001.

[5] CMS Collaboration, "Search for excited leptons in $\ell\ell\gamma$ final states in proton-proton collisions at $\sqrt{s} = 13$ TeV", *JHEP* **04** (2019) 015, arXiv:1811.03052. doi:10.1007/JHEP04(2019)015.

[6] CMS Collaboration, "Search for an excited lepton that decays via a contact interaction to a lepton and two jets in proton-proton collisions at $\sqrt{s} = 13$ TeV", *JHEP* **05** (2020) 052, arXiv:2001.04521. doi:10.1007/JHEP05(2020)052.

[7] F. Capozzi, E. Lisi, A. Marrone et al., "Neutrino masses and mixings: Status of known and unknown 3ν parameters", *Nucl. Phys.* **B908** (2016) 218–234, arXiv:1601.07777. doi:10.1016/j.nuclphysb.2016.02.016.

[8] P. W. Higgs, "Broken symmetries, massless particles and gauge fields", *Phys. Lett.* **12** (1964) 132–133. doi:10.1016/0031-9163(64)91136-9.

[9] F. Englert and R. Brout, "Broken Symmetry and the Mass of Gauge Vector Mesons", *Phys. Rev. Lett.* **13** (1964) 321–323. doi:10.1103/PhysRevLett.13.321.

[10] P. W. Higgs, "Broken Symmetries and the Masses of Gauge Bosons", *Phys. Rev. Lett.* **13** (1964) 508–509. doi:10.1103/PhysRevLett.13.508.

[11] G. Guralnik, C. Hagen, and T. Kibble, "Global Conservation Laws and Massless Particles", *Phys. Rev. Lett.* **13** (1964) 585–587. doi:10.1103/PhysRevLett.13.585.

[12] P. W. Higgs, "Spontaneous Symmetry Breakdown without Massless Bosons", *Phys. Rev.* **145** (1966) 1156–1163. doi:10.1103/PhysRev.145.1156.

[13] T. Kibble, "Symmetry breaking in non-Abelian gauge theories", *Phys. Rev.* **155** (1967) 1554–1561. doi:10.1103/PhysRev.155.1554.

[14] CMS Collaboration, "Observation of a New Boson at a Mass of 125 GeV with the CMS Experiment at the LHC", *Phys. Lett. B* **716** (2012) 30–61, arXiv:1207.7235. doi:10.1016/j.physletb.2012.08.021.

[15] ATLAS Collaboration, "Observation of a new particle in the search for the Standard Model Higgs boson with the ATLAS detector at the LHC", *Phys. Lett. B* **716** (2012) 1–29, arXiv:1207.7214. doi:10.1016/j.physletb.2012.08.020.

[16] F. Halzen and A. D. Martin, "Quarks and leptons: an introductory course in modern particle physics". Wiley, New York, 1984.

[17] D. J. Griffiths, "Introduction to elementary particles". Physics textbook. Wiley-VCH, Weinheim, 2., rev. ed., 5. reprint edition, 2011. OCLC: 711866653.

[18] U. Baur, M. Spira, and P. Zerwas, "Excited Quark and Lepton Production at Hadron Colliders", *Phys. Rev. D* **42** (1990) 815–824. doi:10.1103/PhysRevD.42.815.

[19] F. Low, "Heavy electrons and muons", *Phys. Rev. Lett.* **14** (1965) 238–239. doi:10.1103/PhysRevLett.14.238.

[20] F. Renard, "Limits on Masses and Couplings of Excited Electrons and Muons", *Phys. Lett. B* **116** (1982) 264–268. doi:10.1016/0370-2693(82)90339-2.

[21] S. J. Brodsky and S. Drell, "The Anomalous Magnetic Moment and Limits on Fermion Substructure", *Phys. Rev. D* **22** (1980) 2236. doi:10.1103/PhysRevD.22.2236.

[22] U. Baur, I. Hinchliffe, and D. Zeppenfeld, "Excited Quark Production at Hadron Colliders", *Int. J. Mod. Phys. A* **2** (1987) 1285. doi:10.1142/S0217751X87000661.

[23] I. Bars and I. Hinchliffe, "The Effects of Quark Compositeness at the SSC", *Phys. Rev. D* **33** (1986) 704. doi:10.1103/PhysRevD.33.704.

[24] E. Eichten, I. Hinchliffe, K. D. Lane et al., "Super Collider Physics", *Rev. Mod. Phys.* **56** (1984) 579–707. [Addendum: Rev.Mod.Phys. 58, 1065–1073 (1986)]. doi:10.1103/RevModPhys.56.579.

[25] J. H. Kuhn and P. M. Zerwas, "Excited Quarks and Leptons", *Phys. Lett. B* **147** (1984) 189–196. doi:10.1016/0370-2693(84)90618-X.

[26] K. Hagiwara, D. Zeppenfeld, and S. Komamiya, "Excited Lepton Production at LEP and HERA", *Z. Phys. C* **29** (1985) 115. doi:10.1007/BF01571391.

[27] J. H. Kuhn, H. Tholl, and P. Zerwas, "Signals of Excited Quarks and Leptons", *Phys. Lett. B* **158** (1985) 270. doi:10.1016/0370-2693(85)90969-4.

[28] F. Boudjema, A. Djouadi, and J. Kneur, "Excited fermions at e+ e- and e P colliders", *Z. Phys. C* **57** (1993) 425–450. doi:10.1007/BF01474339.

[29] O. Cakir, C. Leroy, R. R. Mehdiyev et al., "Production and decay of excited electrons at the LHC", *Eur. Phys. J. C* **32** (2004), no. S2, 1–17, arXiv:hep-ph/0212006. doi:10.1140/epjcd/s2003-01-005-5.

[30] O. Eboli, S. Lietti, and P. Mathews, "Excited leptons at the CERN large hadron collider", *Phys. Rev. D* **65** (2002) 075003, arXiv:hep-ph/0111001. doi:10.1103/PhysRevD.65.075003.

[31] N. Cabibbo, L. Maiani, and Y. Srivastava, "Anomalous Z Decays: Excited Leptons?", *Phys. Lett. B* **139** (1984) 459–463. doi:10.1016/0370-2693(84)91850-1.

[32] F. Renard, "Interpretations of $Z \to ee\gamma$ Events and Additional Tests", *Phys. Lett. B* **139** (1984) 449–454. doi:10.1016/0370-2693(84)91848-3.

[33] A. De Rujula, L. Maiani, and R. Petronzio, "Search for Excited Quarks", *Phys. Lett. B* **140** (1984) 253–258. doi:10.1016/0370-2693(84)90930-4.

[34] UA1 Collaboration, "Experimental Observation of Lepton Pairs of Invariant Mass Around 95 GeV/c^2 at the CERN SPS Collider", *Phys. Lett. B* **126** (1983) 398–410. doi:10.1016/0370-2693(83)90188-0.

[35] UA2 Collaboration, "Evidence for $Z^0 \to e^+e^-$ at the CERN $\bar{p}p$ Collider", *Phys. Lett. B* **129** (1983) 130–140. doi:10.1016/0370-2693(83)90744-X.

[36] Muon g-2 Collaboration, "Final Report of the Muon E821 Anomalous Magnetic Moment Measurement at BNL", *Phys. Rev. D* **73** (2006) 072003, arXiv:hep-ex/0602035. doi:10.1103/PhysRevD.73.072003.

[37] T. Sjöstrand, S. Ask, J. R. Christiansen et al., "An Introduction to PYTHIA 8.2", *Comput. Phys. Commun.* **191** (2015) 159–177, arXiv:1410.3012. doi:10.1016/j.cpc.2015.01.024.

[38] S. Biondini, R. Leonardi, O. Panella et al., "Perturbative unitarity bounds for effective composite models", *Phys. Lett. B* **795** (2019) 644–649, arXiv:1903.12285. [Erratum: Phys.Lett.B 799, 134990 (2019)]. doi:10.1016/j.physletb.2019.06.042.

[39] DELPHI Collaboration, "Search for excited leptons in e+ e- collisions at $\sqrt{s}$ = 189 – 209 GeV", *Eur. Phys. J.* **C46** (2006) 277–293, arXiv:hep-ex/0603045. doi:10.1140/epjc/s2006-02501-3.

[40] DESY, "PETRA: updated version of the PETRA proposal". DESY, Hamburg, 1976.

[41] SLAC, "PEP conceptual design report". Lawrence Berkeley Nat. Lab., Berkeley, CA, 1976.

[42] KEK, Tsukuba, "TRISTAN, electron-positron colliding beam project". KEK, Tsukuba, 1987.

[43] CERN, "LEP design report". CERN, Geneva, 1984. Copies shelved as reports in LEP, PS and SPS libraries.

[44] C. Wyss, "LEP design report, v.3: LEP2". CERN, Geneva, 1996. Vol. 1-2 publ. in 1983-84.

[45] Mark J Collaboration, "Experimental Limits on the Production of Excited Leptons and Stable Heavy Leptons", *Phys. Rev. Lett.* **48** (1982) 967. doi:10.1103/PhysRevLett.48.967.

[46] JADE Collaboration, "Measurement of the Processes $e^+e^- \to e^+e^-$ and $e^+e^- \to \gamma\gamma$ at PETRA", *Z. Phys.* **C19** (1983) 197. doi:10.1007/BF01572248.

[47] CELLO Collaboration, "EXCITED LEPTON SEARCH", *Phys. Lett.* **168B** (1986) 420–426. doi:10.1016/0370-2693(86)91656-4.

[48] DELCO Collaboration, "Quasireal Compton Scattering Measurement and e^* Search With Delco at PEP", *Phys. Lett. B* **177** (1986) 109–114. doi:10.1016/0370-2693(86)90025-0.

[49] AMY Collaboration, "Search for the Substructure of Leptons in High-energy QED Processes at Tristan", *Phys. Lett.* **B223** (1989) 476–484. doi:10.1016/0370-2693(89)91636-5.

[50] TOPAZ Collaboration, "A Search for Excited Leptons in the Energy Region $\sqrt{s} = 52 - 60.8$ GeV", *Phys. Lett. B* **228** (1989) 553–559. doi:10.1016/0370-2693(89)90992-1.

[51] Venus Collaboration, "A Search for Excited Electrons in the e^+e^- Reactions Up to the $\sqrt{s}$ of 56 GeV", *Phys. Lett.* **B213** (1988) 400–404. doi:10.1016/0370-2693(88)91784-4.

[52] ALEPH Collaboration, "Search for Excited Leptons in Z^0 Decay", *Phys. Lett.* **B236** (1990) 501–510. doi:10.1016/0370-2693(90)90391-I.

[53] ALEPH Collaboration, "Search for excited leptons at 130 – 140 GeV", *Phys. Lett.* **B385** (1996) 445–453. doi:10.1016/0370-2693(96)00961-6.

[54] L3 Collaboration, "Search for excited leptons at LEP", *Phys. Lett.* **B568** (2003) 23–34, arXiv:hep-ex/0306016. doi:10.1016/j.physletb.2003.05.004.

[55] OPAL Collaboration, "Search for unstable heavy and excited leptons at LEP 2", *Eur. Phys. J.* **C14** (2000) 73–84, arXiv:hep-ex/0001056. doi:10.1007/s100520000345, 10.1007/s100520050734.

[56] OPAL Collaboration, "Search for charged excited leptons in e+ e- collisions at $\sqrt{s}$ = 183 – 209 GeV", *Phys. Lett.* **B544** (2002) 57–72, arXiv:hep-ex/0206061. doi:10.1016/S0370-2693(02)02343-2.

[57] LHeC Study Group Collaboration, "A Large Hadron Electron Collider at CERN: Report on the Physics and Design Concepts for Machine and Detector", *J. Phys. G* **39** (Jun, 2012) 075001. 633 p. doi:10.1088/0954-3899/39/7/075001.

[58] The HERA Collaboration, "HERA - A Proposal for a Large Electron Proton Colliding Beam Facility at DESY". DESY, 1981.

[59] H1 Collaboration, "Search for Excited Electrons in ep Collisions at HERA", *Phys. Lett.* **B666** (2008) 131–139, arXiv:0805.4530. doi:10.1016/j.physletb.2008.07.014.

[60] ZEUS Collaboration, "Searches for excited fermions in *ep* collisions at HERA", *Phys. Lett.* **B549** (2002) 32–47, arXiv:hep-ex/0109018. doi:10.1016/S0370-2693(02)02863-0.

[61] O. S. Brüning, P. Collier, P. Lebrun et al., "LHC Design Report". CERN Yellow Reports: Monographs. CERN, Geneva, 2004.

[62] A. Giammanco, "TOP2017: Experimental Summary", in *Proceedings, 10th International Workshop on Top Quark Physics (TOP2017): Braga, Portugal, September 17-22, 2017*. 2017. arXiv:1712.02177.

[63] B. Autin et al., "Design Study of a Proton-anti-Proton Colliding Beam Facility", Technical Report CERN-PS-AA-78-3, CERN, 1978.

[64] Fermilab, "Fermilab TeV Program, Superconducting Magnet Ring: Energy Doubler, Energy Saver, Colliding Beams", Technical Report FERMILAB-MISC-1977-01, Fermilab, 1977.

[65] UA2 Collaboration, "Search for Exotic Processes at the CERN $p\bar{p}$ Collider", *Phys. Lett.* **B195** (1987) 613. [,473(1987)]. doi:10.1016/0370-2693(87)91583-8.

[66] CDF Collaboration, "Search for excited and exotic electrons in the $e\gamma$ decay channel in $p\bar{p}$ collisions at $\sqrt{s} = 1.96$ TeV", *Phys. Rev. Lett.* **94** (2005) 101802, arXiv:hep-ex/0410013. doi:10.1103/PhysRevLett.94.101802.

[67] Do Collaboration, "Search for excited muons in $p\bar{p}$ collisions at $\sqrt{s}$ = 1.96- TeV", *Phys. Rev.* **D73** (2006) 111102, arXiv:hep-ex/0604040. doi:10.1103/PhysRevD.73.111102.

[68] CDF Collaboration, "Search for excited and exotic muons in the $\mu\gamma$ decay channel in $p\bar{p}$ collisions at $\sqrt{s}$ = 1.96 TeV", *Phys. Rev. Lett.* **97** (2006) 191802, arXiv:hep-ex/0606043. doi:10.1103/PhysRevLett.97.191802.

[69] ATLAS Collaboration, "Search for excited electrons and muons in $\sqrt{s}$=8 TeV proton-proton collisions with the ATLAS detector", *New J. Phys.* **15** (2013) 093011, arXiv:1308.1364. doi:10.1088/1367-2630/15/9/093011.

[70] ATLAS Collaboration, "A search for an excited muon decaying to a muon and two jets in pp collisions at $\sqrt{s}$ = 8 TeV with the ATLAS detector", *New J. Phys.* **18** (2016), no. 7, 073021, arXiv:1601.05627. [Erratum: New J. Phys.21,no.10,109501(2019)]. doi:10.1088/1367-2630/ab46ed, 10.1088/1367-2630/18/7/073021.

[71] ATLAS Collaboration, "Search for excited electrons singly produced in proton–proton collisions at $\sqrt{s} = 13$ TeV with the ATLAS experiment at the LHC", *Eur. Phys. J.* **C79** (2019), no. 9, 803, arXiv:1906.03204. doi:10.1140/epjc/s10052-019-7295-1.

[72] CMS Collaboration, "Search for excited leptons in pp collisions at $\sqrt{s} = 7$ TeV", *Phys. Lett.* **B720** (2013) 309–329, arXiv:1210.2422. doi:10.1016/j.physletb.2013.02.031.

[73] CMS Collaboration, "Search for Excited Leptons in Proton-Proton Collisions at $\sqrt{s}$ = 8 TeV", *JHEP* **03** (2016) 125, arXiv:1511.01407. doi:10.1007/JHEP03(2016)125.

[74] E. Mobs, "The CERN accelerator complex. Complexe des accélérateurs du CERN". https://cds.cern.ch/record/2197559, Jul, 2016.

[75] CMS Collaboration, "The CMS Experiment at the CERN LHC", *JINST* **3** (2008) S08004. doi:10.1088/1748-0221/3/08/S08004.

[76] E. Regenstreif, "The CERN Proton Synchrotron, pt.1". CERN Yellow Reports: Monographs. CERN, Geneva, 1959. French version published as CERN 58-06.

[77] The CERN Study Group on New Accelerators, "Report on the design study of a 300 GeV proton synchrotron". CERN, Geneva, 1964.

[78] M. Schaumann et al., "First Xenon-Xenon Collisions in the LHC", in *Proceedings, 9th International Particle Accelerator Conference (IPAC 2018): Vancouver, BC Canada, April 29-May 4, 2018*, p. MOPMF039. 2018.

[79] ATLAS Collaboration, "The ATLAS Experiment at the CERN Large Hadron Collider", *JINST* **3** (2008) S08003. doi:10.1088/1748-0221/3/08/S08003.

[80] ALICE Collaboration, "The ALICE experiment at the CERN LHC", *JINST* **3** (2008) S08002. doi:10.1088/1748-0221/3/08/S08002.

[81] LHCb Collaboration, "The LHCb Detector at the LHC", *JINST* **3** (2008) S08005. doi:10.1088/1748-0221/3/08/S08005.

[82] M. Aicheler, P. Burrows, M. Draper et al., "A Multi-TeV Linear Collider Based on CLIC Technology: CLIC Conceptual Design Report". CERN Yellow Reports: Monographs. CERN, Geneva, 2012.

[83] ILC Collaboration, "ILC Reference Design Report Volume 1 - Executive Summary", arXiv:0712.1950.

[84] FCC Collaboration, "FCC-ee: The Lepton Collider", *Eur. Phys. J. ST* **228** (2019), no. 2, 261–623. doi:10.1140/epjst/e2019-900045-4.

[85] CEPC Study Group Collaboration, "CEPC Conceptual Design Report: Volume 1 - Accelerator", arXiv:1809.00285.

[86] FCC Collaboration, "FCC-hh: The Hadron Collider", *Eur. Phys. J. ST* **228** (2019), no. 4, 755–1107. doi:10.1140/epjst/e2019-900087-0.

[87] G. Apollinari, I. Béjar Alonso, O. Brüning et al., "High-Luminosity Large Hadron Collider (HL-LHC) : Preliminary Design Report". CERN Yellow Reports: Monographs. CERN, Geneva, 2015.

[88] FCC Collaboration, "HE-LHC: The High-Energy Large Hadron Collider Volume", *Eur. Phys. J. ST* **228** (2019), no. 5, 1109–1382. doi:10.1140/epjst/e2019-900088-6.

[89] CMS Collaboration, "CMS Luminosity - Public Results". https://twiki.cern.ch/twiki/bin/view/CMSPublic/LumiPublicResults, 2019 (accessed October 21, 2019).

[90] F. Antoniou et al., "Can We Predict Luminosity?", in *Proceedings, 7th Evian Workshop, France*. 2016.

[91] R. Bruce et al., "REVIEW OF LHC RUN 2 MACHINE CONFIGURATIONS", in *Proceedings, 9th LHC Operations Evian Workshop, France*. 2019.

[92] J. M. Campbell, J. W. Huston, and W. J. Stirling, "Hard Interactions of Quarks and Gluons: A Primer for LHC Physics", *Rept. Prog. Phys.* **70** (2007) 89, arXiv:hep-ph/0611148. doi:10.1088/0034-4885/70/1/R02.

[93] L. Mether et al., "16L2: OPERATION, OBSERVATIONS AND PHYSICS ASPECTS", in *Proceedings, 8th LHC Operations Evian Workshop, France*. 2018.

[94] NNPDF Collaboration, "Parton distributions from high-precision collider data", *Eur. Phys. J.* **C77** (2017), no. 10, 663, arXiv:1706.00428. doi:10.1140/epjc/s10052-017-5199-5.

[95] G. Altarelli and G. Parisi, "Asymptotic Freedom in Parton Language", *Nucl. Phys. B* **126** (1977) 298–318. doi:10.1016/0550-3213(77)90384-4.

[96] V. Gribov and L. Lipatov, "Deep inelastic electron scattering in perturbation theory", *Phys. Lett. B* **37** (1971) 78–80. doi:10.1016/0370-2693(71)90576-4.

[97] Y. L. Dokshitzer, "Calculation of the Structure Functions for Deep Inelastic Scattering and e+ e- Annihilation by Perturbation Theory in Quantum Chromodynamics.", *Sov. Phys. JETP* **46** (1977) 641–653.

[98] S. Carrazza, S. Forte, Z. Kassabov et al., "An Unbiased Hessian Representation for Monte Carlo PDFs", *Eur. Phys. J.* **C75** (2015), no. 8, 369, arXiv:1505.06736. doi:10.1140/epjc/s10052-015-3590-7.

[99] CMS Collaboration, "Technical proposal for the upgrade of the CMS detector through 2020", Technical Report CERN-LHCC-2011-006. LHCC-P-004, CMS, Jun, 2011.

[100] CMS Collaboration, "Description and performance of track and primary-vertex reconstruction with the CMS tracker", *JINST* **9** (2014), no. 10, P10009, arXiv:1405.6569. doi:10.1088/1748-0221/9/10/P10009.

[101] D. A. Matzner Dominguez, D. Abbaneo, K. Arndt et al., "CMS Technical Design Report for the Pixel Detector Upgrade", Technical Report CERN-LHCC-2012-016, CMS-TDR-011, CMS, 2012.

[102] S. Hasegawa et al., "Operational Experience on Pixel tracker at CMS experiment", in *The 27th International Workshop on Vertex Detectors, Chennai*. 2018.

[103] G. Boudoul et al., "Status of the Strip hit inefficiency (HIP) studies", in *CMS General Meeting: WGM 277*. 2016.

[104] E. Butz et al., "Mitigation of the Strip Tracker Dynamic Inefficiency (previously known as HIP)", in *CMS General Meeting: WGM 278*. 2016.

[105] N. Smith et al., "Status and plans for ECAL endcap prefiring studies", in *CMS Week, Geneva*. 2018.

[106] J. Mans, J. Anderson, B. Dahmes et al., "CMS Technical Design Report for the Phase 1 Upgrade of the Hadron Calorimeter", Technical Report CERN-LHCC-2012-015, CMS-TDR-010, CMS, 2012.

[107] G. Petrucciani, "CMS Status Report", in *130th LHCC Meeting - OPEN Session, Geneva*. 2017.

[108] G. Boudoul, "CMS Status Report", in *139th LHCC Meeting - OPEN Session, Geneva*. 2019.

[109] M. A. Akl et al., "CMS Technical Design Report for the Muon Endcap GEM Upgrade", Technical Report CERN-LHCC-2015-012, CMS-TDR-013, CMS, 2015.

[110] CMS Collaboration, "CMS reconstruction improvement for the muon tracking by the RPC chambers", *PoS* **RPC2012** (2012) 045, arXiv:1209.2646. [JINST8,T03001(2013)]. doi:10.1088/1748-0221/8/03/T03001, 10.22323/1.159.0045.

[111] CMS Collaboration, "Performance of the reconstruction and identification of high-momentum muons in proton-proton collisions at $\sqrt{s} = 13$ TeV", *JINST* **15** (2020), no. 02, P02027, arXiv:1912.03516. doi:10.1088/1748-0221/15/02/P02027.

[112] CMS Collaboration, "Calibration of the CMS Drift Tube Chambers and Measurement of the Drift Velocity with Cosmic Rays", *JINST* **5** (2010) T03016, arXiv:0911.4895. doi:10.1088/1748-0221/5/03/T03016.

[113] CMS Collaboration, "The Phase-2 Upgrade of the CMS Muon Detectors", Technical Report CERN-LHCC-2017-012. CMS-TDR-016, CERN, Geneva, Sep, 2017. This is the final version, approved by the LHCC.

[114] CMS Collaboration, A. Tapper and D. Acosta, "CMS Technical Design Report for the Level-1 Trigger Upgrade", Technical Report CERN-LHCC-2013-011, CMS-TDR-12, CMS-TDR-012, CMS, 2013.

[115] Donato, Silvio, "CMS trigger performance", *EPJ Web Conf.* **182** (2018) 02037. doi:10.1051/epjconf/201818202037.

[116] CMS Collaboration, "Mini-AOD: A New Analysis Data Format for CMS", *J. Phys. Conf. Ser.* **664** (2015), no. 7, 7, arXiv:1702.04685. doi:10.1088/1742-6596/664/7/072052.

[117] R. Brun and F. Rademakers, "ROOT: An object oriented data analysis framework", *Nucl. Instrum. Meth.* **A389** (1997) 81–86. doi:10.1016/S0168-9002(97)00048-X.

[118] I. Antcheva et al., "ROOT: A C++ framework for petabyte data storage, statistical analysis and visualization", *Comput. Phys. Commun.* **180** (2009) 2499–2512, arXiv:1508.07749. doi:10.1016/j.cpc.2009.08.005.

[119] H. P. Bretz et al., "A Development Environment for Visual Physics Analysis", *JINST* **7** (2012) T08005, arXiv:1205.4912. doi:10.1088/1748-0221/7/08/T08005.

[120] M. Erdmann et. al., "Physics eXtension Library". https://vispa.physik.rwth-aachen.de/pxl.

[121] III. Physics Institute A, RWTH Aachen University, "Three A Physics Analysis Software (TAPAS)". https://gitlab.cern.ch/aachen-3a.

[122] CMS Collaboration, "The combine framework". https://github.com/cms-analysis/HiggsAnalysis-CombinedLimit, 2020 (accessed April 24, 2020).

[123] I. Bird, K. Bos, N. Brook et al., "LHC computing Grid. Technical design report". Technical Design Report LCG. CERN, Geneva, 2005.

[124] CMS Collaboration, "Public CMS Data Quality Information". https://twiki.cern.ch/twiki/bin/view/CMSPublic/DataQuality, 2019 (accessed December 05, 2019).

[125] ALEPH Collaboration, "Performance of the ALEPH detector at LEP", *Nucl. Instrum. Meth.* **A360** (1995) 481–506. doi:10.1016/0168-9002(95)00138-7.

[126] CMS Collaboration, "Particle-flow reconstruction and global event description with the CMS detector", *JINST* **12** (2017), no. 10, P10003, arXiv:1706.04965. doi:10.1088/1748-0221/12/10/P10003.

[127] W. Adam, B. Mangano, T. Speer et al., "Track reconstruction in the CMS tracker", Technical Report CMS-NOTE-2006-041, CERN, Geneva, Dec, 2006.

[128] W. Adam, R. Frühwirth, A. Strandlie et al., "Reconstruction of Electrons with the Gaussian-Sum Filter in the CMS Tracker at the LHC", Technical Report CMS-NOTE-2005-001, CERN, Geneva, Jan, 2005.

[129] CMS Collaboration, "Performance of Photon Reconstruction and Identification with the CMS Detector in Proton-Proton Collisions at sqrt(s) = 8 TeV", *JINST* **10** (2015), no. 08, P08010, arXiv:1502.02702. doi:10.1088/1748-0221/10/08/P08010.

[130] CMS Collaboration, "Performance of the CMS muon detector and muon reconstruction with proton-proton collisions at $\sqrt{s} = 13$ TeV", *JINST* **13** (2018), no. 06, P06015, arXiv:1804.04528. doi:10.1088/1748-0221/13/06/P06015.

[131] CMS Collaboration, "Performance of Electron Reconstruction and Selection with the CMS Detector in Proton-Proton Collisions at $\sqrt{s} = 8$ TeV", *JINST* **10** (2015), no. 06, P06005, arXiv:1502.02701. doi:10.1088/1748-0221/10/06/P06005.

[132] G. P. Salam and G. Soyez, "A Practical Seedless Infrared-Safe Cone jet algorithm", *JHEP* **05** (2007) 086, arXiv:0704.0292. doi:10.1088/1126-6708/2007/05/086.

[133] Y. L. Dokshitzer, G. D. Leder, S. Moretti et al., "Better jet clustering algorithms", *JHEP* **08** (1997) 001, arXiv:hep-ph/9707323. doi:10.1088/1126-6708/1997/08/001.

[134] M. Wobisch and T. Wengler, "Hadronization corrections to jet cross-sections in deep inelastic scattering", in *Monte Carlo generators for HERA physics. Proceedings, Workshop, Hamburg, Germany, 1998-1999*, pp. 270–279. 1998. arXiv:hep-ph/9907280.

[135] S. D. Ellis and D. E. Soper, "Successive combination jet algorithm for hadron collisions", *Phys. Rev.* **D48** (1993) 3160–3166, arXiv:hep-ph/9305266. doi:10.1103/PhysRevD.48.3160.

[136] M. Cacciari, G. P. Salam, and G. Soyez, "The anti-k_t jet clustering algorithm", *JHEP* **04** (2008) 063, arXiv:0802.1189. doi:10.1088/1126-6708/2008/04/063.

[137] M. Cacciari, G. P. Salam, and G. Soyez, "FastJet User Manual", *Eur. Phys. J.* **C72** (2012) 1896, arXiv:1111.6097. doi:10.1140/epjc/s10052-012-1896-2.

[138] D. Bertolini, P. Harris, M. Low et al., "Pileup Per Particle Identification", *JHEP* **10** (2014) 059, arXiv:1407.6013. doi:10.1007/JHEP10(2014)059.

[139] CMS Collaboration, "Pileup mitigation at CMS in 13 TeV data", arXiv:2003.00503.

[140] A. J. Larkoski, S. Marzani, G. Soyez et al., "Soft Drop", *JHEP* **05** (2014) 146, arXiv:1402.2657. doi:10.1007/JHEP05(2014)146.

[141] S. D. Ellis, C. K. Vermilion, and J. R. Walsh, "Recombination Algorithms and Jet Substructure: Pruning as a Tool for Heavy Particle Searches", *Phys. Rev.* **D81** (2010) 094023, arXiv:0912.0033. doi:10.1103/PhysRevD.81.094023.

[142] J. Thaler and K. Van Tilburg, "Identifying Boosted Objects with N-subjettiness", *JHEP* **03** (2011) 015, arXiv:1011.2268. doi:10.1007/JHEP03(2011)015.

[143] J. Thaler and K. Van Tilburg, "Maximizing Boosted Top Identification by Minimizing N-subjettiness", *JHEP* **02** (2012) 093, arXiv:1108.2701. doi:10.1007/JHEP02(2012)093.

[144] T. K. Aarrestad, A. Hinzmann, C. Lange et al., "Identification and calibration of boosted hadronic W/Z bosons at 13 TeV", Technical Report AN-2016/215, CMS, 2016.

[145] CMS Collaboration, "Jet algorithms performance in 13 TeV data", Technical Report CMS-PAS-JME-16-003, CERN, Geneva, 2017.

[146] CMS Collaboration, "Jet energy scale and resolution in the CMS experiment in pp collisions at 8 TeV", *JINST* **12** (2017), no. 02, P02014, arXiv:1607.03663. doi:10.1088/1748-0221/12/02/P02014.

[147] CMS Collaboration, "Identification of heavy-flavour jets with the CMS detector in pp collisions at 13 TeV", *JINST* **13** (2018), no. 05, P05011, arXiv:1712.07158. doi:10.1088/1748-0221/13/05/P05011.

[148] CMS Collaboration, "Baseline muon selections for Run-II". https://twiki.cern.ch/twiki/bin/viewauth/CMS/SWGuideMuonIdRun2#HighPt_Muon, 2019 (accessed November 12, 2019).

[149] CMS Collaboration, "Reference muon id, isolation and trigger efficiencies for 2016 legacy re-reco data.". https://twiki.cern.ch/twiki/bin/view/CMS/MuonReferenceEffs2016LegacyRereco, 2019 (accessed November 12, 2019).

[150] CMS Collaboration, "Reference muon id, isolation and trigger efficiencies for 2017 data.". https://twiki.cern.ch/twiki/bin/view/CMS/MuonReferenceEffs2017, 2019 (accessed November 12, 2019).

[151] J. J. Brooke, D. Evans, C. Hill et al., "HEEP (High Energy Electrons and Photons) Strategy Toward First CMS Data", Technical Report CMS-IN-2007-028, CMS, Apr, 2007.

[152] D. Evans, C. Shepherd-Themistocleous, P. Vanlaer et al., "CSA06 Analysis Exercise of the SUSY/BSM High Energy Electron Pair working group", Technical Report CMS-IN-2007-019, CMS, Feb, 2007.

[153] CMS Collaboration, "HEEP Electron ID and isolation". https://twiki.cern.ch/twiki/bin/view/CMS/HEEPElectronIdentificationRun2, 2019 (accessed November 12, 2019).

[154] B. Clerbaux, D. Cockerill, G. Daskalakis et al., "Search for high mass di-electron resonances with the full 2016 data", Technical Report AN-2016/404, CMS, 2016.

[155] B. Clerbaux, D. Cockerill, G. Daskalakis et al., "Search for high-mass resonances in the di-electron final state with 2017 data", Technical Report AN-2018/021, CMS, 2018.

[156] CMS Collaboration, "Performance of missing energy reconstruction in 13 TeV pp collision data using the CMS detector", Technical Report CMS-PAS-JME-16-004, CMS, 2016.

[157] CMS Collaboration, "Jet Identification for the 13 TeV data Run2017". https://twiki.cern.ch/twiki/bin/view/CMS/JetID13TeVRun2017, 2019 (accessed November 12, 2019).

[158] J. Alwall, R. Frederix, S. Frixione et al., "The automated computation of tree-level and next-to-leading order differential cross sections, and their matching to parton shower simulations", *JHEP* **07** (2014) 079, arXiv:1405.0301. doi:10.1007/JHEP07(2014)079.

[159] S. Frixione, P. Nason, and C. Oleari, "Matching NLO QCD computations with Parton Shower simulations: the POWHEG method", *JHEP* **11** (2007) 070, arXiv:0709.2092. doi:10.1088/1126-6708/2007/11/070.

[160] S. Alioli, P. Nason, C. Oleari et al., "A general framework for implementing NLO calculations in shower Monte Carlo programs: the POWHEG BOX", *JHEP* **06** (2010) 043, arXiv:1002.2581. doi:10.1007/JHEP06(2010)043.

[161] P. Nason, "A New method for combining NLO QCD with shower Monte Carlo algorithms", *JHEP* **11** (2004) 040, arXiv:hep-ph/0409146. doi:10.1088/1126-6708/2004/11/040.

[162] S. Frixione, P. Nason, and G. Ridolfi, "A Positive-weight next-to-leading-order Monte Carlo for heavy flavour hadroproduction", *JHEP* **09** (2007) 126, arXiv:0707.3088. doi:10.1088/1126-6708/2007/09/126.

[163] S. Alioli, P. Nason, C. Oleari et al., "NLO single-top production matched with shower in POWHEG: s- and t-channel contributions", *JHEP* **09** (2009) 111, arXiv:0907.4076. [Erratum: JHEP02,011(2010)]. doi:10.1007/JHEP02(2010)011, 10.1088/1126-6708/2009/09/111.

[164] E. Re, "Single-top Wt-channel production matched with parton showers using the POWHEG method", *Eur. Phys. J.* **C71** (2011) 1547, arXiv:1009.2450. doi:10.1140/epjc/s10052-011-1547-z.

[165] T. Melia, P. Nason, R. Rontsch et al., "W+W-, WZ and ZZ production in the POWHEG BOX", *JHEP* **11** (2011) 078, arXiv:1107.5051. doi:10.1007/JHEP11(2011)078.

[166] CMS Collaboration, "Event generator tunes obtained from underlying event and multiparton scattering measurements", *Eur. Phys. J.* **C76** (2016), no. 3, 155, arXiv:1512.00815. doi:10.1140/epjc/s10052-016-3988-x.

[167] CMS Collaboration, C. Collaboration, "Investigations of the impact of the parton shower tuning in Pythia 8 in the modelling of $t\bar{t}$ at $\sqrt{s} = 8$ and 13 TeV", Technical Report CMS-PAS-TOP-16-021, CERN, Geneva, 2016.

[168] CMS Collaboration, "Extraction and validation of a new set of CMS PYTHIA8 tunes from underlying-event measurements", arXiv:1903.12179.

[169] R. D. Ball et al., "Parton distributions with LHC data", *Nucl. Phys.* **B867** (2013) 244–289, arXiv:1207.1303. doi:10.1016/j.nuclphysb.2012.10.003.

[170] NNPDF Collaboration, "Parton distributions for the LHC Run II", *JHEP* **04** (2015) 040, arXiv:1410.8849. doi:10.1007/JHEP04(2015)040.

[171] J. Alwall et al., "Comparative study of various algorithms for the merging of parton showers and matrix elements in hadronic collisions", *Eur. Phys. J.* **C53** (2008) 473–500, arXiv:0706.2569. doi:10.1140/epjc/s10052-007-0490-5.

[172] R. Frederix and S. Frixione, "Merging meets matching in MC@NLO", *JHEP* **12** (2012) 061, arXiv:1209.6215. doi:10.1007/JHEP12(2012)061.

[173] GEANT4 Collaboration, "GEANT4: A Simulation toolkit", *Nucl. Instrum. Meth. A* **506** (2003) 250–303. doi:10.1016/S0168-9002(03)01368-8.

[174] CMS Collaboration, "Search for high-mass resonances in dilepton final states in proton-proton collisions at $\sqrt{s} = 13$ TeV", *JHEP* **06** (2018) 120, arXiv:1803.06292. doi:10.1007/JHEP06(2018)120.

[175] R. Gavin, Y. Li, F. Petriello et al., "FEWZ 2.0: A code for hadronic Z production at next-to-next-to-leading order", *Comput. Phys. Commun.* **182** (2011) 2388–2403, arXiv:1011.3540. doi:10.1016/j.cpc.2011.06.008.

[176] M. Czakon, P. Fiedler, and A. Mitov, "Total Top-Quark Pair-Production Cross Section at Hadron Colliders Through $O(\alpha_S^4)$", *Phys. Rev. Lett.* **110** (2013) 252004, arXiv:1303.6254. doi:10.1103/PhysRevLett.110.252004.

[177] CMS Collaboration, "Search for high-mass resonances in final states with a lepton and missing transverse momentum at $\sqrt{s} = 13$ TeV", *JHEP* **06** (2018) 128, arXiv:1803.11133. doi:10.1007/JHEP06(2018)128.

[178] CMS Collaboration, "Performance of missing transverse momentum reconstruction in proton-proton collisions at $\sqrt{s} = 13$ TeV using the CMS detector", *JINST* **14** (2019), no. 07, P07004, arXiv:1903.06078. doi:10.1088/1748-0221/14/07/P07004.

[179] A. Buckley, J. Ferrando, S. Lloyd et al., "LHAPDF6: parton density access in the LHC precision era", *Eur. Phys. J. C* **75** (2015) 132, arXiv:1412.7420. doi:10.1140/epjc/s10052-015-3318-8.

[180] CMS Collaboration, "CMS Luminosity Measurements for the 2016 Data Taking Period", Technical Report CMS-PAS-LUM-17-001, CMS, Mar, 2017.

[181] CMS Collaboration, "CMS luminosity measurement for the 2017 data-taking period at $\sqrt{s} = 13$ TeV", Technical Report CMS-PAS-LUM-17-004, CMS, Jun, 2018.

[182] CMS Collaboration, "Measurement of the differential cross section for $\mathrm{t\bar{t}}$ production in the dilepton final state at $\sqrt{s} = 13$ TeV", Technical Report CMS-PAS-TOP-16-011, CMS, Mar, 2016.

[183] CMS Collaboration, "Measurement of differential cross sections for top quark pair production using the lepton+jets final state in proton-proton collisions at 13 TeV", *Phys. Rev. D* **95** (2017), no. 9, 092001, arXiv:1610.04191. doi:10.1103/PhysRevD.95.092001.

[184] CMS Collaboration, "Measurement of the differential cross section for top quark pair production in pp collisions at $\sqrt{s} = 8$ TeV", *Eur. Phys. J. C* **75** (2015), no. 11, 542, arXiv:1505.04480. doi:10.1140/epjc/s10052-015-3709-x.

[185] CMS Collaboration, "Measurement of the $\mathrm{t\bar{t}}$ production cross section in the all-jets final state in pp collisions at $\sqrt{s} = 8$ TeV", *Eur. Phys. J. C* **76** (2016), no. 3, 128, arXiv:1509.06076. doi:10.1140/epjc/s10052-016-3956-5.

[186] ATLAS, CMS, LHC Higgs Combination Group, "Procedure for the LHC Higgs boson search combination in summer 2011", Technical Report ATL-PHYS-PUB-2011-011, CMS-NOTE-2011-005, CERN, Aug, 2011.

[187] R. J. Barlow and C. Beeston, "Fitting using finite Monte Carlo samples", *Comput. Phys. Commun.* **77** (1993) 219–228. doi:10.1016/0010-4655(93)90005-W.

[188] J. Conway, "Incorporating Nuisance Parameters in Likelihoods for Multisource Spectra", in *PHYSTAT 2011*, pp. 115–120. 2011. arXiv:1103.0354.

[189] A. L. Read, "Presentation of search results: The $\mathrm{CL_s}$ technique", *J. Phys. G* **28** (2002) 2693. doi:10.1088/0954-3899/28/10/313.

[190] T. Junk, "Confidence level computation for combining searches with small statistics", *Nucl. Instrum. Meth. A* **434** (1999) 435, arXiv:hep-ex/9902006. doi:10.1016/S0168-9002(99)00498-2.

[191] A. N. Kolmogorov, "Sulla determinazione empírica di uma legge di distribuzione", *Giornale dell'Istituto Italiano degli Attuari* **4** (1933) 83–91.

[192] N. V. Smirnov, "On the estimation of the discrepancy between empirical curves of distribution for two independent samples", *Bull. Math. Univ. Moscou* (1939).

[193] T. W. Anderson and D. A. Darling, "Asymptotic Theory of Certain "Goodness of Fit" Criteria Based on Stochastic Processes", *Ann. Math. Statist.* **23** (06, 1952) 193–212. doi:10.1214/aoms/1177729437.

[194] CMS Collaboration, "Identification techniques for highly boosted W bosons that decay into hadrons", *JHEP* **12** (2014) 017, arXiv:1410.4227. doi:10.1007/JHEP12(2014)017.

[195] G. Cowan, K. Cranmer, E. Gross et al., "Asymptotic formulae for likelihood-based tests of new physics", *Eur. Phys. J. C* **71** (2011) 1554, arXiv:1007.1727. [Erratum: Eur.Phys.J.C 73, 2501 (2013)]. doi:10.1140/epjc/s10052-011-1554-0.

[196] CMS Collaboration, "Projected performance of Higgs analyses at the HL-LHC for ECFA 2016", Technical Report CMS-PAS-FTR-16-002, CMS, May, 2017.

[197] S. Catani, "Aspects of QCD, from the Tevatron to the LHC", in *1st Les Houches Workshop on Physics at TeV Colliders*, pp. 4–33. May, 2000. arXiv:hep-ph/0005233.

[198] C. Collaboration, "Search for excited leptons in llgamma final states in proton-proton collisions at the HL-LHC", Technical Report CMS-PAS-FTR-18-029, CERN, Geneva, 2019.

Declaration of Pre-Released Results

Parts of the results presented in this thesis are published in the following journal article:

CMS Collaboration, "Search for an excited lepton that decays via a contact interaction to a lepton and two jets in proton-proton collisions at $\sqrt{s} = 13$ TeV", JHEP 05 (2020) 052, arXiv:2001.04521. DOI: 10.1007/JHEP05(2020)052.

The author of this thesis was the main author of the above publication, which focuses on results derived in this thesis.

Eidesstattliche Erklärung

Jonas Roemer erklärt hiermit, dass diese Dissertation und die darin dargelegten Inhalte die eigenen sind und selbstständig, als Ergebnis der eigenen originären Forschung, generiert wurden.

Hiermit erkläre ich an Eides statt

1. Diese Arbeit wurde vollständig oder größtenteils in der Phase als Doktorand dieser Fakultät und Universität angefertigt;
2. Sofern irgendein Bestandteil dieser Dissertation zuvor für einen akademischen Abschluss oder eine andere Qualifikation an dieser oder einer anderen Institution verwendet wurde, wurde dies klar angezeigt;
3. Wenn immer andere eigene- oder Veröffentlichungen Dritter herangezogen wurden, wurden diese klar benannt;
4. Wenn aus anderen eigenen- oder Veröffentlichungen Dritter zitiert wurde, wurde stets die Quelle hierfür angegeben. Diese Dissertation ist vollständig meine eigene Arbeit, mit der Ausnahme solcher Zitate;
5. Alle wesentlichen Quellen von Unterstützung wurden benannt;
6. Wenn immer ein Teil dieser Dissertation auf der Zusammenarbeit mit anderen basiert, wurde von mir klar gekennzeichnet, was von anderen und was von mir selbst erarbeitet wurde;
7. Ein Teil oder Teile dieser Arbeit wurden zuvor veröffentlicht und zwar in:

CMS Collaboration, "Search for an excited lepton that decays via a contact interaction to a lepton and two jets in proton-proton collisions at $\sqrt{s} = 13$ TeV", JHEP 05 (2020) 052, arXiv:2001.04521. DOI: 10.1007/JHEP05(2020)052.

Aachen, 17. Dezember 2020

Jonas Roemer

Danksagung

Schlussendlich möchte ich die Gelegenheit nutzen einigen Personen zu danken, ohne welche diese Arbeit nicht zu Stande gekommen wäre.

Zunächst möchte ich meinen Dank an Herrn Prof. Hebbeker ausdrücken, der mir die Möglichkeit eröffnet hat, am III. Physikalischen Institut A zu promovieren. Sowohl für die fachliche Betreuung, als auch für das Arbeitsumfeld und die Möglichkeit 1.5 Jahre am CERN zu verbringen, möchte ich mich herzlich bedanken.

Herrn Prof. Pooth danke ich für die Erstellung des Zweitgutachtens und Frau Dr. Hoepfner für die fachlich Betreuung der Arbeit und die vielen Ratschläge während meiner Doktorarbeit.

Auch den anderen Mitgliedern und ehemaligen Mitgliedern des Instituts möchte ich für das angenehme Arbeitsumfeld und die ständige Bereitschaft, Fragen zu beantworten, danken. Für das Korrekturlesen meiner Arbeit bedanke ich mich besonders bei Sebastian Wiedenbeck, Christoph Schuler, Markus Merschmeyer, Tobias Pook, Andreas Albert, Thomas Esch, Giovanni Mocellin und Sebastian Thuer. Auch der IT Abteilung um Thomas Kress und Andreas Nowack und der Verwaltung um Markus Merschmeyer, Melanie Strothotte und Iris Rosewick gilt mein Dank.

Weiterhin möchte ich mich bei der EXO Gruppe am CERN für die vielen Verbesserungsvorschläge und Unterstützung für die Herausgabe meiner Veröffentlichung bedanken.

Zum Abschluss möchte ich mich besonders bei meiner Familie, meinen Eltern Christina und Ernst Roemer und bei meinen Freunden für die Unterstützung während dieser Zeit bedanken.